Three-dimensional plant-derived biomaterials

Scaffolds for tissue engineering and biophysical manipulation

Ryan Joseph Hickey

Thesis submitted to the University of Ottawa in partial fulfillment of the requirements for the degree of Doctor of Philosophy in Physics.

Ottawa-Carleton Institute for Physics
Department of Physics
Faculty of Science
University of Ottawa

Abstract

Cells are complex active materials that display fascinating phenomena in response to changes in their physical environments. It is well established that the physical environment dictates cell fate and function; nevertheless, the standard method of culturing and studying cells is on stiff 2-dimensional Petri dishes and glass cover slips. The difference in the magnitude of the stiffness of the substrate in addition to the 2-dimensional character, leads to an incomplete and perhaps misleading picture of the cellular process under scrutiny. As such, an entire field has been dedicated to developing materials that more closely match the characteristics of the natural cellular milieu: biomaterials. Despite significant progress in the field, we are still far from fully recapturing the native environment. Importantly, many of the current strategies for engineering 3-dimensional biomaterials have specific applications yet lack flexibility to be adapted to a wide variety of functions. Our approach is to repurpose existing complex, readily available materials to create a platform for biomaterial production; our biomaterials are derived from plant tissue. Plants have evolved over millions of years to attain structures with intricate geometries for specialized functions. Due to the wide variety of plant structures, one can easily select a plant-based material with analogous features to the tissue of interest. A series of investigations are presented on these novel biomaterials to demonstrate this approach, quantify the mechanical properties, and study the cellular responses. First, we developed a method of processing plant materials to yield decellularized, cellulose-based, biocompatible scaffolds that can be repopulated with mammalian cells. We then created composite materials by casting hydrogels around the cellulose-based scaffolds, which allowed us to incorporate distinct temporal and spatial cues to the local cell populations. Spatial organization of tissues and tissue interfaces remains a primary challenge in biomedical engineering, as tissue interfaces mark complex transitional zones between distinct cell populations. Replicating and repairing this intricate delineation of cell types and mechanical profiles has proven to be a major concern in regenerative medicine. As such, we sought to develop a platform for engineered tissue interfaces, wherein components are combined in a modular fashion into a functional unit. The mechanical cues of the microenvironment affect a plethora of cellular processes, namely cell migration, proliferation, and differentiation. Consequently, the rheological properties of our decellularized, plant-based scaffolds were thoroughly investigated. An in-depth knowledge of the mechanics of the underlying substrate is required to guide future applications and refinements of this technology. The potential applications of these 3-dimensional constructs, as demonstrated through our findings, include designing in vitro models of tissue interactions, new biomaterials for in vivo applications, and studies on fundamental cellular processes. We highlight the significance of our results in a collection of scientific articles, which are presented in the body of this thesis (Chapters 2-5). This work is focused on the use of plant-derived cellulose materials, which forms a subsection of the cellulose biomaterial field. A review article centered on the use of cellulose materials for tissue engineering serves as an introductory chapter.

Author's note

The scientific method is built upon the notion of forming questions, generating hypotheses, and testing these hypotheses. In order to accomplish this task, a set of objective investigations must be carried out meticulously and with a high degree of scrutiny. As research delves into new regimes, interdisciplinary approaches are required to carry out the objectives of the study and test the hypotheses thoroughly. In diverse fields, such as biophysics, biomaterials, and tissue engineering, the integration of knowledge from different disciplines is essential. In this thesis, we present an interdisciplinary approach to developing and studying novel cellulose-based biomaterials. Here we use techniques from cell biology, molecular biology, organic chemistry, material science, and physics to address specific questions associated with our hypotheses. The major tool used in this body of work is microscopy. Microscopy itself is an interdisciplinary field; advancements in optics, electronics, and biology have led to significant improvements in microscope designs. An excellent example is laser scanning confocal microscopy, which uses lasers and a pinhole to image thin planes within a specimen. The concept of the laser was first predicted by Einstein, and its use in combination with high precision lenses and electronic detection systems has resulted in the creation of a common tool for studying biological processes. In turn, developments in chemistry, biochemistry, and molecular/cell biology have enabled the visualization of specific structures within the cell. The results presented in this thesis would not be possible without the integration of knowledge from diverse areas of science. Scientific endeavors are made possible through collaboration and drawing on previous studies; therefore, we can gain an appreciation for accumulating knowledge for its own sake rather than for solving specific problems, as it is difficult to predict what this knowledge will be used for in the future.

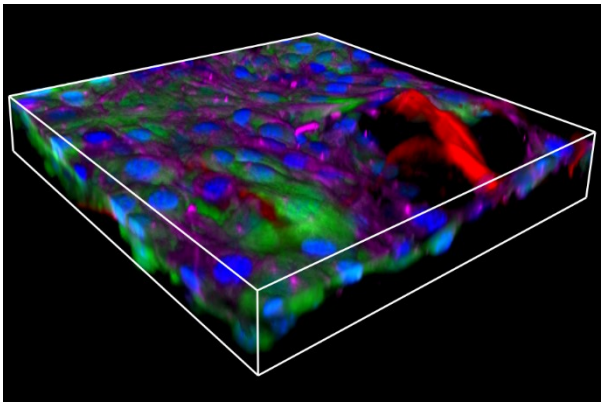

Figure P1. 3D laser scanning confocal microscopy image. 3T3 fibroblast cells on a 3D decellularized apple-derived cellulose-based scaffold. Blue = Hoechst 33342 stained nuclei, green = green fluorescent protein within the cells, red = cellulose stained with Congo red, purple = microtubules stained with SiR-Tubulin. Scale = 211 x 211 x 50 μm.

Statement of contributions

I, Ryan J. Hickey, was the main contributor to the work included in this thesis. The experiments were designed, performed, and analyzed by me under the guidance of Dr. Andrew E. Pelling. In some cases, the work involved collaborations with other researchers. Acknowledgments of their contributions are given before the appropriate manuscript included in the subsequent chapters. Specifically, Dr. Andrew E. Pelling guided the papers and performed editing on all the manuscripts. Dr. James L. Harden aided with rheological studies, provided advice on the corresponding data analysis, and edited the rheological analysis sections in the manuscripts. Dr. Yun Liu performed scanning electron microscopy and energy dispersive spectroscopy. Dr. Charles M. Cuerrier, PhD candidate Daniel J. Modulevksy, and PhD candidate Maxime LeBlanc Latour aided in animal surgeries. Medical student Isabel Shore helped maintain cell cultures. PhD candidate Matthew J. Walker designed and built the custom dynamic mechanical analysis device used in this thesis.

To the best of the author's knowledge, this body of work is novel research. The studies presented in this thesis are included as scientific manuscripts. The first chapter is a review paper that serves as the introduction. Chapter 2 comprises a technical section to supplement the reader with background information of the main tools and themes presented in this thesis. The experimental research components are contained in Chapters 3-6, which are formatted as manuscripts published, submitted, and prepared for scientific journals. Each chapter is prefaced with a brief outline of the context of the study and the main objectives and hypotheses. Lastly, the significance of this body of work and future directions are summarized in Chapter 6.

Contributions

Manuscripts included in this thesis

- Hickey, R. J., Leblanc Latour, M., Harden, J. L. & Pelling, A. E. Engineered Tissue Interfaces – A Platform for Tissue Engineering. Manuscript in preparation (2020).
- Hickey, R. J., Harden, J. L. & Pelling, A. E. Apple-derved biomaterials are viscoelastic scaffolds – A rheological study. Manuscript in preparation (2020).
- Hickey, R. J. & Pelling, A. E. Cellulose Biomaterials for Tissue Engineering. *Front Bioeng Biotechnol.* **7**, 1–15 (2019).
- Hickey, R. J., Modulevsky, D. J., Cuerrier, C. M. & Pelling, A. E. Customizing the Shape and Microenvironment Biochemistry of Biocompatible Macroscopic Plant-Derived Cellulose Scaffolds. *ACS Biomater. Sci. Eng.* **4**, 3726–3736 (2018).
- Hickey, R. & Pelling, A. E. The rotation of mouse myoblast nuclei is dependent on substrate elasticity. *Cytoskeleton* **74**, 184–194 (2017).

Conferences and workshops

- Hickey, R. J. & Pelling, A.E. The dependence of cellular nuclear rotation on substrate elasticity. Oral presentation at the *1st Annual Meeting of the Biophysical Society of Canada* (National) (June 2015).
- Hickey, R. J. & Pelling, A.E. The dependence of cellular nuclear rotation on substrate elasticity. Poster at the *3rd Annual Cell Dynamics Workshop* (National) (May 2014).

Other contributions

During my time conducting research for my doctoral thesis, I have also contributed to other bodies of work in related yet distinct branches of biophysics.

Contributions to other manuscripts

- Modulevsky, D. J., *et al.* Plant-derived cellulose scaffolds as a novel platform for spinal cord injury in complete transection rat models. Manuscript in preparation (2020).
- Leblanc Latour, M. *et. al.* Plant-derived cellulose scaffolds for bone tissue engineering. *ACS Biomater. Sci. Eng.* Submitted (2020).
- Alshehri, A. M. *et al.* Selective cell adhesion on femtosecond laser-microstructured polydimethylsiloxane. *Biomed. Mater.* **11**, (2016).
- Haase, K.*et al.* Simultaneous optical and mechanical probes to investigate complex cellular responses to physical cues. *Proc. SPIE **9327**, Optical Elastography and Tissue Biomechanics II, 93270I* (2015).

Art-Science exhibitions

- Whittaker, E., Hickey R. J. & Pelling A. E. Murky Bodies. *Red Head Gallery, Toronto* (2020).
- Whittaker, E., Hickey R. J. & Pelling A. E. Contained. *La Fabrique du Vivant : Pompidou Centre, Paris, France* (2019).
- Whittaker, E., Hickey R. J. & Pelling A. E. Contained. *Red Head Gallery, Toronto* (2018).

Industrial reports

- Hickey, R. J. & Pelling, A.E. Mycelium Scaffolds for Bone Tissue Engineering. *A technical report submitted to Ecovative,* 2019
- Hickey, R. J. & Pelling, A.E. Biocompatibility of FRESH hydrogels. *Results presented to IRNAS,* 2018

Acknowledgements

I would like to thank Dr. Andrew E. Pelling for all that he has done and all that I have learned in his lab since I first began research as an undergraduate student. Along with many other qualities, his passion for knowledge and inquisitive nature are inspiring. Under his guidance, I was able to develop many technical and analytical skills, but most importantly, I gained an appreciation for applying rigorous exploration to questions that do not have immediate or evident applications. I have been fortunate to be taught by many fantastic instructors throughout my academic career thus far. Specifically, I would like to thank Dr. James L. Harden for his mentorship as well as captivating my interest in biophysics and encouraging me to pursue physics. Thank you to Dr. Delphine Gourdon and Dr. Bela Joos for their support and guidance. I would like to extend a thank you to the entire Faculty of Science and the Support Staff at the University of Ottawa for a wonderful experience. I am grateful for all the students I got the opportunity to work alongside, learn from, and develop friendships with. I would also like to thank Mr. Beingessner for starting me down this road. Most importantly, thank you to Isabel, Tim, Emma, Steph, and Chelsea for your support and encouragement in all areas of my life.

Abbreviations

- 2,2,6,6-tetramethylpiperidine-1-oxyl (TEMPO)
- 2-dimensional (2D)
- 3-dimensional (3D)
- Adenosine triphosphate (ATP)
- Amphiphilic comb-like polymer (APCLP)
- Atomic force microscopy (AFM)
- Bone morphogenic protein (BMP)
- Carbon nanotubes (CNTs)
- Cell Counting Kit-8 (CCK-8)
- Charged coupled device (CCD)
- Cluster of differentiation (CD)
- Computerized numerical control (CNC)
- Deoxyribonucleic acid DNA
- Difference of Gaussians (DoG)
- Dulbecco's modified eagle medium (DMEM)
- Electron dispersion spectroscopy (EDS)
- Engineered tissue interfaces (ETI)
- Extracellular matrix (ECM)
- Fetal bovine serum (FBS)
- Gelatin (GE)
- Gelatin crosslinked with glutaraldehyde (GXG)
- Glutaraldehyde (GA)
- Green fluorescent protein (GFP)
- Guided assembly-based biolithography (GAB)
- Hematoxylin and eosin (H&E)
- Human microvascular endothelial cells (HMECs)
- Human umbilical vein endothelial cells (HUVECs)
- Intermediate filaments (IFs)
- Laser scanning confocal microscopy (LSCM)
- Linear assignment problem (LAP)
- Linear viscoelastic region (LVR)
- Linker of nucleoskeleton and cytoskeleton (LINC)
- Masson's trichrome (MT)
- Mean squared angular displacement (MSAD)
- Paraformaldehyde (PFA)
- Pharmacologically active microcarriers (PAMs)
- Phosphate buffered saline (PBS)
- Poly(3,4-ethylenedioxythiophene) (PEDOT)
- Polyethylene glycol (PEG)
- Poly(ethylene terephthalate) (PET)
- Polydimethylsiloxane (PDMS)
- Polylactic acid (PLA)
- Polytetrafluoroethylene (ePTFE)
- Polyvinyl alcohol (PVA)
- Polyvinyl chloride (PVC)
- Revolutions per minute (RPM)
- Scanning electron microscopy (SEM)
- Small angle neutron scattering (SANS)
- Small-diameter replacement vascular grafts (SDRVGs)
- Sodium dodecyl sulfate (SDS)
- Standard deviation (s.d.)
- Standard error of the mean (s.e.m.)
- Subcutaneous (s.c.)
- (2,3,6,6-Tetramethylpiperidin-1-yl)oxyl (TEMPO)
- Sum frequency generation (SFG)
- Wheat germ agglutinin (WGA)

Table of Contents

List of Figures

List of Tables

Thesis overview and scope

This thesis is comprised of novel research presented as scientific manuscripts and pertinent background knowledge. First, I present a review of the field of cellulose-based biomaterials to establish context for the subsequent chapters and the state of the current research. In Chapter 2, I provide a technical and theoretical background section to provide the reader with background information of the main tools and themes presented in this thesis. The experimental research components are contained in Chapters 3-6, which are formatted as manuscripts published, submitted, and prepared for scientific journals. In Chapter 3 we test the hypothesis that cellulose-based biomaterials complexed with temporary and permanent hydrogels are biocompatible. We prove that temporary and permanent hydrogels can be used to provide spatial and temporal cues to cells on customized scaffold geometries. In Chapter 4, we investigate the hypothesis that engineered tissue interfaces (ETIs) can be created by combining highly porous, decellularized, plant-derived scaffolds in a modular fashion. We establish a platform for creating tissue interfaces from interlocking scaffolds for in vitro and in vivo models. In Chapter 5, we perform a rheological characterization of the novel biomaterial. As hypothesized, we show that the materials are viscoelastic and have a largely elastic contribution. In Chapter 6, we extend our research of cellular nuclear rotation that we previously performed on 2D gelatin hydrogels, which is included in the Appendix, and prove that our biomaterial can be used as an in vitro modelling system to further study this phenomenon in physiologically relevant contexts. Lastly, in Chapter 7, I comment on the future investigations and significance of this body of work.

Thesis statement and hypotheses

The overarching thesis statement for this body of work is that plant-derived cellulose-based scaffolds can be used as biomaterials for tissue engineering. Several specific hypotheses were developed to test this claim. In the following chapters, these hypotheses are identified and challenged with experimental data acquired using the scientific method.

Chapter 1

Introduction: Cellulose Biomaterials for Tissue Engineering

This chapter was previously published as a review paper:

Hickey, R. J. & Pelling, A. E. Cellulose Biomaterials for Tissue Engineering. *Frontiers in Bioengineering and Biotechnology.* 7, 1–15 (2019).

§1 Motivation

The natural microenvironment of cells is drastically different from stiff glass or plastic culture plates; however, these substrates are the standard materials used to culture and study cells. Expanding to 3D cell culture on soft, porous materials is required to advance fundamental research and tissue engineering. Creating biomimetic microenvironments is critical as the physical and biochemical characteristics of the cellular niche dictates cell fate and function. Several groups have been testing the hypothesis that cellulose-based biomaterials constitute a viable class of materials for 3D cell scaffolds and tissue engineering. Here, I present a review paper to serve as an introductory chapter on the field of cellulose biomaterials. Recent advances in the field are highlighted, and different approaches for creating cellulose-based scaffolds and composites are discussed. The work of several key studies reveal that cellulose materials can be used as biocompatible 3D constructs both in vitro and in vivo.

1.1 Abstract

In this review, we highlight the importance of nanostructure of cellulose-based biomaterials to allow cellular adhesion, the contribution of nanostructure to macroscale mechanical properties, and several key applications of these materials for fundamental scientific research and biomedical engineering. Different features on the nanoscale can have macroscale impacts on tissue function. Cellulose is a diverse material with tunable properties and is a promising platform for biomaterial development and tissue engineering. Cellulose-based biomaterials offer some important advantages over conventional synthetic materials. Here we review cellulose-based biomaterials in the context of bottom-up approaches for tissue engineering.

1.2 Introduction

A fundamental understanding of the nanoscale details of the environment is essential for designing biomaterials that mimic the natural cellular milieu. Many features of the local environment have profound influences on cell adhesion, proliferation, maturation, and differentiation. As such, small differences in nanostructure can have macroscale impacts on tissue function. In this review, we highlight the importance of nanostructure of cellulose-based biomaterials to allow cellular adhesion, the contribution of nanostructure to macroscale mechanical properties, and several key applications of these materials for fundamental scientific research and biomedical engineering. Cellulose is a diverse material with tunable properties and can be applied to systems with vastly different biochemical and biophysical environments. It should be noted that many polymers can be functionalized; therefore, polymers in general are diverse materials. Cellulose-based biomaterials offer some important advantages over conventional synthetic materials and show great promise to advance the frontier of scientific knowledge. Here we provide an up-to-date summary of the status of the field of cellulose-based biomaterials in the context of bottom-up approaches for tissue engineering. We anticipate that cellulose-based material research will continue to expand because of the diversity and versatility of biochemical and biophysical characteristics highlighted in this review.

1.3 Cellular attachment at the nanoscale

1.3.1 Cell adhesion

It is well established that the extracellular matrix (ECM) not only allows for cell attachment, but also provides biochemical and biophysical cues to the nascent cells and tissues [1–6]. In order for cells to sense and respond to their physical environment, they must first establish a physical connection [7,8]. This physical connection is often mediated by the integrin protein complexes that recognize the widely conserved tripeptide recognition sequence of the ECM [9]. It is important to note that the integrin-based attachment to the RGD motif is not the only method of attachment; however, it has been studied in depth. The integrin receptor complexes constitute a variable class of proteins that are heterodimeric with two membrane-spanning subunits [9,11–13]. The integrin receptors are linked to the cytoskeleton by focal adhesion complexes[14]. The focal adhesions are multi-protein complexes organized in specific strata. The base layer establishes a membrane-apposed integrin signaling layer [10]. The basal layer is followed by the force transduction zone (cytoskeletal adaptors), and the upper most layer mediates the cytoskeleton regulatory protein connections [10]. Evidently, the physical cues of the environment on the nanoscale elicit specific responses and dictate cellular function [15–21]. A schematic of the cell attachment is presented in Figure 1.1. Specifically, the topography, adhesion chemistry and localization, and mechanics play crucial roles in regulating cell fate and function [22–24]. The cell adhesion machinery along with the

hydrophilic hydroxyl moieties of the cellulose and specialized cellulose binding domains allow cells to attach to cellulose [25–27].

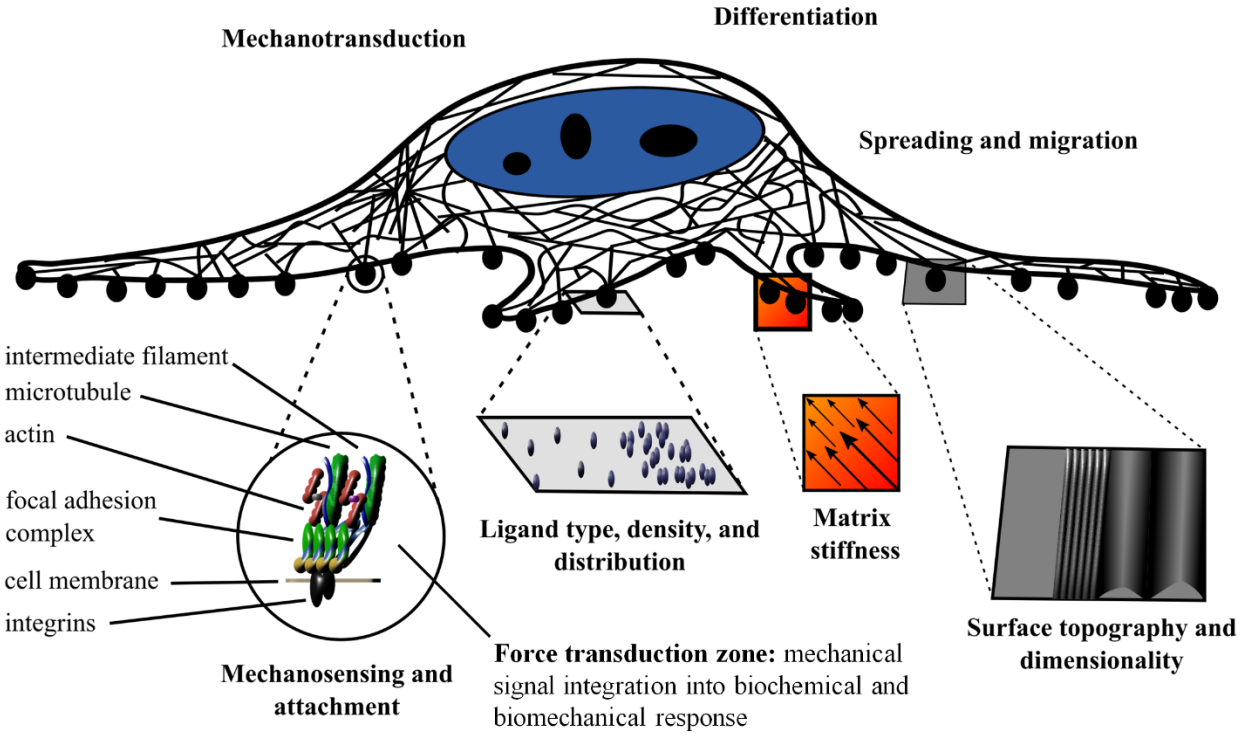

Figure 1.1: Schematic of the influence of the local physical and biochemical environment on cell fate and function. Mechanosensing and mechanotransduction are mediated by cell adherence to the substrate via integrins and the interaction of focal adhesions and the cytoskeleton. The ligand type, density, and distribution as well as the matrix stiffness, surface topography, and dimensionality provide distinct cues to the cell and elicit specific responses.

1.3.2 Effects of the nanoenvironment

The biochemistry of the surrounding environment has effects on cell morphology, adhesion, and proliferation [28]. Cell attachment is dependent on the type of ligand in the ECM and the spacing of the ligand. Cells can modulate their environment by secreting ECM proteins [29]. The nanoscale distribution of adsorbed proteins in both area and clustering affects cell adhesion [30]. The ligand density at the nanoscale level and integrin clustering affects spreading, focal contact formation, stress fibre arrangement, cell motility, and filopodia and lammelipodia development [31,32] . For example, different ligand densities give rise to the apparent paradoxal enhanced tumor growth with RGD analogues [32]. The paradoxal enhanced tumor growth with RGD analogues is the phenomenon where tumors grow and spread where contact and adhesion are suppressed. It occurs

as the density is shifted from the optimal density to the permissive density region [32]. The permissive density mimics receptor blocking drugs and sheds light on the paradoxal enhanced tumor growth with RGD analogues [32]. Nanostructure dimensions are important in addition to substrate rigidity [33]. There has been debate over whether matrix stiffness or ligand density regulates differentiation; however, after decoupling the surface chemistry and stiffness effects, it was elucidated that matrix stiffness is an independent regulator of stem cell differentiation [34,35]. Both the matrix stiffness and nanoscale spatial organization of the ligands direct stem cell fate [16,29,32,34–36]. The physical cues are not restricted to elasticity; local changes in surface structure, hydrophobicity, roughness, and charge density lead to different cell adhesion and proliferation properties [37–39]. Taken together, there is an integrated response to external and internal stimuli on the nanoscale, both physical and biochemical in nature [1] (Fig. 1.1). Mimicking the complexity of the nanoscale environment is essential for tissue engineering.

1.4 The potential of cellulose as a biomaterial

1.4.1 Suitability for biomaterials and scaffolding

In order to replicate important aspects of the in vivo environment, biomaterials must be biocompatible and contain specific mechanical, biochemical, and physical properties. As a polymer of glucose subunits [40], cellulose is an ideal candidate for biomaterial manufacturing because of its tunable chemical, physical, and mechanical properties [41–44]. The source material is abundant in nature and is easily produced; consequently, cellulose-based materials constitute a low cost platform for tissue engineering. Biocompatibility, bioactivity, and biomechanics are three integral requirements of any biomaterial; cellulose-based biomaterials satisfy each of these criteria [41–43]. The reader is encouraged to consider inertness as a requirement as well. A biologically inert material is desired to eliminate foreign body responses. Nevertheless, completely biologically inert materials do not exist. Hence we argue proper bioactivity is a key requirement to elicit certain responses. To that end, biodegradability is another feature to be considered. Cellulose is not biodegradable in humans. Thus, the regenerated new tissue cannot take the place of the cellulose. There is significant debate on the use of degradable materials compared to permanent constructs. Both have advantages and drawbacks. In the case of cellulose, a possible drawback is that the cellulose will occupy space that the tissue cannot. A potential advantage of using this long-lasting material is continuous structural support. Cellulose-based materials can be derived from bacteria, tunicates, and plants [41–43]. The scaffolds can be naturally derived or synthetically manufactured. The nanoscale presentation of functional chemical groups and the associated physical properties are dependent on the source material along with the fabrication process.

1.4.2 Molecular and crystal structure

The structure of cellulose is hierarchical, and the associated physical properties are a consequence of the different structural allomorphs and assemblies of elementary microfibrils [45–47]. The allomorphs of cellulose arise from the different arrangements of the chains of β-(1,4')-D-glucopyranose monomers [48–53]. Cellulose I, the native form of cellulose, is defined by specific intrachain, interchain, and intersheet hydrogen bonding and van der Waals interactions. In cellulose I, the chains run parallel to one another and are present in two main crystal structures: cellulose I_α (triclinic) and cellulose I_β (monoclinic) (Sarko and Muggli, 1974). Although both crystalline forms of cellulose I are present together, cellulose I_β is the predominant form in higher plants, whereas cellulose I_α is in abundance in bacterial and algal cellulose [58]. In contrast to the naturally occurring cellulose I, cellulose II is a synthetic material. Although the fundamental cellobiose subunits are the same as in cellulose I, the interchain and intersheet hydrogen bonding are altered due to its antiparallel arrangement [45–48,50,51,53,55–57]. Cellulose II is derived from cellulose I with alkali treatment and is an irreversible transition (Gupta et al., 2013; Jin et al., 2016; Oudiani et al., 2011a, 2011b). The third class of cellulose structure, cellulose III, is characterized by hydrogen bonding between separate sheets [50,52,63,64]. Moreover, cellulose III can be arranged in the parallel direction (cellulose III_I) or the antiparallel direction (cellulose III_{II})). Cellulose III can be made by exposing cellulose I (parallel) or cellulose II (antiparallel) to liquid ammonia and amine treatment). The formation of cellulose III is a reversible reaction; restoration to cellulose I and II respectively can be achieved with thermal treatment [50,64]. The different crystal structures and hydrogen bonding arrangements are highlighted in Figure 1.2.

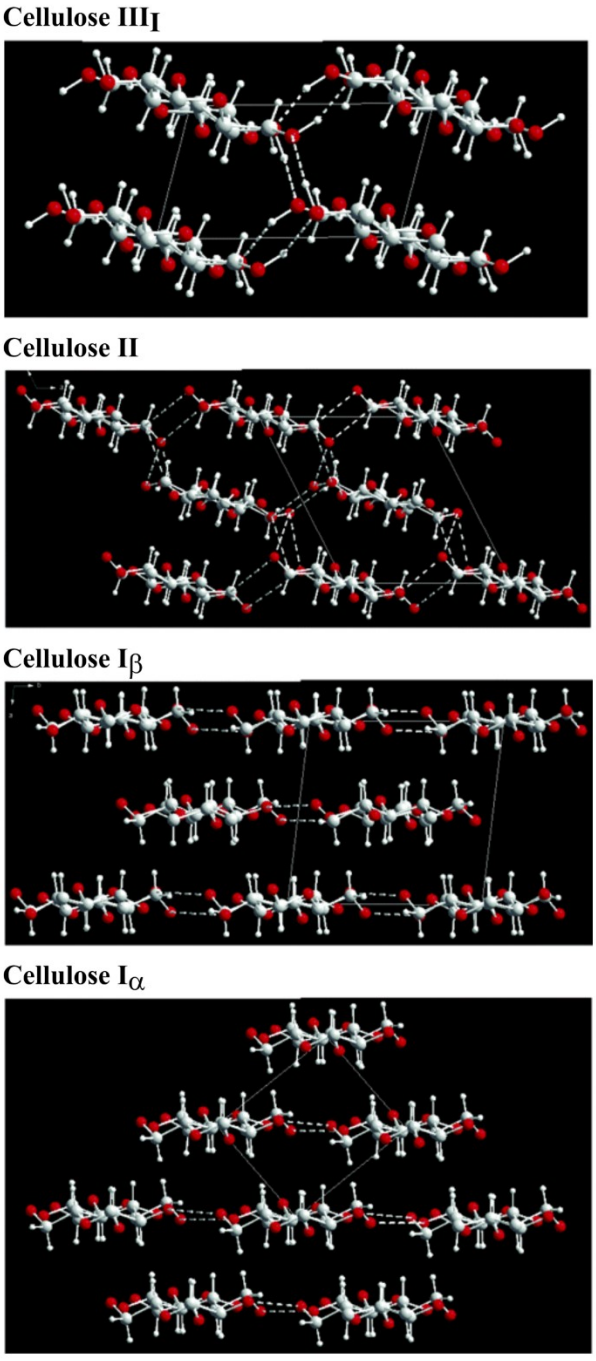

Figure 1.2: Crystal structure cellulose strands and the corresponding major hydrogen bonding arrangements. [52]. Copyright 2004. Reproduced with permission from Elsevier Inc.

1.4.3 Nanostructure dictates physical properties

The crystal structure and degree of crystallization have a profound effect on the mechanical and physical properties [46,49,66]. Importantly, the different hydrogen bonding results in different Young's moduli: cellulose I = 138 GPa, cellulose II = 88 GPa, cellulose III_I = 87 GPa, and cellulose III_{II} = 58 GPa [66]. In addition to the different moduli, the stability of the different allomorphs is also variable; in general, the order of decreasing stability is cellulose I, II, III, then amorphous [65,67–72]. In nature, cellulose exists as a mixture of crystalline and amorphous structures, plausibly organized in a fringed fibril arrangement [73]. The combination of crystalline and amorphous elements results in the observed leveling off degree of polymerization, wherein the amorphous regions depolymerize before the crystalline domains [73–75]. The stability and degradation rates are crucial factors for the design of biomaterials [76]. These amorphous regions reduce the stiffness of the microfibril. Elementary microfibrils aggregate to form larger bundles; hence, an even greater diversity of mechanical and physical properties is available because of the different microfibril arrangements of the source materials. As such, the nanoscale properties such as the disorder and coalescence ratio along with the surface chemistry dictate the macroscopic properties. Cellulose-based materials have been selected for use as biomaterials because of their diverse and tunable properties [41–43].

1.5 Bacterial and plant cellulose

1.5.1 Natural vs synthetic materials

In general, cellulose-based materials can be divided into naturally derived and synthetic materials (Fig 1.3). As shown in Figure 1.3, naturally derived (such as bacterial and plant based scaffolds) as well as synthetic materials can be used as biomaterials. The naturally derived celluloses have a cellulose I crystal structure [50,72], whereas the synthetic materials are cellulose II and III [52,62]. Pulp and paper is an entire industry dedicated to refining the production process and modifications of synthetic cellulose [77]. A discussion of the vast processing of synthetic cellulose is beyond the scope of this review; however, we highlight that the crystal structure is different, and the different crystal structures lead to significantly different physical properties.

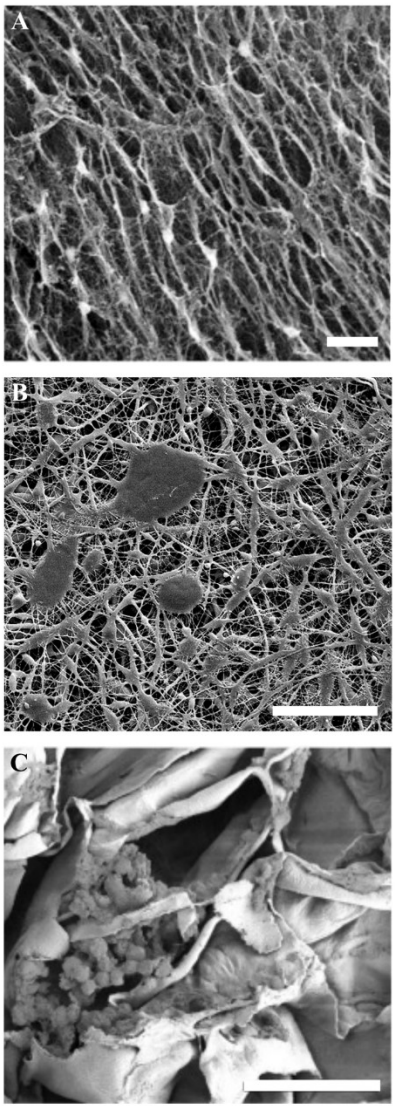

Figure 1.3: SEM images of cellulose biomaterials. (A) NIH 3T3 cells cultured on a bacterial cellulose film, scale = 10 μm. [78] Copyright 2013. Reproduced with permission from Elsevier Inc. (B) Schwann cells cultured on a synthetic electrospun cellulose matrix, scale = 100 μm. [79] Copyright 2017. Reproduced with permission from Elsevier Inc. (C) C2C12 cells cultured on decellularized apple cellulose scaffolds, scale = 50 μm. [80] Copyright 2014. Reproduced with permission from PLOS.

1.5.2 Nanostructure differences

Although bacterial and plant based cellulose are both type I, the slight differences in the crystal structure and microfibril arrangements lead to considerably different material properties [50,66,69,72]. The significant differences between bacterial and plant-based cellulose are the purity, water retention, mechanical characteristics, crystallinity, and porosity. Bacterial cellulose is pure

cellulose, while plant cellulose contains impurities such as hemicellulose and lignin [49,50,81,82]. Moreover, plant based cellulose contains a higher fraction of cellulose I_β and is less crystalline [58,81,82]. In general, the microfibrils of bacterial cellulose are smaller than those of plants; consequently, the bacterial cellulose is highly porous and exhibits extensive water retention [81,83]. It should be noted that these are general statements and the actual physical parameters of each material are influenced by many factors, not just the choice of source material. Notably, the growth medium and production method (static vs agitated vs bio reactor/trickling bead method) lead to different nanoscale arrangements of microfibrils [50,83,84]. Different strains and culture conditions produce different structures, mechanics, morphologies, crystallinity, and pore sizes [81,83,85,86]. Cellulose is a diverse material as evidenced by the wide range of physical properties. The microfibril formation and crystallization can be adjusted by changing the culture conditions and the source organism [85].

1.5.3 Mechanical properties

The relatively high Young's modulus of bacterial cellulose is attributed to the super-molecular nanostructure [81,87]. The thinner ribbon structures compared to plant based and synthetic fibres are formed through intra- and inter-hydrogen bonding [81,87]. For instance, bacterial cellulose sheets can have a Young's modulus greater than 15 GPa as well as a tensile strength of 250 MPa [87]. The extensive hydrogen bonding leads to the high thermal stability, tensile strength, and Young's modulus [81]. Moreover, these materials have suitable elastic properties and ultimate strengths, as evidenced by rheological analysis [81]. Comparatively, plant-based cellulose also has a vast range of mechanical properties and porosities [49]. Although modifications are feasible [76,80,88–90], the mechanical and physical properties can be selected by choosing specific source materials [49] (Fig. 1.4). As cellulose is abundant in nature, the enumerations of different mechanical and physical parameters are extensive. Recently, it was shown that the existing structures of plant tissue can be exploited and repurposed for tissue engineering [76,80,88–90]. This new angle on biomaterial design allows for the intricate structures of plant tissue that have been optimized for analogous functions through years of evolution to be selected for applications of interest. The nanoscale features of cellulose-based materials, both naturally derived and synthetic, can be chosen for specific biological and mechanical functions [82]. These nanoscale features are integral components of the macroscopic 3D biomaterial as they dictate cellular form and function.

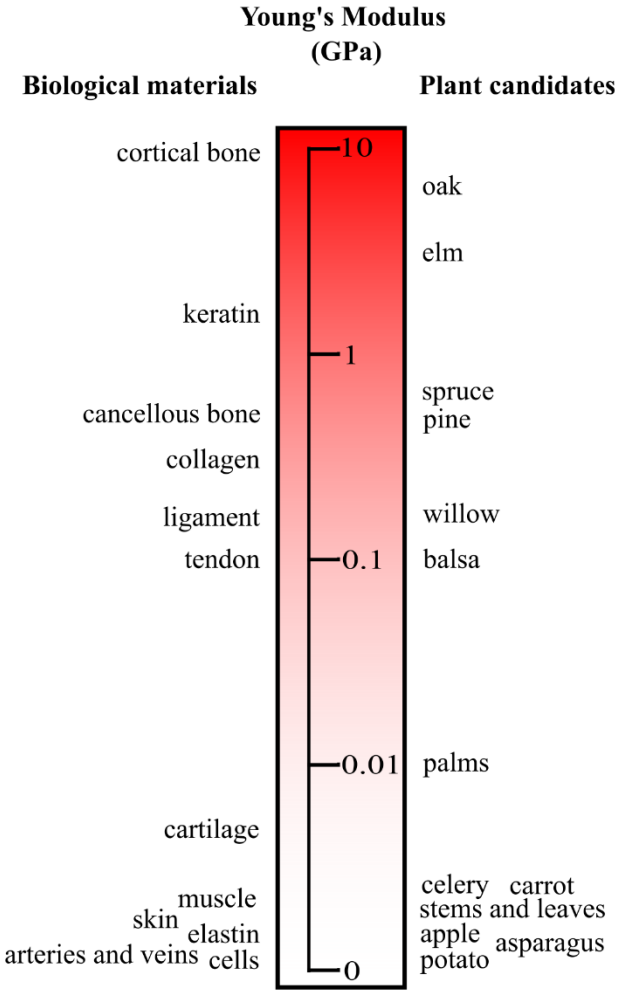

Figure 1.4: Young's modulus of plant materials and human tissues. A small subset of plant candidates are compared to key biological tissue stiffnesses. The source material can be selected to match the elasticity of the native tissue. It should be noted that with processing and modifications the moduli of the plant candidates can be tuned. Adapted from [91] with permission from Cambridge University Press.

1.6 Scaling up to 3D macrostructures with specific nano- and micro-features

1.6.1 Engineering materials with features on different length scales

The challenge of engineering biomaterials with high efficacy is incorporating particular features on the nano-, micro-, and macro-scale. Cellulose materials are highly attractive because of the customizability and control over the features at all levels [92]. At the nanoscale, different

crystallinities can be obtained; moreover, the chemical structure of the cellulose can be modified to include specific functional groups to elicit particular cellular responses [42,44,92–94]. For example, collagen can be chemically attached to the cellulose scaffold via linker molecules such as succinic acid [95]. At the microscale, the porosities of the materials can be tuned to suit the intended application. In addition, hydrogels and other composites can be created to increase the functionality [42,90,92]. On the macroscale, specific structural components and arrangements are required for proper tissue function. Bacterial and synthetic cellulose are often molded or fabricated into the desired configurations [96–98]. Importantly, guided assembly-based biolithography (GAB) is a molding technique used to transfer nanoscale functional topographies to the surface of the cellulose [99]. The mold is introduced at the gas/liquid interface where the cellulose is being synthesized, and the cellulose nanofibers are directionally assembled in a three-dimensional network dictated by the mold [99]. Significantly, the 3D macrostructure of bacterial and synthetic cellulose can be controlled [84,85,99,100]. For example, free standing, biocompatible hollow spheres and lenses with porous BC membranes can be synthesized [100]; the control over the geometry is attained through tuning and patterning the hydrophobicity of the synthesis surface [100]. Conversely, for plant derived scaffolds, the complex pre-existing 3D structures can be selected from nature and subsequently modified to suit the application of the biomaterial [49,76,80,82,89,90]. The plant derived scaffolds, as in the case of bacterial and synthetic cellulose, can be tuned chemically and physically, are biocompatible, exhibit vascularization, and are widely available and feasibly produced [49,76,80,82,89,90].

As a result, there are vast production methods available for producing 3D cellulose scaffolds engineered to have specific features at the nano-, micro-, and macro-scale. The advantage of the molding and fabrication approach is having control over the design of particular structures; the advantage to exploiting the existing structures in nature is the high complexity. Combining both approaches opens up even more possibilities and potential applications [76,80,88–90]. Figure 1.5 depicts two approaches to create macroscopic ear structures: carving and 3D printing/molding.

1.6.2 Characterization of nano- and micro-features in macrostructures

Interestingly, incorporation of deuterium has been shown to have no significant differences in the molecular and morphological properties of bacterial cellulose [101]. Consequently, small angle neutron scattering (SANS) methods can be used to probe cellulose structure and dynamics in addition to conventional techniques [101]. Furthermore, Lee et al. have shown that the noncentrosymmetry and phase synchronization requirements of vibrational sum frequency generation (SFG) spectroscopy can be used to decipher the 3D organization cellulose of plants, tunicates, and bacteria [82]. In plant cell walls, this signal is unique to cellulose, as all other matrix polymers in plant cell walls such as hemicellulose, pectin, and lignin are amorphous and do not produce detectable SFG signals [82]. The cellulose structure and packing have been investigated on the mesoscale of plant cell walls, tunicate tests, and bacterial films [82]. Armed with the knowledge

of the characteristics of the cellulose material at each length scale of interest, researchers can design complex biomaterials for specific applications. In the subsequent sections, we highlight several key applications of these constructs.

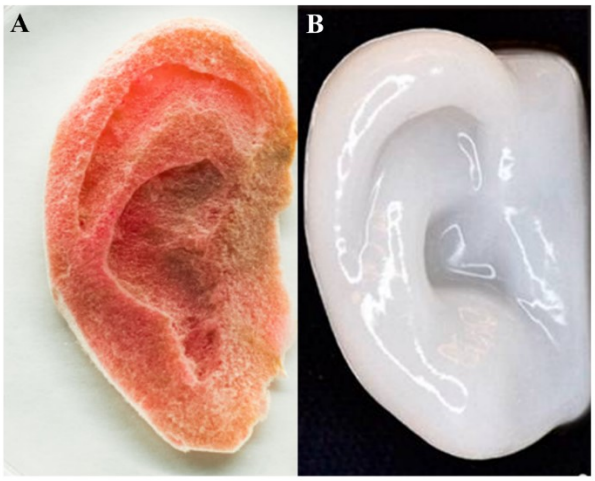

Figure 1.5: Human ear scaffolds carved out of plant-based cellulose (A) and 3D printed with nanofibrillated cellulose both cultured with human cells (HeLa and chondrocytes respectively). (A): (Hickey et al., 2018) Copyright 2018. Reproduced with permission from American Chemical Society. (B): (Markstedt et al., 2015) Copyright 2015. Reproduced with permission from American Chemical Society.

1.7 Applications

1.7.1 Skin and wound dressings

Significant interest in using cellulose biomaterials for artificial skin and wound dressings stems from the tunable mechanical properties, high biocompatibility, versatile and customizable surface structure and chemistry, drug releasing capabilities, and moisture maintenance. As a result, several artificial skin products are commercially available.

As such, topical features are required to guide cell infiltration, proliferation, and angiogenesis [99]. These topical features of cellulose materials can be conferred with GAB methods [99]. In another approach, nanocellulose can be used as a bioink for printing and modifying film surfaces [102]. In this regard, chemically modified nanocellulose fibrils reduce the viscosity and yield a bioink with suitable rheological properties for printing and skin applications [102]. The bioprinting allows for the construction of porous nanocellulose structures [102]. For instance, C-Periodate nanocellulose has

been used to print highly porous, 3D track structures with the capacity to carry and release antimicrobial components [102].

In an attempt to recreate the complexity of the in vivo nanoenvironment, electrospinning has also been employed [103,104]. This technique allows for the creation of 3D porous matrices that mimic the natural structure of skin [103,104]. Of particular interest is the electrospinning of composites of cellulose acetate and hydrogels such as gelatin and polyurethane to form the scaffold [103,104]. The addition of the hydrogel can change nanoscale features of the cellulose material such as fibre diameter [103]. Moreover, the porosity, stiffness, hydrophilicity, fluid uptake, and surface area can be tuned by varying the ratio of the constituents to increase the rate of wound healing [103,104]. One common issue in designing artificial skins and wound dressings is that the material must adhere to the wound to support healing but then must be easily removed without damaging the regenerated tissue [103]. Varying the relative amounts of constituents in composites can achieve the desired adherency features of the material [103]. Notably, electrospun cellulose acetate/gelatin composites at a ratio of 25:75 promote cell proliferation and collagen deposition, while a ratio of 75:25 can act as a low-adherent wound dressing [103].

Nanofibrillar cellulose has also been used in clinical trials [105]. Functionalized nanofibrillar cellulose dressings have been applied to heal and regenerate skin for burn victims [105]. The physical and mechanical properties of the nanocellulose dressings can be optimized to suit the patient's needs [105]. Hakkarainen et al. demonstrated that functionalized cellulose dressings can be superior to the existing commercially available products such as Suprathel® [105]. Epithelialized skin regeneration and a lack of inflammatory response to the cellulose dressing were observed [105]. The dressing attaches easily to the wound, yet detaches on its own after skin regeneration is completed [105]. Although the dressing itself was not antibacterial, it did not promote bacterial growth [105]. Bacterial nanocellulose is biocompatible and has been applied to full-thickness skin defect models [78]. Using these porous membranes stimulates an increase in the healing rate along with a decrease in inflammation [78].

During the synthesis of the cellulose materials, the pore size can vary with the thickness of the membrane [78,96]. For example, the bottom side of BC films has a looser and rougher structure than the top side [96]. It has been shown that the increased porosity improved the wound healing rate and reduced the inflammatory response compared to control gauze and the more dense top side, as cell migration and diffusion were more permissible [96]. The less porous top side was more effective in preventing infection and water-loss [96]. Polyvinyl alcohol (PVA)/cellulose nanowhisker nanocomposite hydrogels have also been applied to wound healing applications [106]. Including nanowhiskers endows greater control over the physical properties of the hydrogels [106]. Specifically, the porosity can be tuned; the presence of the cellulose nanowhiskers decreases the pore size, but it does not affect the gel formation process [106]. Adding cellulose nanowhiskers mechanically reinforces the composite materials [106]. In the context of the skin application, the presence of nanowhiskers does not increase the drying rate beyond the in vivo optimal range [106]. The composite materials offer protection from bacterial invasion as well [106].

As bacterial cellulose alone does not exhibit antibacterial properties, and infection prevention is vital for wound healing applications, antimicrobial agents such as octenidine and minocycline have been combined with cellulose biomaterials [107,108]. For the use of thin films, a Fickian diffusion model is applicable; however, the swelling of the polymer often results in non-Fickian drug diffusion dynamics [107–110]. The scaffold thickness, surface area to volume ratio, structure, and chemistry at the nanoscale influence the diffusion and release of the drugs [104,107,108]. Mortiz et al. demonstrated that incorporating octenidine did not alter the mechanical properties or stability; nevertheless, this assumption cannot be assumed for different drugs or production methods [107]. Combining cellulose nanowhiskers with hydrogels is an effective method of tuning the physical characteristics and drug release properties [108]. By adding the nanoscale cellulose crystals, higher control over the drug release is obtained [108]. These composite materials did not exhibit thrombogenesis or hemolysis [108]. Conversely, protein adsorption, antibacterial, and antifungal properties were observed [108]. When combined with antimicrobial agents, the resultant material is viable to cells, is antibiotic, and induces a low inflammatory response [104,107,108]. Another approach to prevent bacterial infection is to incorporate silver nanoparticles [109,110]. In particular, silver nanoparticles were generated and self-assembled on the surface of cellulose nanofibers [109,110]. These materials are antibacterial and enable the proliferation of cells with low cytotoxicity [109,110]. In addition, these materials have been applied to wound models [109,110]. Significantly, these dressings regenerated epidermal and dermis more effectively than untreated wounds [109,110].

1.7.2 Bone tissue

As a consequence of the versatility of cellulose, these biomaterials can be adapted to be applicable to the stiff and mechanically demanding environment of bone [92,111,112].

As discussed in the skin and wound healing section, templating the biomaterial structure is a viable approach used to build biomimetic constructs. In the context of bone, it has been shown that a reverse templating method can be used to create gyroidal cellulose scaffolds [113]. This approach allows researchers to mathematically define and control pore geometries [113]. As this review stresses, the nanoscale details dictate macroscopic properties; therefore, bottom-up methods of creating 3D scaffolds are instrumental.

In contrast to templating, a popular method of creating nanocomposites for bone tissue replacements is electrospinning. As the mechanical properties of hydrogels are insufficient for withstanding the physical stress exerted on bones, they are often fortified with nanocellulose [114–117]. For example, cellulose nanocrystals can act as physical supports to electrospun matrices of poly lactic acid (PLA) and poly vinyl alcohol (PVA) hydrogels [114–116]. Modifying the surface chemistry with strategies such as maleic anhydride grafting, PEG grafting, and sodium dodecyl sulfate (SDS) improves the interfacial adhesion between the cellulose and PLA along with the tensile strength [115,116]. Moreover, the nanocrystals reduce the diameter and polydispersity of the

matrix fibres [114]. The mechanical and thermal stability increases with the addition of the cellulose nanocrystals [114]. These scaffolds have a tensile strength >10 MPa and are biocompatible [114,115]. The electrospun nanofibers with different weight ratios can be used to produce biomimetic bone structures [118].

Natural bone is highly porous; therefore, methods of creating highly porous biomimetic materials for bone tissue engineering are integral [119]. One approach of introducing pores is laser ablation of cellulose acetate electrospun fibres [119]. Pore sizes ranging from 50-300 μm can be fabricated without affecting the surrounding material [119]. These constructs can be further processed on the nanoscale to become mineralized to an extent that resembles in vivo hydroxyapatite levels [118,119]. The porous mineralized scaffolds increase osteoblast attachment and cell density at the pore sites [119].

Natural bone consists mainly of collagen and minerals similar in composition to hydroxyapatite [120]. Mimicking this complex composition is essential for bone tissue engineering. Cellulose nanofibers/hydroxyapatite composites can be used to emulate natural bone, namely the compressive strength (0.1–12 MPa), compressive modulus (6–330 MPa), porosity, and biocompatibility [116,120–123]. The proper dispersion of hydroxyapatite is required to emulate the natural environment [122]. In the absence of other composites, hydroxyapatite aggregates and precipitates; hence, the colloidal stability must be increased prior to its use in 3D scaffolding materials. Cellulose oxidation with compounds such as 2,2,6,6-tetramethylpiperidine-1-oxyl (TEMPO) can be used to accomplish the desired dispersion [122]. The oxidation yields negatively charged nanofibres onto which the hydroxyapatite adsorbs and creates a hydrogel that can be crosslinked [122]. The modified cellulose structure yields a highly porous bioactive material [120,123]. The mineralization of the macroporous scaffolds results in an environment resembling native bone tissues' mineralized extra cellular matrix both topographically and chemically[124]. Messenchymal stem cells can proliferate and differentiate towards osteoblasts on these scaffolds, confirming the material as a potential candidate for use in bone tissue engineering [122–124]. In vivo studies involving cellulose scaffolds combined with gelatin hydrogels that were subsequently coated with hydroxyapatite revealed that this approach enhanced new bone formation [123].

Bone implant integration is a major concern in the field of bone tissue engineering. In an attempt to improve integration of implants, cellulose alternatives to conventional ceramic and metal implants have been proposed. The surface functionalization with 45S5 bioactive glass individually wrapped and interconnected with fibrous cellulose nanocrystals was deposited on 316L stainless steel [125]. Rapid mineralization including hydroxapatite occurred in the presence of simulated body fluid [125]. The mineralized scaffold expedited cell attachment, spreading, proliferation, differentiation, and ECM mineralization, showing cellulose-based implants are a promising alternative to conventional methods that are not viable long term [125].

Carbon nanotubes (CNTs) have many potential applications in biology; however, a significant challenge is introducing them into a suitable 3D structure [126,127]. Furthermore, similar to the issue

with the hydrophobic hydrogels and the hydroxyapatite, the CNTs tend to aggregate together. To circumvent this effect, an amphiphilic comb-like polymer (APCLP) can be adsorbed onto CNTs. In situ hybridization of CNTs coated with an APCLP with cellulose produces a homogeneous 3D microporous structure that is osteoconductive and osteoinductive [126,127].

As cellulose fibres resemble the collagen fibres of bone tissue, cellulose has been implicated in bone tissue engineering applications [128]. In particular, bacterial cellulose can serve as a localized delivery system to increase the local concentration of cytokines [128]. It has been shown that the biocompatible scaffolds supported osteodifferentiation in the presence of bone morphogentic protein 2 (BMP-2) [128]. Greater in vivo bone formation and calcium deposition was stimulated with BMP-2 loading [128]. Likewise, cellulose nanocrystal – hydrogel composites can be implicated in the transport bioplymeric nanoparticles to bone marrow [117].

Although further investigation is required to uncover the full potential of cellulose-based materials for bone tissue engineering, the current body of work contests that cellulose materials present a promising approach to solving a major biomedical issue. Significantly, cellulose membranes have been shown to guide bone regeneration in vivo [129].

Neural applications

Cellulose scaffolds are a suitable material for 3D nerve cell proliferation and differentiation because of the adjustable surface chemistry and mechanical/physical properties [130,131]. Chemical modification and protein coating of cellulose materials can be used to enhance integrin based attachment and cell – scaffold interactions [130,131].

Nerve tissue engineering presents an issue that is unique to a subset of cell types including neurons and myocytes: electrical stimulation. As a result, electroactive, flexible, 3D nanostructured biomaterials are required. To satisfy these criteria, cellulose scaffolds coated with conductive materials such as poly(3,4-ethylenedioxythiophene) (PEDOT) and multi-walled carbon nanotubes, or carbonization can be used [132,133]. Such materials have tunable pore sizes, mechanical properties, and electrical conductivities; moreover, they are biocompatible and foster neural differentiation [132,133].

It is often desirable to incorporate growth factors into the surrounding nano- and micro-environments of stem cells [134,135]. Recently, cellulose bases scaffolds have been used to transport and release growth factors to guide neural differentiation and repair damaged tissue caused by strokes [134,135]. Pharmacologically active microcarriers (PAMs) and stem cells can be delivered via cellulose-based biomaterials including scaffolds and injectable gels [134,135]. Different release profiles, namely biphasic dynamics, of drugs can be designed by tuning the properties of the cellulose construct [134,135]. Similarly, growth factor delivery in the context of spinal cord injuries

has been studied using tubular cellulose composite materials [136]. Cellulose biomaterials implicated in spinal cord injury have been shown to promote the regeneration of neurons [137].

In addition to growth factor loading, drug loading has important implications in psychiatry [79]. Loading cellulose-based biomaterials with drugs is a promising avenue for drug delivery [79]. The tunable mechanical properties, highly porous structure, adjustable stability, and excellent biocompatibility make cellulose an ideal candidate for nerve tissue repair and drug delivery systems [79,133,135,138,139]. Significantly, it has been shown that cellulose constructs can be used as nerve guidance conduits for sciatic nerve defects in rats [79]. The results of this study revealed that citalopram-loaded cellulose materials can mediate the functional recovery of the sciatic nerve [79].

1.7.3 Blood vessels

The two most commonly used vascular graft materials are expanded polytetrafluoroethylene (ePTFE) and poly(ethylene terephthalate) (PET). Despite the high success rate of these materials, their applicability to small vessels is limited due to thrombosis [140,141]. As such, there is a need for blood compatible materials with appropriate biochemical and physical properties for vasculature engineering [140,141]. In comparison to conventionally-used graft materials, bacterial cellulose constructs exhibit no significant difference in platelet consumption and coagulation, as compared with PET, ePTFE, and heparin coated PVC [140]. However, it should be noted that the complement activation parameters sC3a and sC5b-9 were much higher for BC, as compared with the other materials for both 4 and 6 mm tubes diameter tubes [140]. In addition, an in vivo model using hamsters demonstrates the high biocompatibility and low immune response to these materials [141]. Likewise, in vivo implantation of a bacterial cellulose blood vessel in the carotid arteries of sheep showed epithelial cell coverage and patency for up to 13 months [142]. Nevertheless, the patency of the unmodified structures used in this study was inconsistent [142]. On the contrary, bacterial cellulose blood vessels molded in oxygen permeable polydimethylsiloxane (PDMS) templates yield appropriate mechanical properties and high stability [97]. These vessels have been successfully implanted into rabbit femoral arteries, and endothelialization was observed [97].

In order to improve the adhesion of human microvascular endothelial cells (HMEC) to cellulose grafts, chimeric proteins containing both a cellulose-binding domain and an adhesion peptide motif can be incorporated [143]. The recombinant proteins improve both the attachment and spreading of HMECs on the cellulose grafts [143]. Blood vessels are complex structures that not only act as a transport system, but also involve the transvascular migration of different cell types and molecules [144]. Simulated vascular lumens consisting of human umbilical vein endothelial cells (HUVECs) and a cellulose/collagen scaffold can replicate the transvascular migration and hemodynamics of native vessels [144].

Nanocomposite materials consisting of nanocrystalline cellulose and fibrin are applicable to small-diameter replacement vascular grafts (SDRVGs) [145]. Chemical attachment of fibrin to the cellulose can be mediated and tailored with periodate oxidation of the cellulose [145]. The nanocrystalline cellulose provides the elastic hydrogel with rigidity. Interestingly, the maximum strength and elongation of the composites were comparable to those of native blood vessels [145]. Similarly, a composite material of cellulose nanowhiskers and cellulose acetate propionate can be used as an alternative to conventional synthetic blood vessels [146]. The nanowhiskers act as reinforcements, while the cellulose acetate propionate provides the hydrogel matrix [146]. Resultantly, the percolated structure with improved mechanical properties can withstand the physiological pressure surface features of human blood vessels [146].

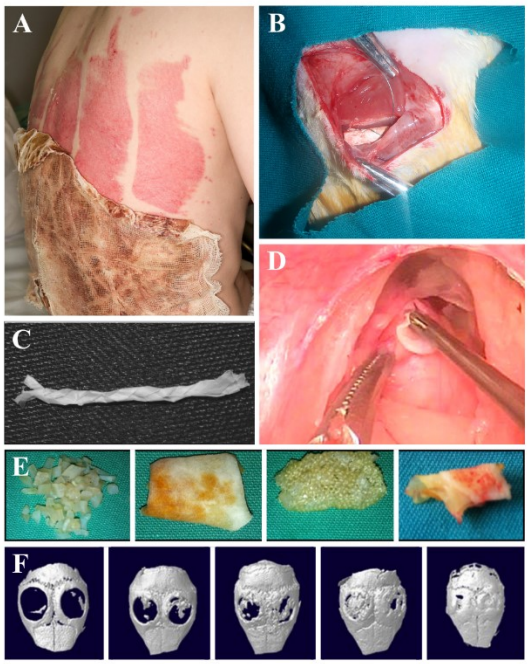

Figure 1.6: Applications of cellulose biomaterials. (A) Skin, (B) nerve, (C) tendon/ligament, (D) larynx, (E) cartilage, (F) bone, . (A): [105] Copyright 2016. Reproduced with permission from Elsevier Inc. (B): [79] Copyright 2017. Reproduced with permission from Elsevier Inc. (C): [158] Copyright 2013. Reproduced with permission from John Wiley and Sons. (D): [147] Copyright 2011. Reproduced with permission from Elsevier Inc. (E): [151] Copyright 2015. Reproduced with permission from John Wiley and Sons. (F): [127] Copyright 2015. Reproduced with permission from Elsevier Inc.

1.7.4 Other applications

This review highlights several key applications of cellulose-based materials that have been extensively investigated (Fig. 1.6). The fact that cellulose-based materials can be applied to such a wide range of tissue is a testament to its versatility and adaptability (Fig. 1.6). We stress that the potential uses of cellulose-based materials are not restricted to the categories reviewed here. For example, studies have shown that muscle, tendons/ligaments, cartilage, vertebrae disks, urinary tracts, and larynx tissues are applicable because of the tunable physical and chemical properties of cellulose [98,147–158] (Fig. 1.6).

1.8 Remaining challenges and future directions

Although substantial progress has been made in the field of tissue engineering, there are no materials that fully capture the intricacies of the native tissue nor restore function to an ideal level. As a result, the remaining challenges will be to innovate new composite materials with nanoscale engineering methods to produce fully biomimetic tissues. As the complexity of the application increases, such as in highly dynamic tissues, an active remodeling of the scaffolding will be required. Thus, the complex interplay between the cells and the artificial matrix will be paramount.

1.9 Conclusion

In order to recreate fully functional tissue, the biochemical and biophysical properties must be designed from the nanoscale up. The nanoscale features dictate cell function and scaffold applicability. Here we have condensed a wealth of knowledge in the field of cellulose-based biomaterials in the context of bottom-up approaches for tissue engineering. Evidently, cellulose-based materials have great potential to become the next generation of standard biomaterials because of their diversity and versatility of biochemical and biophysical characteristics.

1.10 References

(1) Wickström, S. A.; Niessen, C. M. Cell adhesion and mechanics as drivers of tissue organization and differentiation: local cues for large scale organization. *Curr. Opin. Cell Biol.* **2018**, *54*, 89–97 DOI: 10.1016/j.ceb.2018.05.003.

(2) Plotnikov, S. V; Waterman, C. M. Guiding cell migration by tugging. *Curr. Opin. Cell Biol.* **2013**, *25* (5), 619–626 DOI: 10.1016/j.ceb.2013.06.003.

(3) Holle, A. W.; Engler, A. J. More than a feeling: discovering, understanding, and influencing mechanosensing pathways. *Curr. Opin. Biotechnol.* **2011**, *22* (5), 648–654 DOI: 10.1016/j.copbio.2011.04.007.

(4) Jaalouk, D. E.; Lammerding, J. Mechanotransduction gone awry. *Nat. Rev. Mol. Cell Biol.* **2009**, *10* (1), 63–73 DOI: 10.1038/nrm2597.

(5) Gautrot, J. E.; Malmström, J.; Sundh, M.; Margadant, C.; Sonnenberg, A.; Sutherland, D. S. The nanoscale geometrical maturation of focal adhesions controls stem cell differentiation and mechanotransduction. *Nano Lett.* **2014**, *14* (7), 3945–3952 DOI: 10.1021/nl501248y.

(6) Gregor, M.; Osmanagic-myers, S.; Burgstaller, G.; Wolfram, M.; Fischer, I.; Walko, G.; Resch, G. P.; Jörgl, A.; Herrmann, H.; Wiche, G. Mechanosensing through focal adhesion-anchored intermediate filaments. *FASEB J.* **2014**, *28* (2), 715–729 DOI: 10.1096/fj.13-231829.

(7) Lazarides, E.; Burridge, K. Localization of a Muscle Structural Protein in Nonmuscle Cells. *Cell* **1975**, *6*, 289–298.

(8) Geiger, B.; Tokuyasu, K. T.; Dutton, A. H.; Singer, S. J. Vinculin, an intracellular protein localized at specialized sites where microfilament bundles terminate at cell membranes. *Proc. Natl. Acad. Sci. U. S. A.* **1980**, *77* (7), 4127–4131.

(9) Ruoslahti, E.; Pierschbacher, M. D. New Perspectives in Cell Adhesion: RGD and Integrins. *Science (80-.).* **1987**, *238* (4826), 491–497.

(10) Kanchanawong, P.; Shtengel, G.; Pasapera, A. M.; Ramko, E. B.; Davidson, M. W.; Hess, H. F.; Waterman, C. M. Nanoscale architecture of integrin-based cell adhesions. *Nature* **2010**, *468* (7323), 580–584 DOI: 10.1038/nature09621.

(11) Horwitz, A.; Duggan, K.; Buckt, C.; Beckerle, M. C.; Burridge, K. Interaction of plasma membrane fibronectin receptor with talin-a transmembrane linkage. *Nature* **1986**, *320* (10), 30–32.

(12) Chen, C. S.; Alonso, J. L.; Ostuni, E.; Whitesides, G. M.; Ingber, D. E. Cell shape provides global control of focal adhesion assembly. *Biochem. Biophys. Res. Commun.* **2003**, *307*, 355–361 DOI: 10.1016/S0006-291X(03)01165-3.

(13) Hynes, R.; Destree, A. T. Relationships between Fibronectin (LETS Protein) and Actin. *Cell* **1976**, *15* (November), 875–896.

(14) Heath, J. P.; Dunn, G. A.; Causeway, W. Cell to substratum contacts of chick fibroblasts and their relation to the microfilament system. A correlated interference-reflection and high-voltage electron-microscope study. *J. Cell Sci.* **1978**, *29*, 197–212.

(15) Murray, M. E.; Mendez, M. G.; Janmey, P. A. Substrate stiffness regulates solubility of cellular vimentin. *Mol. Biol. Cell* **2014**, *25* (1), 87–94 DOI: 10.1091/mbc.E13-06-0326.

(16) Engler, A. J.; Griffin, M. a; Sen, S.; Bönnemann, C. G.; Sweeney, H. L.; Discher, D. E. Myotubes differentiate optimally on substrates with tissue-like stiffness: pathological

implications for soft or stiff microenvironments. *J. Cell Biol.* **2004**, *166* (6), 877–887 DOI: 10.1083/jcb.200405004.
(17) Higuchi, S.; Watanabe, T. M.; Kawauchi, K.; Ichimura, T.; Fujita, H. Culturing of mouse and human cells on soft substrates promote the expression of stem cell markers. *J. Biosci. Bioeng.* **2013**, *xx* (xx), 1–7 DOI: 10.1016/j.jbiosc.2013.11.011.
(18) Al-Rekabi, Z.; Pelling, A. E. Cross talk between matrix elasticity and mechanical force regulates myoblast traction dynamics. *Phys. Biol.* **2013**, *10* (6), 066003 DOI: 10.1088/1478-3975/10/6/066003.
(19) Knight, E.; Przyborski, S. Advances in 3D cell culture technologies enabling tissue-like structures to be created in vitro. *J. Anat.* **2015**, *227* (6), 746–756 DOI: 10.1111/joa.12257.
(20) Ravi, M.; Paramesh, V.; Kaviya, S. R.; Anuradha, E.; Paul Solomon, F. D. 3D cell culture systems: Advantages and applications. *J. Cell. Physiol.* **2015**, *230* (1), 16–26 DOI: 10.1002/jcp.24683.
(21) Hickey, R.; Pelling, A. E. The rotation of mouse myoblast nuclei is dependent on substrate elasticity. *Cytoskeleton* **2017**, *74* (4), 184–194 DOI: 10.1002/cm.21357.
(22) Harris, A. K.; Wild, P.; Stopak, D. Silicone Rubber Substrata: A New Wrinkle in the Study of Cell Locomotion Auth. *Science (80-.).* **1980**, *208* (4440), 177–179.
(23) Dalby, M. J.; Yarwood, S. J.; Riehle, M. O.; Johnstone, H. J. H.; Affrossman, S.; Curtis, A. S. G. Increasing Fibroblast Response to Materials Using Nanotopography : Morphological and Genetic Measurements of Cell Response to 13-nm-High Polymer Demixed Islands. *Exp. Cell Res.* **2002**, *9* (276), 1–9 DOI: 10.1006/excr.2002.5498.
(24) Dalby, M. J.; Gadegaard, N.; Tare, R.; Andar, A.; Riehle, M. O.; Herzyk, P.; Wilkinson, C. D. W.; Oreffo, R. O. C. The control of human mesenchymal cell differentiation using nanoscale symmetry and disorder. *Nat. Mater.* **2007**, *6* (12), 997–1003 DOI: 10.1038/nmat2013.
(25) Levy, I.; Shoseyov, O. Cellulose-binding domains: Biotechnological applications. *Biotechnol. Adv.* **2002**, *20* (3–4), 191–213 DOI: 10.1016/S0734-9750(02)00006-X.
(26) Tormo, J.; Lamed, R.; Chirino, A. J.; Morag, E.; Bayer, E. A.; Shoham, Y.; Steitz, T. A. Crystal structure of a bacterial family-III cellulose-binding domain: a general mechanism for attachment to cellulose. *EMBO J.* **1996**, *15* (21), 5739–5751 DOI: 10.1002/j.1460-2075.1996.tb00960.x.
(27) Rakotoarivonina, H.; Hebraud, M.; Mosoni, P.; Forano, E.; Jubelin, G.; Gaillard-Martinie, B. Adhesion to cellulose of the Gram-positive bacterium Ruminococcus albus involves type IV pili. *Microbiology* **2002**, *148* (6), 1871–1880 DOI: 10.1099/00221287-148-6-1871.
(28) Liu, G. F.; Zhang, D.; Feng, C. L. Control of three-dimensional cell adhesion by the chirality of nanofibers in hydrogels. *Angew. Chemie - Int. Ed.* **2014**, *53* (30), 7789–7793 DOI: 10.1002/anie.201403249.
(29) Muth, C. A.; Steinl, C.; Klein, G.; Lee-Thedieck, C. Regulation of Hematopoietic Stem Cell Behavior by the Nanostructured Presentation of Extracellular Matrix Components. *PLoS One* **2013**, *8* (2) DOI: 10.1371/journal.pone.0054778.
(30) Hiraguchi, Y.; Nagahashi, K.; Shibayama, T.; Hayashi, T.; Yano, T. A.; Kushiro, K.; Takai, M. Effect of the distribution of adsorbed proteins on cellular adhesion behaviors using surfaces of nanoscale phase-reversed amphiphilic block copolymers. *Acta Biomater.* **2014**, *10* (7), 2988–2995 DOI: 10.1016/j.actbio.2014.03.019.
(31) Maheshwari, G.; Brown, G.; Lauffenburger, D. a; Wells, a; Griffith, L. G. Cell adhesion

and motility depend on nanoscale RGD clustering. *J. Cell Sci.* **2000**, *113 (Pt 1*, 1677–1686 DOI: 10.1083/jcb.144.5.1019.
(32) Amschler, K.; Erpenbeck, L.; Kruss, S.; Schön, M. P. Nanoscale Integrin Ligand Patterns Determine Melanoma Cell Behavior. *ACS Nano* **2014**, *8* (9), 9113–9125 DOI: 10.1021/nn502690b.
(33) Kuo, C. W.; Chueh, D. Y.; Chen, P. Investigation of size-dependent cell adhesion on nanostructured interfaces. *J. Nanobiotechnology* **2014**, *12* (1), 1–10 DOI: 10.1186/s12951-014-0054-4.
(34) Harris, G. M.; Shazly, T.; Jabbarzadeh, E. Deciphering the combinatorial roles of geometric, mechanical, and adhesion cues in regulation of cell spreading. *PLoS One* **2013**, *8* (11), e81113 DOI: 10.1371/journal.pone.0081113.
(35) Ye, K.; Wang, X.; Cao, L.; Li, S.; Li, Z.; Yu, L.; Ding, J. Matrix Stiffness and Nanoscale Spatial Organization of Cell-Adhesive Ligands Direct Stem Cell Fate. *Nano Lett.* **2015**, *15* (7), 4720–4729 DOI: 10.1021/acs.nanolett.5b01619.
(36) Engler, A. J.; Sen, S.; Sweeney, H. L.; Discher, D. E. Matrix elasticity directs stem cell lineage specification. *Cell* **2006**, *126* (4), 677–689 DOI: 10.1016/j.cell.2006.06.044.
(37) Kiroshka, V. V.; Yurchuk, T. A.; Repin, N. V.; Petrova, V. A.; Gofman, I. V.; Skorik, Y. A.; Kiroshka, E. V.; Bondarenko, T. P. Adhesion, Growth, and Proliferation of Endothelial Cells on Biopolymer Extracellular Film Matrices. *Bull. Exp. Biol. Med.* **2014**, *158* (1), 153–158 DOI: 10.1007/s10517-014-2712-9.
(38) Pedraz, P.; Casado, S.; Rodriguez, V.; Giordano, M. C.; Mongeot, F. B. De; Ayuso-Sacido, A.; Gnecco, E. Adhesion modification of neural stem cells induced by nanoscale ripple patterns. *Nanotechnology* **2016**, *27* (12) DOI: 10.1088/0957-4484/27/12/125301.
(39) Alshehri, A. M.; Hadjiantoniou, S.; Hickey, R. J.; Al-Rekabi, Z.; Harden, J. L.; Pelling, A. E.; Bhardwaj, V. R. Selective cell adhesion on femtosecond laser-microstructured polydimethylsiloxane. *Biomed. Mater.* **2016**, *11* (1) DOI: 10.1088/1748-6041/11/1/015014.
(40) Haworth, W. The structure of carbohydrates. *Helv. Chim. Acta* **1928**, *11* (1910), 534–548 DOI: 10.1002/hlca.19280110166.
(41) Mohite, B. V.; Patil, S. V. A novel biomaterial: Bacterial cellulose and its new era applications. *Biotechnol. Appl. Biochem.* **2014**, *61* (2), 101–110 DOI: 10.1002/bab.1148.
(42) Courtenay, J. C.; Sharma, R. I.; Scott, J. L. Recent advances in modified cellulose for tissue culture applications. *Molecules* **2018**, *23* (3) DOI: 10.3390/molecules23030654.
(43) Domingues, R. M. A.; Gomes, M. E.; Reis, R. L. The Potential of Cellulose Nanocrystals in Tissue Engineering Strategies. *Biomacromolecules* **2014**, *15* (7), 2327–2346 DOI: 10.1021/bm500524s.
(44) Courtenay, J. C.; Deneke, C.; Lanzoni, E. M.; Costa, C. A.; Bae, Y.; Scott, J. L.; Sharma, R. I. Modulating cell response on cellulose surfaces; tunable attachment and scaffold mechanics. *Cellulose* **2018**, *25* (2), 925–940 DOI: 10.1007/s10570-017-1612-3.
(45) Yamane, C.; Miyamoto, H.; Hayakawa, D.; Ueda, K. Folded-chain structure of cellulose II suggested by molecular dynamics simulation. **2013** DOI: 10.1016/j.carres.2013.06.012.
(46) Kroon-Batenburg, L. M. J.; Kroon, J. The crystal and molecular structures of cellulose I and II. *Glycoconj. J.* **1997**, *14* (5), 677–690 DOI: 10.1023/A:1018509231331.
(47) Miyamoto, H.; Umemura, M.; Aoyagi, T.; Yamane, C.; Ueda, K.; Takahashi, K. Structural reorganization of molecular sheets derived from cellulose II by molecular dynamics simulations. *Carbohydr. Res.* **2009**, *344* (9), 1085–1094 DOI:

10.1016/j.carres.2009.03.014.
(48) Hayakawa, D.; Nishiyama, Y.; Mazeau, K.; Ueda, K. Evaluation of hydrogen bond networks in cellulose Iβ and II crystals using density functional theory and Car–Parrinello molecular dynamics. *Carbohydr. Res.* **2017**, *449*, 103–113 DOI: 10.1016/j.carres.2017.07.001.
(49) Gibson, L. J. The hierarchical structure and mechanics of plant materials. *J. R. Soc. Interface* **2012**, *9* (76), 2749–2766 DOI: 10.1098/rsif.2012.0341.
(50) Pérez, S.; Mazeau, K. Conformations, Structures, and Morphologies of Celluloses. *Polysaccharides* **2004**, No. January 2005 DOI: 10.1201/9781420030822.ch2.
(51) Nishiyama, Y.; Sugiyama, J.; Chanzy, H.; Langan, P. Crystal Structure and Hydrogen Bonding System in Cellulose Iα from Synchrotron X-ray and Neutron Fiber Diffraction. *J. Am. Chem. Soc.* **2003**, *125* (47), 14300–14306 DOI: 10.1021/ja037055w.
(52) Wada, M.; Chanzy, H.; Nishiyama, Y.; Langan, P. Cellulose III I crystal structure and hydrogen bonding by synchrotron X-ray and neutron fiber diffraction. *Macromolecules* **2004**, *37* (23), 8548–8555 DOI: 10.1021/ma0485585.
(53) Nishiyama, Y.; Langan, P.; Chanzy, H. Crystal structure and hydrogen-bonding system in cellulose Iβ from synchrotron X-ray and neutron fiber diffraction. *J. Am. Chem. Soc.* **2002**, *124* (31), 9074–9082 DOI: 10.1021/ja0257319.
(54) Moon, R. J.; Martini, A.; Nairn, J.; Simonsen, J.; Youngblood, J. *Cellulose nanomaterials review: Structure, properties and nanocomposites*; 2011; Vol. 40.
(55) Gross, A. S.; Chu, J. W. On the molecular origins of biomass recalcitrance: The interaction network and solvation structures of cellulose microfibrils. *J. Phys. Chem. B* **2010**, *114* (42), 13333–13341 DOI: 10.1021/jp106452m.
(56) Sarko, A.; Muggli, R. Packing Analysis of Carbohydrates and Polysaccharides. III. Valonia Cellulose and Cellulose II. *Macromolecules* **1974**, *7* (4), 486–494 DOI: 10.1021/ma60040a016.
(57) Kim, N. H.; Imai, T.; Wada, M.; Sugiyama, J. Molecular directionality in cellulose polymorphs. *Biomacromolecules* **2006**, *7* (1), 274–280 DOI: 10.1021/bm0506391.
(58) Atalla, R. H.; VanderHart, D. L. Native Cellulose: A Composite of Two Distinct Crystalline Forms. *Adv. Sci.* **1984**, *223* (4633), 283–285.
(59) Oudiani, A. El; Chaabouni, Y.; Msahli, S.; Sakli, F. Crystal transition from cellulose I to cellulose II in NaOH treated Agave americana L. fibre. *Carbohydr. Polym.* **2011**, *86* (3), 1221–1229 DOI: 10.1016/j.carbpol.2011.06.037.
(60) Gupta, P. K.; Uniyal, V.; Naithani, S. Polymorphic transformation of cellulose I to cellulose II by alkali pretreatment and urea as an additive. *Carbohydr. Polym.* **2013**, *94* (2), 843–849 DOI: 10.1016/j.carbpol.2013.02.012.
(61) Oudiani, A. El; Chaabouni, Y.; Msahli, S.; Sakli, F. Crystal transition from cellulose I to cellulose II in NaOH treated Agave americana L. fibre. *Carbohydr. Polym.* **2011**, *86* (3), 1221–1229 DOI: 10.1016/J.CARBPOL.2011.06.037.
(62) Jin, E.; Guo, J.; Yang, F.; Zhu, Y.; Song, J.; Jin, Y.; Rojas, O. J. On the polymorphic and morphological changes of cellulose nanocrystals (CNC-I) upon mercerization and conversion to CNC-II. *Carbohydr. Polym.* **2016**, *143*, 327–335 DOI: 10.1016/j.carbpol.2016.01.048.
(63) Wada, M.; Heux, L.; Nishiyama, Y.; Langan, P. X-ray crystallographic, scanning microprobe X-ray diffraction, and cross-polarized/magic angle spinning 13C NMR studies of the structure of cellulose III(II). *Biomacromolecules* **2009**, *10* (2), 302–309 DOI:

10.1021/bm8010227.
(64) Wada, M. In situ observation of the crystalline transformation from cellulose IIII to Iβ. *Macromolecules* **2001**, *34* (10), 3271–3275 DOI: 10.1021/ma0013354.
(65) Mittal, A.; Katahira, R.; Himmel, M. E.; Johnson, D. K. Effects of alkaline or liquid-ammonia treatment on crystalline cellulose: Changes in crystalline structure and effects on enzymatic digestibility. *Biotechnol. Biofuels* **2011**, *4* (1), 41 DOI: 10.1186/1754-6834-4-41.
(66) Nishino, T.; Takano, K.; Nakamae, K. Elastic modulus of the crystalline regions of cellulose polymorphs. *J. Polym. Sci. Part B Polym. Phys.* **1995**, *33* (11), 1647–1651 DOI: 10.1002/polb.1995.090331110.
(67) Chundawat, S. P. S.; Bellesia, G.; Uppugundla, N.; Da Costa Sousa, L.; Gao, D.; Cheh, A. M.; Agarwal, U. P.; Bianchetti, C. M.; Phillips, G. N.; Langan, P.; et al. Restructuring the crystalline cellulose hydrogen bond network enhances its depolymerization rate. *J. Am. Chem. Soc.* **2011**, *133* (29), 11163–11174 DOI: 10.1021/ja2011115.
(68) Igarashi, K.; Uchihashi, T.; Koivula, A.; Wada, M.; Kimura, S.; Okamoto, T.; Penttilä, M.; Ando, T.; Samejima, M. Traffic Jams Reduce Hydrolytic Efficiency of Cellulase on Cellulose Surface. *Science (80-.).* **2011**, *333* (September), 1279–1282.
(69) Nishiyama, Y.; Langan, P.; Wada, M.; Forsyth, V. T. Looking at hydrogen bonds in cellulose. *Acta Crystallogr. Sect. D Biol. Crystallogr.* **2010**, *66* (11), 1172–1177 DOI: 10.1107/S0907444910032397.
(70) Igarashi, K.; Wada, M.; Samejima, M. Activation of crystalline cellulose to cellulose IIII results in efficient hydrolysis by cellobiohydrolase. *FEBS J.* **2007**, *274* (7), 1785–1792 DOI: 10.1111/j.1742-4658.2007.05727.x.
(71) Wada, M.; Ike, M.; Tokuyasu, K. Enzymatic hydrolysis of cellulose I is greatly accelerated via its conversion to the cellulose II hydrate form. *Polym. Degrad. Stab.* **2010**, *95* (4), 543–548 DOI: 10.1016/j.polymdegradstab.2009.12.014.
(72) Kim, U. J.; Eom, S. H.; Wada, M. Thermal decomposition of native cellulose: Influence on crystallite size. *Polym. Degrad. Stab.* **2010**, *95* (5), 778–781 DOI: 10.1016/j.polymdegradstab.2010.02.009.
(73) Hearle, J. W. S. A Fringed Fibril Theory of Structure in Crystalline Polymers. *J. Polym. Sci.* **1957**, *XXVIII* (117), 432–435.
(74) Nishiyama, Y.; Kim, U. J.; Kim, D. Y.; Katsumata, K. S.; May, R. P.; Langan, P. Periodic disorder along ramie cellulose microfibrils. *Biomacromolecules* **2003**, *4* (4), 1013–1017 DOI: 10.1021/bm025772x.
(75) Battista, O. A.; Coppick, S.; Howsmon, J. A.; Morehead, F. F.; Sisson, W. A. Level-Off Degree of Polymerization. *Ind. Eng. Chem.* **1956**, *48* (2), 333–335 DOI: 10.1021/ie50554a046.
(76) Modulevsky, D. J.; Cuerrier, C. M.; Pelling, A. E. Biocompatibility of Subcutaneously Implanted Plant-Derived Cellulose Biomaterials. *PLoS One* **2016**, *11* (6), 1–19 DOI: 10.1371/journal.pone.0157894.
(77) Torres, C. E.; Negro, C.; Fuente, E.; Blanco, A. Enzymatic approaches in paper industry for pulp refining and biofilm control. *Appl. Microbiol. Biotechnol.* **2012**, *96* (2), 327–344 DOI: 10.1007/s00253-012-4345-0.
(78) Fu, L.; Zhou, P.; Zhang, S.; Yang, G. Evaluation of bacterial nanocellulose-based uniform wound dressing for large area skin transplantation. *Mater. Sci. Eng. C* **2013**, *33* (5), 2995–3000 DOI: 10.1016/j.msec.2013.03.026.

(79) Naseri-Nosar, M.; Salehi, M.; Hojjati-Emami, S. Cellulose acetate/poly lactic acid coaxial wet-electrospun scaffold containing citalopram-loaded gelatin nanocarriers for neural tissue engineering applications. *Int. J. Biol. Macromol.* **2017**, *103*, 701–708 DOI: 10.1016/j.ijbiomac.2017.05.054.
(80) Modulevsky, D. J.; Lefebvre, C.; Haase, K.; Al-Rekabi, Z.; Pelling, A. E. Apple derived cellulose scaffolds for 3D mammalian cell culture. *PLoS One* **2014**, *9* (5) DOI: 10.1371/journal.pone.0097835.
(81) Feng, X.; Ullah, N.; Wang, X.; Sun, X.; Li, C.; Bai, Y.; Chen, L.; Li, Z. Characterization of Bacterial Cellulose by Gluconacetobacter hansenii CGMCC 3917. *J. Food Sci.* **2015**, *80* (10), E2217–E2227 DOI: 10.1111/1750-3841.13010.
(82) Lee, C. M.; Kafle, K.; Park, Y. B.; Kim, S. H. Probing crystal structure and mesoscale assembly of cellulose microfibrils in plant cell walls, tunicate tests, and bacterial films using vibrational Sum Frequency Generation (SFG) spectroscopy. *Phys. Chem. Chem. Phys.* **2014**, *16* (22), 10844–10853 DOI: 10.1039/c4cp00515e.
(83) Lu, H.; Jiang, X. Structure and properties of bacterial cellulose produced using a trickling bed reactor. *Appl. Biochem. Biotechnol.* **2014**, *172* (8), 3844–3861 DOI: 10.1007/s12010-014-0795-4.
(84) Jozala, A. F.; Pértile, R. A. N.; dos Santos, C. A.; de Carvalho Santos-Ebinuma, V.; Seckler, M. M.; Gama, F. M.; Pessoa, A. Bacterial cellulose production by Gluconacetobacter xylinus by employing alternative culture media. *Appl. Microbiol. Biotechnol.* **2014**, *99* (3), 1181–1190 DOI: 10.1007/s00253-014-6232-3.
(85) Bi, J. C.; Liu, S. X.; Li, C. F.; Li, J.; Liu, L. X.; Deng, J.; Yang, Y. C. Morphology and structure characterization of bacterial celluloses produced by different strains in agitated culture. *J. Appl. Microbiol.* **2014**, *117* (5), 1305–1311 DOI: 10.1111/jam.12619.
(86) Luo, H.; Zhang, J.; Xiong, G.; Wan, Y. Evolution of morphology of bacterial cellulose scaffolds during early culture. *Carbohydr. Polym.* **2014**, *111*, 722–728 DOI: 10.1016/j.carbpol.2014.04.097.
(87) Yamanaka, S.; Watanabe, K.; Kitamura, N.; Iguchi, M.; Mitsuhashi, S.; Nishi, Y.; Uryu, M. The structure and mechanical properties of sheets prepared from bacterial cellulose. *J. Mater. Sci.* **1989**, *24* (9), 3141–3145 DOI: 10.1007/BF01139032.
(88) Gershlak, J.; Hernandez, S.; Fontana, G.; Perreault, L.; Hansen, K.; Larson, S.; Binder, B.; Dolivo, D.; Yang, T.; Dominko, T.; et al. Crossing kingdoms: Using decellularized plants as perfusable tissue engineering scaffolds. *Biomaterials* **2017**, *125*, 13–22 DOI: 10.1016/j.biomaterials.2017.02.011.
(89) Fontana, G.; Gershlak, J.; Adamski, M.; Lee, J.-S.; Matsumoto, S.; Le, H. D.; Binder, B.; Wirth, J.; Gaudette, G.; Murphy, W. L. Biofunctionalized Plants as Diverse Biomaterials for Human Cell Culture. *Adv. Healthc. Mater.* **2017**, 1601225 DOI: 10.1002/adhm.201601225.
(90) Hickey, R. J.; Modulevsky, D. J.; Cuerrier, C. M.; Pelling, A. E. Customizing the Shape and Microenvironment Biochemistry of Biocompatible Macroscopic Plant-Derived Cellulose Scaffolds. *ACS Biomater. Sci. Eng.* **2018**, *4*, 3726–3736 DOI: 10.1021/acsbiomaterials.8b00178.
(91) Gibson, L. J.; Ashby, M. F.; Harley, B. A. *Cellular materials in nature and medicine*, 1st ed.; Cambridge University Press, 2010.
(92) Stumpf, T. R.; Yang, X.; Zhang, J.; Cao, X. In situ and ex situ modifications of bacterial cellulose for applications in tissue engineering. *Mater. Sci. Eng. C* **2018**, *82*, 372–383

DOI: 10.1016/j.msec.2016.11.121.
(93) Shao, W.; Wu, J.; Liu, H.; Ye, S.; Jiang, L.; Liu, X. Novel bioactive surface functionalization of bacterial cellulose membrane. *Carbohydr. Polym.* **2017**, *178* (September), 270–276 DOI: 10.1016/j.carbpol.2017.09.045.
(94) He, X.; Xiao, Q.; Lu, C.; Wang, Y.; Zhang, X.; Zhao, J.; Zhang, W.; Zhang, X.; Deng, Y. Uniaxially aligned electrospun all-cellulose nanocomposite nanofibers reinforced with cellulose nanocrystals: Scaffold for tissue engineering. *Biomacromolecules* **2014**, *15* (2), 618–627 DOI: 10.1021/bm401656a.
(95) Ribeiro-Viana, R. M.; Faria-Tischer, P. C. S.; Tischer, C. A. Preparation of succinylated cellulose membranes for functionalization purposes. *Carbohydr. Polym.* **2016**, *148*, 21–28 DOI: 10.1016/j.carbpol.2016.04.033.
(96) Li, Y.; Wang, S.; Huang, R.; Huang, Z.; Hu, B.; Zheng, W.; Yang, G.; Jiang, X. Evaluation of the Effect of the Structure of Bacterial Cellulose on Full Thickness Skin Wound Repair on a Microfluidic Chip. *Biomacromolecules* **2015**, *16* (3), 780–789 DOI: 10.1021/bm501680s.
(97) Zang, S.; Zhang, R.; Chen, H.; Lu, Y.; Zhou, J.; Chang, X.; Qiu, G.; Wu, Z.; Yang, G. Investigation on artificial blood vessels prepared from bacterial cellulose. *Mater. Sci. Eng. C* **2015**, *46*, 111–117 DOI: 10.1016/j.msec.2014.10.023.
(98) Entcheva, E.; Bien, H.; Yin, L.; Chung, C. Y.; Farrell, M.; Kostov, Y. Functional cardiac cell constructs on cellulose-based scaffolding. *Biomaterials* **2004**, *25* (26), 5753–5762 DOI: 10.1016/j.biomaterials.2004.01.024.
(99) Bottan, S.; Robotti, F.; Jayathissa, P.; Hegglin, A.; Bahamonde, N.; Heredia-Guerrero, J. A.; Bayer, I. S.; Scarpellini, A.; Merker, H.; Lindenblatt, N.; et al. Surface-structured bacterial cellulose with guided assembly-based biolithography (GAB). *ACS Nano* **2015**, *9* (1), 206–219 DOI: 10.1021/nn5036125.
(100) Laromaine, A.; Tronser, T.; Pini, I.; Parets, S.; Levkin, P. A.; Roig, A. Free-standing three-dimensional hollow bacterial cellulose structures with controlled geometry: Via patterned superhydrophobic-hydrophilic surfaces. *Soft Matter* **2018**, *14* (19), 3955–3962 DOI: 10.1039/c8sm00112j.
(101) Bali, G.; Foston, M. B.; O'Neill, H. M.; Evans, B. R.; He, J.; Ragauskas, A. J. The effect of deuteration on the structure of bacterial cellulose. *Carbohydr. Res.* **2013**, *374*, 82–88 DOI: 10.1016/j.carres.2013.04.009.
(102) Rees, A.; Powell, L. C.; Chinga-Carrasco, G.; Gethin, D. T.; Syverud, K.; Hill, K. E.; Thomas, D. W. 3D bioprinting of carboxymethylated-periodate oxidized nanocellulose constructs for wound dressing applications. *Biomed Res. Int.* **2015**, *2015* DOI: 10.1155/2015/925757.
(103) Vatankhah, E.; Prabhakaran, M. P.; Jin, G.; Mobarakeh, L. G.; Ramakrishna, S. Development of nanofibrous cellulose acetate/gelatin skin substitutes for variety wound treatment applications. *J. Biomater. Appl.* **2014**, *28* (6), 909–921 DOI: 10.1177/0885328213486527.
(104) Liu, X.; Lin, T.; Gao, Y.; Xu, Z.; Huang, C.; Yao, G.; Jiang, L.; Tang, Y.; Wang, X. Antimicrobial electrospun nanofibers of cellulose acetate and polyester urethane composite for wound dressing. *J. Biomed. Mater. Res. - Part B Appl. Biomater.* **2012**, *100 B* (6), 1556–1565 DOI: 10.1002/jbm.b.32724.
(105) Hakkarainen, T.; Koivuniemi, R.; Kosonen, M.; Escobedo-Lucea, C.; Sanz-Garcia, A.; Vuola, J.; Valtonen, J.; Tammela, P.; Mäkitie, A.; Luukko, K.; et al. Nanofibrillar

cellulose wound dressing in skin graft donor site treatment. *J. Control. Release* **2016**, *244*, 292–301 DOI: 10.1016/j.jconrel.2016.07.053.
(106) Gonzalez, J. S.; Ludueña, L. N.; Ponce, A.; Alvarez, V. A. Poly(vinyl alcohol)/cellulose nanowhiskers nanocomposite hydrogels for potential wound dressings. *Mater. Sci. Eng. C* **2014**, *34* (1), 54–61 DOI: 10.1016/j.msec.2013.10.006.
(107) Moritz, S.; Wiegand, C.; Wesarg, F.; Hessler, N.; Müller, F. A.; Kralisch, D.; Hipler, U. C.; Fischer, D. Active wound dressings based on bacterial nanocellulose as drug delivery system for octenidine. *Int. J. Pharm.* **2014**, *471* (1–2), 45–55 DOI: 10.1016/j.ijpharm.2014.04.062.
(108) Bajpai, S. K.; Pathak, V.; Soni, B. Minocycline-loaded cellulose nano whiskers/poly(sodium acrylate) composite hydrogel films as wound dressing. *Int. J. Biol. Macromol.* **2015**, *79*, 76–85 DOI: 10.1016/j.ijbiomac.2015.04.060.
(109) Wu, J.; Zheng, Y.; Wen, X.; Lin, Q.; Chen, X.; Wu, Z. Silver nanoparticle/bacterial cellulose gel membranes for antibacterial wound dressing: Investigation in vitro and in vivo. *Biomed. Mater.* **2014**, *9* (3) DOI: 10.1088/1748-6041/9/3/035005.
(110) Wu, J.; Zheng, Y.; Song, W.; Luan, J.; Wen, X.; Wu, Z.; Chen, X.; Wang, Q.; Guo, S. In situ synthesis of silver-nanoparticles/bacterial cellulose composites for slow-released antimicrobial wound dressing. *Carbohydr. Polym.* **2014**, *102* (1), 762–771 DOI: 10.1016/j.carbpol.2013.10.093.
(111) Kim, D. S.; Jung, S. M.; Yoon, G. H.; Lee, H. C.; Shin, H. S. Development of a complex bone tissue culture system based on cellulose nanowhisker mechanical strain. *Colloids Surfaces B Biointerfaces* **2014**, *123*, 838–844 DOI: 10.1016/j.colsurfb.2014.10.031.
(112) Torgbo, S.; Sukyai, P. Bacterial cellulose-based scaffold materials for bone tissue engineering. *Appl. Mater. Today* **2018**, *11*, 34–49 DOI: 10.1016/j.apmt.2018.01.004.
(113) Torres-Rendon, J. G.; Femmer, T.; De Laporte, L.; Tigges, T.; Rahimi, K.; Gremse, F.; Zafarnia, S.; Lederle, W.; Ifuku, S.; Wessling, M.; et al. Bioactive gyroid scaffolds formed by sacrificial templating of nanocellulose and nanochitin hydrogels as instructive platforms for biomimetic tissue engineering. *Adv. Mater.* **2015**, *27* (19), 2989–2995 DOI: 10.1002/adma.201405873.
(114) Zhou, C.; Shi, Q.; Guo, W.; Terrell, L.; Qureshi, A. T.; Hayes, D. J.; Wu, Q. Electrospun bio-nanocomposite scaffolds for bone tissue engineering by cellulose nanocrystals reinforcing maleic anhydride grafted PLA. *ACS Appl. Mater. Interfaces* **2013**, *5* (9), 3847–3854 DOI: 10.1021/am4005072.
(115) Zhang, C.; Salick, M. R.; Cordie, T. M.; Ellingham, T.; Dan, Y.; Turng, L. S. Incorporation of poly(ethylene glycol) grafted cellulose nanocrystals in poly(lactic acid) electrospun nanocomposite fibers as potential scaffolds for bone tissue engineering. *Mater. Sci. Eng. C* **2015**, *49*, 463–471 DOI: 10.1016/j.msec.2015.01.024.
(116) Eftekhari, S.; El Sawi, I.; Bagheri, Z. S.; Turcotte, G.; Bougherara, H. Fabrication and characterization of novel biomimetic PLLA/cellulose/ hydroxyapatite nanocomposite for bone repair applications. *Mater. Sci. Eng. C* **2014**, *39* (1), 120–125 DOI: 10.1016/j.msec.2014.02.027.
(117) Rescignano, N.; Fortunati, E.; Montesano, S.; Emiliani, C.; Kenny, J. M.; Martino, S.; Armentano, I. PVA bio-nanocomposites: A new take-off using cellulose nanocrystals and PLGA nanoparticles. *Carbohydr. Polym.* **2014**, *99*, 47–58 DOI: 10.1016/j.carbpol.2013.08.061.
(118) Chalal, S.; Hussain, F. S. J.; Yusoff, M. B. M. Biomimetic growth of bone-like apatite via

simulated body fluid on hydroxyethyl cellulose/polyvinyl alcohol electrospun nanofibers. *Biomed. Mater. Eng.* **2014**, *24* (1), 799–806 DOI: 10.3233/BME-130871.
(119) Rodríguez, K.; Sundberg, J.; Gatenholm, P.; Renneckar, S. Electrospun nanofibrous cellulose scaffolds with controlled microarchitecture. *Carbohydr. Polym.* **2014**, *100*, 143–149 DOI: 10.1016/j.carbpol.2012.12.037.
(120) Li, K.; Wang, J.; Liu, X.; Xiong, X.; Liu, H. Biomimetic growth of hydroxyapatite on phosphorylated electrospun cellulose nanofibers. *Carbohydr. Polym.* **2012**, *90* (4), 1573–1581 DOI: 10.1016/j.carbpol.2012.07.033.
(121) Garai, S.; Sinha, A. Biomimetic nanocomposites of carboxymethyl cellulose-hydroxyapatite: Novel three dimensional load bearing bone grafts. *Colloids Surfaces B Biointerfaces* **2014**, *115*, 182–190 DOI: 10.1016/j.colsurfb.2013.11.042.
(122) Park, M.; Lee, D.; Shin, S.; Hyun, J. Effect of negatively charged cellulose nanofibers on the dispersion of hydroxyapatite nanoparticles for scaffolds in bone tissue engineering. *Colloids Surfaces B Biointerfaces* **2015**, *130*, 222–228 DOI: 10.1016/j.colsurfb.2015.04.014.
(123) Huang, Y.; Wang, J.; Yang, F.; Shao, Y.; Zhang, X.; Dai, K. Modification and evaluation of micro-nano structured porous bacterial cellulose scaffold for bone tissue engineering. *Mater. Sci. Eng. C* **2017**, *75*, 1034–1041 DOI: 10.1016/j.msec.2017.02.174.
(124) Sundberg, J.; Götherström, C.; Gatenholm, P. Biosynthesis and in vitro evaluation of macroporous mineralized bacterial nanocellulose scaffolds for bone tissue engineering. *Biomed. Mater. Eng.* **2015**, *25* (1), 39–52 DOI: 10.3233/BME-141245.
(125) Chen, Q.; Garcia, R. P.; Munoz, J.; Pérez De Larraya, U.; Garmendia, N.; Yao, Q.; Boccaccini, A. R. Cellulose Nanocrystals-Bioactive Glass Hybrid Coating as Bone Substitutes by Electrophoretic Co-deposition: In Situ Control of Mineralization of Bioactive Glass and Enhancement of Osteoblastic Performance. *ACS Appl. Mater. Interfaces* **2015**, *7* (44), 24715–24725 DOI: 10.1021/acsami.5b07294.
(126) Gutiérrez-Hernández, J. M.; Escobar-García, D. M.; Escalante, A.; Flores, H.; González, F. J.; Gatenholm, P.; Toriz, G. In vitro evaluation of osteoblastic cells on bacterial cellulose modified with multi-walled carbon nanotubes as scaffold for bone regeneration. *Mater. Sci. Eng. C* **2017**, *75*, 445–453 DOI: 10.1016/j.msec.2017.02.074.
(127) Park, S.; Park, J.; Jo, I.; Cho, S. P.; Sung, D.; Ryu, S.; Park, M.; Min, K. A.; Kim, J.; Hong, S.; et al. In situ hybridization of carbon nanotubes with bacterial cellulose for three-dimensional hybrid bioscaffolds. *Biomaterials* **2015**, *58*, 93–102 DOI: 10.1016/j.biomaterials.2015.04.027.
(128) Shi, Q.; Li, Y.; Sun, J.; Zhang, H.; Chen, L.; Chen, B.; Yang, H.; Wang, Z. The osteogenesis of bacterial cellulose scaffold loaded with bone morphogenetic protein-2. *Biomaterials* **2012**, *33* (28), 6644–6649 DOI: 10.1016/j.biomaterials.2012.05.071.
(129) Lee, Y. J.; An, S. J.; Bae, E. Bin; Gwon, H. J.; Park, J. S.; Jeong, S. I.; Jeon, Y. C.; Lee, S. H.; Lim, Y. M.; Huh, J. B. The effect of thickness of resorbable bacterial cellulose membrane on guided bone regeneration. *Materials (Basel).* **2017**, *10* (3) DOI: 10.3390/ma10030320.
(130) Jonsson, M.; Brackmann, C.; Puchades, M.; Brattås, K.; Ewing, A.; Gatenholm, P.; Enejder, A. Neuronal Networks on Nanocellulose Scaffolds. *Tissue Eng. Part C Methods* **2015**, *21* (11), 1162–1170 DOI: 10.1089/ten.tec.2014.0602.
(131) Innala, M.; Riebe, I.; Kuzmenko, V.; Sundberg, J.; Gatenholm, P.; Hanse, E.; Johannesson, S. 3D Culturing and differentiation of SH-SY5Y neuroblastoma cells on

bacterial nanocellulose scaffolds. *Artif. Cells, Nanomedicine Biotechnol.* **2014**, *42* (5), 302–308 DOI: 10.3109/21691401.2013.821410.
(132) Chen, C.; Zhang, T.; Zhang, Q.; Feng, Z.; Zhu, C.; Yu, Y.; Li, K.; Zhao, M.; Yang, J.; Liu, J.; et al. Three-Dimensional BC/PEDOT Composite Nanofibers with High Performance for Electrode-Cell Interface. *ACS Appl. Mater. Interfaces* **2015**, *7* (51), 28244–28253 DOI: 10.1021/acsami.5b07273.
(133) Kuzmenko, V.; Kalogeropoulos, T.; Thunberg, J.; Johannesson, S.; Hägg, D.; Enoksson, P.; Gatenholm, P. Enhanced growth of neural networks on conductive cellulose-derived nanofibrous scaffolds. *Mater. Sci. Eng. C* **2016**, *58*, 14–23 DOI: 10.1016/j.msec.2015.08.012.
(134) Kandalam, S.; Sindji, L.; Delcroix, G. J. R.; Violet, F.; Garric, X.; André, E. M.; Schiller, P. C.; Venier-Julienne, M. C.; des Rieux, A.; Guicheux, J.; et al. Pharmacologically active microcarriers delivering BDNF within a hydrogel: Novel strategy for human bone marrow-derived stem cells neural/neuronal differentiation guidance and therapeutic secretome enhancement. *Acta Biomater.* **2017**, *49*, 167–180 DOI: 10.1016/j.actbio.2016.11.030.
(135) Wang, Y.; Cooke, M. J.; Sachewsky, N.; Morshead, C. M.; Shoichet, M. S. Bioengineered sequential growth factor delivery stimulates brain tissue regeneration after stroke. *J. Control. Release* **2013**, *172* (1), 1–11 DOI: 10.1016/j.jconrel.2013.07.032.
(136) Hackett, J. M.; Dang, T. N. T.; Tsai, E. C.; Cao, X. Electrospun biocomposite polycaprolactone/collagen tubes as scaffolds for neural stem cell differentiation. *Materials (Basel).* **2010**, *3* (6), 3714–3728 DOI: 10.3390/ma3063714.
(137) Tsai, E. C.; Dalton, P. D.; Shoichet, M. S.; Tator, C. H. Matrix inclusion within synthetic hydrogel guidance channels improves specific supraspinal and local axonal regeneration after complete spinal cord transection. *Biomaterials* **2006**, *27* (3), 519–533 DOI: 10.1016/j.biomaterials.2005.07.025.
(138) Min, S. K.; Jung, S. M.; Ju, J. H.; Kwon, Y. S.; Yoon, G. H.; Shin, H. S. Regulation of astrocyte activity via control over stiffness of cellulose acetate electrospun nanofiber. *Vitr. Cell. Dev. Biol. - Anim.* **2015**, *51* (9), 933–940 DOI: 10.1007/s11626-015-9925-8.
(139) Du, J.; Tan, E.; Kim, H. J.; Zhang, A.; Bhattacharya, R.; Yarema, K. J. Comparative evaluation of chitosan, cellulose acetate, and polyethersulfone nanofiber scaffolds for neural differentiation. *Carbohydr. Polym.* **2014**, *99*, 483–490 DOI: 10.1016/j.carbpol.2013.08.050.
(140) Fink, H.; Hong, J.; Drotz, K.; Risberg, B.; Sanchez, J.; Sellborn, A. An in vitro study of blood compatibility of vascular grafts made of bacterial cellulose in comparison with conventionally-used graft materials. *J. Biomed. Mater. Res. - Part A* **2011**, *97 A* (1), 52–58 DOI: 10.1002/jbm.a.33031.
(141) Esguerra, M.; Fink, H.; Laschke, M. W.; Jeppsson, A.; Delbro, D.; Gatenholm, P.; Menger, M. D.; Risberg, B. Intravital fluorescent microscopic evaluation of bacterial cellulose as scaffold for vascular grafts. *J. Biomed. Mater. Res. - Part A* **2010**, *93* (1), 140–149 DOI: 10.1002/jbm.a.32516.
(142) Malm, C. J.; Risberg, B.; Bodin, A.; Bckdahl, H.; Johansson, B. R.; Gatenholm, P.; Jeppsson, A. Small calibre biosynthetic bacterial cellulose blood vessels: 13-months patency in a sheep model. *Scand. Cardiovasc. J.* **2012**, *46* (1), 57–62 DOI: 10.3109/14017431.2011.623788.
(143) Andrade, F. K.; Costa, R.; Domingues, L.; Soares, R.; Gama, M. Improving bacterial

cellulose for blood vessel replacement: Functionalization with a chimeric protein containing a cellulose-binding module and an adhesion peptide. *Acta Biomater.* **2010**, *6* (10), 4034–4041 DOI: 10.1016/j.actbio.2010.04.023.
(144) Wang, X. Y.; Pei, Y.; Xie, M.; Jin, Z. H.; Xiao, Y. S.; Wang, Y.; Zhang, L. N.; Li, Y.; Huang, W. H. An artificial blood vessel implanted three-dimensional microsystem for modeling transvascular migration of tumor cells. *Lab Chip* **2015**, *15* (4), 1178–1187 DOI: 10.1039/c4lc00973h.
(145) Brown, E. E.; Hu, D.; Abu Lail, N.; Zhang, X. Potential of nanocrystalline cellulose-fibrin nanocomposites for artificial vascular graft applications. *Biomacromolecules* **2013**, *14* (4), 1063–1071 DOI: 10.1021/bm3019467.
(146) Pooyan, P.; Tannenbaum, R.; Garmestani, H. Mechanical behavior of a cellulose-reinforced scaffold in vascular tissue engineering. *J. Mech. Behav. Biomed. Mater.* **2012**, *7*, 50–59 DOI: 10.1016/j.jmbbm.2011.09.009.
(147) De Souza, F. C.; Olival-Costa, H.; Da Silva, L.; Pontes, P. A.; Lancellotti, C. L. P. Bacterial cellulose as laryngeal medialization material: An experimental study. *J. Voice* **2011**, *25* (6), 765–769 DOI: 10.1016/j.jvoice.2010.07.005.
(148) Dugan, J. M.; Collins, R. F.; Gough, J. E.; Eichhorn, S. J. Oriented surfaces of adsorbed cellulose nanowhiskers promote skeletal muscle myogenesis. *Acta Biomater.* **2013**, *9* (1), 4707–4715 DOI: 10.1016/j.actbio.2012.08.050.
(149) Silveira, R. K.; Coelho, A. R. B.; Pinto, F. C. M.; de Albuquerque, A. V.; de Melo Filho, D. A.; de Andrade Aguiar, J. L. Bioprosthetic mesh of bacterial cellulose for treatment of abdominal muscle aponeurotic defect in rat model. *J. Mater. Sci. Mater. Med.* **2016**, *27* (8) DOI: 10.1007/s10856-016-5744-z.
(150) Borges, A. C.; Eyholzer, C.; Duc, F.; Bourban, P. E.; Tingaut, P.; Zimmermann, T.; Pioletti, D. P.; Månson, J. A. E. Nanofibrillated cellulose composite hydrogel for the replacement of the nucleus pulposus. *Acta Biomater.* **2011**, *7* (9), 3412–3421 DOI: 10.1016/j.actbio.2011.05.029.
(151) Guler, I.; Billur, D.; Aydin, S.; Kocaturk, S. Efficacy of platelet-rich fibrin matrix on viability of diced cartilage grafts in a rabbit model. *Laryngoscope* **2015**, *125* (3), E104–E111 DOI: 10.1002/lary.25097.
(152) Hendriks, J.; Riesle, J.; Blitterswijk, C. A. van. Co-culture in cartilage tissue engineering. *J. Tissue Eng. Regen. Med.* **2010**, *4* (7), 524–531 DOI: 10.1002/term.
(153) Martínez Ávila, H.; Schwarz, S.; Feldmann, E. M.; Mantas, A.; Von Bomhard, A.; Gatenholm, P.; Rotter, N. Biocompatibility evaluation of densified bacterial nanocellulose hydrogel as an implant material for auricular cartilage regeneration. *Appl. Microbiol. Biotechnol.* **2014**, *98* (17), 7423–7435 DOI: 10.1007/s00253-014-5819-z.
(154) Markstedt, K.; Mantas, A.; Tournier, I.; Martínez Ávila, H.; Hägg, D.; Gatenholm, P. 3D bioprinting human chondrocytes with nanocellulose-alginate bioink for cartilage tissue engineering applications. *Biomacromolecules* **2015**, *16* (5), 1489–1496 DOI: 10.1021/acs.biomac.5b00188.
(155) Yin, N.; Stilwell, M. D.; Santos, T. M. A.; Wang, H.; Weibel, D. B. Agarose particle-templated porous bacterial cellulose and its application in cartilage growth in vitro. *Acta Biomater.* **2015**, *12* (1), 129–138 DOI: 10.1016/j.actbio.2014.10.019.
(156) Bodin, A.; Bharadwaj, S.; Wu, S.; Gatenholm, P.; Atala, A.; Zhang, Y. Tissue-engineered conduit using urine-derived stem cells seeded bacterial cellulose polymer in urinary reconstruction and diversion. *Biomaterials* **2010**, *31* (34), 8889–8901 DOI:

10.1016/j.biomaterials.2010.07.108.
(157) Yang, J.; Jiang, J.; Li, Y.; Li, H.; Jing, Y.; Wu, P.; Yu, D.; Chen, S. A new strategy to enhance artificial ligament graft osseointegration in the bone tunnel using hydroxypropylcellulose. *Int. Orthop.* **2013**, *37* (3), 515–521 DOI: 10.1007/s00264-012-1723-2.
(158) Mathew, A. P.; Oksman, K.; Pierron, D.; Harmand, M. F. Biocompatible Fibrous Networks of Cellulose Nanofibres and Collagen Crosslinked Using Genipin: Potential as Artificial Ligament/Tendons. *Macromol. Biosci.* **2013**, *13* (3), 289–298 DOI: 10.1002/mabi.201200317.

Chapter 2

Technical and Theoretical Background

§1 Scope

This section serves to provide an overview of the physical concepts behind some of the key techniques used in this body of work. As the techniques relate to complicated physical properties that entire theses and text books have been dedicated to, only the main topics are presented in this chapter. Three main techniques used to acquire data for this collection of studies were microscopy, rheometry, and atomic force microscopy.

2.1 Microscopy

2.1.1 Numerical aperture

The numerical aperture indicates how much light can be gathered for a specific working distance. As light enters the objective as a light cone, the angle of the cone is dictated by the focal length of the objective. The numerical aperture is defined by the following equation:

$$NA = nsin(\alpha)\ ,$$

where NA is the numerical aperture, n is the refractive index, and α is the half angle of the light cone.

A larger numerical aperture corresponds to greater magnification as the cone angle increases. Furthermore, the NA tends to increase with additional correction factors for chromatic and spherical aberrations. The NA of the most commonly used objectives for the work presented in this thesis are included in Table I below.

Table I: NA of commonly used Nikon objectives

Objective	NA
4X	0.13
10X	0.30
40X	0.60
60X	1.2

2.2 Resolution

The resolution is the ability to distinguish two points as separate bodies. Light exhibits diffraction; therefore, there is a lower limit when the distance between two objects is insufficient for resolving their point spread functions as the diffracted light overlaps. The irradiance of the diffracted light for a circular aperture is given by the Fraunhofer diffraction[1]:

$$I(\theta) = I(0)\left[\frac{2J_1\left(krsin(\theta)\right)}{krsin(\theta)}\right]^2,$$

where I is the irradiance, J_1 is the first order Bessel function, k is the wavenumber, r is the radius, and θ is the angle.

The diffraction patterns of light form Airy disk diffraction patterns. Two objects cannot be resolved if their separation is less than the Airy disk. This phenomenon is highlighted in the Rayleigh Criterion[2]:

$$\sin(\theta) = 1.22\frac{\lambda}{d},$$

where θ is the angle, λ is the wavelength, and d is the diameter of the aperture.

In addition to the NA and the wavelength of light, the alignment of the optical system affects the overall resolution as does the sampling rate dictated by the Nyquist Theorem[3]. Clearly, the resolution depends on the experimental setup. In the context of confocal microscopy, the resolution exceeds that of standard wide field microscopy because confocal microscopy employs shared volume point scanning. In general, the resolution r can be estimated as:

$$r_{lateral} = 0.61\lambda/NA \text{ widefield}$$

$$r_{lateral} = 0.4\lambda/NA \text{ confocal}$$

$$r_{axial} = 1.4n\lambda/NA\,.$$

Several techniques have been developed to work around the diffraction limit of light and are classified as super-resolution techniques. Although they are very powerful, they were not required to study the processes investigated in the studies presented here.

2.2.1 Confocal microscopy

Laser scanning confocal microscopy was widely used in the work compiled in this thesis. This technique allows for optical sectioning of specimens. Thin planes of light are collected, and the out of focus light above and below these planes are filtered out via a pinhole. The use of the pinhole effectively restricts the point spread functions to their central maxima for each plane; consequently, the blurring effects of the diffracted light from the planes above and below the section of interest are not collected as they do not pass through the pin hole.

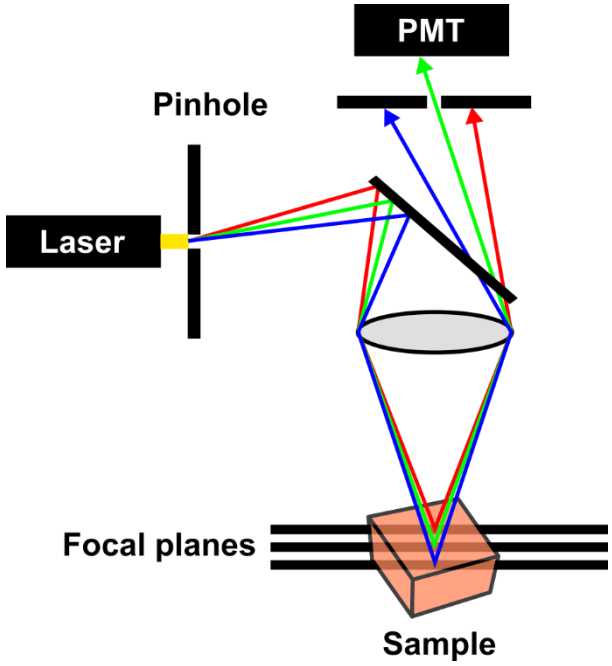

Figure 2.1. Confocal microscope light path. The use of the pin holes allows light from unfocussed planes to be filtered out. As a result, only light from a thin plane is collected. 3D reconstruction can be accomplished by imaging different planes and creating a z-stack of the in-focus planes.

2.2.2 Phase contrast microscopy

In addition to confocal microscopy, phase contrast imaging was extensively used in these projects. The principle of phase contrast microscopy is accentuating differences in the amplitude of the signal that arises from shifts in the light path due to variations in the refractive index of the medium. This phase shift is

$$\delta = \frac{2\pi(n_2 - n_1)t}{\lambda},$$

where: δ is the phase shift, λ is the wavelength, n is the refractive index, and t is the thickness.

As this equation reveals, the phase shift is very small for cell biology applications. The enhancement provided by this technique is the inclusion of a condenser annulus and a phase plate to increase the phase shift and enhance contrast. The condenser annulus is an opaque disk with a void annular ring. If the Köhler illumination is properly aligned, the rear focal plane of the objective contains the conjugate bright ring from the condenser annulus. Thus, the bright ring is superimposed over the phase plate; this alignment is essential for phase contrast imaging as it allows diffracted and undiffracted light to be segregated and shifted. The surrounding light is either advanced (positive) or retarded (negative) 90° in phase by the phase plate. The surrounding light interferes with the diffracted light that has been retarded by 90° at the specimen destructively and constructively for positive and negative phase contrast systems respectively. As a result, large refractive index differences compared to the surrounding area produce dark spots in positive phase contrast, whereas the opposite occurs in negative phase contrast. Here, we exclusively used positive phase contrast. An excellent resource for more information on microscopy and interactive tutorials on each subject matter can be found on the Nikon MicroscopyU webpage [4].

2.3 Rheology

2.3.1 Context

Rheology is defined as the study of the deformation and flow of matter. As the cells and tissue in our body are subject to a variety of internal and external forces, they deform and flow. It is well established that the physical environment affects cellular processes; thus, when designing a biomaterial, it is imperative to understand the rheological properties of the construct. Here we present a brief overview of some key concepts in rheology that are central for characterizing our cellulose-based scaffolds. For a more comprehensive discussion of rheology, we point the readers to *Rheophysics* by Patrick Oswald [5] and *Physics of Continuous Matter* by B Lautrup [6].

2.3.2 Hooke's law of elasticity

Hooke's law relates the force needed to deform an elastic material and the distance that the material deforms. It can be visualized, in its most basic form, as the force required to extend or compress a spring a certain distance for a particular spring stiffness. This concept is readily applied to the uniaxial deformation of an elastic body [6].

$$F = kx$$
$$k = F/x$$
$$E = \frac{FL_0}{A\Delta L}$$

Where F is the force, k is the spring constant, x is the deformation, E is the Young's modulus, , A is the area, L_0 is the original length, ΔL is the change in length.

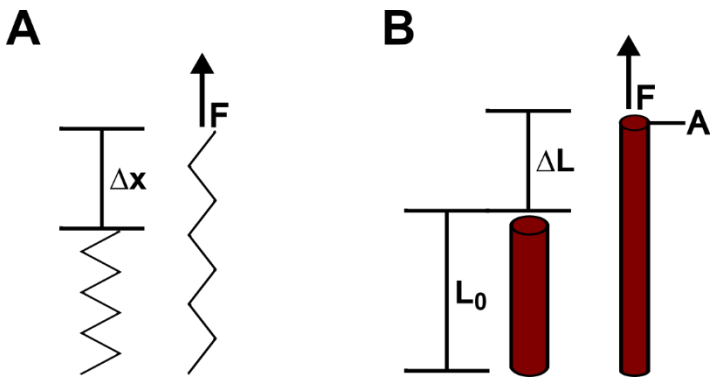

Figure 2.2. Visualization of Hooke's law. (A) A spring is stretched (**Δx**) when a force (**F**) is applied to it. (B) The simple spring extension can be extended to general objects such as a cylinder. In this case, the force (**F**) is acting over a certain area (**A**) and the body extends (**ΔL**) from its initial length of (**L_0**).

In order to describe how materials deform and respond to forces, the strain and stress tensors are required. The strain tensor is necessary as vector displacements do not fully capture the change in spatial relations between local sections of a material. In other words, it is a quantity that captures both translation and rotation in addition to size changes. The strain tensor is therefore the symmetrized displacement gradient tensor, which is valid for small deformations:

$$u_{ij} = \frac{1}{2}\left(\nabla_i u_j + \nabla_j u_i\right)$$

where u is the displacement.

The stress tensor is composed of nine components corresponding to the forces acting on a surface element. For instance, a surface element dS_x would have stress components $\sigma_{xx}, \sigma_{xy}, and\ \sigma_{xz}$.

The general form of Hooke's Law is

$$\sigma_{ij} = 2\mu u_{ij} + \lambda\delta_{ij}\sum_{\mathrm{k}} u_{kk}$$

and upon inverting:

$$u_{ij} = \frac{\sigma_{ij}}{2\mu} - \frac{\lambda}{2\mu(3\lambda + 2\mu)}\delta_{ij}\sum_{k}\sigma_{kk}\ ,$$

where σ is the stress tensor, u is the strain tensor, λ and μ (shear modulus) are the Lamé coefficients, and δ is the Kronecker delta.

2.3.3 Young's modulus and Poisson's ratio

It is often more convenient and useful to express the strains and stresses in terms of the Young's modulus (or bulk modulus for certain cases) and Poisson's ratio. Poisson's ratio is a measure of the tendency of a material to expand or contract in the direction that is perpendicular to the applied stress. A value of 0.5 corresponds to a perfectly isotropic incompressible material, and is the assumed value for many biophysical measurements. Here we present the Young's modulus relationship to the Lamé coefficients as it was more pertinent for this collection of work than the bulk modulus [6].

$$E = \frac{\mu(2\mu + 3\lambda)}{\mu + \lambda}$$

$$\nu = \frac{\lambda}{2(\mu + \lambda)}$$

$$\lambda = \frac{E\nu}{(1 - 2\nu)(1 + \nu)}$$

$$\mu = \frac{E}{2(1 + \nu)}$$

$$u_{ij} = \frac{1 + \nu}{E}\sigma_{ij} - \frac{\nu}{\mathrm{E}}\delta_{ij}\sum_{k}\sigma_{kk}$$

2.3.4 Elastic shear

The generalized form of Hooke's law extends beyond uniaxial deformation and includes shear components. From these general expressions, we can relate the stress to the strains of a body.

As shear components are significant and relevant to the types of stresses that are applied in vivo, it is appropriate to present the underlying continuum mechanics equations for shear as well. The shear corresponds to the off-diagonal components of the stress and strain tensors. Like the Young's modulus and Hooke's spring law, the shear force can be expressed by the following relations:

$$G = \frac{FL}{A\Delta x},$$

where G is the shear modulus, which is μ from above, F is the force, A is the area, L is the distance between the two surfaces, and Δx is the displacement of one plane relative to the other.

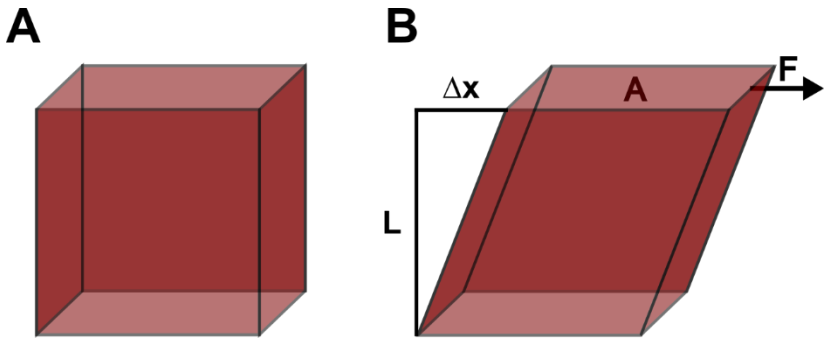

Figure 2.3. Visualization of shear. An undeformed body (A) experiences an applied force on its top face (B). The material of height (***L***) is sheared to the right (**Δ*x***) when a force (**F**) is applied to the top face area (**A**).

2.3.5 General equation of linear viscoelasticity

The previous sections highlighted some important aspects of elastic theory. The materials used in this thesis were not perfectly elastic. They were hydrated materials, and therefore had a fluid component. Fluids can be classified as Newtonian and non-Newtonian; non-Newtonian fluids have strain rate dependence. Real materials are a combination of elastic and fluid components.

From Figure 2.3, the quantity $\frac{\Delta x}{L}$ can be expressed as γ, the strain. When the strains are small, they remain proportional to the stress. In general, the stress can be related to the shear rate with the stress relaxation modulus $G(t)$: [5]

$$\sigma(t) = \int_{-\infty}^{t} G(t-t')\dot{\gamma}(t')dt'.$$

The creep compliance $J(t)$ is given by

$$\gamma(t) = \int_{-\infty}^{t} J(t-t')\dot{\sigma}(t')dt' \,,$$

and relates the rate of applied stress to the shear. It is only the inverse of the shear stress relaxation modulus in specific and simple cases. Real viscoelastic materials often involve complex combinations and arrangement of both spring and dashpot elements. To complicate matters, nonlinear effects result in peculiar phenomena and make modelling large deformations arduous[5].

In practice, it is useful to investigate shear with oscillatory techniques. Moreover, oscillations are commonplace in vivo as well. In this case the shear strain and stress can be defined respectively as

$$\gamma(t) = \gamma_0 e^{i\omega t}$$
$$\sigma(t) = i\omega\gamma_0 \int_{-\infty}^{t} G(t-t')e^{i\omega t'}dt',$$

and a simple variable change results in

$$\sigma(t) = i\omega\gamma_0 e^{i\omega t} \int_{0}^{\infty} G(u)e^{-i\omega u}du \,.$$

In this form, it is immediately clear that the shear modulus is a complex function; therefore, it can be expressed as

$$\sigma(t) = G^*\gamma(t)$$
$$G^*(\omega) = G'(\omega) + iG"(\omega) \,.$$

The *G'* is referred to as the storage modulus as it pertains to the ability to store elastic energy. The *G"* is the loss modulus as it is the viscous dissipation contribution. As the complex modulus contains both components, it is used to characterize viscoelastic materials. A purely elastic material would have $G"(\omega) = 0$, whereas a purely viscous fluid would have $G'(\omega) = 0$. From the equations above, it is evident that an elastic material is in phase with the strain, and a viscous fluid is 90° out of phase with the strain because it is in phase with the strain rate.

2.3.6 Loss factor

The materials that this thesis is focused on are viscoelastic in nature. Therefore, it is valuable to consider the relative contribution of each factor in the rheology of these materials. The loss factor $tan\delta$ is a convenient measure of the proportion of each component. A perfectly elastic material would have $\delta = 0$ and $G" = 0$. Likewise, a solely viscous fluid would have $\delta = \pi/2$ and $G' = 0$.

$$tan\delta = G"/G'.$$

2.3.7 Viscosity

Our materials contain both elastic and fluid components. When the material deforms, friction with the fluid as well as the solid components results in resistance. The viscosity (η) of the material is formally defined as [5]

$$\eta = \sigma/\dot{\gamma}$$

which is also a complex function under oscillatory conditions:

$$\eta^*(\omega) = \eta'(\omega) - i\eta"(\omega)$$
$$\eta^*(\omega) = \frac{G^*(\omega)}{i\omega}$$
$$\eta' = G"/\omega$$
$$\eta" = G'/\omega\ .$$

The η' is commonly referred to as the dynamic viscosity.

2.3.8 Maxwell Model

Real materials are complex, and in order to model them, the elastic and viscous components are arranged in different combinations. Two main models are the Maxwell model and the Kelvin-Voigt model. The simplest form of the Maxwell model involves a spring (s) in series with a dashpot (d). As a result, the strain is additive [5].

$$\gamma = \gamma_s + \gamma_d$$
$$\dot{\gamma} = \dot{\gamma_s} + \dot{\gamma_d}$$

The spring component yields a stress

$$\sigma_s = G\gamma_s\ ,$$

whereas the dashpot has a stress that is dependent on the strain rate $\dot{\gamma}$

$$\sigma_d = \eta\dot{\gamma}_d \, .$$

Therefore, the strain rate can be expressed as

$$\dot{\gamma} = \frac{\dot{\sigma}}{G} + \frac{\sigma}{\eta},$$

which can be rewritten as

$$\sigma + \tau\dot{\sigma} = \eta\dot{\gamma}$$
$$\sigma(t) = \frac{\eta}{\tau}\int_{-\infty}^{t} \exp\left[-\frac{t-t'}{\tau}\right]\dot{\gamma}(t')dt'$$
$$\sigma(t) = \eta\dot{\gamma}[1 - \exp\left(-\frac{t}{t'}\right)].$$

This model can then be extended to multiple variations wherein Maxwell elements are connected together and a distribution of relaxation times are present[5].

The Maxwell and Kelvin-Voigt models both capture aspects of the observed behaviours of viscoelastic materials. Namely the Maxwell model predicts stress relaxation, but fails to include creep; the opposite occurs in the Kelvin-Voigt model.

2.3.9 Kelvin-Voigt

In contrast to the Maxwell model, the Kelvin-Voigt model involves spring and dashpot elements connected in parallel. In this arrangement, the stress is additive [5].

$$\sigma = \sigma_s + \sigma_d$$
$$\sigma = G\gamma + \eta\dot{\gamma}$$

Upon rearranging, the relaxation time $\tau = \eta/G$ is evident.

$$\frac{\sigma}{G} = \gamma + \tau\dot{\gamma}$$

This is formally equivalent to the Burgers model, which consists of two Maxwell elements in parallel. One of the elements has infinite viscosity, and the other has infinite stiffness. The constitutive equation for the Burgers model is [5]

$$(\eta_1 + \eta_2)\dot{\gamma} = (\eta_1\tau_2 + \eta_2\tau_1)\ddot{\gamma} = \sigma + (\tau_1 + \tau_2)\dot{\sigma} + (\tau_1\tau_2)\ddot{\sigma} \, .$$

As a result, many of the quantities derived from the Maxwell model including those presented above are applicable to viscoelastic solids. The Kelvin-Voigt model is better suited for modelling viscoelastic solids, as it successfully models creep, which is evident from the parallel arrangement of the spring and dashpot elements. The materials used in this thesis are viscoelastic solids. As shown in the subsequent chapters, the elasticity dominates the viscous component and the materials experience a small amount of creep[5].

2.4 Atomic force microscopy

2.4.1 Concept

Atomic force microscopy (AFM) is a technique that can probe and image fine features of a sample. The basic concept of AFM is that a cantilever probes the surface features and a laser reflects off of the cantilever and its deflection is monitored on a detector. There are a variety of different applications of AFM including imaging, force mapping, object manipulation, and force spectroscopy. Unlike the other microscopy techniques used in this thesis, AFM does not use lenses or beams, and therefore is not impeded by the diffraction limit. Instead, tip-sample interactions such as Van der Waals forces, electrostatic forces, and dipole-dipole interactions are measured. In this body of work, AFM was used for force spectroscopy: measuring the Young's modulus.

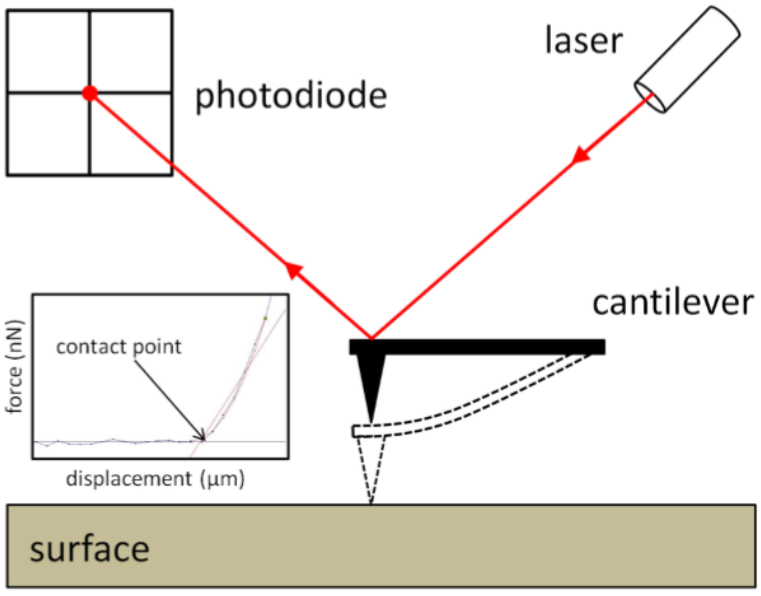

Figure 2.4. Schematic of AFM. As the cantilever deflects from surface interactions, the laser is deflected onto different regions of the photodiode. As a result, the deflection of the probe and the tip sample interaction force can be measured. Inset: force-distance curve of a soft gelatin hydrogel.

2.4.2 Force-distance measurements

The AFM measures force-distance data with a fixed lateral position. The cantilever acts as a spring; therefore, estimates of the elasticity of the surface can easily be calculated from geometrical arguments. The z position of the cantilever can be adjusted via several methods. Here we used the JPK Nanowizard II AFM, which employs piezoelectric control. The characteristic force-distance curve for a force spectroscopy experiment has five distinct regions[7]:

1. Approach from distant position
2. Tip snaps to contact (attractive force)
3. Increase in repulsive forces until the setpoint is reached
4. Retraction while in contact with the surface
5. Removal from the surface

Clearly there is hysteresis, and the approach curve and retraction curve contain different information.

2.4.3 Calibration

In order to extract data from the force-distance curves, the device must be calibrated. The raw data consists of the position of the reflected laser spot on the photodiode, and the value is reported in volts (V). This voltage signal is converted into a physical length in nanometers (nm) by measuring the sensitivity of the cantilever. When a hard surface, such as glass, is used, a linear relationship between the distance and the voltage is obtained. It should be noted that the surrounding medium affects this conversion factor. When using live cells or measuring the stiffness of biological samples that are immersed in fluid, the calibration should be repeated in the appropriate medium. The other calibration that is required is the spring constant calibration of the cantilever. Several methods can be employed to measure the spring constant; here the thermal noise method was used. In this method, the resonant frequencies and the corresponding harmonic frequencies arising from thermal fluctuations are used in conjunction with the equipartition of energy theorem[8].

$$H = \frac{p^2}{2m} + \frac{1}{2}m\omega_0^2 q^2$$

$$\langle \frac{1}{2}m\omega_0^2 q^2 \rangle = \frac{1}{2}k_B T \,,$$

where H is the Hamiltonian of the harmonic spring oscillator, p is the momentum, m is the mass, q is the displacement, ω_0 is the resonant frequency, k_B is Boltzmann's constant, and T is the absolute temperature.

Naturally, the force constant is given as:

$$k = m\omega_0^2 ;$$

hence, the mean-square displacement can be used to calculate the force constant:

$$k = k_B T .$$

Fitting the resonance peak with a Lorentz curve enables the spring constant to be calculated. These calibrations are integral for accurate data collection and must be repeated every time. The reported values of the spring constant from the manufacturer are a guide, but should not be used as the actual value.

The thickness (t), length (L), width (w), and elastic modulus (E) of the cantilever are used to calculate the spring constant (k):

$$k = \frac{Ewt^3}{4L^3} .$$

As evidenced by the preceding relationship, the spring constant is highly dependent on the thickness of the cantilever; the thickness is the parameter that is most difficult to obtain a high precision during fabrication. Moreover, the thickness of the cantilever is linearly related to the resonance frequency (f_n):

$$f_n = \omega_0 = \frac{\alpha_n^2}{2\pi\sqrt{12}} \frac{t}{L^2} \sqrt{\frac{E}{\rho}},$$

where: n is the mode number, ρ is the density, and α_n is the flexural vibration modes solution.

Therefore, the spring constant is proportional to the resonant frequency to the third power[9]

$$k \propto f_n^3 .$$

2.4.4 Young's modulus

Upon successful calibration, the force-distance curves can be collected and used to measure the Young's modulus of the material by considering geometric properties of the tip. The Sneddon-Hertz model for a cone was used to solve the deformation profile of the sample, which was modelled as an isotropic infinite half-space elastic material. In this body of work, the pyramidal tip geometry was used. The geometries of the pyramid shape and cone are similar and yield nearly identical expressions relating the force, Young's modulus, and deformation; therefore, the tip can be modelled as a conical indenter[10].

$$F_{cone} = \frac{2}{\pi}\frac{E}{1-\nu^2}\tan\alpha\,\delta^2$$
$$F_{pyramid} = \frac{1}{\sqrt{2}}\frac{E}{1-\nu^2}\tan\alpha\,\delta^2$$
$$\frac{F_{cone}}{F_{pyramid}} = \frac{2\sqrt{2}}{\pi}$$
$$\cong 0.9\,,$$

where: F is the force, E is the Young's modulus, ν is the Poisson's ratio, δ is the deformation, and α is the opening angle of the cone.

2.4.5 Analyzing force curves for cells and soft materials

AFM force curves on biological samples and soft materials are commonly modelled with a variation of the Hertz model. The Hertz model describes the shape and deformation profile of two curved bodies under stress. This model is widely applicable as the assumptions that the material is an isotropic linear elastic solid are simple to use and approximate the data well; nevertheless, this is an oversimplification. This model fails to include the intrinsic viscous component of these viscoelastic materials. This viscous component is clearly visible as the loading and unloading force curves display hysteresis. As the relaxation time depends on the viscous component of the material, different measurement rates and penetration depths will yield different Young's moduli. In addition, the assumption of homogeneity does not hold when investigating complex structures, such as cells, which are comprised of a collection of heterogenous components. Despite the shortcomings of the oversimplified view of soft and biological samples, the Hertz model provides important and useful information on the elastic character of the materials. When fitting the force curves, another assumption is used: the Poisson's ratio is often set to 0.5. This approximation is valid for soft and small samples where the volume changes are minute. Moreover, the experiment set-up usually requires the substrate to be modelled as an infinite half space in order to apply the Boussinesq solution and to avoid underlying surface effects. Practically, this results in indentations on the order of 200 nm for cells[10–12]. Here, we present the Sneddon-Hertz model used to analyze the force-distance curves in this thesis. Rico et al. provide the complete derivation[10].

Starting from the force (F) – indentation (δ) relationship:

$$F = \int\int_A \frac{p^*(r,\phi)f(r,\phi)}{\delta^*} r\,dr\,d\phi\,,$$

where p^* is the pressure distribution, and f is the interpenetration function.

As p^* only has a known analytical solution for the elliptical contact geometry, the blunted pyramidal tip can be approximated as a circle of radius a.

Therefore,

$$p^*(r,\phi) = \frac{E\delta^*}{\pi(1-\nu^2)(a^2-r^2)^{\frac{1}{2}}}$$

$$F = \int\int_A \frac{E}{\pi(1-\nu^2)(a^2-r^2)^{\frac{1}{2}}} f(r,\phi) r dr d\phi$$

$$F = \frac{E}{\pi(1-\nu^2)} \int\int_A \frac{f(r,\phi)}{(a^2-r^2)^{\frac{1}{2}}} r dr d\phi \ .$$

For four-sided pyramidal tips:

$$F = \frac{2E}{1-\nu^2}\left[\delta a - \frac{2^{\frac{1}{2}}}{\pi}\left(\frac{a^2}{\tan\delta}\right)\left(\frac{\pi}{2} - \sin^{-1}\frac{b}{a}\right) - \frac{a^3}{3R_c} + (a^2-b^2)^{\frac{1}{2}}\left(\frac{2^{\frac{1}{2}}}{\pi}\left(\frac{b}{\tan\theta} + \frac{a^2-b^2}{3R_c}\right)\right)\right],$$

where R_c is the spherical cap of the blunted pyramidal tip, b is the radial distance of the transition from the spherical cap to the pyramidal face.

In the limit of $b = 0$ (no defect), the ideal four-sided pyramid equation is derived:

$$F_{\lim\ b\to 0} = \frac{1}{2^{\frac{1}{2}}} \frac{E\tan\theta}{(1-\nu^2)} \delta^2 \ .$$

2.5 References

(1) Parrent, G. B.; Thompson, B. J. On the Fraunhofer (Far Field) Diffraction Patterns of Opaque and Transparent Objects with Coherent Background. *Opt. Acta Int. J. Opt.* **1964**, *11* (3), 183–193 DOI: 10.1080/713817880.

(2) Hauch, K. D.; Ratner, B. D. Microscopy for Biomaterials Science. In *Biomaterials Science: An Introduction to Materials: Third Edition*; Elsevier Inc., 2013; pp 677–692.

(3) Vangindertael, J.; Camacho, R.; Sempels, W.; Mizuno, H.; Dedecker, P.; Janssen, K. P. F. An introduction to optical super-resolution microscopy for the adventurous biologist. *Methods and Applications in Fluorescence*. IOP Publishing Ltd March 16, 2018.

(4) MicroscopyU - The Source for Microscopy Education https://www.microscopyu.com/ (accessed Dec 30, 2019).

(5) Oswald, P. *Rheophysics : the deformation and flow of matter*; Cambridge University Press: New York, 2009.

(6) Lautrup, B. *Physics of Continuous Matter : Exotic and Everyday Phenomena in the*

Macroscopic World., 2nd ed.; CRC PRESS: New York, 2011.

(7) JPK Instruments. *Technical Note - A practical guide to AFM force spectroscopy*; 2019.

(8) Hutter, J. L.; Bechhoefer, J. Calibration of atomic-force microscope tips. *Rev. Sci. Instrum.* **1993**, *64* (7), 1868–1873 DOI: 10.1063/1.1143970.

(9) Gavan, K. B.; Van Der Drift, E. W. J. M.; Venstra, W. J.; Zuiddam, M. R.; Van Der Zant, H. S. J. Effect of undercut on the resonant behaviour of silicon nitride cantilevers. *J. Micromechanics Microengineering* **2009**, *19*, 8 DOI: 10.1088/0960-1317/19/3/035003.

(10) Rico, F.; Roca-Cusachs, P.; Gavara, N.; Farré, R.; Navajas, D. Probing mechanical properties of living cells by atomic force microscopy with blunted pyramidal cantilever tips. *Phys. Rev. E* **2005**, *72* DOI: 10.1103/PhysRevE.72.021914.

(11) Sneddon, I. N. *The Relation Between Load and Penetration in the Axisymmetric Boussinesq Problem for a Punch of Arbitrary Profile*; Pergamon Press, 1965; Vol. 3.

(12) JPK Instruments. *Determining the elastic modulus of biological samples using atomic force microscopy*; 2019.

Chapter 3

Customizing the Shape and Microenvironment Biochemistry of Biocompatible Macroscopic Plant-Derived Cellulose Scaffolds

This chapter is a reprint of a previously published research paper:

Hickey, R. J., Modulevsky, D. J., Cuerrier, C. M. & Pelling, A. E. Customizing the Shape and Microenvironment Biochemistry of Biocompatible Macroscopic Plant-Derived Cellulose Scaffolds. *ACS Biomaterials Science & Engineering* 4, 3726–3736 (2018).

§1 Motivation

There is a need for engineering new and augmented artificial tissues, and these new constructs must capture the physical cues that dictate cell and tissue function. Our group has pioneered the use of plant-derived scaffolds for mammalian cell culture in an attempt to solve these issues. The novel plant-derived, cellulose-based biomaterials exploit the existing structure of plants that are stripped of their cellular content with decellularization techniques. Functionalizing and customizing these materials to create composite scaffolds provides an advancement to the field of tissue engineering and adds another layer of complexity to this class of material. In the body, cells reside in complex environments with many different components; therefore, creating composites is an essential progression towards materials that recapitulate the native environment.

§2 Hypothesis and Objectives

The goal of this study was to create composite cellulose scaffolds to confer customizability to the biocompatible base material. We hypothesized that different hydrogels could be used to provide spatial and temporal cues to the residing cells. We investigated both temporary and permanent hydrogel composites along with a new preparation and fabrication approach.

3.1 Abstract

Plant-derived cellulose scaffolds constitute a highly viable and interesting biomaterial. They retain a high flexibility in shape and structure, present the ability to tune surface biochemistry, display a high degree of biocompatibility, exhibit vascularization, and are widely available and easily produced. What is also immediately clear is that pre-existing cellulose structures in plants can also provide candidates for specific tissue engineering applications. Here we report a new preparation and fabrication approach for producing large scale scaffolds with customizable macroscopic structures that support cell attachment and invasion, both in vitro and in vivo. This new fabrication method significantly improves cell attachment compared to our previous work. Moreover, the materials remain highly biocompatible and retain vascularization properties in vivo. We present proof-of-concept studies that demonstrate how hydrogels can be temporarily or permanently cast onto the macroscopic scaffolds to create composite plant-derived cellulose biomaterials. This 'inverse moulding' approach allows us to provide temporary or permanent biochemical cues to invading cells in vitro. The development of a new-generation of rapidly and efficiently produced composite plant-derived biomaterials provides an important proof that such biomaterials have the potential for numerous applications in tissue engineering.

3.2 Introduction

Designing biomaterials that support cell growth and function is essential for tissue engineering and regenerative medicine. As such, biomaterials are often designed to be intricate constructs with tuneable structural, chemical, and mechanical properties [1]. Moreover, substantial research has focused on developing 3D biomaterials that resemble the complex in vivo cellular microenvironment [2].

Biomaterials typically consist of two main classes: synthetic and naturally derived scaffolds [3,4]. The synthetic biomaterials are often constructed with the use of synthetic polymers that mimic structural characteristics of the extracellular matrix (ECM), sometimes even functionalized with ECM proteins [5]. On the other hand, naturally derived scaffolds involve repurposing existing biological materials and structures [6]. Natural biomaterials can often be acquired using decellularization techniques [7]. Decellularization refers to the process of removing the existing cellular structures while leaving behind an intact ECM [8]. The remaining ECM is then used as a 3D biocompatible scaffold [9].

For many years there has been a significant interest in synthetic, bacterial, and plant-derived cellulose as a potential biomaterial for tissue engineering applications [10–27]. Cellulose is widely available in many forms and easily incorporated into composite materials. It is now well established that bacterial and synthetic cellulose can act as scaffolds in a variety of tissue

engineering applications, both in vitro and in vivo [28–30]. Importantly, synthetic/bacterial cellulose is often moulded or cast into a desired shape, and requires synthesis or cell culture protocols to produce scaffolds [31]. On the other hand, the pre-existing structures of plant-derived cellulose scaffolds can be exploited directly with minimal processing and expense [32,33].

Several years ago we demonstrated that native plant tissue can be decellularized, and the remaining cellulose scaffold can be used as a suitable platform for in vitro mammalian cell culture and also as an implantable in vivo biomaterial [32,33]. Our work [32,33] and recent studies [34,35] have shown that a multitude of plant-derived cellulose scaffolds are suitable in vitro. The choice of the specific plant depends on the chemical, physical, and mechanical properties of the plant and the intended application [32–35]. Although not necessary for in vitro cell growth, biofunctionalizations of the plant-derived cellulose scaffolds have also been employed as steps in preparing cellulose scaffolds as we and others have shown [32,34,35]. In addition, the similarities between the vascular structures of plants and animal tissues have been exploited via perfusion based decellularization [35]. However, as shown previously, the need for a pre-existing vascular template is not a requirement for the vascularization of plant-derived cellulose biomaterials in vivo. In fact, we have shown that decellularized, yet otherwise unmodified, plant cellulose is biocompatible and pro-angiogenic in vivo [33]. In this case [33], vascularization occurs in the highly amorphous and porous plant-derived cellulose scaffolds without any necessary functionalization or dependence on pre-existing vascular structures.

Extending our previous work, here we report a new preparation and fabrication approach for producing large scale scaffolds with pre-defined structures and improved cell attachment and invasion, both in vitro and in vivo. Specifically, we demonstrate that apple-derived scaffold biomaterials can be hand- or machine-cut into desired shapes as opposed to approaches that might rely on the use of 3D printing, moulding, or casting [7,8]. We also present proof-of-principle studies that demonstrate how hydrogels can be temporarily or permanently cast onto the macroscopic scaffolds. Similar approaches have been employed in tissue engineering [36,37]; however, to our knowledge, this is first time they have been used in combination with decellularized plant scaffolds. These ‘inverse moulding’ approaches allowed us to provide temporary or permanent biochemical cues to invading cells in vitro.

Moving beyond simple in vitro studies of plant-derived cellulose scaffolds, we also demonstrate that these biomaterials maintain their ability to become vascularized in vivo while improving cell invasion as compared to our previous in vivo study [33]. We show that these plant-derived cellulose scaffolds continue to display high biocompatibility in vitro and in vivo, with cell invasion occurring much more rapidly and completely [33]. Using decellularized cellulose scaffolds as biomaterials is a promising approach because of their availability, versatility, and ease of use [32–35]. What is also immediately clear is that pre-existing cellulose structures in plants can also provide candidates for specific tissue engineering applications.

The results of this study and our previous work [32,33] suggest cellulose scaffolds constitute a highly viable and interesting biomaterial. Specifically, they tend to overcome many of the complications that often arise with other traditional biomaterials, while also retaining a high flexibility in shape and structure, presenting the ability to tune surface biochemistry, displaying a high degree of biocompatibility, exhibiting vascularization, and being widely available and easily produced. This is the first time that this new-generation of plant-derived biomaterial has been combined with hydrogels. These composite cellulose-based biomaterials provide a very important proof that such a platform can potentially be applied to many tissue engineering applications. The new fabrication process reported here is simple and supports high cell growth. Moreover, the processes and protocols described in our study really open up dramatic new possibilities for biomaterial engineering with respect to the large size and geometric complexity that are now attainable. The biomaterials we describe are simply produced by hand or even on a computerized numerical control (CNC) machine within minutes, without molding, complex chemistry, and restrictions to small sizes. The materials for these composites are easily and cheaply sourced, biocompatible in vitro, and once implanted are biocompatible and display clear vascularization. No special coatings or functionalization are required, and all studies were conducted in immune-competent animals. This study contributes many significant advantages to the field and opens up new possibilities for existing hydrogels and biopolymers to be used in combination with plant-derived cellulose biomaterials.

3.3 Results

3.3.1 Improving cell attachment on minimally processed plant-derived cellulose scaffolds

Decellularization with the surfactant sodium dodecyl sulfate (SDS) was used to obtain 3D cellulose scaffolds void of any native apple cells or nucleic acids [32,33]. With smaller scaffolds (as used previously [32,33]), the concentration of SDS required was low; however, larger objects require higher concentrations of SDS to undergo complete decellularization [2,6,7,34,35]. We have found that the removal of all remaining SDS at higher concentration is very time consuming through washing alone. Here, a Ca^{2+} salt buffer was added to induce phase separation of the detergent due to a change in cloud point. This was carried out after washing steps in order to further remove any residual SDS [38]. However, due to the need of a sufficiently high salt concentration to stimulate micelle formation [39], a salt residue does form on the cellulose surfaces (Fig. 3.1A). The resulting salt residue was then removed by incubating the scaffold in dH_2O (Fig. 3.1B), though several other techniques were found to be effective, such as incubation with acetic acid, DMSO or through sonication (data not shown). A significantly increased number of cells was found to attach to the scaffolds after treatment as compared to the control (Fig. 3.1C,D). Two days after the cells were seeded onto the biomaterial, cell density was quantified with the use of the CCK-8 cell counting

kit (Fig. 3.1E). A significantly greater number of cells were found attached to the treated scaffolds ($3.7x10^1 \pm 2.9$ cells/mm^3) compared to the controls ($2.6x10^1 \pm 2.5$ cells/mm^3) ($P = 1.8x10^{-2}$, N = 5). We also showed that when preparing small biomaterial constructs, the remnant SDS can alternatively be removed with extensive washing without using the salt pre-treatment, and a comparable viable cell attachment can be achieved; this method is time-consuming and ineffective with larger samples (Supporting Information Fig. S3.1) ($P = 9.2x10^{-1}$, N = 4).

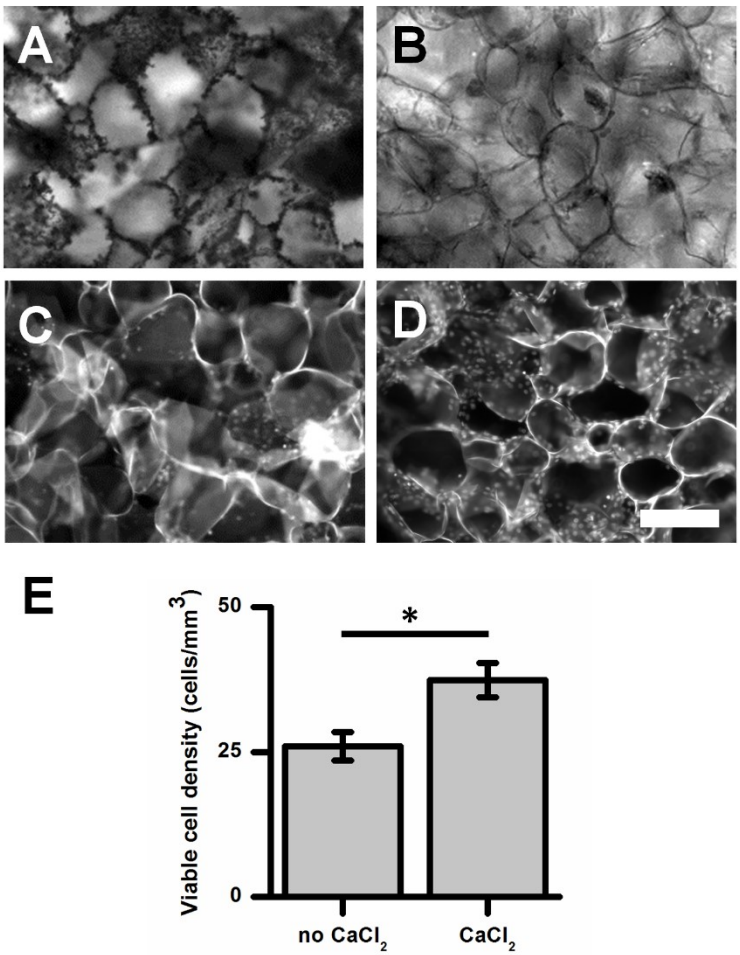

Figure 3.1: $CaCl_2$ pre-treatment. A $CaCl_2$ pre-treatment was used to remove remnant surfactant from the scaffold. (A) The salt/micelles crash out of solution onto the scaffold. (B) Removal of the salt residue. (C) C2C12 myoblasts cultured on the scaffold without the $CaCl_2$ pre-treatment. (D) C2C12 myoblasts cultured on the scaffold with the $CaCl_2$ pre-treatment. (E) CCK-8 quantification of cell density shows an increased number of viable cells attached to the SDS + salt treated scaffolds ($3.7x10^1 \pm 2.9$ cells/mm^3) compared to SDS alone ($2.6x10^1 \pm 2.5$ cells/mm^3) ($P = 1.8x10^{-2}$, N = 5) after 2 days of culture. All values are mean ± s.e.m. Scale = 200 μm.

3.3.2 Construction of macroscopic cellulose scaffolds and surface modification

Here we show how decellularized cellulose can be further processed by cutting them into macroscopic ring shapes from bulk hypanthium tissue (Fig. 3.2). Many studies produce large scaffolds utilizing gel casting or 3D printing techniques [36]. Here, as a proof-of-concept, we created ring shaped scaffolds (Fig. 3.2). A ring was chosen simply as a model of a "complex" feature that would typically be created through other techniques. Of course, a broad array of desired shapes can conceivably be created (Supporting Information Fig. S3.2). Although the ring was chosen only as a proof-of-concept structure, this shape has complex properties that are of significant biological relevance. The ring contains two flat faces, two curved surfaces, two radii of curvature, four sharp edges connecting each face to the curved surfaces, and a porous 3D interior (Fig. 3.2).

First an apple was sliced into thin (1.2 mm sections) using a mandolin slicer (Fig.3.2A). A 5 mm diameter disk with a 1.2 mm thickness was then carved out of the slice using a 5 mm biopsy punch. To complete the ring, a 2 mm biopsy punch was used to remove a 2 mm disk from the centre of the 5 mm disk (Fig. 3.2B). After fabrication, the samples were transferred to a 0.1% SDS solution and decellularized as described above for 48 h while being shaken at 180 RPM (Fig. 3.2C). A distinct change in transparency was observed during decellularization.

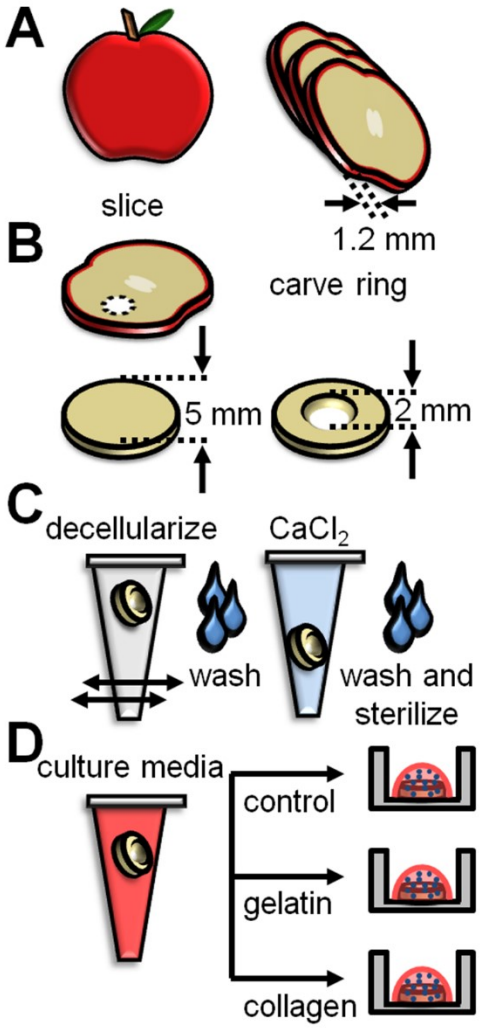

Figure 3.2: Schematic of biomaterial preparation. (A) The apple was cut and sliced on a Mandolin slicer. (B) A 5 mm biopsy punch was used to cut out a disk from the apple slice; a 2 mm biopsy punch was used to cut out a disk from the 5 mm disk to make the ring. (C) The ring was decellularized in 0.1% SDS for 48 h, washed, incubated with salt buffer for 24 h, and washed and sterilized. (D) Seeding the scaffold with cells in media, gelatin, and collagen.

C2C12 mouse myoblast cells were seeded onto the scaffolds, and the cells were allowed to proliferate and invade the structure for 2 weeks (Fig. 3.2D and Fig. 3.3). After 2 weeks, the rings were found to be completely invaded by cells (Fig. 3.3). We note that at this stage, no deliberate surface functionalization has been required to achieve these results as opposed to other studies [34,35]. These results demonstrate that complex 3D cellular constructs can be simply produced in plant-derived cellulose scaffolds.

The ring scaffolds also present another potential use in tissue engineering applications. We now show that hydrogels can be cast onto the macroscopic structure, after which the gel assumes the

shape of the scaffold itself as opposed to the traditional approach of casting hydrogels into moulds [29,40,41]. In this "inverse-moulding" scenario, we chose to cast a gelatin or collagen hydrogel onto the scaffolds simply to demonstrate feasibility (Fig. 3.3). In the case of gelatin hydrogels, a 10% (m/v) gelatin solution in Dulbecco's Modified Eagle Medium (DMEM) was first prepared. Gelatin has a melting temperature of 32°C [42]; therefore, the gelatin solution was kept at 37°C in order to remain in its liquid state until the cells were introduced into the solution and the gelatin-cell suspension was cast around the cellulose ring (Fig. 3.2D). The gelatin solution then cooled below its melting temperature and was left to gel for 15 minutes at room temperature. Here, the hydrogel containing the cells was left on the scaffold in its gelled state for a further 45 minutes. Following this period, the sample was immersed in culture media and placed in the incubator at 37°C and 5% CO_2. Once above the melting temperature, the gelatin gel slowly diffuses out of the scaffold while the cells remain on the biomaterial (Fig. 3.3B). In this temporary inverse moulding scenario, the cells are temporarily exposed to a distinct biochemical cue during the attachment process.

Conversely, the cellulose scaffold can also act as an inverse mould for permanent gels. Cellulose rings were covered in a 1.5 mg/mL collagen solution containing cells in a method very similar to the gelatin scenario (Fig. 3.2D). The collagen solution rapidly polymerizes and forms a permanent gel containing the biomaterial and the cells. After 15 minutes of incubation at room temperature, culture media was added to the collagen coated cellulose ring. The sample was then placed in the incubator at 37°C and 5% CO_2. After incubation, the collagen gel was not observed to melt (as expected) and was also found to fill the hole in the ring as a compacted structure (Fig. 3.3C,D). This creates a composite biomaterial in which cells are found in two distinct regions: in the cellulose and collagen ring, or in the collagen gel suspended in the ring-hole.

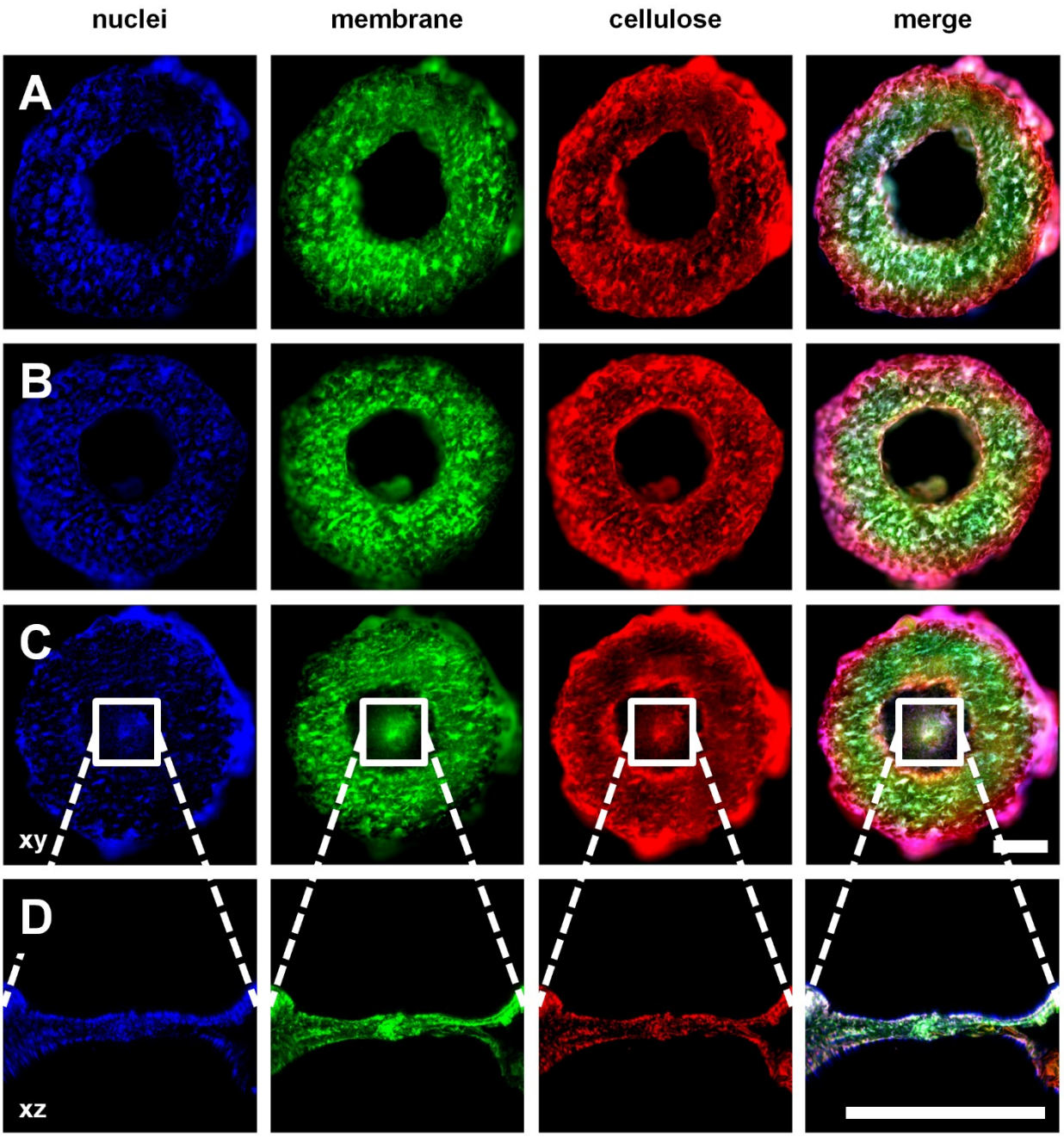

Figure 3.3: Ring structures with temporary and permanent hydrogels. C2C12 myoblasts were grown on the ring scaffolds for 2 weeks after being seeded with culture media (A), gelatin (B), and collagen (C and D). The scaffolds were stained for the nuclei (blue), cell membrane (green), and cellulose (red), and imaged using confocal microscopy. The permanent collagen hydrogel created a compacted collagen suspension over the ring-hole (C and D). It should be noted that the collagen gel suspended over the ring-hole contained cells as well. Scale = 1000 μm.

3.3.3 Cell invasion and proliferation

The CCK-8 assay was used to quantify and compare the initial attachment of the cells (1 day post-seeding) on the scaffolds with the temporary and permanent hydrogels. It was found that a significantly greater population of viable cells remained in the biomaterial used in combination with the permanent hydrogel (Fig. 3.4) ($P = 1.2x10^{-3}$ and $P = 1.1x10^{-2}$ for the collagen compared to the control and gelatin samples respectively, N= 4). The CCK-8 cell counting kit is a powerful assay used to measure cell proliferation and viability; however, there is a maximum number of cells that can be detected. After 2 weeks of cell growth, the number of cells on the biomaterial exceeded the detection limit of the CCK-8 assay. As a result, the live:dead cell ratio was calculated to further assess the biocompatibility of the cellulose based biomaterials (N = 3 scaffolds for each condition). After two weeks, no statistically significant difference in the ratio of live:dead cells was observed (Fig. 3.4) ($P > 0.05$, N = 6 images for each condition), and the spatial distributions of the live and dead cells were uniform for the limit of detection.

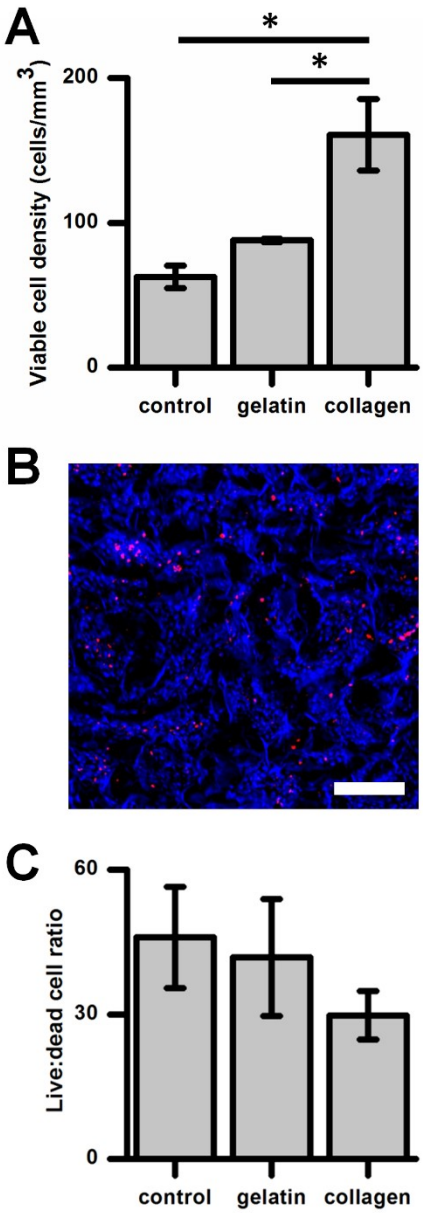

Figure 3.4: Initial cell attachment and viability. (A) The initial attachment of the cells 1 day post-seeding was quantified using CCK-8. A significantly greater initial cell density was obtained with the permanent collagen hydrogel ($P = 1.2x10^{-3}$ and $P = 1.1x10^{-2}$ for the collagen compared to the control and gelatin samples respectively, N= 4). (B) The cells on the biomaterials were stained after two weeks of culture with Hoechst 33342 (stains all cell nuclei) and propidium iodide (stains only dead cell nuclei) and were imaged with confocal microscopy to assess cell viability (N = 3 scaffolds for each condition). Scale = 200 μm. (C) No statistically significant difference in the ratio of live:dead cells was observed ($P > 0.05$, N = 6 images for each condition).

In addition to assessing the in vitro biocompatibility, the mechanical properties of the biomaterial were also investigated (Supporting Information Fig. S3.3). Employing bulk compression testing, the Young's moduli of the scaffolds were measured after 2 weeks of culture using a custom-built device. The Young's modulus of the scaffolds without the $CaCl_2$ treatment (8.0 ± 1.7 kPa) was significantly lower than that of the treated samples ($1.7x10^1$ ± 1.1 kPa) ($P = 4.9x10^{-2}$, no $CaCl_2$: N = 5, $CaCl_2$: N = 6). Moreover, although the addition of the hydrogels did increase the moduli, they were not significantly different from the $CaCl_2$-treated scaffolds ($1.5\ x10^1$ ± 3.6 kPa, $2.3x10^1$ ± 1.7 kPa, gelatin and collagen respectively, $P > 0.05$, N=6). Importantly, the mechanical properties of all the scaffolds fall well within the range of native animal tissues such as muscle [44,45].

Confocal laser scanning microscopy was used to image the top and bottom of the scaffolds after cells were allowed to proliferate for 2 weeks (N = 6 scaffolds for each condition). Both sides of the ring were imaged to confirm that cell invasion was similar on both faces revealing complete penetration. Figure 3.5A-C shows the xy and zy projections of the cells on the cellulose biomaterial. The nuclei of the cells were found along the cellulose cell walls. Orthogonal views of confocal scans reveal that the cells invaded the scaffold to the limit of detection (~300 μm imaging depth). In order to assess how well cells penetrated the entire 1.2 mm thickness of the biomaterial, the scaffolds were also cut perpendicular to the ring diameter (Fig. 3.5D), and the cross-sectional areas of the rings were imaged (N = 3) (Fig. 3.5E-G). Confocal imaging for cell invasion and proliferation revealed similar cell density under all conditions reported above. Quantification of confocal data allowed the number of cells in randomly selected $2.7x10^7$ um^3 volumes to be calculated. We observed no statistical differences in cell numbers under any of the three ring fabrication conditions ($P > 0.05$, N = 12 images for each condition) (Supporting Information Fig. S3.4). Importantly, temporary and permanent inverse moulding does not appear to impair cell proliferation after 2 weeks of culture when compared to bare scaffolds. However, it should also be noted that C2C12 myoblasts deposit their own ECM when cultured on 3D scaffolds [43]. Consequently, the three different techniques – bare scaffold, temporary gelatin functionalization, and permanent collagen functionalization – can be used interchangeably without affecting cell invasion and proliferation in the scaffolds with the particular size and geometry used in this study, all while exposing cells to three distinct biochemical cues. The result of this proof-of-concept study is that the decellularized cellulose biomaterials can be used in combination with temporary and permanent inverse moulding hydrogel techniques. Naturally, this concept is not restricted to gelatin and collagen: a wide variety of temporary and permanent biochemical cues can be supplied through the use of other polymers, proteins, and biomolecules. The use of specific proteins will of course depend on the goals and interests of individual investigators who might employ this approach.

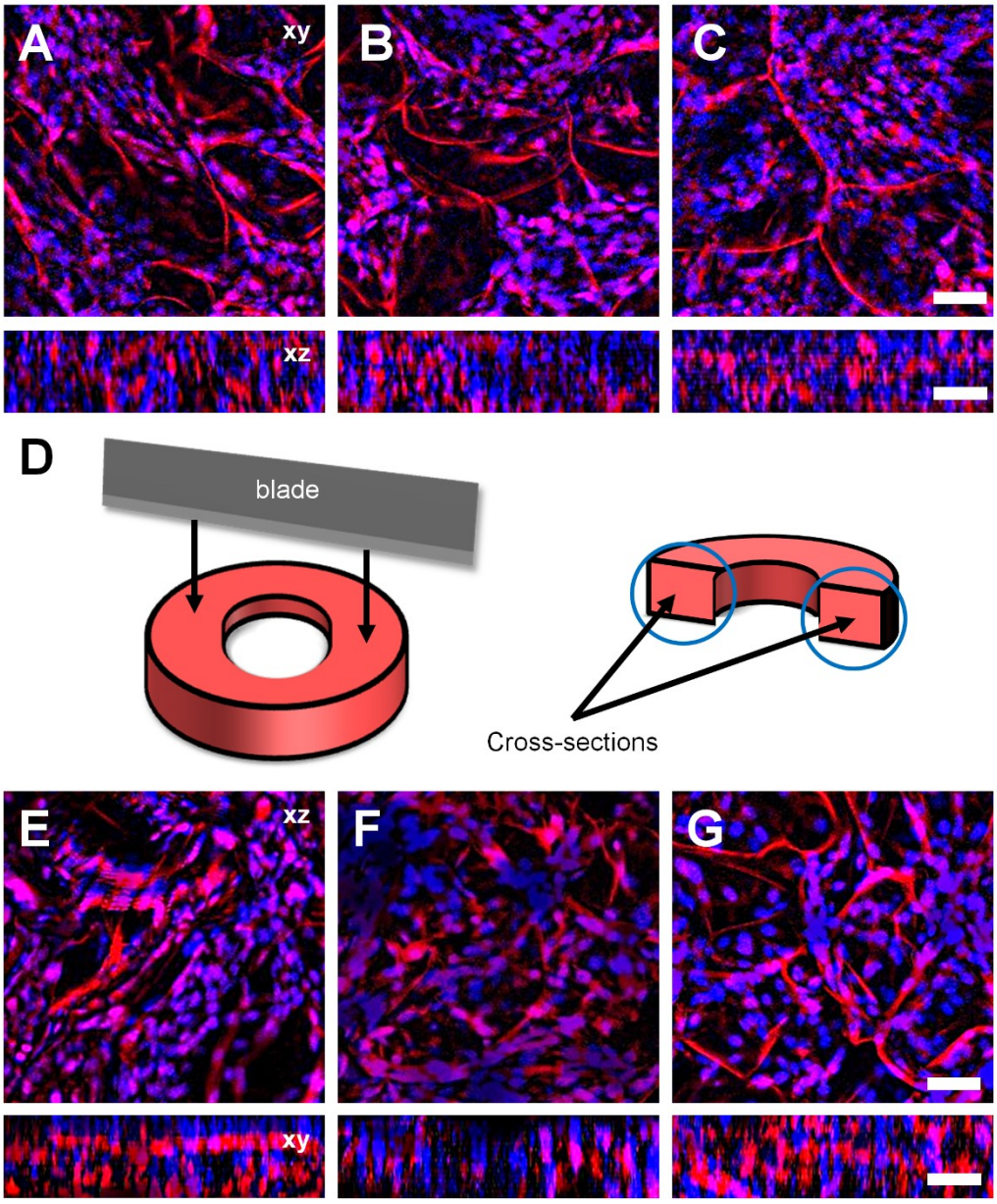

Figure 3.5: Cell invasion and proliferation. (A-C) XY and XZ maximum projection confocal images of C2C12 myoblasts on the ring scaffolds. C2C12 myoblasts were grown on the ring scaffolds for 2 weeks after being seeded with culture media (A), gelatin (B), and collagen (C). (D) The rings were cut with a razor blade to expose the cross-sectional areas. (E-G) Cross-sectional areas XZ and XY maximum projections of confocal images of the control (E), gelatin (F), and collagen (G) biomaterials. Blue = nuclei, red = cellulose. Scale = 50 μm.

Total cell growth after 2 weeks was not statistically different under the three conditions described here. As a result, the 2 week time period was sufficient for full invasion of the biomaterials used in this study. However, when compared to our original protocol [32], a drastic improvement in the cell invasion and proliferation is apparent. After 2 weeks, the samples with the calcium chloride incubation purification process ($1.5x10^2 \pm 8.2$ cells) showed comparable cell invasion ($P = 3.4x10^{-1}$, $N = 3$) to that of our previous study after 12 weeks ($1.8x10^2 \pm 2.3x10^1$ cells) despite the greater cell density seeding used in our previous study.

3.3.4 In vivo biocompatibility of subcutaneously implanted scaffolds

We next sought to confirm that the addition of the salt treatment to our protocol did not create any negative impact in vivo, however unlikely[33]. Although we have shown that the scaffolds support cell growth in vitro, a true test of biocompatibility requires an in vivo study. Here, we subcutaneously implanted salt treated plant-derived cellulose scaffolds under the skin of wild type mice (N = 8 mice with two 5 mm x 5 mm x 1.2 mm scaffolds implanted per mouse). As with our original subcutaneous study which employed a different decellularization protocol [33], here there were no cases of mice exhibiting behaviour indicative of pain induced by the cellulose scaffold throughout the study. The cellulose constructs were then resected after 4 weeks. Histological analysis was used to investigate the cell infiltration, proliferation, collagen deposition, and angiogenesis. Importantly, 4-weeks post-implantation, healthy tissue can be observed surrounding the cellulose scaffold. Moreover, significant cell infiltration into the scaffold is readily apparent (Fig. 3.6). In fact, the inclusion of a $CaCl_2$ buffer in our preparation promoted greater cell proliferation and invasion compared to our previous report [33]. The scaffolds also displayed vascularisation, which is reflected in a number of clearly visible blood vessels (with blood cells) in the Masson's Trichrome images (Fig. 3.6A,B,C). We further confirmed vascularization with CD-31 staining for endothelial cells (Fig. 3.6D,E,F). It is important to recognize that vascularization was able to occur even in the absence of any templating physical structures or need for biochemical functionalization of the cellulose scaffolds with pro-angiogenic factors. These results confirm the biocompatibility of salt treated plant-derived cellulose scaffolds and indicate their applicability as a possible platform for tissue-engineering applications. While we explored the use of inverse molding techniques for hydrogels, gelatin and collagen functionalization were only employed as a proof-of-concept rather than an end-product or application of these materials. Ultimately, investigators will have to assess the in vitro and in vivo biocompatibility of any cellulose scaffold functionalized with their target bio-molecules in a manner as described above.

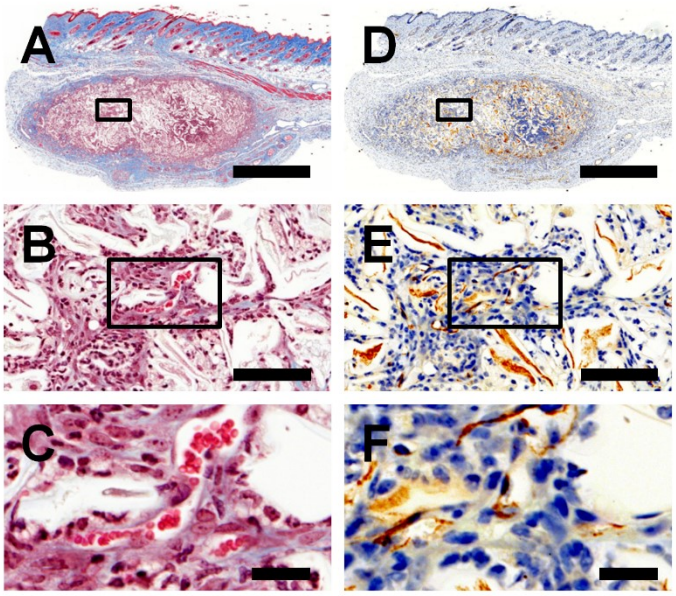

Figure 3.6: In vivo biocompatibility of $CaCl_2$ treated samples. Cross-sectional images of decellularized apples treated with $CaCl_2$ subcutaneously implanted into mice for 4 weeks. Samples were stained with Masson's Trichrome (A-C) and CD 31 (D-F). Scale (A,D) = 1000 µm. Scale (B,E) = 100 µm. Scale (C,F) = 25 µm.

3.4 Discussion

The use of cellulose scaffolds as biomaterials has many advantages such as low cost, ease of production, biocompatibility, functionalization, tunable mechanical properties, and successful subdermal implantation within relatively static tissues. In recent years, there have been major advances in 3D cell culture and scaffolding techniques that aim to capture the complexity of the in vivo microenvironment [46,47]. Numerous methods have now been developed for the production of biomaterial scaffolds for tissue engineering and regenerative medicine applications, each with their own benefits and drawbacks [46,47]. In general, biomaterial scaffolds should provide structural support, promote cell invasion and proliferation, prevent or minimize severe immune responses, and be pro-angiogenic and induce vascularization of the scaffold in order to support cellular function.

Several years ago, we pioneered the production of biomaterials derived directly from plants and proved the efficacy both in vitro and in vivo [32,33]. This early work has now inspired other recent studies [34,35]. Biomaterials derived directly from plants carry several interesting advantages, including straightforward production methods, widespread availability of material, and the potential for utilizing pre-existing microstructures within plant tissues [32,33]. Moreover, we have shown that the cellulose based biomaterials remain stable in vivo [33]. Taken together, it is now clear

that many cell types will attach and proliferate on plant-derived cellulose scaffolds. In recent work, the contraction of a small group of cardiac cells was examined on leaf cellulose scaffolds [35]. However, it was clear from the study that the scaffolds appeared unable to support complete invasion and proliferation. As revealed in the same study, the contractile dynamics of cardiac cells were impaired on cellulose scaffolds as compared to traditional substrates and biomaterials [35,48,49]. These results point to the need for robust strategies for the preparation of plant-derived cellulose scaffolds that are optimized for a high degree of cellular invasion and proliferation both in vitro and in vivo.

Here, we present a preparation and fabrication approach for producing highly novel macroscopic plant-derived cellulose scaffolds with pre-defined structures. For the first time, we demonstrate that this new-generation of plant-derived biomaterials can be combined with hydrogels. Consequently, this study establishes a platform that can potentially be applied to many tissue engineering applications. This new platform for composite cellulose biomaterials combines the advantages of hydrogel-based biomaterials with the ease of production and efficiency of the cellulose based scaffolds. In this proof-of-concept study, we show how plant based scaffolds with complex features can be hand- or machine-crafted, and then repurposed for new biological characteristics.

The anionic detergent SDS was used to decellularize the apple hypanthium tissue to obtain the cellulose scaffold [7,32]. Hence, an effective way to remove SDS prior to cell seeding was required. In this study we added a salt treatment to our previous protocol to promote any residual SDS molecules to form micelles [38]. Several salt buffers can accomplish this task, but divalent cations form tighter micelles than their monovalent counterparts [38]. The addition of the salt alters the critical micelle concentration of the surfactant [39]; at a certain concentration known as the cloud point, a phase transition occurs, and the micelles become insoluble and can be easily washed away [50]. The salt treatment can be useful in cases where simple washing is not practical. For instance, large 3D constructs (several centimeters in size) can require high concentrations of SDS (~5%) for complete decellularization (Supporting Information Fig. S3.2). This high concentration of SDS makes removing remnant surfactant difficult. Recently two other studies have taken advantage of the structures of decellularized plant tissues for 3D mammalian cell culture [34,35]. In these studies, harsh decellularization conditions were used to render the scaffold free of the native plant cells and nuclear content [34,35]. Moreover, both studies show incomplete cell proliferation and invasion of the plant-derived constructs. It is possible that remnant detergents and chemicals are responsible for the incomplete invasion of the scaffolds; however, experimental validation is required to confirm this speculation. Importantly, it also remains unclear if the production methods described in these previous studies result in biocompatible and pro-angiogenic scaffolds in vivo as animal studies were not carried out by the authors [34,35]. The new fabrication process reported here is simple and supports high cell growth. Moreover, the processes and protocols described in our study, really open up dramatic new possibilities for biomaterial engineering with respect to the large size and geometric complexity that are now attainable. The biomaterials we describe are simply produced

by hand or even on a computerized numerical control (CNC) machine within minutes, without molding, complex chemistry, and restrictions to small sizes.

Many synthetic 3D biomaterials rely on moulding techniques to achieve their intended shape [51]. An advantage of using decellularized plant cellulose as a 3D biomaterial is that it can simply be cut into the desired shape. Here, we demonstrated the production of cellulose rings as scaffolds for tissue engineering in vivo. Of course, the maximum size of the construct (without any further processing) will be limited by the plant being employed as a starting material. We presented proof-of-concept studies to show how the versatility of the biomaterial can be further increased by casting temporary or permanent hydrogels onto the macroscopic scaffolds with inverse moulding techniques [51]. While this technique has been previously applied to synthetic tissue engineering [36,37], this appears to be the first time it has been used to exploit the pre-existing structures of plants. This approach allowed us to provide temporary or permanent biochemical cues to the invading cells. The molding techniques can be particularly useful if intricate features of the biomaterial need to be populated with cells. Conventionally, cells are suspended in culture media and are seeded onto the substrate [52]. The cell culture medium is of low viscosity; therefore, the media can easily pass through the porous scaffold without allowing enough time for cell attachment. This problem can be overcome by using temporary or permanent inverse moulding techniques. Temporary moulding is advantageous when a standalone cellulose biomaterial with complex features is desired. As evidenced by our gelatin experiments, the temporary mould can extend the time the cells are in contact with the biomaterial and then melt away after its function is complete. Moreover, the temporary mould can supply biochemical cues to the cells that are desirable for only a short period of time. On the other hand, in other scenarios it is desirable to create a permanent gel encompassing the biomaterial. Unlike gelatin, collagen remains in its gel state at 37°C, which is particularly useful for cell culture applications that require a permanent gel or persistent biochemical cues.

Importantly, cell invasion was comparable for the three different conditions: bare cellulose, gelatin temporary mould, and collagen permanent mold. The significance of these findings is that the same result can be obtained regardless of the moulding technique that is used. As this work and our previous studies [32,33] demonstrate, plant-derived cellulose scaffolds are inert, and simply provide a stable 3D structure on which cells can proliferate and function. Therefore, the choice of bio-functionalization seeding technique depends on the intended application of the material. It should be noted that different cells deposit and require varying extracellular matrices [43]. Therefore, the outcome of using the plant-based decellularized biomaterial in conjunction with hydrogels containing cells that produce an insufficient ECM may increase cell invasion and proliferation in comparison to culturing the cells on bare scaffolds. Our in vitro results reveal that the scaffolds are highly biocompatible. The live:dead cell ratios confirm the presence of mostly viable cells. However, we urge researchers to employ caution when interpreting the results of the live and dead cell experiments. The scaffold size and geometry used here certainly affect the results. Although not found in this study, we do expect a necrotic core to be present in larger biomaterials with

insufficient porosity or without supplemented perfusion as a result of hypoxia and inadequate diffusion of metabolites [53]. When compared to the physiological condition at approximately $1x10^8$ cells/mL [54], our in vitro experiments have a lower cell density. Nevertheless, our in vivo results show a relatively high cell density, similar to the surrounding native tissue. Many factors influence cell density, such as cell type, mechanical properties, structural characteristics, and biochemical features. It should be noted that our motivation for presenting these proof-of-principle experiments was to establish a potential tissue engineering platform with plant-derived cellulose scaffolds. Increasing the cell seeding density to approach the physiological limit or determining the maximum limit was unnecessary; the in vivo results address this issue. It is important to note that matching cell density in vitro is not our end goal. Rather, we are developing implantable biomaterials; therefore, in vivo biocompatibility, vascularization, and cell invasion are of primary concern. In future work, specific tissue engineering goals will be examined, as opposed to fully exploring the landscape of possibilities of employing gelatin/collagen in the present study. To that end, the composite material can be selected to match the mechanical and physical properties of the local microenvironment. In our case, the gelatin and collagen hydrogels did not appear to alter the pore size or pore size distribution of the cellulose pores, consistent with our previous studies [32,33]. Obviously, the physical properties, such as porosity, depend on the choice of the material. Here the choice of composite material was arbitrary; extensive characterization of the physical properties was unnecessary. Nevertheless, the mechanical properties are of significant interest; thus, the Young's modulus was quantified. Interestingly, the treatment with the $CaCl_2$ increased the Young's modulus, while the addition of the hydrogels did not have a significant effect. The increase in the Young's modulus after the salt treatment was likely the result of remnant salt adsorbed on the surface. We note however, the mechanical properties of the scaffolds which vary between ~5-20 kPa fall well within the range of native animal tissues such as muscle [44,45].

Our in vivo results also show that the scaffolds never become calcified or fibrotic. Rather, collagen matrix deposition is observed concomitantly with extensive cell invasion [33] Crucially, the plant-derived cellulose biomaterial exhibited vascularization, which results in the formation of blood vessels that supply the invading cells with nutrients. Apple-hypanthium tissue is highly porous and sponge-like in structure, and lacks the presence of pre-existing vascular structures, which might act as a template for blood vessel formation. Despite this, and existing hypotheses that such templating structures are important [29,35,41], we show that such pre-existing structures are not a requirement for vascularization. In fact, it is likely that the highly porous nature of plant-derived cellulose biomaterials is the critical element which promotes vascularization [55]. Although, plant-derived cellulose scaffolds are stable and robust as subdermal implants and in tissues/structures that are relatively stable [33], it is unclear how applicable they will be in applications that involve the repair of cardiac and/or muscle tissues. Such tissues are mechanically dynamic, which leads to the application of large stresses to any implanted biomaterial. Plant-derived cellulose scaffolds, without any further processing, are highly brittle and likely inappropriate for such applications, especially when other more effective biomaterials have already been developed [56,57]. It is also unclear at this point if such plant-derived cellulose scaffolds will be effective for de novo organ

engineering. At present, these materials do appear to be highly effective in tissue engineering/repair strategies within certain criteria as discussed here. Future studies will continue to elucidate the full potential of these plant-derived cellulose biomaterials in regenerative medicine.

Combining the scaffold with hydrogels expands the potential applications of these materials, and we anticipate this work will have significant impacts in the field. We stress that this study is a proof-of-concept study that will provide the foundation for more sophisticated investigations in the near future. Improved cell adhesion, both in vitro and in vivo, combined with inverse moulding provides an important platform for future tissue engineering applications. The materials for these composites are easily and cheaply sourced, biocompatible in vitro and in vivo, and display clear vascularization. This study opens up new possibilities for existing hydrogels and biopolymers to be used in combinations with plant-derived cellulose biomaterials. The choice of gelatin and collagen as the comparison materials was quite arbitrary as there are many biomaterials available. The combination of scaffolds with temporary or permanent hydrogels will be useful in delivering biochemical cues (matrix proteins, growth factors, small molecules, etc.) to attract or promote the growth of specific cell types. Control over the organization and invasion of specific cell types remains an important challenge in 3D tissue engineering. Future work will focus on combining the inverse moulding techniques with in vivo experiments in order to direct and template specific cells in 3D space. Nevertheless, emerging plant-derived cellulose scaffolds present an affordable, accessible, easy to use, and versatile 3D biomaterial that holds important promise for future applications. The simplistic approach to biomaterial fabrication is a very attractive feature of this novel biomaterial, and we anticipate that it will benefit the continued development of novel biomaterials by many different research groups.

3.5 Materials and methods

3.5.1 Scaffold production

A mandolin slicer was used to slice McIntosh Red apples (Canada Fancy) into thin 1.2 mm sections, measured with a Vernier caliper. A 5 mm diameter disk with a 1.2 mm thickness was then carved out of the hypanthium tissue of the slice using a 5 mm biopsy punch. A 2 mm biopsy punch was used to remove a 2 mm disk from the centre of the 5 mm disk. Thus, a macroscopic ring was obtained with an inner diameter of 2 mm, an outer diameter of 5 mm, and a thickness of 1.2 mm. The samples were transferred to a 0.1% SDS solution and decellularized for 48 h while being shaken at 180 RPM. After decellularization, the samples were washed three times with dH_2O. Next, the rings were incubated in 100 mM $CaCl_2$ for 24 h at room temperature to remove any surfactant residue. The samples were washed three times with dH_2O to remove the salt residue, and then they were incubated with 70% ethanol for sterilization. After the removal of the ethanol,

three washes with dH_2O were performed to yield a sterile ring, free of contaminants. Alternatively, the samples can be autoclaved to be sterilized.

3.5.2 Cell culture

C2C12 mouse myoblast cells were maintained at 37°C and 5% CO_2. The cells were cultured in Delbecco's Modified Eagle Medium – High Glucose (DMEM), supplemented with 10% fetal bovine serum and 1% penicillin/streptomycin (100 U/mL and 100 μg/mL respectively) (Hyclone Laboratories Inc.). The C2C12 myoblast cells cultured on cell culture plates were trypsinized and resuspended in DMEM. The cells were counted and centrifuged in order to separate the cells from the trypsin and the media. The supernatant was aspirated, and the pellet containing $5x10^4$ cells was resuspended in either fresh culture medium, a 10% (m/v) Porcine Type-A Gelatin (GE) (Sigma-Aldrich) solution in culture medium, or a 1.5 mg/mL collagen solution. The collagen gel was made by mixing 50% (v/v) of 3 mg/mL type 1 collagen (Gibco) with 1.25% of 1N NaOH, 10% of 150 mM D-ribose, 1% FBS, 10% of 10X DMEM, and 27.25% autoclaved dH_2O at 4°C. In each condition, C2C12 mouse myoblast cells were seeded onto the biomaterial, and the cells were allowed to proliferate and invade the scaffold for 2 weeks. The culture media was replaced every 2 days and the samples were transferred to new culture plates after 1 week of growth.

The GE solution was used as a temporary inverse mould. The resuspension in the GE solution was performed at 37°C. After the gelatin-cell solution was pipetted onto the scaffold, the gelatin solution cooled below its melting temperature was left to gel for 15 minutes at room temperature. Here, the hydrogel containing the cells was left on the scaffold in its gelled state for a further 45 minutes. Following this period, 2 mL of room temperature cell culture medium was added to the Petri dish containing the gelatin coated ring. The sample was then placed in the incubator at 37°C and 5% CO_2.

The collagen solution was used as a permanent inverse mould. Here, the inverse principle applied: the gel was in its liquid form at 4°C and solidified at room temperature. A collagen gel-cell mixture was produced by resuspending the pellet of cells in a 4°C collagen solution. The collagen solution rapidly polymerizes within 5 minutes and formed a permanent gel containing the biomaterial and the cells. After 15 minutes of incubation at room temperature, 2 mL of room temperature culture medium was added to the Petri dish containing the collagen coated ring. The sample was then placed in the incubator at 37°C and 5% CO_2.

3.5.3 Staining

Prior to staining, the cells were washed 3 times with PBS and then fixed with 3.5% paraformaldehyde for 10 minutes. Staining of the decellularized apple scaffold was accomplished

as described previously [32,58]. Briefly, the samples were rinsed with water and incubated in 1% periodic acid (Sigma-Aldrich) at room temperature for 40 minutes. The tissue was rinsed again with water and incubated in Schiff reagent (100 mM sodium metabisulfite and 0.15 N HCl) with 100 μg/mL of propidium iodide (Invitrogen) for 2 hours. The samples were then washed with PBS. The myoblast cell membranes and nuclei were stained with a solution of 5 μg/mL wheat germ agglutinin (WGA) 488 (Invitrogen) and 1 μg/mL Hoechst 33342 (Invitrogen) in PBS respectively for 30 minutes.

3.5.4 Microscopy

The cells and biomaterials were imaged with epi-fluorescence and laser scanning confocal microscopy. A Nikon Eclipse TiE epi-fluorescence and phase contrast microscope (Nikon, Canada) with a CCD camera (Photometric Cool Snap HQ^2), and 4X and 10X objective lenses were used to image the biomaterials. In addition, the samples were imaged with a Nikon TiE A1-R high speed resonant scanner confocal microscope with a 10X objective. ImageJ (Fiji) was used to process the images. Confocal images presented here are maximum intensity projections of confocal volumes. Brightness/contrast settings were adjusted to maximize the fluorophore signal; otherwise, no other image manipulations were performed.

3.5.5 In vitro cell invasion and proliferation quantification

Cell Counting Kit-8 (CCK-8) (Dojindo Molecular Technologies, Inc.) was used to measure the number of viable cells in the scaffold after the initial seeding. A standard curve ($R^2 = 0.998$) was produced by creating serial dilutions of $5x10^4$ cells with a dilution factor of 2 in a 96-well plate for a final volume of 100 μL of cells and media + 10 μL of CCK-8 reagent, after a pre-incubation of 12 h. The absorbance of the solution was measured at 450 nm after 3 h of incubation at 37 °C, 5% CO_2. For the experimental measurements, the rings were seeded with cells as described above, then transferred to a 96-well plate with 100 μL of media + 10 μL of CCK-8 reagent after a pre-incubation period of 12 h. The absorbance of the solution was measured at 450 nm after 3 h of incubation at 37 °C, 5% CO_2. The values presented are mean values ± the standard error of the mean (s.e.m.).

The confocal images of the cell nuclei were thresholded using the ImageJ (Fiji) adaptive threshold plugin, and the analyze particles plugin was used to count the number of cells in a 300 μm x 300 μm area (analysis after 2 days of culture) or a 300 μm x 300 μm x 300 μm volume (analysis after 2 weeks of culture). The values presented are mean values ± the standard error of the mean (s.e.m.).

3.5.6 Live/dead cell analysis

After 2 weeks of culture, the scaffolds were incubated with 10 μg/mL of Hoechst 33342 (Invitrogen) and 1 μg/mL of propidium iodide (Invotrogen) for 20 min in order to stain the nuclei of the live and dead cells respectively. The biomaterials were then imaged with confocal microscopy. The images of the cell nuclei were thresholded using the ImageJ (Fiji) adaptive threshold plugin, and the analyze particles plugin was used to count the number of cells. Here, the live:dead cell ratio expression is unitless. The values presented are mean values for multiple volumes ± the standard error of the mean (s.e.m.).

3.5.7 Young's modulus

The Young's modulus was measured after 2 weeks of culture by compressing the material to a 10% strain, at a strain rate of 50 μm/s, using a custom-built compression device and LabVIEW software. The force-indentation curves were converted to stress-strain curves, and they were fitted in Origin 8.5 to calculate the Young's modulus.

3.5.8 Animals

Wild-type immunocompetent C57BL/10ScSnJ mice (males and females; 6–9 weeks old; N = 8) were purchased from The Jackson Laboratory (Bar Harbor, Maine, USA) and bred in our facilities. The mice were housed at constant room temperature (22°C) and humidity (52%), fed a normal chow diet, and kept under a controlled 12 hours light/dark cycle. The subcutaneous implantation procedures and related protocols were approved by the Animal Care and Use Committee of the University of Ottawa.

3.5.9 Cellulose implantation

The mice were anesthetized using 2% Isoflurane USP-PPC (Pharmaceutical partners of Canada, Richmond, ON, Canada). The eyes of the mice were kept from drying with the application of ophthalmic liquid gel (Alco Canada In., ON, Canada). The breathing of the mouse was constantly monitored to ensure that the animal was in the correct plane of anesthesia. The mouse dorsal ventral region was shaved with the underlying skin cleaned and sterilized using ENDURE 400 Scrub-Stat4 Surgical Scrub (chlorhexidine gluconate, 4% solution; Ecolab Inc., Minnesota, USA) and Soluprep (2% w/v chlorhexidine and 70% v/v isopropyl alcohol; 3M Canada, London, ON, Canada). Animal hydration was maintained via subcutaneous injection (s.c.) of 1 ml of 0.9% sodium chloride solution (Hospira, Montréal, QC, Canada) on the opposite side of the cellulose

implantation site. Throughout the surgical procedures, the body temperature of the mouse was maintained at 37ºC to maximize recovery of the animal. All strict sterility measures were upheld for survival surgeries. To implant the scaffolds, two 8 mm incisions were cut on the dorsal section of each mouse (upper and lower). Two cellulose scaffold samples were separately and independently implanted into each mouse. The incisions were then sutured using Surgipro II monofilament polypropylene 6–0 (Covidien, Massachusetts, USA), and transdermal bupivicaine 2% (as monohydrate; Chiron Compounding Pharmacy Inc., Guelph, ON, Canada) was topically applied to the surgery sites to prevent infection. Additionally, buprenorphine (0.03mg/ml; Chiron Compounding Pharmacy Inc. Guelph, ON, Canada) was administrated s. c. as a pain reliever. All animals were then carefully monitored for the following 3 days by animal care services and received replicate pharmacological treatments.

3.5.10 Scaffold resections

At 4 weeks post-implantation, the mice were euthanized using CO_2 inhalation and exsanguination via heart dissection. The dorsal skin was carefully resected and immediately immersed in sterile PBS solution. The underlying skin containing cellulose scaffolds was then photographed, cut, and fixed in 10% formalin for at least 48 hours. The samples were then kept in 70% ethanol before being embedded in paraffin by the PALM Histology Core Facility of the University of Ottawa.

3.5.11 Histology

For histological analysis, serial 5 μm thick sections starting 1 mm inside the cellulose scaffold were cut. The sections were stained with Masson's Trichrome. For immunocytochemistry, heat induced epitope retrieval was performed at 110°C for 12 min with citrate buffer (pH 6.0). Anti-CD31/PECAM1 (1:100; Novus Biologicals, NB100-2284, Oakville, ON, Canada) primary antibodies were incubated for an hour at room temperature. The blocking reagent (Background Sniper, Biocare, Medical, Concord, CA, USA) and the MACH 4 detection system (Biocare Medical, Concord, CA, USA) were used according to manufacturer specifications. A Zeiss MIRAX MIDI Slide Scanner (Zeiss, Toronto, Canada) with 40x objective was used to image slices for cell infiltration, extracellular matrix deposition, and vascularisation (angiogenesis). The micrographs were analysed with the Pannoramic Viewer (3DHISTECH Ltd., Budapest, Hungary) software.

3.5.12 Statistical analysis

In order to assess statistical differences between the cells cultured on the biomaterials under the different conditions, one way ANOVA tests were used. The Tukey post hoc analysis was performed to determine the statistical difference between the individual samples. For the comparison of more than two samples, the one-way ANOVA was used instead of multiple Student's t-tests to reduce the risk of type 1 statistical errors. When only two samples were compared, the Student's t-test was used. All values presented are the mean ± the standard error of the mean (s.e.m.). When dealing with biological samples it is not possible to study the whole population; the standard error of the mean was used instead of the standard deviation because a representative sample is used as an estimate for the population. Statistical significance (indicated by an asterisk) refers to $P < 0.05$.

3.6 Acknowledgments

This work was supported by a Natural Sciences and Engineering Research Council (NSERC) Discovery Grant. R.J.H. was supported by an NSERC postgraduate scholarship and an Ontario Graduate Scholarship (OGS). D.J.M. was supported by a graduate student fellowship from the "Fonds de Recherche du Québec – Santé" (FRQS). A.E.P. gratefully acknowledges generous support from the Canada Research Chairs (CRC) program.

3.7 References

(1) Wang, H.; van Blitterswijk, C. A. The role of three-dimensional polymeric scaffold configuration on the uniformity of connective tissue formation by adipose stromal cells. *Biomaterials* **2010**, *31* (15), 4322–4329 DOI: 10.1016/j.biomaterials.2010.02.008.

(2) Syedain, Z.; Reimer, J.; Lahti, M.; Berry, J.; Johnson, S.; Tranquillo, R. T. Tissue engineering of acellular vascular grafts capable of somatic growth in young lambs. *Nat. Commun.* **2016**, *7*, 12951 DOI: 10.1038/ncomms12951.

(3) Wan, S.; Borland, S.; Richardson, S. M.; L.R. Merry, C.; Saiani, A.; Gough, J. E. Self-assembling peptide hydrogel for intervertebral disc tissue engineering. *Acta Biomater.* **2016** DOI: 10.1016/j.actbio.2016.09.033.

(4) Petrosyan, A.; Da Sacco, S.; Tripuraneni, N.; Kreuser, U.; Lavarreda-Pearce, M.; Tamburrini, R.; De Filippo, R. E.; Orlando, G.; Cravedi, P.; Perin, L. A step towards clinical application of acellular matrix: A clue from macrophage polarization. *Matrix Biol.* **2016** DOI: 10.1016/j.matbio.2016.08.009.

(5) Madl, C. M.; Katz, L. M.; Heilshorn, S. C. Bio-Orthogonally Crosslinked, Engineered

Protein Hydrogels with Tunable Mechanics and Biochemistry for Cell Encapsulation. *Adv. Funct. Mater.* **2016**, 3612–3620 DOI: 10.1002/adfm.201505329.

(6) Sánchez, P. L.; Fernández-Santos, M. E.; Costanza, S.; Climent, A. M.; Moscoso, I.; Gonzalez-Nicolas, M. A.; Sanz-Ruiz, R.; Rodríguez, H.; Kren, S. M.; Garrido, G.; et al. Acellular human heart matrix: A critical step toward whole heart grafts. *Biomaterials* **2015**, *61*, 279–289 DOI: 10.1016/j.biomaterials.2015.04.056.

(7) Khorramirouz, R.; Sabetkish, S.; Akbarzadeh, A.; Muhammadnejad, A.; Heidari, R.; Kajbafzadeh, A. M. Effect of three decellularisation protocols on the mechanical behaviour and structural properties of sheep aortic valve conduits. *Adv. Med. Sci.* **2014**, *59* (2), 299–307 DOI: 10.1016/j.advms.2014.08.004.

(8) Gilbert, T. W.; Sellaro, T. L.; Badylak, S. F. Decellularization of tissues and organs. *Biomaterials* **2006**, *27* (19), 3675–3683 DOI: 10.1016/j.biomaterials.2006.02.014.

(9) Wang, Q.; Yang, H.; Bai, A.; Jiang, W.; Li, X.; Wang, X.; Mao, Y.; Lu, C.; Qian, R.; Guo, F.; et al. Functional engineered human cardiac patches prepared from nature's platform improve heart function after acute myocardial infarction. *Biomaterials* **2016**, *105*, 52–65 DOI: 10.1016/j.biomaterials.2016.07.035.

(10) de Oliveira Barud, H. G.; da Silva, R. R.; da Silva Barud, H.; Tercjak, A.; Gutierrez, J.; Lustri, W. R.; de Oliveira, O. B.; Ribeiro, S. J. L. A multipurpose natural and renewable polymer in medical applications: Bacterial cellulose. *Carbohydr. Polym.* **2016**, *153*, 406–420 DOI: 10.1016/j.carbpol.2016.07.059.

(11) de Olyveira, G. M.; Basmaji, P.; Costa, L. M. M.; dos Santos, M. L.; dos Santos Riccardi, C.; Guastaldi, F. P. S.; Scarel-Caminaga, R. M.; de Oliveira Capote, T. S.; Pizoni, E.; Guastaldi, A. C. Surface physical chemistry properties in coated bacterial cellulose membranes with calcium phosphate. *Mater. Sci. Eng. C* **2017**, *75*, 1359–1365 DOI: 10.1016/j.msec.2017.03.025.

(12) Jin, L.; Zeng, Z.; Kuddannaya, S.; Wu, D.; Zhang, Y.; Wang, Z. Biocompatible, Free-Standing Film Composed of Bacterial Cellulose Nanofibers-Graphene Composite. *ACS Appl. Mater. Interfaces* **2016**, *8* (1), 1011–1018 DOI: 10.1021/acsami.5b11241.

(13) Huang, J. W.; Lv, X. G.; Li, Z.; Song, L. J.; Feng, C.; Xie, M. K.; Li, C.; Li, H. B.; Wang, J. H.; Zhu, W. D.; et al. Urethral reconstruction with a 3D porous bacterial cellulose scaffold seeded with lingual keratinocytes in a rabbit model. *Biomed Mater* **2015**, *10* (5), 55005 DOI: 10.1088/1748-6041/10/5/055005.

(14) Galateanu, B.; Bunea, M.; Stanescu, P.; Vasile, E.; Casarica, A.; Iovu, H.; Hermenean, A.; Zaharia, C.; Costache, M. In Vitro Studies of Bacterial Cellulose and Magnetic Nanoparticles Smart Nanocomposites for Efficient Chronic Wounds Healing. *Stem Cells Int.* **2015**, *2015*, 1–10 DOI: 10.1155/2015/195096.

(15) Varma, D. M.; Gold, G. T.; Taub, P. J.; Nicoll, S. B. Injectable carboxymethylcellulose hydrogels for soft tissue filler applications. *Acta Biomater.* **2014**, *10* (12), 4996–5004 DOI: 10.1016/j.actbio.2014.08.013.

(16) Unnithan, A. R.; Gnanasekaran, G.; Sathishkumar, Y.; Lee, Y. S.; Kim, C. S. Electrospun antibacterial polyurethane-cellulose acetate-zein composite mats for wound dressing. *Carbohydr. Polym.* **2014**, *102* (1), 884–892 DOI: 10.1016/j.carbpol.2013.10.070.

(17) Pandit, V.; Zuidema, J. M.; Venuto, K. N.; Macione, J.; Dai, G.; Gilbert, R. J.; Kotha, S. P. Evaluation of multifunctional polysaccharide hydrogels with varying stiffness for bone tissue engineering. *Tissue Eng. Part A* **2013**, *19* (21–22), 2452–2463 DOI: 10.1089/ten.TEA.2012.0644.

(18) Nimeskern, L.; Martínez Ávila, H.; Sundberg, J.; Gatenholm, P.; Müller, R.; Stok, K. S. Mechanical evaluation of bacterial nanocellulose as an implant material for ear cartilage replacement. *J. Mech. Behav. Biomed. Mater.* **2013**, *22*, 12–21 DOI: 10.1016/j.jmbbm.2013.03.005.

(19) Pértile, R.; Moreira, S.; Andrade, F.; Domingues, L.; Gama, M. Bacterial cellulose modified using recombinant proteins to improve neuronal and mesenchymal cell adhesion. *Biotechnol. Prog.* **2012**, *28* (2), 526–532 DOI: 10.1002/btpr.1501.

(20) Fang, B.; Wan, Y.-Z.; Tang, T.-T.; Gao, C.; Dai, K.-R. Proliferation and Osteoblastic Differentiation of Human Bone Marrow Stromal Cells on Hydroxyapatite/Bacterial Cellulose Nanocomposite Scaffolds. *Tissue Eng. Part A* **2009**, *15* (5), 1091–1098 DOI: 10.1089/ten.tea.2008.0110.

(21) Bodin, A.; Ahrenstedt, L.; Fink, H.; Brumer, H.; Risberg, B.; Gatenholm, P. Modification of nanocellulose with a xyloglucan-RGD conjugate enhances adhesion and proliferation of endothelial cells: Implications for tissue engineering. *Biomacromolecules* **2007**, *8* (12), 3697–3704 DOI: 10.1021/bm070343q.

(22) Helenius, G.; Bäckdahl, H.; Bodin, A.; Nannmark, U.; Gatenholm, P.; Risberg, B. In vivo biocompatibility of bacterial cellulose. *J. Biomed. Mater. Res. - Part A* **2006**, *76* (2), 431–438 DOI: 10.1002/jbm.a.30570.

(23) Svensson, A.; Nicklasson, E.; Harrah, T.; Panilaitis, B.; Kaplan, D. L.; Brittberg, M.; Gatenholm, P. Bacterial cellulose as a potential scaffold for tissue engineering of cartilage. *Biomaterials* **2005**, *26* (4), 419–431 DOI: 10.1016/j.biomaterials.2004.02.049.

(24) Scherner, M.; Reutter, S.; Klemm, D.; Sterner-Kock, A.; Guschlbauer, M.; Richter, T.; Langebartels, G.; Madershahian, N.; Wahlers, T.; Wippermann, J. In vivo application of tissue-engineered blood vessels of bacterial cellulose as small arterial substitutes: Proof of concept? *J. Surg. Res.* **2014**, *189* (2), 340–347 DOI: 10.1016/j.jss.2014.02.011.

(25) Lee, C. M.; Kafle, K.; Park, Y. B.; Kim, S. H. Probing crystal structure and mesoscale assembly of cellulose microfibrils in plant cell walls, tunicate tests, and bacterial films using vibrational Sum Frequency Generation (SFG) spectroscopy. *Phys. Chem. Chem. Phys.* **2014**, *16* (22), 10844–10853 DOI: 10.1039/c4cp00515e.

(26) Barbié, C.; Chauveaux, D.; Barthe, X.; Baquey, C.; Poustis, J. Biological behavior of cellulosic materials after bone implantation: preliminary results. *Clin. Mater.* **1990**, *5* (2–4), 251–258.

(27) Miyamoto, T.; Takahashi, S. ???i; Ito, H.; Inagaki, H.; Noishiki, Y. Tissue biocompatibility of cellulose and its derivatives. *J. Biomed. Mater. Res.* **1989**, *23* (1), 125–133 DOI: 10.1002/jbm.820230110.

(28) Martínez Ávila, H.; Feldmann, E. M.; Pleumeekers, M. M.; Nimeskern, L.; Kuo, W.; de Jong, W. C.; Schwarz, S.; Müller, R.; Hendriks, J.; Rotter, N.; et al. Novel bilayer bacterial nanocellulose scaffold supports neocartilage formation invitro and invivo. *Biomaterials* **2015**, *44*, 122–133 DOI: 10.1016/j.biomaterials.2014.12.025.

(29) Wang, X.-Y.; Jin, Z.-H.; Gan, B.-W.; Lv, S.-W.; Xie, M.; Huang, W.-H.; Carmeliet, P.; Bae, H.; Puranik, A. S.; Gauvin, R.; et al. Engineering interconnected 3D vascular networks in hydrogels using molded sodium alginate lattice as the sacrificial template. *Lab Chip* **2014**, *14* (15), 2709 DOI: 10.1039/c4lc00069b.

(30) Kirdponpattara, S.; Khamkeaw, A.; Sanchavanakit, N.; Pavasant, P.; Phisalaphong, M. Structural modification and characterization of bacterial cellulose-alginate composite scaffolds for tissue engineering. *Carbohydr. Polym.* **2015**, *132*, 146–155 DOI: 10.1016/j.carbpol.2015.06.059.

(31) Bottan, S.; Robotti, F.; Jayathissa, P.; Hegglin, A.; Bahamonde, N.; Heredia-Guerrero, J. A.; Bayer, I. S.; Scarpellini, A.; Merker, H.; Lindenblatt, N.; et al. Surface-structured bacterial cellulose with guided assembly-based biolithography (GAB). *ACS Nano* **2015**, *9* (1), 206–219 DOI: 10.1021/nn5036125.

(32) Modulevsky, D. J.; Lefebvre, C.; Haase, K.; Al-Rekabi, Z.; Pelling, A. E. Apple derived cellulose scaffolds for 3D mammalian cell culture. *PLoS One* **2014**, *9* (5) DOI: 10.1371/journal.pone.0097835.

(33) Modulevsky, D. J.; Cuerrier, C. M.; Pelling, A. E. Biocompatibility of Subcutaneously Implanted Plant-Derived Cellulose Biomaterials. *PLoS One* **2016**, *11* (6), 1–19 DOI: 10.1371/journal.pone.0157894.

(34) Fontana, G.; Gershlak, J.; Adamski, M.; Lee, J.-S.; Matsumoto, S.; Le, H. D.; Binder, B.; Wirth, J.; Gaudette, G.; Murphy, W. L. Biofunctionalized Plants as Diverse Biomaterials for Human Cell Culture. *Adv. Healthc. Mater.* **2017**, 1601225 DOI: 10.1002/adhm.201601225.

(35) Gershlak, J.; Hernandez, S.; Fontana, G.; Perreault, L.; Hansen, K.; Larson, S.; Binder, B.; Dolivo, D.; Yang, T.; Dominko, T.; et al. Crossing kingdoms: Using decellularized plants as perfusable tissue engineering scaffolds. *Biomaterials* **2017**, *125*, 13–22 DOI: 10.1016/j.biomaterials.2017.02.011.

(36) Zhu, W.; Zhao, Y.; Ma, Q.; Wang, Y.; Wu, Z.; Weng, X. 3D-printed porous titanium changed femoral head repair growth patterns: osteogenesis and vascularisation in porous titanium. *J. Mater. Sci. Mater. Med.* **2017**, *28* (4), 62 DOI: 10.1007/s10856-017-5862-2.

(37) Hinton, T. J.; Jallerat, Q.; Palchesko, R. N.; Park, J. H.; Grodzicki, M. S.; Shue, H.-J.; Ramadan, M. H.; Hudson, A. R.; Feinberg, A. W. Three-dimensional printing of complex biological structures by freeform reversible embedding of suspended hydrogels. *Sci. Adv.*

2015, *1* (9), e1500758–e1500758 DOI: 10.1126/sciadv.1500758.

(38) Sammalkorpi, M.; Karttunen, M.; Haataja, M. Ionic surfactant aggregates in saline solutions: Sodium dodecyl sulfate (SDS) in the presence of excess sodium chloride (NaCl) or calcium chloride (CaCl2). *J. Phys. Chem. B* **2009**, *113* (17), 5863–5870 DOI: 10.1021/jp901228v.

(39) Corrin, M. L.; Harkins, W. D. The effect of salts on the critical concentration for the formation of micelles in colloidal electrolytes. *J. Am. Chem. Soc.* **1947**, *69* (3), 683–688 DOI: 10.1021/ja01195a065.

(40) Yang, J.; Shrike Zhang, Y.; Yue, K.; Khademhosseini, A. Cell-Laden Hydrogels for Osteochondral and Cartilage Tissue Engineering. *Acta Biomater.* **2017** DOI: 10.1016/j.actbio.2017.01.036.

(41) Sugibayashi, K.; Kumashiro, Y.; Shimizu, T.; Kobayashi, J.; Okano, T. A molded hyaluronic acid gel as a micro-template for blood capillaries. *J. Biomater. Sci. Polym. Ed.* **2013**, *24* (2), 135–147 DOI: 10.1163/156856212X627847.

(42) Ninan, G.; Joseph, J.; Aliyamveettil, Z. A. A comparative study on the physical, chemical and functional properties of carp skin and mammalian gelatins. *J. Food Sci. Technol.* **2012**, *51* (9), 2085–2091 DOI: 10.1007/s13197-012-0681-4.

(43) Chaturvedi, V.; Dye, D. E.; Kinnear, B. F.; Van Kuppevelt, T. H.; Grounds, M. D.; Coombe, D. R. Interactions between skeletal muscle myoblasts and their extracellular matrix revealed by a serum free culture system. *PLoS One* **2015**, *10* (6), 1–27 DOI: 10.1371/journal.pone.0127675.

(44) Al-Rekabi, Z.; Pelling, A. E. Cross talk between matrix elasticity and mechanical force regulates myoblast traction dynamics. *Phys. Biol.* **2013**, *10* (6), 66003 DOI: 10.1088/1478-3975/10/6/066003.

(45) Engler, A. J.; Griffin, M. a; Sen, S.; Bönnemann, C. G.; Sweeney, H. L.; Discher, D. E. Myotubes differentiate optimally on substrates with tissue-like stiffness: pathological implications for soft or stiff microenvironments. *J. Cell Biol.* **2004**, *166* (6), 877–887 DOI: 10.1083/jcb.200405004.

(46) Ravi, M.; Paramesh, V.; Kaviya, S. R.; Anuradha, E.; Paul Solomon, F. D. 3D cell culture systems: Advantages and applications. *J. Cell. Physiol.* **2015**, *230* (1), 16–26 DOI: 10.1002/jcp.24683.

(47) Knight, E.; Przyborski, S. Advances in 3D cell culture technologies enabling tissue-like structures to be created in vitro. *J. Anat.* **2015**, *227* (6), 746–756 DOI: 10.1111/joa.12257.

(48) Qin, X.; Riegler, J.; Tiburcy, M.; Zhao, X.; Chour, T.; Ndoye, B.; Nguyen, M.; Adams, J.; Ameen, M.; Denney, T. S.; et al. Magnetic Resonance Imaging of Cardiac Strain Pattern Following Transplantation of Human Tissue Engineered Heart Muscles. *Circ. Cardiovasc. Imaging* **2016**, *9* (11), e004731 DOI: 10.1161/CIRCIMAGING.116.004731.

(49) Sun, H.; Zhou, J.; Huang, Z.; Qu, L.; Lin, N.; Liang, C.; Dai, R.; Tang, L.; Tian, F. Carbon

nanotube-incorporated collagen hydrogels improve cell alignment and the performance of cardiac constructs. *Int. J. Nanomedicine* **2017**, *12*, 3109–3120.

(50) Paleologos, E. K.; Giokas, D. L.; Karayannis, M. I. Micelle-mediated separation and cloud-point extraction. *TrAC - Trends Anal. Chem.* **2005**, *24* (5), 426–436 DOI: 10.1016/j.trac.2005.01.013.

(51) Park, J. H.; Jung, J. W.; Kang, H.-W.; Cho, D.-W. Indirect three-dimensional printing of synthetic polymer scaffold based on thermal molding process. *Biofabrication* **2014**, *6* (2), 25003 DOI: 10.1088/1758-5082/6/2/025003.

(52) Käpylä, E.; Delgado, S. M.; Kasko, A. M. Shape-Changing Photodegradable Hydrogels for Dynamic 3D Cell Culture. *ACS Appl. Mater. Interfaces* **2016**, *8* (28), 17885–17893 DOI: 10.1021/acsami.6b05527.

(53) Hendriks, J.; Riesle, J.; Blitterswijk, C. A. van. Co-culture in cartilage tissue engineering. *J. Tissue Eng. Regen. Med.* **2010**, *4* (7), 524–531 DOI: 10.1002/term.

(54) Sender, R.; Fuchs 2¤, S.; Milo, R. Revised Estimates for the Number of Human and Bacteria Cells in the Body. *PLoS Biol.* **2016**, *14* (8), 1–14 DOI: 10.1371/journal.pbio.1002533.

(55) Feng, B.; Jinkang, Z.; Zhen, W.; Jianxi, L.; Jiang, C.; Jian, L.; Guolin, M.; Xin, D. The effect of pore size on tissue ingrowth and neovascularization in porous bioceramics of controlled architecture in vivo. *Biomed. Mater.* **2011**, *6* (1), 15007 DOI: 10.1088/1748-6041/6/1/015007.

(56) Sandiford, N.; Doctor, C.; Rajaratnam, S. S.; Ahmed, S.; East, D. J.; Miles, K.; Butler-Manuel, A.; Shepperd, J. A. N. Primary total hip replacement with a Furlong fully hydroxyapatite-coated titanium alloy femoral component: Results at a minimum follow-up of 20 years. *Bone Jt. J.* **2013**, *95 B* (4), 467–471 DOI: 10.1302/0301-620X.95B4.30445.

(57) Van Nooten, G. J.; Bové, T.; Van Belleghem, Y.; François, K.; Caes, F.; Vandenplas, G.; De Pauw, M.; Taeymans, Y. Twenty-year single-center experience with the medtronic open pivot mechanical heart valve. *Ann. Thorac. Surg.* **2014**, *97* (4), 1306–1313 DOI: 10.1016/j.athoracsur.2013.11.035.

(58) Truernit, E.; Bauby, H.; Dubreucq, B.; Grandjean, O.; Runions, J.; Barthelemy, J.; Palauqui, J. C. High-resolution whole-mount imaging of three-dimensional tissue organization and gene expression enables the study of Phloem development and structure in Arabidopsis. *Plant Cell* **2008**, *20* (6), 1494–1503 DOI: 10.1105/tpc.107.056069.

3.8 Supplementary Figures

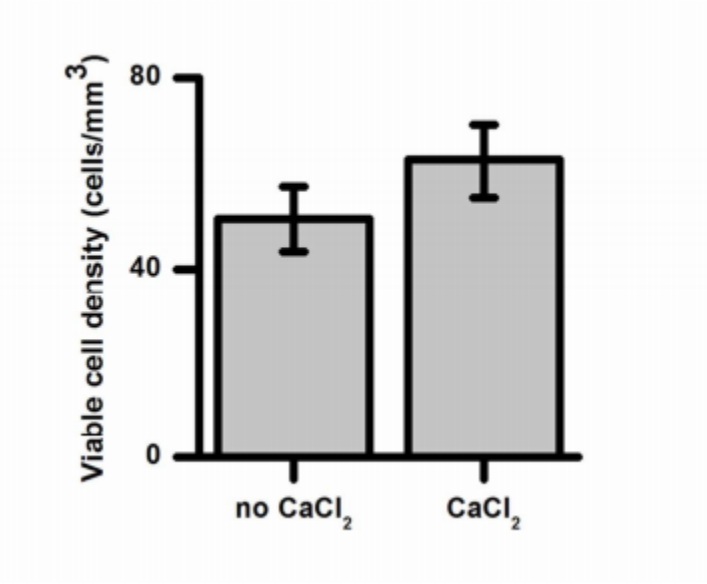

Supporting Information Figure S3.1: $CaCl_2$ pre-treatment and excessive washing. A CaCl2 pre-treatment along with excessive washing was used to remove remnant surfactant from the scaffolds. CCK-8 quantification of cell density shows that on small samples, excessive washing to remove the remnant surfactant yields comparable results to the salt pre-treatment protocol after 2 days of culture ($P = 9.2 \times 10^{-1}$, N = 4). All values are mean ± s.e.m.

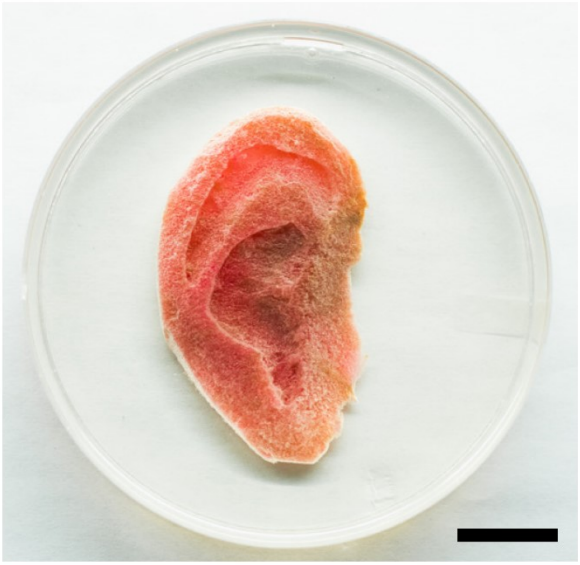

Supporting Information Figure S3.2: Cells cultured on a biomaterial carved out of apple hypanthium tissue in the shape of an ear (Scale = 2 cm).

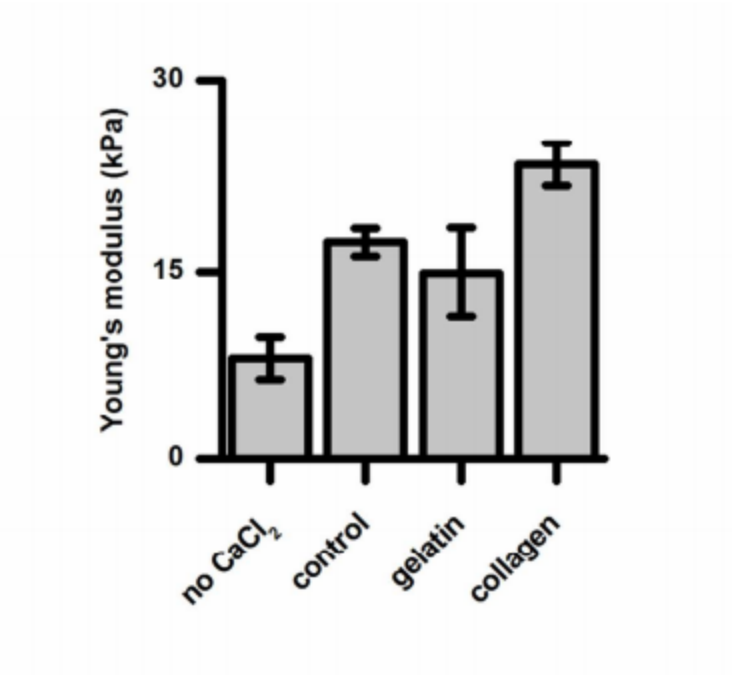

Supporting Information Figure S3.3: Young's modulus. The Young's modulus was measured after 2 weeks of culture by compressing the material to a 10% strain, at a strain rate of 50 µm/s, The Young's modulus of the scaffolds without the $CaCl_2$ treatment was significantly lower than that of the treated samples (1.7x101 ± 1.1 kPa) ($P = 4.9x10^{-2}$, no $CaCl_2$: N = 5, $CaCl_2$: N = 6). The addition of the hydrogels did not significantly alter the moduli from the CaCl2-treated scaffolds ($1.5 x10^{1} \pm 3.6$ kPa, $2.3x10^{1} \pm 1.7$ kPa, gelatin and collagen respectively, $P > 0.05$, N=6).

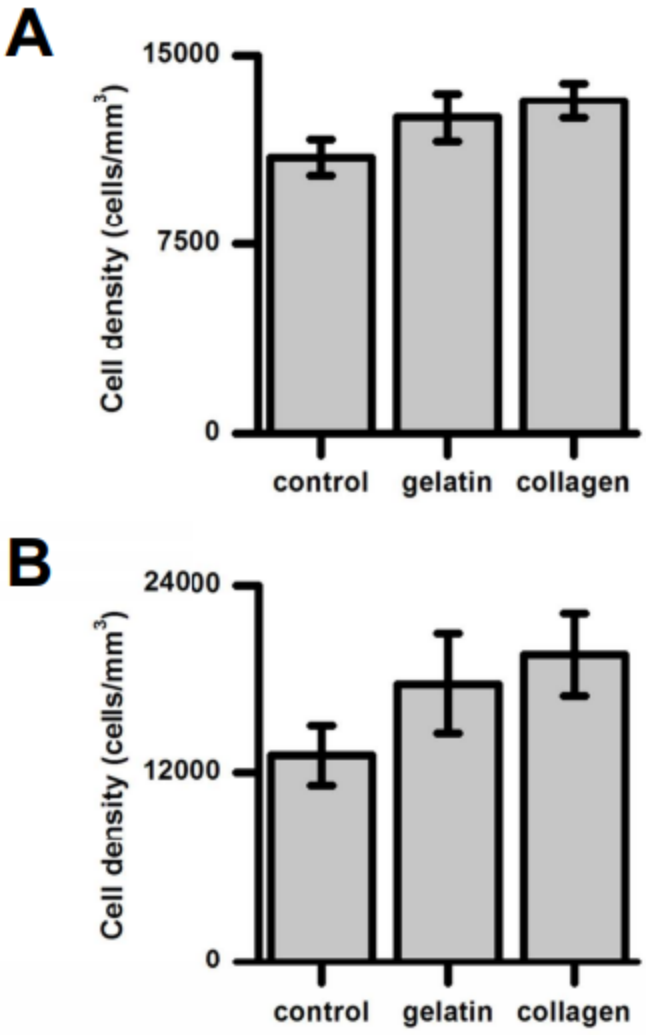

Supporting Information Figure S3.4: Cell invasion and proliferation quantification. The cell density in the ring-shaped biomaterials that were either bare or created with temporary (gelatin) and permanent (collagen) hydrogels after 2 weeks of culture. No statistical differences in cell density under any of the three ring fabrication conditions were observed ($P > 0.05$, $N = 12$ images for each condition). (A) Top/bottom face of the ring. (B) Cross-section of the ring. All values are mean ± s.e.m.

Chapter 4

Engineered Tissue Interfaces for In Vitro Modelling and In Vivo Regeneration

This chapter is a manuscript in preparation:

Hickey, R. J., Leblanc Latour, M., Harden, J. L. & Pelling, A. E. Engineered Tissue Interfaces – A Platform for Tissue Engineering. Manuscript in preparation (2020).

§1 Motivation

Although significant efforts have been focused on creating single tissue types, tissue interface design is lacking, which constitutes a gap in knowledge. Tissue interfaces mark transitional zones between tissues and microenvironments, and are inherently complex. As there are many tissue interfaces in the body, a platform for creating and studying these interfaces that can be adapted to suit or model specific applications is needed.

§2 Hypothesis and Objectives

Here I hypothesize that engineered tissue interfaces (ETIs) can be created by combining highly porous, decellularized, plant-derived scaffolds in a modular fashion. Our objective was to establish a platform for creating tissue interfaces from interlocking scaffolds for in vitro and in vivo models.

4.1 Abstract

In regenerative medicine, the healing of the interfacial zone between tissues is a major challenge, yet approaches for engineering and studying the complex microenvironment of this interface remain lacking [1–3]. Here, we create and study these complex living interfaces by manufacturing modular "blocks" of decellularized plant-derived scaffolds[4–6] with varying shapes and sizes with a computer numerical controlled mill. Each block can then be seeded with different cell types and easily assembled in a manner akin to LEGO™ bricks to create an engineered tissue interface (ETI). As a proof-of-concept study we utilize ETIs to investigate the interaction between lab grown bone and connective tissues. We also demonstrate how ETIs are biocompatible in vivo, stimulating the formation of blood vessels, cell infiltration, and tissue integration after implantation. This work creates possibilities for new tissue design avenues for understanding fundamental biological processes or the development of synthetic artificial tissues.

4.2 Main

The body consists of a variety of tissues , and the interface between them presents a unique juxtaposition of interacting cellular environments [7–9]. Traditionally, bioengineers design scaffolds for one environment, but there is a need to develop model systems to create and investigate tissue interfaces [10–14]. We constructed living engineered tissue interfaces (ETIs) by combining highly porous, decellularized, plant-derived scaffolds in a modular fashion. Plant-derived scaffolds can be selected to mimic natural human structures in vitro and in vivo [4–6,15–23]. Intense research has been focused on designing biomaterials to enhance tissue integration in specific cases [24–27]; however, the widespread potential of this technology necessitates a platform that can be adapted to suit particular biomedical needs. We hypothesized that the modular assembly of biomaterial subunits could create ETIs. We found that combining scaffolds in a LEGO™-like fashion is a viable approach for establishing an ETI platform.

In order to create ETIs, we combined subunit components without the use of additional crosslinkers or glues. Interlocking composite pieces were fabricated to yield scaffolds that could be repopulated with distinct or identical cell types and subsequently re-combined into a single unit (Fig. 4.1) [6]. To create such scaffolds, we employed 3D milling with a computer numerical controlled (CNC) router to reproducibly carve the structures from apple hypanthium tissue (Fig. 4.1a, Supplementary Video 4.1, Supplementary Table 4.1). A simple design for interlocking materials is the common stud and anti-stud geometry of LEGO™ bricks (Fig. 4.1b and Supplementary Fig. 4.1). We designed single stud and anti-stud bricks, wherein the stud subunit consisted of a 5 mm x 5 mm x 2 mm base with a 2 mm (height and diameter) cylindrical peg protruding from the center, and the anti-stud subunit had a 2 mm diameter cylindrical hole in the center of the 5 mm x 5 mm x 2 mm base (Fig. 4.1b). Tissue interface formation was a direct

consequence of interlocking the components together (Fig. 4.1c). Prior to assembly, the individual subunits were decellularized, processed, and repopulated with mammalian cells as previously described [6] (Fig. 4.1d and Supplementary Fig. 4.2).

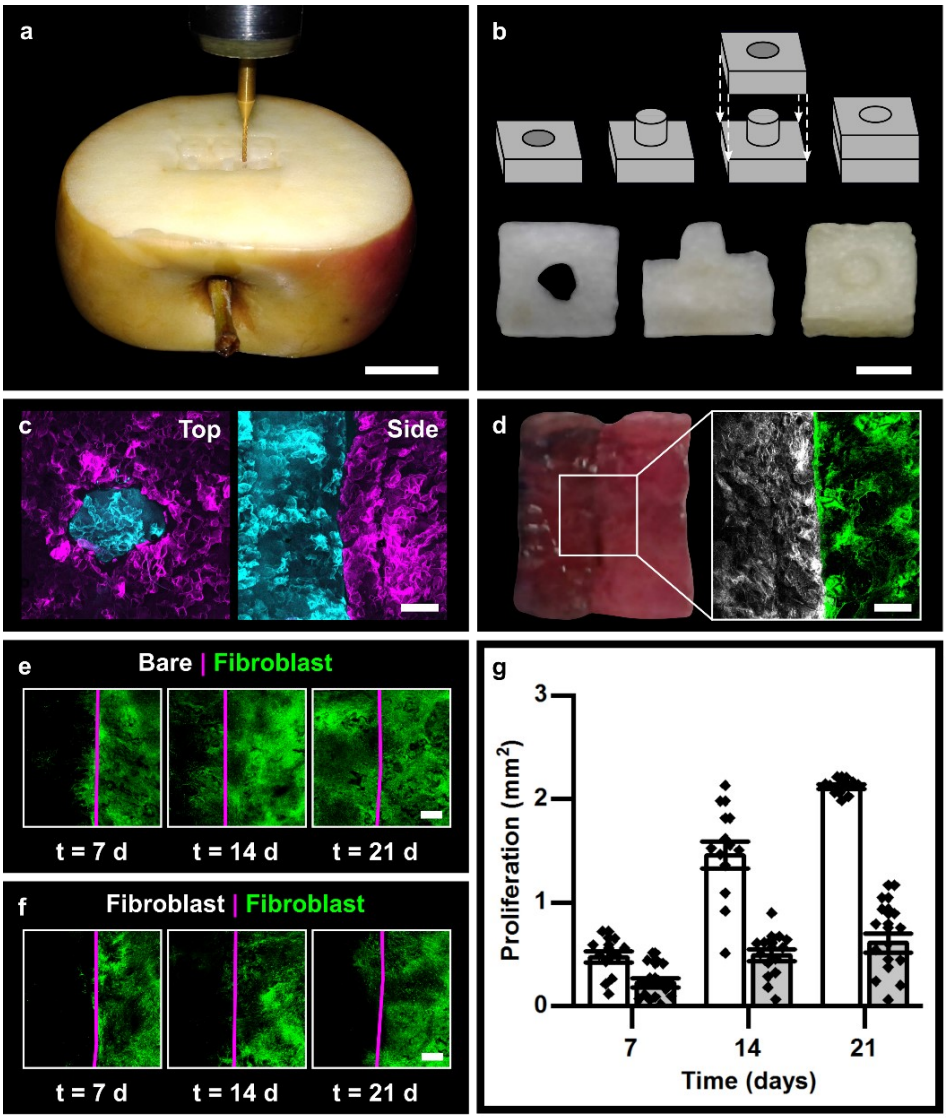

Figure 4.1: Interlocked biomaterials for ETI formation. (a) A CNC router was used to carve the interlocking materials. Scale = 15 mm. **(b)** Geometry of the single stud and anti-stud interlocked units as well as the decellularized subunits and the combined entity. Scale = 2.5 mm. **(c)** Maximum z-projected confocal image of the top view and side view of the interlocked unit with one subunit stained with Calcofluor white (cyan) and the other stained with Congo Red (magenta), scale = 500 µm. **(d)** Tissue interface formation: left = side view of interlocked unit, right = maximum z-projected confocal image of the two cell populations. White = Hoechst 33342 stained nuclei of NIH 3T3 cells, green = GFP NIH 3T3 cells. Scale = 500 µm. Fibroblast cell (green) migration across the interface (magenta) of the interlocked unit with **(e)** one subunit

preloaded with cells and the other void of cells, and **(f)** both loaded with cells (only one population transfected with GFP). Scale = 500 μm. **(g)** Quantification of cell migration across the interface. White = bare | fibroblast, grey = fibroblast | fibroblast, N = 12.

Cells must be able to traverse the interface and interact with the adjacent population when required [28]. Controlled in vitro cell migration assays were carried out, which revealed that when a scaffold pre-loaded with fibroblast cells was interlocked with a bare subunit, the cells migrated across the interface and invaded the bare scaffold (Fig. 4.1e). The proliferation was monitored weekly for 3 weeks, and each week presented a significant increase in cell infiltration ($P < 0.001$) (Fig. 4.1e,g). After 3 weeks of culture, the initially barren scaffold had a comparable cell number density to the pre-seeded subunit (Fig. 4.1e,g). In the absence of an existing cell population, such as an implanted biomaterial void of cells, this extensive cell migration and infiltration is usually desirable [29]. We repeated the cell migration assays with fibroblasts loaded on both subunits. The two fibroblast groups were distinguishable, as only one population contained green fluorescent protein (GFP) (Fig. 4.1d-f). We found that GFP-labelled cells crossed the interface; however, when comparing the dual and single cell migration assays, there was significantly less migration when both scaffolds were pre-loaded with cells ($P < 0.002$), in which case the cells did not fully invade the adjacent scaffold. Therefore, the two cell populations remained largely distinct away from the interface on their respective sides but were well integrated at the interface (Fig. 4.1e-g). This result is pertinent for tissue interfaces, as a uniform co-culture of cells does not replicate entheses in vivo. Two obstacles in entheses design are the achievement of adequate cell invasion and the creation of an appropriate transitional zone between segregated microenvironments [30–32]. The modular assembly with porous scaffolds enables cells from two distinct regions to form an intermediate zone at the interface between the subunits [33]. ETIs can be designed to replicate specific tissue interfaces, such as the bone-connective tissue interface, which delineates two separate regimes. A lack of integration of the two regions is a key factor in implant failure [2]. Bone cells are surrounded by a mineralized extracellular network; however, this mineralization is absent in the connective tissue [1–3,24–27]. Several models have been developed in an attempt to recreate this interface; the approach consists of creating different environments within a single stratified material or two or more adjacent components [1–3,24–27]. Nevertheless, a universal “plug and play” system has not been established for engineering and designing models of interfaces. To investigate this specific application of our ETI platform, we replicated the bone/connective tissue interface (Fig. 4.2). This was achieved by culturing MC 3T3 E1 subclone 4 pre-osteoblasts on one subunit to confluency followed by differentiation into osteoblasts, which mineralized the scaffold. An opposing scaffold was also cultured until confluence with mouse NIH 3T3 fibroblasts and interlocked with the calcified subunit (Fig. 4.2).

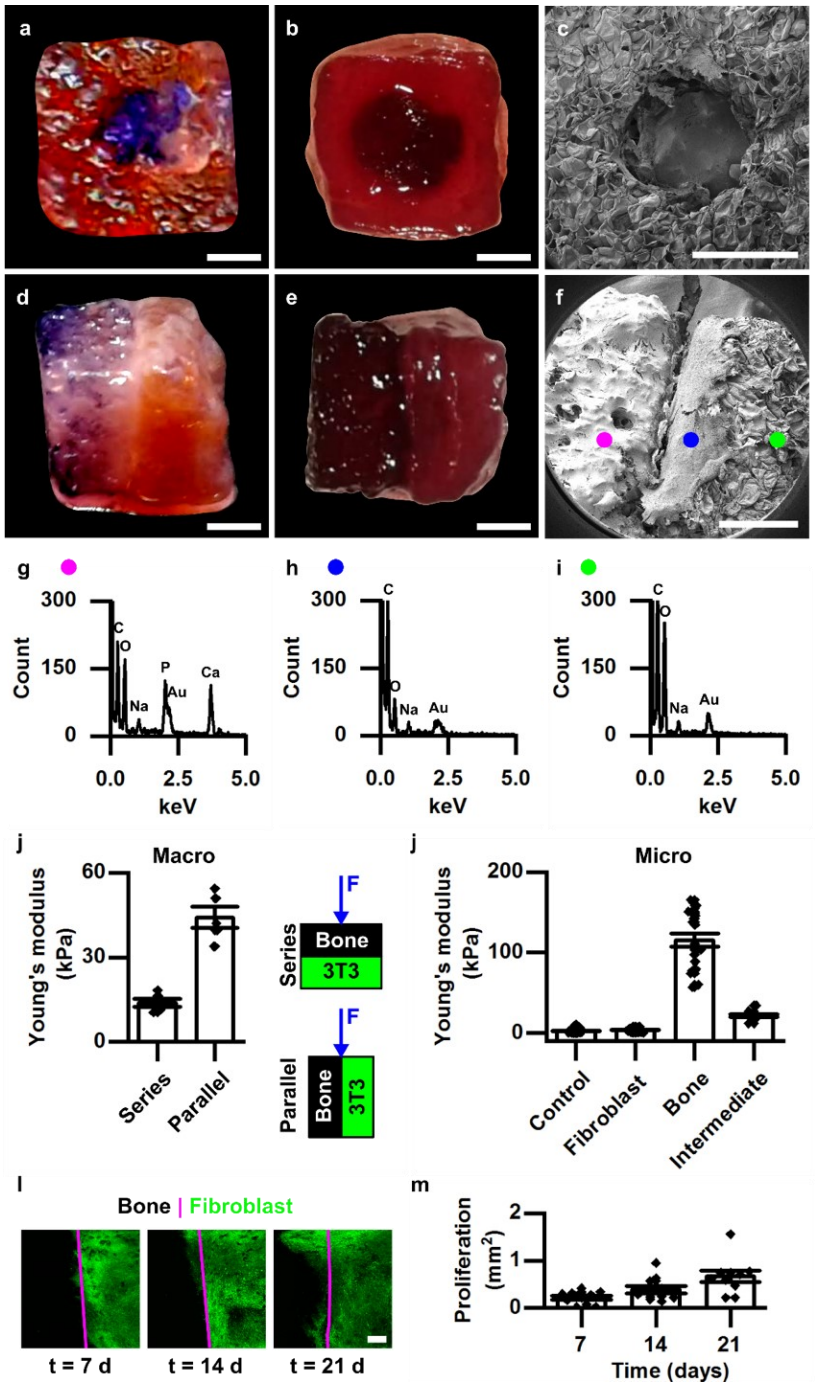

Figure 4.2: Bone-connective tissue ETI. **(a)** Top view of scaffolds stained to reveal alkaline phosphate. Purple = positive for alkaline phosphatase activity, orange/red = negative. **(b)** Top view of scaffolds stained for the presence of calcium staining. Deep red = calcified scaffold, light red = non-calcified. **(c)** Top view of SEM of bone-connective tissue ETI with smooth mineralized peg inserted into the non-mineralized fibroblast covered subunit. Corresponding side views of the scaffolds stained for **(d)** alkaline phosphatase amd **(e)** calcium. **(f)** Corresponding side view of the scaffold imaged with. Scale bar **(a-f)** = 1 mm. **(g-i)** EDS chemical analysis of the corresponding

regions (magenta = bone subunit, blue = fibroblast covered subunit adjacent to the interface, green = fibroblast covered subunit). **(j)** Compressive moduli of the bone-fibroblast ETI compressed in the series and parallel directions, N = 5. **(k)** Local mechanical probing: nanoindentations with AFM. **(l)** Fibroblast cell (GFP NIH 3T3) migration across the bone-connective tissue ETI, scale = 500 μm. **(m)** Quantification of cell migration, N = 10.

As osteoblasts deposit calcium and mineralize their extracellular matrix, there are different biochemical and physical environments of the two cell populations forming the bone-connective tissue ETI. Alkaline phosphatase and calcium staining revealed that the composite was comprised of two distinct regions away from the interface (Fig. 4.2a,d;b,e and Supplementary Fig. 4.3). We then probed the local cellular environments using scanning electron microscopy (SEM) and electron dispersion spectroscopy (EDS). SEM revealed two distinct surface topographies (Fig. 4.2c,f and Supplementary Fig. 4.4). On the bone component, a smooth coating was deposited on the scaffold (Fig. 4.2c,f and Supplementary Fig. 4.4). This coating was absent on the fibroblast side; instead, thick layers of cells were observed (Fig. 4.2c,f and Supplementary Fig. 4.4). EDS was employed to confirm that the smooth coating on the differentiated bone component was mineralization. The characteristic X-rays confirmed the presence of calcium (~3.69 keV) and phosphorous (~2.01 keV) on the bone scaffolds (Fig. 4.2g). These elements were not present to a detectable level on the fibroblast side (Fig. 4.2h,i). The interfacial region was also devoid of mineralization. In vivo, there is a similar zone in the enthesis known as the uncalcified avascular fibrocartilage zone, which is a non-mineralized, avascular region found between the fibrous connective tissue and the tidemark separating the hard and soft tissues [34].

The separation of the mineralized and non-mineralized tissue resulted in two regions with different mechanical profiles (Fig. 4.2). All tissue interfaces in our bodies experience stress shielding when the mechanical environments of the constituents vary. The phenomenon of stress shielding is the difference in the stress applied to each body in a cohesive system. The composite is composed of materials with different elastic moduli; therefore, an effective Young's modulus can be obtained from the geometry, direction of applied force, and the moduli of the constituents (Fig. 4.2j). ETIs consisting of components with different mechanical profiles allows stress shielding biomaterials to be formed [7,35,36] (Fig. 4.2j and Supplementary Fig. 4.5). For example, two prototype geometries can be considered: two bricks are stacked on top of one another and a force is applied normal to the interface (series orientation) or parallel to it. The effective Young's modulus in the series arrangement was 13.8 ± 3.3 kPa which was significantly less than the parallel conformation with a value of 44.2 ± 8.4 kPa ($P < 0.001$). In addition to macroscale compressions, atomic force microscopy was used to probe the local mechanics in both regions (Fig. 4.2k); the two stiffness regimes observed were comparable to the reported literature values for bone and fibroblast cells [37,38]. The bone component had a Young's modulus of $1.15 \times 10^2 \pm 8.2$ kPa, whereas the fibroblast component had a significantly lower modulus of 3.88 ± 0.3 kPa ($P < 0.001$). Interestingly, there was an intermediate stiffness found in the interfacial

region with a modulus of $2.17 \times 10^1 \pm 1.7$ kPa, as expected for a region composed of fibroblasts, undifferentiated pre-osteoblasts, and differentiated osteoblasts surrounded by their mineralized matrix. A cell migration assay from the fibroblast component onto the bone section demonstrated that cells intermixed at the interface and exhibited a 13% proliferation increase as in the previous experiment ($P = 0.971$ compared to the dual fibroblast migration assay), which is similar to the natural bone-connective tissue interface [34,39] (Fig. 4.2l,m).

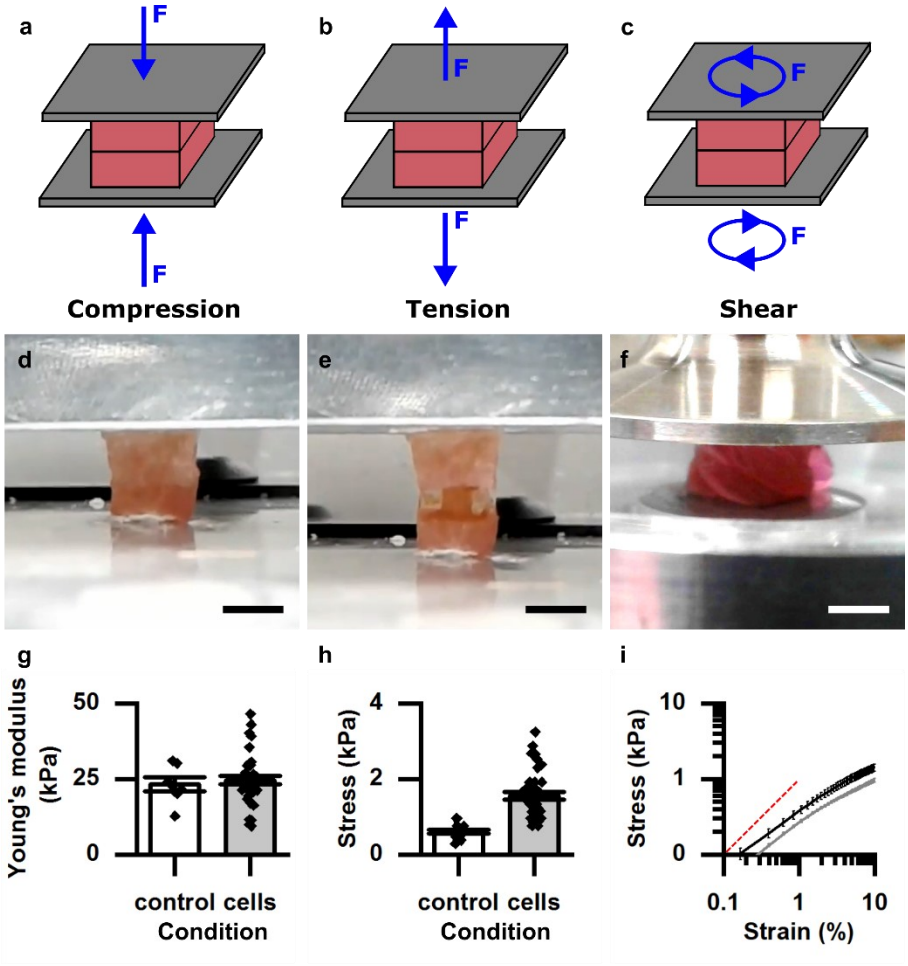

Figure 4.3. Mechanical testing of ETIs. **(a-c)** Cartoon illustrations of the three classes of mechanical tests that were performed: compression, tension, and shear. **(d-f)** Interlocked ETIs under compressive, tensile, and shear stresses. Scale = 4 mm. **(g)** Compressive Young's modulus with (N = 36) and without fibroblast cells (N = 7) with cells. **(h)** Maximum tensile stress prior to subunit separation with (N = 39) and without fibroblast cells (N = 15). **(i)** Shear stress σ vs strain ε in a controlled steady shear rate experiment at a strain rate of 0.01 s^{-1}, N = 3. Black = without cells, grey = with cells. The red dashed line is provided as a guide for the linear regime. Power-law behavior is observed at low strains: $\sigma \sim \varepsilon^y$ for $y = 0.74 \pm 0.02$ without cells and $y = 0.72 \pm 0.02$ with cells.

Mechanical characterization is integral for designing tissue interfaces with specialized structure-function relationships [39]. Three separate mechanical characterizations are of particular interest for these interlocked composite materials: compression, tension, and shear (Fig. 4.3a-f). We examined scaffolds with and without added fibroblast cells in the blocks. Compression tests probe the bulk elastic properties of the two blocks in series, and the interface between blocks plays a minor role. It was found that the presence of cells had no significant impact on the apparent stiffness of the material: $2.44 \text{ x } 10^1 \pm 1.3 \text{ kPa}, P = 0.68$ (Fig. 4.3g), as intrinsic cell elasticity is relatively weak compared to that of the matrix material. Under tension, the mechanical response is dominated by the cohesiveness of the interfacial region. This can be seen clearly in Fig. 4.4e, which shows a progressively decreasing contact area between blocks as two blocks separate under the applied tension. In this case, the stress required to initiate separation of the two subunits was greater when fibroblasts were seeded on the scaffolds (cells: $1.56 \pm 0.10 \text{ kPa}$, control: $0.60 \pm 0.05 \text{ kPa}, P < 0.001$) (Fig. 4.3h), as cell-matrix and cell-cell adhesion both contribute to the mechanical integrity of the interfacial region. Applied shear provides direct probe of interfacial cohesion and integrity. Controlled steady shear rate experiments were characterized by an initial reversible response, where stress σ is found to be a sub-linear power law of applied strain ε, $\sigma \sim \varepsilon^y$ with $y \cong 3/4$, followed by subsequent strain softening (Fig. 4.3i). The lack of a linear stress-strain relationship at low strains is indicative of mechanics dominated by stick-slip events at the interface. For larger strains, eventually transient failure in the slip plane of the interface occurs, which is followed by a steady state friction response (Supplementary Fig. 4.6). Interestingly, the power-law stress-strain response was found to be reversible even after failure in the slip plane for both relatively slow and fast applied strain rates (Supplementary Fig. 4.6), which may serve as a valuable design feature for preventing the scaffolds from irreversible fracturing under large loads in situ. In shear conditions, the presence of fibroblast cells did not qualitatively change the stress-strain relationship; however, samples with cells were found to be somewhat more compliant (Fig. 4.3i). An interfacial region containing cells, which have a relatively lower intrinsic modulus, would be more compliant than an interface composed of pure matrix. A different dependence on cells would be plausible for other scenarios such as different cell types and/or different interlocking geometries (e.g. multi-post blocks). The potential applications of ETIs are not limited to *in vitro* studies of tissue interfaces; we foresee ETIs playing an essential role in biomaterial implant design. As a proof-of-concept experiment, we implanted the interlocked composite materials subcutaneously in an immunocompetent rat model for 4 weeks [5,6] (Fig. 4.4a). The subunits remained interlocked despite simply being placed under the skin (Fig. 4.4b). Histological analysis revealed that the cells invaded the peripheral regions of the biomaterials, and blood vessel formation was clearly observed (Fig. 4.4c-f and Supplementary Fig. 4.7) [5,6]. The invading fibroblasts from the surrounding animal tissue laid down their own collagen network within the cellulose-based scaffold (Fig. 4.4d,f).

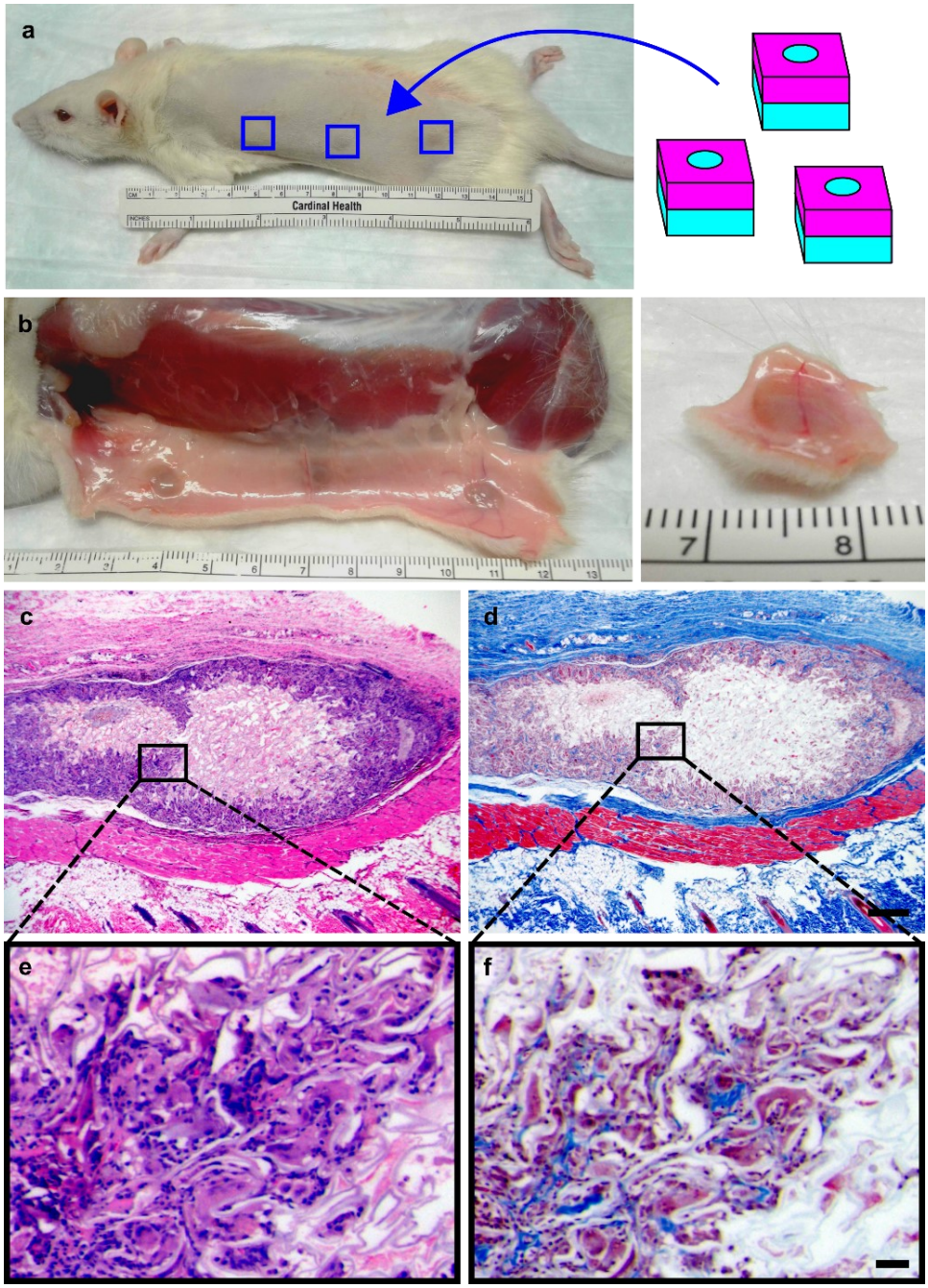

Figure 4.4. In vivo implantation of ETIs. (a) Schematic showing the location of three subcutaneous implanted ETIs in a rat model. **(b)** ETI sample resection showing the subunits remained interlocked and underwent compression after 4 weeks. **(c,e)** H&E staining revealing substantial of the cell invasion in the outer regions of the interlocked biomaterial. **(d,f)** Masson's Trichrome staining showing collagen deposition (blue) on the scaffold. Scale **(c,d)** = 500 µm, **(e,f)** = 50 µm.

As demonstrated in this study, ETIs establish a novel approach for studying and implementing tissue interface models. Significant insights in matrix composition, mechanical loading, and cell organization have been gained from specific tissue interface models of entheses, such as the lack of transition and insertion zones at interfaces post-operations [1,2,39,3,7,24–28,33], yet platforms to study tissue interfaces are lacking. We have shown that decellularized plant-derived scaffolds can be shaped into complementary interlocking subunits. Cells were shown to migrate across the interface between such subunits, and we highlighted the specific example of creating a bone-connective tissue interface. Spatial organization and transitional zones within tissues and tissue interfaces are highly complex and integral to proper function; thus, the ability to combine them in a spatially controlled manner is essential. The modular assembly of components into a functional unit allows customizable designer interfaces to be formed. The modular assembly approach of ETIs presented here ultimately provides an exciting new framework for the design of living tissues.

4.3 References

(1) Boys, A. J.; McCorry, M. C.; Rodeo, S.; Bonassar, L. J.; Estroff, L. A. Next generation tissue engineering of orthopedic soft tissue-to-bone interfaces. *MRS Commun.* **2017**, *7* (3), 289–308 DOI: 10.1557/mrc.2017.91.

(2) Patel, S.; Caldwell, J.-M.; Doty, S. B.; Levine, W. N.; Rodeo, S.; Soslowsky, L. J.; Thomopoulos, S.; Lu, H. H. Integrating Soft and Hard Tissues Via Interface Tissue Engineering. *J Orthop Res.* **2018**, *36* (24), 6072–6078 DOI: 10.1002/cncr.27633.Percutaneous.

(3) Harris, E.; Liu, Y.; Cunniffe, G.; Morrissey, D.; Carroll, S.; Mulhall, K.; Kelly, D. J. Biofabrication of soft tissue templates for engineering the bone–ligament interface. *Biotechnol. Bioeng.* **2017**, *114* (10), 2400–2411 DOI: 10.1002/bit.26362.

(4) Modulevsky, D. J.; Lefebvre, C.; Haase, K.; Al-Rekabi, Z.; Pelling, A. E. Apple derived cellulose scaffolds for 3D mammalian cell culture. *PLoS One* **2014**, *9* (5) DOI: 10.1371/journal.pone.0097835.

(5) Modulevsky, D. J.; Cuerrier, C. M.; Pelling, A. E. Biocompatibility of Subcutaneously Implanted Plant-Derived Cellulose Biomaterials. *PLoS One* **2016**, *11* (6), 1–19 DOI: 10.1371/journal.pone.0157894.

(6) Hickey, R. J.; Modulevsky, D. J.; Cuerrier, C. M.; Pelling, A. E. Customizing the Shape and Microenvironment Biochemistry of Biocompatible Macroscopic Plant-Derived Cellulose Scaffolds. *ACS Biomater. Sci. Eng.* **2018**, *4*, 3726–3736 DOI: 10.1021/acsbiomaterials.8b00178.

(7) Bayrak, E.; Yilgor Huri, P. Engineering Musculoskeletal Tissue Interfaces. *Front. Mater.* **2018**, *5*, 24 DOI: 10.3389/fmats.2018.00024.

(8) Place, E. S.; Evans, N. D.; Stevens, M. M. Complexity in biomaterials for tissue engineering. *Nat. Mater.* **2009**, *8* (6), 457–470 DOI: 10.1038/nmat2441.

(9) Das, R. K.; Zouani, O. F. A review of the effects of the cell environment physicochemical nanoarchitecture on stem cell commitment. *Biomaterials* **2014**, *35* (20), 5278–5293 DOI: 10.1016/j.biomaterials.2014.03.044.

(10) Skylar-Scott, M. A.; Uzel, S. G. M.; Nam, L. L.; Ahrens, J. H.; Truby, R. L.; Damaraju, S.; Lewis, J. A. Biomanufacturing of organ-specific tissues with high cellular density and embedded vascular channels. *Sci. Adv.* **2019**, *5* (9), eaaw2459 DOI: 10.1126/sciadv.aaw2459.

(11) Mironov, V.; Visconti, R. P.; Kasyanov, V.; Forgacs, G.; Drake, C. J.; Markwald, R. R. Organ printing: tissue spheroids as building blocks. *Biomaterials* **2009**, *30* (12), 2164–2174 DOI: 10.1016/j.biomaterials.2008.12.084.

(12) Valentin, T. M.; Dubois, E. M.; Machnicki, C. E.; Bhaskar, D.; Cui, F. R.; Wong, I. Y. 3D printed self-adhesive PEGDA-PAA hydrogels as modular components for soft actuators and microfluidics. *Polym. Chem.* **2019**, *10* (16), 2015–2028 DOI: 10.1039/c9py00211a.

(13) Grigoryan, B.; Paulsen, S. J.; Corbett, D. C.; Sazer, D. W.; Fortin, C. L.; Zaita, A. J.; Greenfield, P. T.; Calafat, N. J.; Gounley, J. P.; Ta, A. H.; et al. Multivascular networks and functional intravascular topologies within biocompatible hydrogels. *Science* **2019**, *364* (6439), 458–464 DOI: 10.1126/science.aav9750.

(14) Marti-Figueroa, C. R.; Ashton, R. S. The case for applying tissue engineering methodologies to instruct human organoid morphogenesis. *Acta Biomater.* **2017**, *54*, 35–44 DOI: 10.1016/j.actbio.2017.03.023.

(15) Gershlak, J.; Hernandez, S.; Fontana, G.; Perreault, L.; Hansen, K.; Larson, S.; Binder, B.; Dolivo, D.; Yang, T.; Dominko, T.; et al. Crossing kingdoms: Using decellularized plants as perfusable tissue engineering scaffolds. *Biomaterials* **2017**, *125*, 13–22 DOI: 10.1016/j.biomaterials.2017.02.011.

(16) Fontana, G.; Gershlak, J.; Adamski, M.; Lee, J.-S.; Matsumoto, S.; Le, H. D.; Binder, B.; Wirth, J.; Gaudette, G.; Murphy, W. L. Biofunctionalized Plants as Diverse Biomaterials for Human Cell Culture. *Adv. Healthc. Mater.* **2017**, 1601225 DOI: 10.1002/adhm.201601225.

(17) Phan, N. V.; Wright, T.; Rahman, M. M.; Xu, J.; Coburn, J. M. In Vitro Biocompatibility of Decellularized Cultured Plant Cell-Derived Matrices. *ACS Biomater. Sci. Eng.* **2020**, *6* (2), 822–832 DOI: 10.1021/acsbiomaterials.9b00870.

(18) Robbins, E. R.; Pins, G. D.; Laflamme, M. A.; Gaudette, G. R. Creation of a contractile biomaterial from a decellularized spinach leaf without ECM protein coating: An in vitro study. *J. Biomed. Mater. Res. - Part A* **2020**, *108* (10), 2123–2132 DOI: 10.1002/jbm.a.36971.

(19) Contessi Negrini, N.; Toffoletto, N.; Farè, S.; Altomare, L. Plant Tissues as 3D Natural Scaffolds for Adipose, Bone and Tendon Tissue Regeneration. *Front. Bioeng. Biotechnol.* **2020**, *8* (June), 1–15 DOI: 10.3389/fbioe.2020.00723.

(20) Iravani, S.; Varma, R. S. Plants and plant-based polymers as scaffolds for tissue engineering. *Green Chem.* **2019**, *21* (18), 4839–4867 DOI: 10.1039/c9gc02391g.

(21) Cheng, Y.-W.; Shiwarski, D. J.; Ball, R. L.; Whitehead, K. A.; Feinberg, A. W. Engineering Aligned Skeletal Muscle Tissue Using Decellularized Plant-Derived Scaffolds. *ACS Biomater. Sci. Eng.* **2020**, *6* (5), 3046–3054 DOI: 10.1021/acsbiomaterials.0c00058.

(22) Lee, J.; Jung, H.; Park, N.; Park, S. H.; Ju, J. H. Induced Osteogenesis in Plants Decellularized Scaffolds. *Sci. Rep.* **2019**, *9* (1), 1–10 DOI: 10.1038/s41598-019-56651-0.

(23) Toker, M.; Rostami, S.; Kesici, M.; Gul, O.; Kocaturk, O.; Odabas, S.; Garipcan, B. Decellularization and characterization of leek: a potential cellulose-based biomaterial. *Cellulose* **2020**, *27* (13), 7331–7348 DOI: 10.1007/s10570-020-03278-4.

(24) Atesok, K.; Doral, M. N.; Karlsson, J.; Egol, K. A.; Jazrawi, L. M.; Coelho, P. G.; Martinez, A.; Matsumoto, T.; Owens, B. D.; Ochi, M.; et al. Multilayer scaffolds in orthopaedic tissue engineering. *Knee Surgery, Sport. Traumatol. Arthrosc.* **2016**, *24* (7), 2365–2373 DOI: 10.1007/s00167-014-3453-z.

(25) Lu, H. H.; Subramony, S. D.; Boushell, M. K.; Zhang, X. Tissue engineering strategies for the regeneration of orthopedic interfaces. *Ann. Biomed. Eng.* **2010**, *38* (6), 2142–2154 DOI: 10.1007/s10439-010-0046-y.

(26) Allan, K. S.; Pilliar, R. M.; Wang, J.; Grynpas, M. D.; Kandel, R. A. Formation of biphasic constructs containing cartilage with a calcified zone interface. *Tissue Eng.* **2007**, *13* (1), 167–177 DOI: 10.1089/ten.2006.0081.

(27) Alhadlaq, A.; Mao, J. J. Tissue-engineered osteochondral constructs in the shape of an articular condyle. *J. Bone Jt. Surg. - Ser. A* **2005**, *87* (5), 936–944 DOI: 10.2106/JBJS.D.02104.

(28) Wang, I.-N. E.; Shan, J.; Choi, R.; Oh, S.; Kepler, C. K.; Chen, Faye, H.; Lu, H. H. Role of Osteoblast–Fibroblast Interactions in the Formation of the Ligament-to-Bone Interface. *J. Orthop. Res.* **2007**, *25*, 16091620 DOI: 10.1002/jor.

(29) Joly, P.; Duda, G. N.; Schöne, M.; Welzel, P. B.; Freudenberg, U.; Werner, C.; Petersen, A. Geometry-Driven Cell Organization Determines Tissue Growths in Scaffold Pores: Consequences for Fibronectin Organization. *PLoS One* **2013**, *8* (9), 1–11 DOI: 10.1371/journal.pone.0073545.

(30) Chow, L. W.; Fischer, J. F. Creating biomaterials with spatially organized functionality. *Exp. Biol. Med. (Maywood).* **2016**, *241* (10), 1025–1032 DOI: 10.1177/1535370216648023.

(31) Li, Q.; Ma, L.; Gao, C. Biomaterials for in situ tissue regeneration: Development and perspectives. *J. Mater. Chem. B* **2015**, *3* (46), 8921–8938 DOI: 10.1039/c5tb01863c.

(32) Sakaguchi, K.; Shimizu, T.; Okano, T. Construction of three-dimensional vascularized cardiac tissue with cell sheet engineering. *J. Control. Release* **2015**, *205*, 83–88 DOI: 10.1016/j.jconrel.2014.12.016.

(33) Yang, P. J.; Temenoff, J. S. Engineering orthopedic tissue interfaces. *Tissue Eng. - Part B Rev.* **2009**, *15* (2), 127–141 DOI: 10.1089/ten.teb.2008.0371.

(34) Apostolakos, J.; Durant, T. J. S.; Dwyer, C. R.; Russell, R. P.; Weinreb, J. H.; Alaee, F.; Beitzel, K.; McCarthy, M. B.; Cote, M. P.; Mazzocca, A. D. The enthesis: A review of the tendon-to-bone insertion. *Muscles. Ligaments Tendons J.* **2014**, *4* (3), 333–342 DOI: 10.11138/mltj/2014.4.3.333.

(35) Pakvis, D. F. M.; Heesterbeek, P. J. C.; Severens, M.; Spruit, M. Cancellous and cortical bone mineral density around an elastic press-fit socket in total hip arthroplasty: A prospective 2-year follow-up study using quantitative CT BMD measurements in 25 patients. *Acta Orthop.* **2016**, *87* (6), 583–588 DOI: 10.1080/17453674.2016.1237439.

(36) Weinans, H.; Huiskes, R. I. K. The Relationship Between Stress Shielding and Bone Resorption Around Total Hip Stems and the Effects of Flexible Materials. *Clin. Orthop. Relat. Res.* **1992**, *274* (January), 124–134 DOI: 10.1097/00003086-199201000-00014.

(37) Takai, E.; Costa, K. D.; Shaheen, A.; Hung, C. T.; Guo, X. E. Osteoblast Elastic Modulus Measured by Atomic Force Microscopy Is Substrate Dependent. *Ann. Biomed. Eng.* **2005**, *33* (7), 963–971 DOI: 10.1007/s10439-005-3555-3.

(38) Ford, A. J.; Rajagopalan, P. Measuring Cytoplasmic Stiffness of Fibroblasts as a Function of Location and Substrate Rigidity Using Atomic Force Microscopy. *ACS Biomater. Sci. Eng.* **2018**, *4* (12), 3974–3982 DOI: 10.1021/acsbiomaterials.8b01019.

(39) Lu, H. H.; Thomopoulos, S. Functional Attachment of Soft Tissues to Bone: Development, Healing, and Tissue Engineering. *Annu. Rev. Biomed. Eng.* **2013**, *15* (1), 201–226 DOI: 10.1146/annurev-bioeng-071910-124656.

(40) Das Murtey, M.; Ramasamy, P. Sample Preparations for Scanning Electron Microscopy - Life Sciences. In *Modern Electron Microscopy in Physical and Life Sciences*; Janecek, M., Kral, R., Eds.; Intech Open, 2016; Vol. 1, p 13.

4.4 Supplementary Material

Supplementary Fig. 4.1: Classic 3x2 Lego™ block design. Two blocks were made from decellularized apple hypanthium tissue and were stained with Congo Red (magenta) and Calcofluor White (cyan). Scale = 1.5 cm.

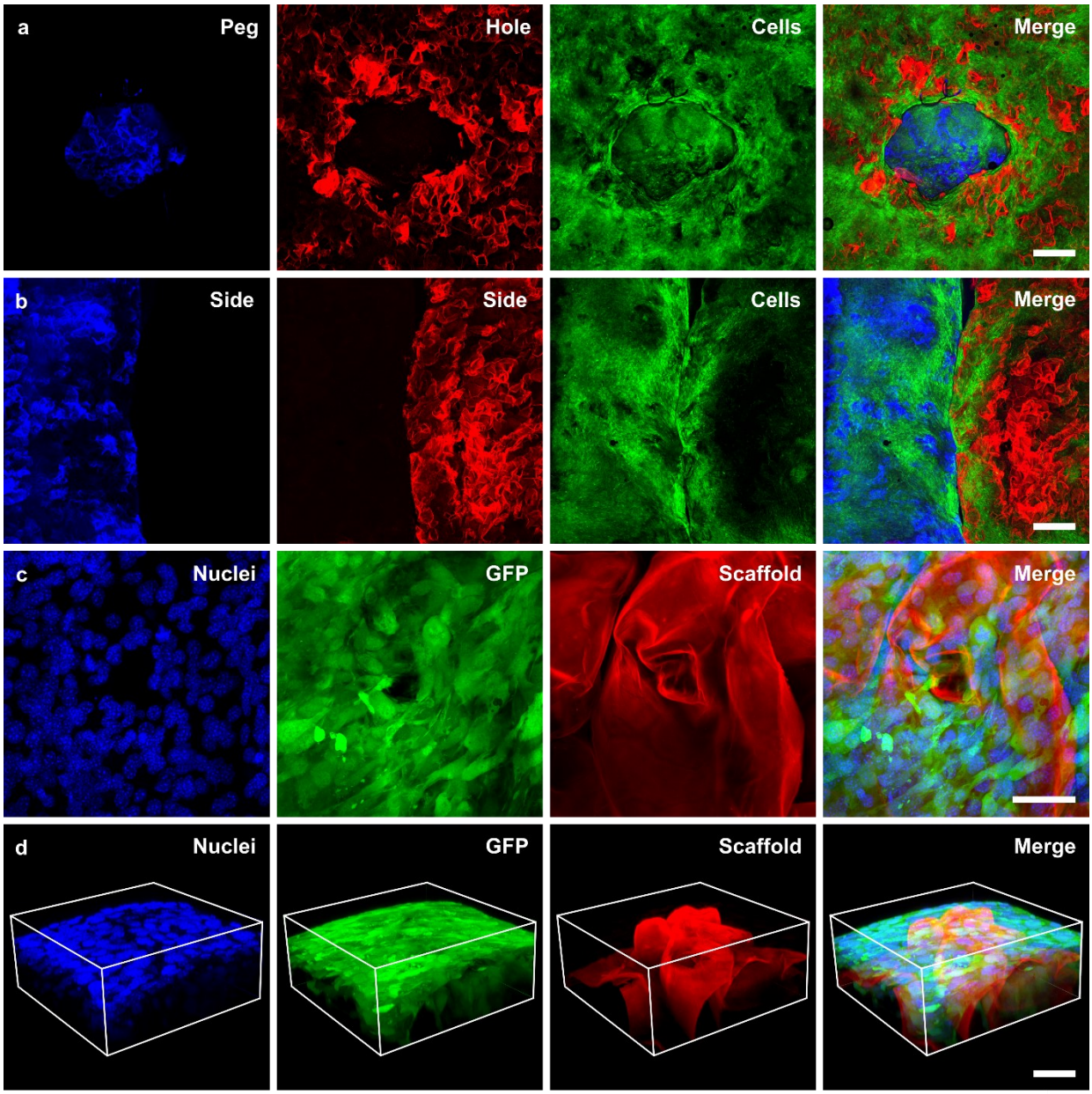

Supplementary Fig. 4.2: Maximum intensity z-projected confocal images of interlocked ETIs and fibroblasts. (a) Top view of interlocked peg (blue stained with Calcofluor white), hole (red stained with Congo Red), and GFP NIH 3T3 cells (green) on both subunits. **(b)** Side view of interlocked subunits. Subunit 1 (blue stained with Calcofluor white), subunit 2 (red stained with Congo Red), and GFP NIH 3T3 cells (green) on both subunits. Scale **(a,b)** = 500 μm. **(c)** Hoechst 33342 stained nuclei (blue), GFP NIH 3T3 cells (green), and scaffold stained with Congo Red (red). **(d)** 3D view of GFP NIH 3T3 cells on the cellulose-based scaffold. Blue = Hoechst 33342 stained nuclei, green = GFP, red = cellulose. Scale (**c,d**) = 50 μm.

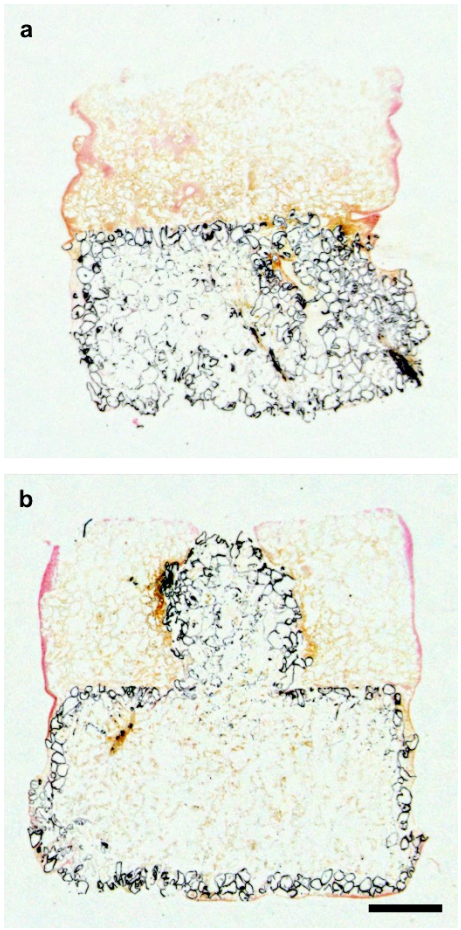

Supplementary Fig. 4.3: Von Kossa staining of in vitro bone-connective tissue ETI. (a) Cross-section of outer region of the interlocked composite. **(b)** Inner cross-section showing the peg and hole geometry of the stud and anti-stud subunits. Black = mineralized scaffold. Scale = 1 mm.

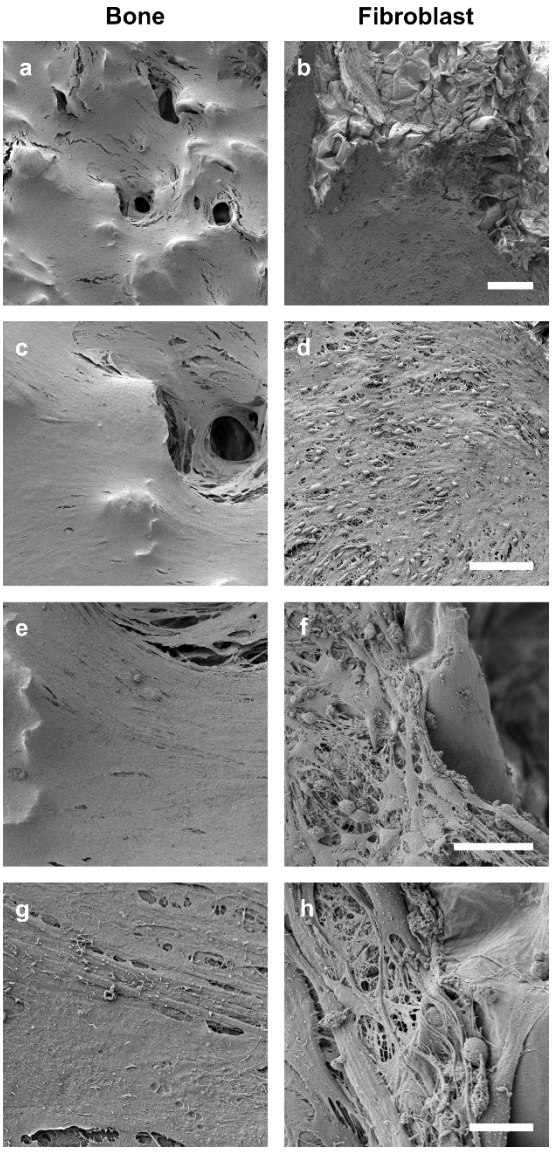

Supplementary Fig. 4.4: SEM of bone-connective tissue ETI. **(a,c,e,g)** MC 3T3 differentiated osteoblast seeded subunit. **(b,d,f,h)** NIH 3T3 fibroblast seeded subunit. Scale: **(a,b)** = 200 μm, **(c,d)** = 100 μm, **(e,f)** = 50 μm, **(g,h)** = 10 μm.

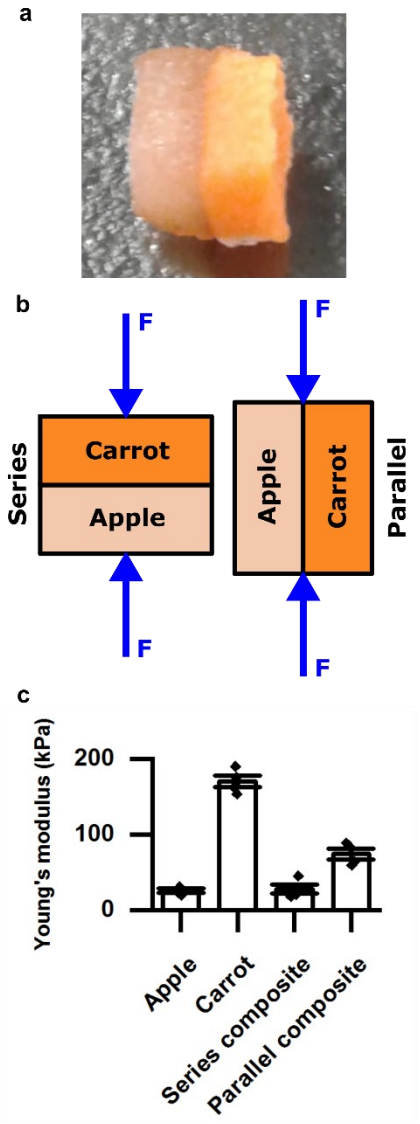

Supplementary Fig. 4.5: Stress shielding with different source materials. Apple and carrot-derived scaffolds were interlocked **(a)** and compressed in the series and parallel configurations **(b).** The effective Young's moduli for the materials and the isolated components **(c)**, N =4. The series and parallel composites were not statistically significantly different (P > 0.05) than the simplified model of two elastic rectangular prisms arranged in series $\left(\frac{1}{E_{mix}} = \frac{X_A}{E_A} + \frac{X_C}{E_C}\right)$ and parallel ($E_{mix} = X_A E_A + X_C E_C$) with individual moduli of the isolated apple and carrot components.

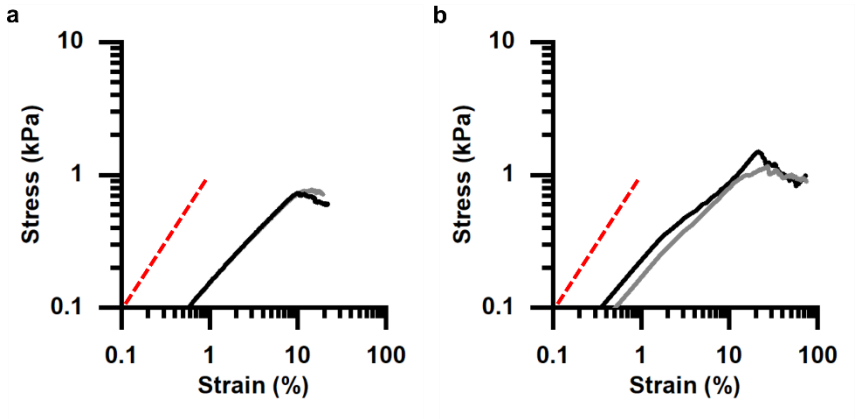

Supplementary Fig. 4.6: Repeat controlled steady shear rate testing. Controlled steady shear rate testing at a strain rate of **(a)** 0.001 s^{-1} and **(b)** 0.01 s^{-1}. The black curve is the initial measurement, and the grey curve depicts a repeat trial on the same sample after a 5 min incubation period. The red dashed line is provided as a guide for the linear regime. The slow shear resulted in a failure point that was not as abrupt as it allowed time for more viscous dissipation. Reversible power-law behavior is observed at low strains: $\sigma \sim \varepsilon^{y}$ with (a) $y = 0.72 \pm 0.02$ at 0.001 s^{-1} and (b) $y = 0.75 \pm 0.02$ at 0.01 s^{-1}.

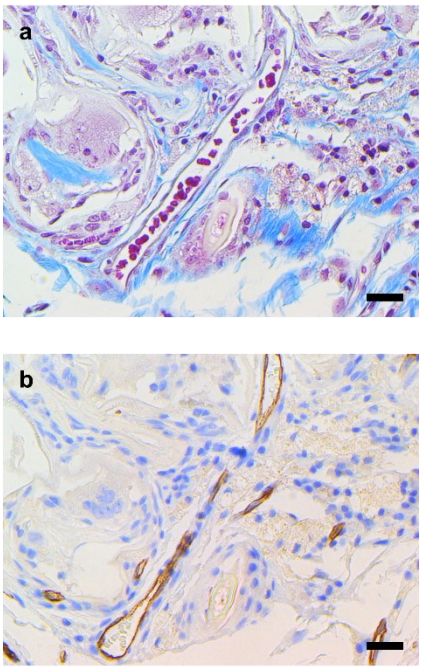

Supplementary Fig. 4.7: Angiogenesis in the biomaterials in vivo. (a) Masson's Trichrome staining showing red blood cells flowing through a large vessel inside the scaffold. **(b)** CD 31 staining for endothelial cells lining the blood vessel. Scale = 25 μm.

4.5 Materials and Methods

4.5.1 Scaffold production

A Shapeoko 3 CNC router with a 0.8 mm, 180° drill bit was used to carve McIntosh Red apples (Canada Fancy) into arrays of complementary stud and anti-stud geometries. Cutting was performed at a speed of 1 mm/s. A Mandolin slicer was then used to cut the arrays of the subunits to their desired thickness. The stud piece consisted of a 5 mm x 5 mm x 2mm base with a 2 mm cylindrical peg protruding from the center, and the anti-stud subunit had a 2 mm cylindrical hole in the center of the 5 mm x 5 mm x 2mm base. As done previously, the samples were transferred to a 0.1% SDS solution and decellularized for 48 h while being shaken at 180 RPM, then were washed three times with dH_2O. Following the washes, the subunits were incubated in 100 mM $CaCl_2$ for 24 h and were then washed three times with dH_2O to remove the salt residue. To sterilize the samples, a 70% ethanol incubation was performed, followed by three more wash cycles with dH_2O.

4.5.2 Cell culture

All cells were maintained at 37°C and 5% CO_2. NIH 3T3 fibroblast cells were cultured in Delbecco's Modified Eagle Medium – High Glucose (DMEM), supplemented with 10% fetal bovine serum and 1% penicillin/streptomycin (100 U/mL and 100 µg/mL respectively) (Hyclone Laboratories Inc.). Conversely, the MC 3T3 E1 Subcone 4 pre-osteoblast cells were culture in MEM-alpha supplemented with 10% fetal bovine serum and 1% penicillin/streptomycin (100 U/mL and 100 µg/mL respectively). In order to invoke differentiation of the pre-osteoblasts, 4 mM inorganic phosphate (Sigma) and 50 µg/mL ascorbic acid (Sigma) were added. For sub-culturing, cells cultured on cell culture plates were trypsinized and resuspended in the appropriate medium. The cells were counted and centrifuged in order to separate the cells from the trypsin and the media. The supernatant was aspirated, and the pellet containing $5x10^4$ cells was resuspended in fresh culture medium. The cells were seeded onto the biomaterial, and the cells were allowed to proliferate and invade the scaffold for 2 weeks prior to interlocking the complementary subunits. After 2 weeks, the subunits were manually clicked together using sterile tweezers by pressing down the stud subunit into the hole of the anti-stud piece. The culture media was replaced every day and the samples were transferred to new culture plates after 1 week of growth.

4.5.3 Confocal microscopy

The biomaterials were imaged with a Nikon TiE A1-R confocal microscope. The plant-derived scaffold was visualized with Calcofluor white staining (30 min, 1 µg/mL, Sigma) and Congo Red (30 min, 0.1 µg/mL, Sigma). Cell nuclei were stained with Hoechst 33342 (Invitrogen) (5 min incubation, 10 µg/mL). ImageJ (Fiji) was used to process the images; brightness/contrast settings were adjusted to maximize the fluorophore signal.

4.5.4 Alkaline phosphatase staining

Prior to fixation, the scaffolds were washed with PBS. They were then fixed for 90 s with 3.5 % paraformaldehyde and then washed with wash buffer (0.05% Tween in PBS). The BCIP-NBT SigmaFast^{TM}). During the staining, the samples were kept into the dark and were monitored. Once the staining was complete, the samples were washed and photographed.

4.5.5 Alizarin Red S staining

Alizarin Red S (Sigma) was prepared by adding 1 g of the powder to 45 mL of dH_2O. The pH was then adjusted to 4.3 with HCl and NaOH before raising the volume to 50 mL. Prior to staining, the samples were fixed as outlined above, except the duration of the fixation process was > 1h. The biomaterials were then washed with PBS. Calcium staining was performed with a 0.22 μm filtered Alizarin Red S stain pH 4.3 at a concentration of 200 mg/mL. The samples were submerged in the stain and incubated for 45 min. Following the calcium staining, the samples were thoroughly washed with dH_2O until the colour ceased to run out of the samples. The samples imaged shortly afterwards.

4.5.6 Cell migration assays

The confocal images of the GFP 3T3 cells were thresholded using the ImageJ (Fiji) adaptive threshold plugin, and the analyze particles plugin was used to measure the proliferation area on the adjacent scaffold. The data was normalized to the average scaffold area. The values presented are mean values ± the standard error of the mean (s.e.m.).

4.5.7 Compression and tension testing

The compressive Young's modulus and the maximum tensile stress were measured using the compression and tension modes of a custom built dynamic mechanical analysis (DMA) device and LabVIEW. During the compression tests, the material was compressed to a 10% strain, at a strain rate of 50 μm/s. The force-displacement curves were converted to stress-strain curves, and they were fitted in Origin 8.5 to calculate the Young's modulus. Likewise, the tensile measurements involved recording the minimum force required to separate the subunits at the same motor speed).

4.5.8 SEM and EDS

Samples were fixed with 3.5 % paraformaldehyde for 48 h and washed with PBS. The samples were serially dehydrated with ethanol as indicated in Intech Open's sample preparation guide[40]. The samples were dried with a samdri-PVT-3D critical point drier, and then gold-coated in a Hitachi E-1010 ion sputter. Scanning electron microscopy (SEM) and energy dispersive X-ray

spectroscopy (EDS) were performed on a JOEL JSM-7500F field emission SEM at the Centre for Advanced Materials Research (CAMaR) at the University of Ottawa. The SEM images were recorded at 3 kV, and the EDS spectra were recorded at 15 kV.

4.5.9 AFM

A Nanowizard II atomic force microscope (AFM) (JPK Instruments, Germany) was used to determine the substrate elasticity in all experiments. PNP-TR-50 cantilevers were used for each measurement and had an experimentally determined spring constant of 63.5 ± 7.2 mN/m. Force-indentation curves were acquired on substrates at 546 Hz with a set point of 1.0 nN. Substrate elasticity was calculated by fitting the force curves to the Sneddon-Hertz model for a conical indenter for shallow 200 nm indentations, assuming a Poisson ratio of 0.5 (PUNIAS 3D Software). For each substrate, N = 3 plates were prepared and 10 force curves were acquired at 25 random locations on the substrate for a total of 250 force curves.

4.5.10 Rheometry

An MCR 301 Anton Paar Rheometer was used to determine the shear properties of the materials. The samples were measured using a parallel-plate geometry with a circular 12 mm diameter. The samples were glued to the surface using Permabond Instant Adhesive 102 Medium Viscosity General Purpose Glue: a thin layer of the glue was evenly spread on the surface and the samples were gently pressed onto it and were incubated for 10 minutes prior to experimentation. Repeat runs of frequency sweeps revealed the samples were well adhered and did not slip. The samples were hydrated with CO_2 independent media (25 mM HEPES) to prevent the samples from drying and resulting changes to scaffold mechanical properties.

4.5.11 Animal surgeries and implantation

The subcutaneous implantation protocol was similar to what we have used previously. Briefly, immunocompetent rats were anesthetized using 2% Isoflurane USP-PPC (Pharmaceutical partners of Canada, Richmond, ON, Canada). ENDURE 400 Scrub-Stat4 Surgical Scrub (chlorhexidine gluconate, 4% solution; Ecolab Inc., Minnesota, USA) and Soluprep (2% w/v chlorhexidine and 70% v/v isopropyl alcohol; 3M Canada, London, ON, Canada) were used to prepare the shaved dorsal ventral area. Three 8 mm incisions were cut on the dorsal section of each rat, and a combined barren scaffold was placed in each incision. The incisions were then sutured using Surgipro II monofilament polypropylene 6–0 (Covidien, Massachusetts, USA). Transdermal bupivicaine 2% (as monohydrate; Chiron Compounding Pharmacy Inc., Guelph, ON, Canada) was topically applied to the surgery sites to prevent infection, and buprenorphine (0.03mg/ml; Chiron Compounding Pharmacy Inc. Guelph, ON, Canada) was administrated to alleviate pain. Animals were monitored and the sutures were removed after one week.

4.5.12 Scaffold resections

At 4 weeks post-implantation, the mice were euthanized using CO_2 inhalation and exsanguination via heart dissection. The dorsal skin was carefully resected and fixed in 10% formalin for at 72 h. The samples were then kept in 70% ethanol before being embedded in paraffin by the PALM Histology Core Facility of the University of Ottawa.

4.5.13 Histology

Serial 4 μm thick microtome sections starting at the edge of the cellulose scaffolds were cut at 100 μm levels. The sections were stained with Hematoxylin and Eosin (H&E) and Masson's Trichrome. For immunohistochemistry, the sections stained with Rabbit anti-CD45 (Abcam) or Rabbit anti-CD31 (Novus) were pre-treated using heat mediated antigen retrieval with a citrate buffer (pH 6.0, epitope retrieval solution 1) for 20 minutes. The sections were then incubated using a 1:1600 dilution (CD45) or 1:100 (CD31) for 30 minutes at room temperature and detected using an HRP conjugated compact polymer system. The slides were then stained with DAB as the chromogen, counterstained with Hematoxylin, mounted, and cover slipped.

4.5.14 Statistical analysis

For multiple samples, one-way and two-way ANOVA tests were used to assess the statistical differences for samples with one or two factors respectively. The Tukey post hoc analysis was used to determine the value of the statistical difference between the individual samples. In the cases where only two sets of data were compared, the Student's t-tests was used. All values presented are the mean ± the standard error of the mean (s.e.m.). Statistical significance refers to $P < 0.05$.

Chapter 5

Apple-derived Biomaterials are Viscoelastic Scaffolds – A Rheological Study

This chapter is a manuscript in preparation:

Hickey, R. J., Harden, J. L. & Pelling, A. E. Apple-derved biomaterials are viscoelastic scaffolds – A rheological study. Manuscript in preparation (2020).

§1 Motivation

Our previous work reveals that the decellularized plant-derived scaffolds have a Young's modulus that is comparable to that of various human tissues and cell types; moreover, as indicated in the introductory review chapter, specific plant candidates can be chosen to mimic particular structures in the body. Nevertheless, simple compression measurements fail to fully characterize the mechanical properties of these scaffolds. As such, an in-depth rheological investigation of these materials is required. In the body our tissues are subjected to complex shear forces in addition to simple tensile and compressive loads.

§2 Hypothesis and Objectives

The main objective of this study was to provide a more thorough mechanical characterization of our biomaterial. We hypothesize that these materials are viscoelastic materials that behave largely as elastic bodies.

5.1 Abstract

A mechanical investigation of plant-derived, cellulose-based biomaterials beyond simple compression has yet to be performed. The forces exerted on the tissues of the body are rarely purely compressive; however, the response of the material to shear is poorly understood. Here, we quantify the limits of the linear viscoelastic regime and characterize the yield point of the material. We show how these viscoelastic biomaterials are largely elastic bodies, and that the shear moduli of these constructs are biologically relevant. The soft compliant nature of these scaffolds results in the alteration of the rheological properties in the presence of mammalian cells. This timely rheometric study provides a preliminary material characterization to launch further investigations and serves as a platform to direct future tissue engineering endeavors.

5.2 Introduction

The physical environment affects many cellular processes including differentiation, migration, force generation, proliferation, spreading, alignment, and gene expression[1–4]. The interplay between the physical characteristics of the microenvironment and biochemical signaling is complex, and intense research has been dedicated to elucidating the mechanisms responsible for these phenomena[5]. A significant physical set of parameters that dictate cell fate and function are the mechanics of the cellular niche. An entire field has been dedicated to the integration of mechanical cues to intracellular signaling. Mechanosensing and mechanotransduction enable exogenous forces to be converted into endogenous biochemical responses[6,7].

There is a large body of evidence endorsing the transition from standard glass and plastic culture conditions to biomimetic constructs that more closely match the mechanical properties of the native environment of the cell[8]. As cells and tissues function differently on artificially stiff surfaces, this transition is necessary to gain a more accurate and complete understanding of how cells and tissues function in vivo. It is important to note that the use of substrates with vastly different mechanical properties does not only fail to capture the biologically relevant response of the process under scrutiny, but it may also misguide researchers as processes that would not normally occur can be elicited[9]. Moreover, mechanical matching with the surrounding environment has been shown to be integral for effective biomaterial design and performance[10–12].

In an attempt to develop a viable biomaterial platform, we have pioneered the use of decellularized plant tissue for mammalian cell culture and biomaterial design[13]. In this approach, the natural complexity of the cellulose and extracellular architecture of the plant material is exploited to yield a porous 3D scaffold. This class of biomaterial is biocompatible in vitro and in vivo, and significant research has been dedicated to the use of this platform for designing and studying new biomaterials[14–17]. Although simple tensile and compression measurements have been completed,

an in-depth rheological study has yet to be performed. The forces exerted on the cells and tissues in our bodies are rarely purely compressive or tensile. The vast majority of the forces involve a shear component as well; therefore, a more complete rheological investigation is necessary[18–20]. We hypothesize that these materials are viscoelastic. Cells and tissues are viscoelastic in nature as well, and we anticipate that mechanical profiling of the scaffolding material will advance the potential applications of this technology and guide future studies through the development of mechanobiomimetic materials. This report entails a rheological characterization of apple-derived, cellulose-based biomaterials.

5.3 Results

5.3.1 Cellulose scaffolds

The scaffolds used in this study were created with the same procedure as used previously, with one modification: the size of the samples was adjusted to match that of the tool for the rheometer. Using computer numerical controlled (CNC) milling, 12 mm disks of apple hypanthium tissue were carved and then cut to a thickness of 1.2 mm. The samples were then decellularized, processed, and sterilized; all samples, including the controls, were immersed in cell culture media. The cell laden scaffolds consisted of C2C12 myoblasts cells which grew extensively throughout the material as expected (Fig. 5.1).

5.3.2 Oscillatory strain sweeps and the linear viscoelastic region

The first characterization step when performing rheometry is usually a strain sweep to decipher where the linear viscoelastic region (LVR) lies. Refer to Chapter 2 for a brief discussion of linear viscoelasticity.

For a viscoelastic deformation, the shear modulus G dictates the relationship between the stress (σ) and strain (γ) and is defined as

$$\sigma(t) = \int_{-\infty}^{t} G(t - t')\dot{\gamma}(t')dt'.$$

Viscoelastic materials contain both viscous and elastic components. This proportional relationship is valid for small deformations. Beyond the LVR, the deformations exceed those required for the Cauchy strain tensor and nonlinearities arise. Measurements within the LVR allow material parameters to be calculated within the range of deformations that do not destroy the sample.

An oscillatory strain sweep carried out at an angular frequency of 1 Hz was used on the bare scaffolds (Fig. 5.2). It was found that the material did not display a completely linear region. (Fig.

5.2 and Supplementary Fig. 1). Nevertheless, for small strain amplitudes, the resultant curves were reproducible. This indicated that although the material was not behaving in an elastic manner for the small deformations tested, likely due to microfractures in the material, large scale material destruction did not occur in this regime.

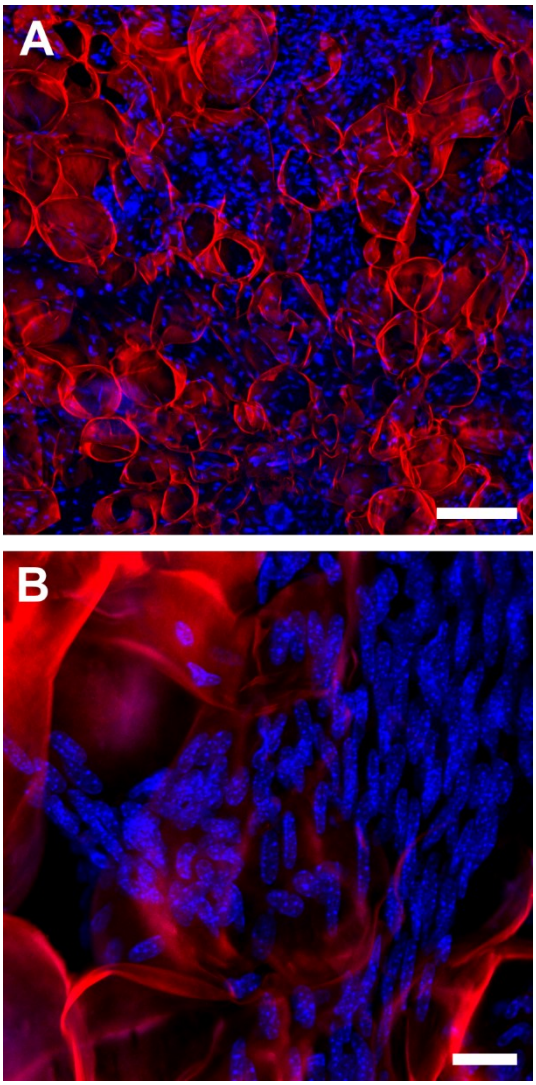

Figure. 5.1. Cell laden, plant-derived, cellulose scaffolds. The decellularized scaffolds were investigated as bare scaffolds and as cell-seeded biomaterials. The scaffold was stained with Congo Red, and the C2C12 myoblasts nuclei were stained with Hoechst 33342 to identify the mammalian cells. Scale = 200 μm (A), 25 μm (B).

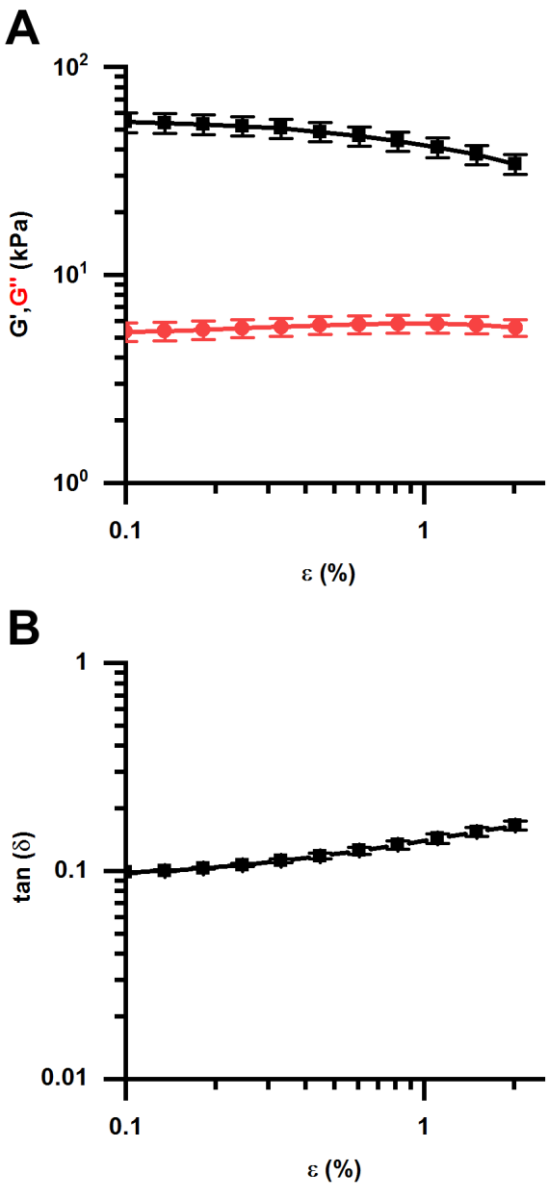

Figure 5.2. Linear viscoelastic region. An oscillatory strain sweep was used to investigate the presence of a LVR. (A) The storage (black) and loss (red) moduli of the bare scaffolds as a function of strain. (B) The loss factor as a function of strain. N = 10, values are mean and s.e.m.

5.3.3 Frequency dependence of the storage and loss moduli

The bare scaffolds were first characterized without cells to investigate the baseline mechanical properties of the material. An oscillatory frequency sweep experiment with a strain amplitude of 0.1% was performed to investigate the frequency dependence of the storage and loss moduli. In this case the shear strain and stress can be defined respectively as

$$\gamma(t) = \gamma_0 e^{i\omega t}$$
$$\sigma(t) = i\omega\gamma_0 \int_{-\infty}^{t} G(t-t')e^{i\omega t'}dt' \,,$$

and a simple variable change results in

$$\sigma(t) = i\omega\gamma_0 e^{i\omega t} \int_{0}^{\infty} G(u)e^{-i\omega u}du \,,$$

where γ is the shear strain, t is the time, ω is the angular frequency, σ is the shear stress, and G is the shear modulus. In this form, it is immediately clear that the shear modulus is a complex function; therefore, it can be expressed as

$$\sigma(t) = G^*(\omega)\gamma(t)$$
$$G^*(\omega) = G'(\omega) + iG"(\omega) \,.$$

The real part, *G'*, is referred to as the storage modulus, as it pertains to the ability to store elastic energy; the imaginary part *G"*, is the loss modulus, as it is the viscous dissipation contribution.

It was found that the plant-derived scaffold's moduli were affected by the frequency of oscillation (Fig. 5.3A). As complex shear modulus is a combination of the storage and loss moduli, both the elastic and viscous contributions could be assessed. The storage moduli ranged from 45 ± 3 kPa to 58 ± 4 kPa, while the loss moduli ranged from 5.5 ± 0.3 kPa to 5.9 ± 0.3 kPa (Fig. 3a). Clearly, as shown in Figure 5.3, the material is viscoelastic. The material primarily consists of a porous cellulose scaffold (elastic component) that is hydrated with cell culture media (viscous component). The oscillatory frequency sweep allowed the complex viscosity (η^*) to be investigated; it ranged from $4.5\text{x}10^5 \pm 3\text{x}10^4$ Pa s to $5.9\text{x}10^3 \pm 4\text{x}10^2$ Pa s (Fig. 5.3A). The complex viscosity is the sum of the dynamic viscosity (η') and the out of phase viscosity ($\eta"$), where they correspond to the real and imaginary parts respectively. The dynamic viscosity is the ratio of the loss modulus to the angular frequency and can be interpreted as the internal resistance to flow in the material.

$$\eta^*(\omega) = \eta'(\omega) - i\eta"(\omega)$$
$$\eta^*(\omega) = \frac{G^*(\omega)}{i\omega}$$
$$\eta' = G"/\omega$$
$$\eta" = G'/\omega$$

The viscoelastic nature of the material can be further evaluated by comparing the relative contribution of the elastic and viscous components. The loss factor $\tan(\delta) = G"/G'$ measures the ratio between the two components of the shear modulus (Fig. 5.3B). The results indicate that the elastic moduli were greater than the loss moduli for the frequency range investigated here, and the

material was viscoelastic with a dominating elastic response. The loss factor was nearly uniform and significantly below 1 for the range of frequencies measured.

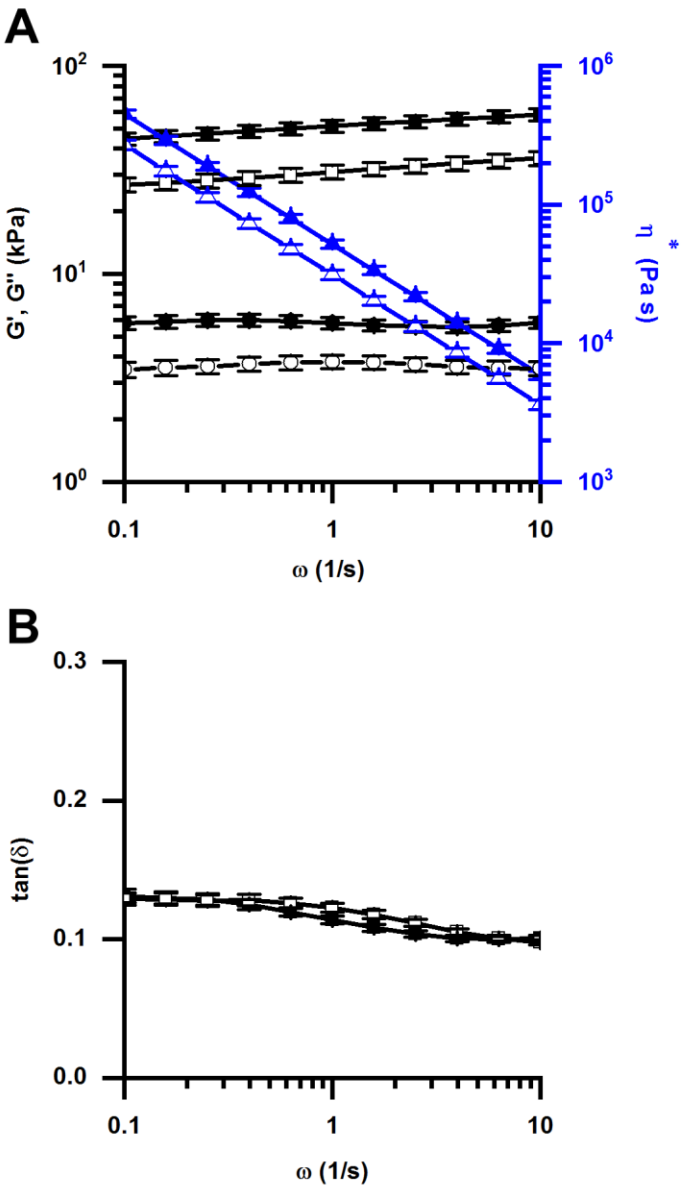

Figure 5.3. Frequency sweep. (A) An oscillatory frequency sweep was used to determine the frequency dependence of the storage (squares) and loss (circles) moduli as well as the complex viscosity (triangles). Both the bare scaffolds (shaded) and the cell laden constructs (hollow) were investigated. (B) The loss factor as a function of frequency. N = 10, values are mean and s.e.m.

5.3.4 The effect of cells on the shear moduli and viscosity

Next, the shear moduli and viscosity measurements were repeated for scaffolds that had been loaded with C2C12 myoblast cells. The frequency sweeps revealed that the presence of cells significantly reduced the apparent moduli (Fig. 5.3A). Interestingly, the loss factor remained fairly stable regardless of the addition of the cells (Fig. 5.3B). The loss factor is more instructive as it shows that the ratio between the viscous and elastic components is the same for both the cell laden and unadorned scaffolds. The most probable explanation for the moduli reduction is that the cells interfered with the adherence to the tool surface. Reduced adherence can lead to slip and a reduction in the torque values. The loss factor also demonstrates that the materials are solid-like with some imperfections stemming from the low viscosity media.

5.3.5 Step stress and biomaterial ringing

As shown, both the bare scaffold and the cell infiltrated scaffolds are viscoelastic materials. An interesting property of such materials is the phenomenon of hydrogel ringing. Normally, rheology takes the overdamped limit. However, it is possible to probe the transient regime as well. This phenomenon, the ringing, stems from the fact that the material is not perfectly elastic. A perfectly elastic body subjected to a sudden force or torque would oscillate forever, but when small viscous elements are included, the strain oscillates about its equilibrium value, analogous to overshooting and overcompensating around a target value. In other words, the viscous components damp the elastic oscillations. The higher the ratio between the elastic and viscous components, the greater the "ringing". An increased viscous component leads to more damping, so the oscillations are not as noticeable. The relative contributions affect both the amplitude period of the ringing. In essence the ringing is a property that pertains to the relative contributions of the elastic and viscous character of the material, and the ringing is highly sensitive to changes in viscosity. In order to assess the response of the material to a sudden step strain, a constant shear stress was applied and the resultant strain response was recorded (Fig. 5.4 and Supplementary Fig. 5.2). Normally, viscoelastic materials are too damped to observe this process, but as the highly elastic body used here contained fluid that moved in and out of the porous scaffold, the material exhibited oscillations on short timescales before stabilizing (Fig. 5.4 and Supplementary Fig. 5.2). Creep was observed to a minor extent on longer timescales (Supplementary Fig. 5.2) as the viscous and elastic regimes dominate at short and long timescales respectively.

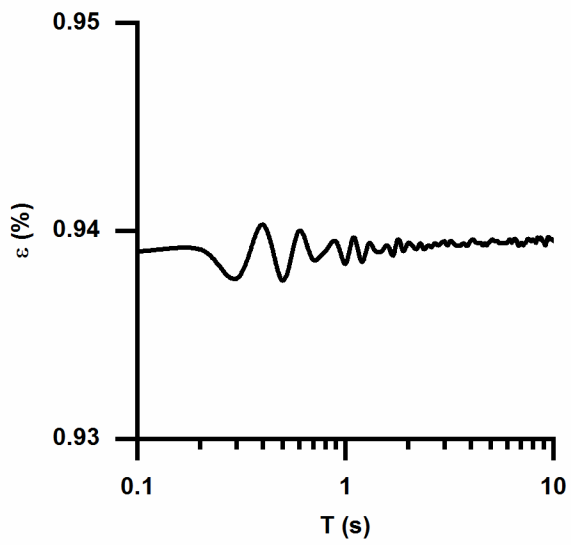

Figure 5.4. Step-stress ringing. A step-stress experiment was conducted at 1 Pa. Ringing was observed as the strain oscillated around an equilibrium that experienced a minor degree of creep. N = 10, values are mean and s.e.m.

5.3.6 Continuous shear strain

Another important characterization is the relationship of the shear stresses and strains in a continuous, rather than oscillatory, mode where the strain rate was held at a constant rate of $1x10^{-3}$ s^{-1}. Moreover, the extension into the nonlinear viscoelastic regime and mechanical breakdown of the material was included (Fig. 5.5). As shown in Figure 5.5, the stress increases, but then strain softening is observed. After considerable deformation, close to the extension limit of the material, strain hardening is observed until failure occurred. The red dashed line is presented as a guide for deviations from linearity (power law = 1). At a strain of 45 % the biomaterial reached its yield stress of 4 kPa (Fig. 5.5).

5.4 Discussion

The use of plant-derived cellulose-based biomaterials is becoming increasingly widespread and is an established platform for biomaterial design[21]. Preliminary investigations employing uniaxial compression and tension revealed that the stiffnesses of these materials is within the biologically relevant regime[21]. Although the results from these studies are promising, a more rigorous rheological investigation is required in order to develop a deeper understanding of the mechanics of these materials. It is well known that the mechanical properties of the microenvironment play

key roles in cell biology. Moreover, injured and diseased tissues often display altered mechanical profiles; even healthy cells invading the abnormal site will function differently than in their native environment [22]. A simple example is the formation of scar tissue, which has vastly different elasticities than the surrounding tissue, and can lead to impaired functionality[23].

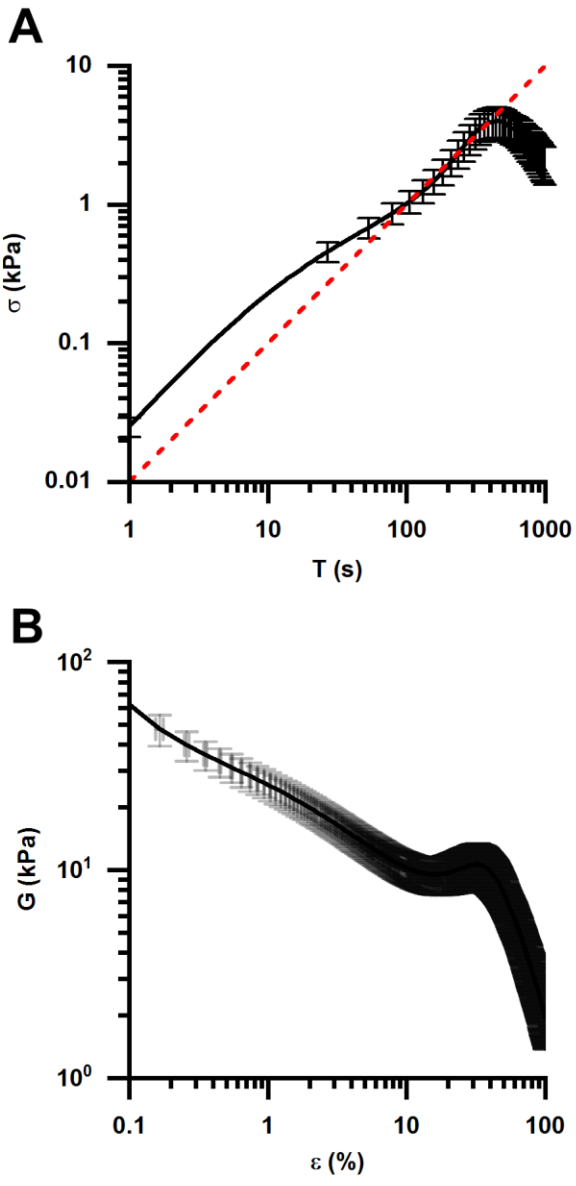

Figure 5.5 Continuous shear. A continuous shear experiment was performed at a constant strain rate of $1x10^{-3}$ s^{-1}. (A) The shear stress (black) as a function of time. The red dashed line is provided as a reference (linear). (B) the relaxation modulus as a function of strain during the constant strain rate experiment. N = 10, values are mean and s.e.m.

Cells and tissues are viscoelastic materials; therefore, a biomaterial designed for in vitro modeling or in vivo implantation should share the same viscoelastic properties. Our apple-derived constructs consist of a hydrated cellulose-based scaffold. As expected, these two components contribute to both elastic and viscous character; hence, the material is viscoelastic. The congruency of the cellulose-based, plant-derived material and several natural tissues reinforces the suitability of this class of material for tissue engineering[24].

The oscillatory frequency sweeps used in this study are pertinent to the frequencies of oscillations regularly experienced by the tissues in our bodies[23]; consequently, the range of values of the storage and loss moduli can be compared to those of natural tissues[25–27]. The frequency dependence of the shear moduli results in different material responses in difference scenarios. This phenomenon is a common occurrence in the body and it essential for proper tissue function[28]. Another important factor to be considered is the loss factor: the relative contribution of the storage and loss moduli, which correspond to the elastic and viscous components respectively. It is critical that the internal friction within the material in addition to the elastic character match that of the native tissue. The internal friction and viscosity affect many processes such as energy dissipation, flow type, and diffusion, all of which are variables that alter cell fate and function[29].

Interestingly, the moduli of the cell-laden constructs were less than those of the bare scaffold. As the presence of the cells may have interfered with the contact and adhesion of the scaffold to the tool, it is plausible that slip could occur, or a reduced effective area could lead to the apparent reduction in the moduli. As cells are viscoelastic materials as well, and they modulate the effective porosity of the scaffold, it was hypothesized that the presence of cells would result in a biomaterial with different storage and loss moduli. In this report we demonstrate how the presence of myoblasts reduced the storage and loss moduli. However, when investigating the loss factor, it is clear that the ratio between the two moduli remains the same with or without cells. This important result suggests that the shift in the moduli is due to the disruption of the adherence since the ratio of the moduli is the same in both conditions. Another potential effect is the role of the pH of the highly proliferative cell population on and in the biomaterial[30–32].

The relative contributions of the elastic and viscous components resulted in the presence of hydrogel ringing on short timescales in response to a step stress. Although the ringing has limited implications on macroscopic tissue function, it highlights the fact that minute differences in the rheological properties of the material can result in unique phenomena; therefore, slight mechanical mismatch between the biomaterial and the surrounding native tissue may lead to impaired tissue performance. It is commonplace to consider the elastic modulus of the material of interest; however, the viscoelastic properties of the biomaterial should not be ignored and plays an important role in biomaterial function[33].

A direct consequence of the materials falling within the mechanical profiles of soft human tissues, is that the scaffolds can be designed and adapted to fit a variety of applications. Future investigations will focus on specialized differentiated tissues such as bone, cartilage, tendons, and ligaments; these tissues involve matrix and mineral depositions that drastically affect the stiffness of the material. An in-depth rheological characterization with additional fatigue testing will assess long term viability of these materials as well as establish a more complete mechanical profile. This study presents a preliminary rheometric analysis of plant-derived, cellulose-based biomaterials beyond simple compression and tensile characterization.

5.5 Materials and methods

5.5.1 Scaffold production

Disks of apple (McIntosh - Canada Fancy) hypanthium tissue with a 12 mm diameter and a thickness of 1.2 mm were carved with a Shapeoko 3 CNC router. A 1 mm, 180° drill bit was used at a speed of 1 mm/s. The thickness was specified by a Mandolin slicer. As done previously, decellularization was accomplished with a 0.1% SDS solution incubation for 48 h while being shaken at 180 RPM. The samples were washed in triplicate with sterile dH_2O and then immersed in 100 mM $CaCl_2$ for 24 h. After another round of washing with dH_2O to remove the salt residue, a 70% ethanol sterilization solution was added, which was followed by three more wash cycles with dH_2O.

5.5.2 Cell culture

C2C12 myoblast cells were cultured in Delbecco's Modified Eagle Medium – High Glucose (DMEM), supplemented with 10% characterized fetal bovine serum (Hyclone) and 1% penicillin/streptomycin (100 U/mL and 100 µg/mL respectively) (Hyclone). The cultures were maintained at 37°C and 5% CO_2 prior to experimentation. During rheometric experiments, the media was supplemented with 25 mM HEPES to render the media CO_2 independent over the mechanical testing period. Sub-culturing occurred on cell culture plates and was accomplished with trypsinization (Hyclone). Cell seeding on the scaffolds was performed by pipetting $5x10^4$ cells onto the decellularized cellulose-based material. Seeding rounds were replicated three times in three-day intervals. The cells proliferated on the scaffolds for 3 weeks prior to experimentation. The culture media was replaced every day and the samples were transferred to new culture plates after 1 week of growth.

5.5.3 Confocal microscopy

Maximum intensity z-projections were obtained by taking z-stacked images with a Nikon TiE A1-R confocal microscope. The cells were visualized with nuclear staining. Cell nuclei were stained

with Hoechst 33342 (Invitrogen) (5 min incubation, 10 µg/mL). The decellularized apple scaffold was stained with Congo red (30 min, 0.1 µg/mL, Sigma). ImageJ (Fiji) was used to process the images; brightness/contrast settings were adjusted to maximize the fluorophore signal.

5.5.4 Rheometry

Rheometry was performed on an MCR 301 Anton Paar Rheometer. A parallel-plate geometry with a circular 12 mm diameter was used. Slip was prevented by gluing the samples to the surface of the plate with Permabond Instant Adhesive 102 Medium Viscosity General Purpose Glue. After the glue was applied, the samples were gently pressed onto it and were incubated for 10 minutes prior to experimentation. Repeat runs of frequency sweeps within the linear viscoelastic regime (LVR) revealed the samples were well adhered and did not slip. CO_2 independent media (complete cell culture media supplemented with 25 mM HEPES) was pipetted on the periphery of the scaffold to prevent the samples from drying after the samples had adhered to the plates. Oscillatory strain (amplitude) sweeps were conducted at 1 Hz. Frequency sweeps were performed at a strain amplitude of 0.1%. Step-stress tests were carried out at 1, 5, and 10 Pa. In continuous shear mode, the samples were sheared at a constant rate of $1x10^{-3}$ s^{-1}.

5.6 References

(1) Liu, K.; Mihaila, S. M.; Rowan, A.; Oosterwijk, E.; Kouwer, P. H. J. Synthetic Extracellular Matrices with Nonlinear Elasticity Regulate Cellular Organization. *Biomacromolecules* **2019**, *20* (2), 826–834 DOI: 10.1021/acs.biomac.8b01445.

(2) Toyjanova, J.; Hannen, E.; Bar-Kochba, E.; Darling, E. M.; Henann, D. L.; Franck, C. 3D Viscoelastic traction force microscopy. *Soft Matter* **2014**, *10* (40), 8095–8106 DOI: 10.1039/c4sm01271b.

(3) Rens, E. G.; Merks, R. M. H. Cell Shape and Durotaxis Follow from Mechanical Cell-Substrate Reciprocity and Focal Adhesion Dynamics: A Unifying Mathematical Model. **2019**.

(4) Hwang, J. H.; Han, U.; Yang, M.; Choi, Y.; Choi, J.; Lee, J. M.; Jung, H. S.; Hong, J.; Hong, J. H. Artificial cellular nano-environment composed of collagen-based nanofilm promotes osteogenic differentiation of mesenchymal stem cells. *Acta Biomater.* **2019**, *86*, 247–256 DOI: 10.1016/j.actbio.2018.12.044.

(5) Gasiorowski, J. Z.; Murphy, C. J.; Nealey, P. F. Biophysical Cues and Cell Behavior: The Big Impact of Little Things. *Annu. Rev. Biomed. Eng.* **2013**, *15* (1), 155–176 DOI: 10.1146/annurev-bioeng-071811-150021.

(6) Ohashi, K.; Fujiwara, S.; Mizuno, K. JB Review Roles of the cytoskeleton, cell adhesion and rho signalling in mechanosensing and mechanotransduction. *J.Biochem.* **2017**, *161*

(3), 245–254 DOI: 10.1093/jb/mvw082.

(7) Isermann, P.; Lammerding, J. Nuclear mechanics and mechanotransduction in health and disease. *Current Biology*. 2013.

(8) Duval, K.; Grover, H.; Han, L. H.; Mou, Y.; Pegoraro, A. F.; Fredberg, J.; Chen, Z. Modeling physiological events in 2D vs. 3D cell culture. *Physiology*. American Physiological Society June 14, 2017, pp 266–277.

(9) Hickey, R.; Pelling, A. E. The rotation of mouse myoblast nuclei is dependent on substrate elasticity. *Cytoskeleton* **2017**, *74* (4), 184–194 DOI: 10.1002/cm.21357.

(10) Weinans, H.; Huiskes, R. I. K. The Relationship Between Stress Shielding and Bone Resorption Around Total Hip Stems and the Effects of Flexible Materials. *Clin. Orthop. Relat. Res.* **1992**, *274* (January), 124–134 DOI: 10.1097/00003086-199201000-00014.

(11) Pakvis, D. F. M.; Heesterbeek, P. J. C.; Severens, M.; Spruit, M. Cancellous and cortical bone mineral density around an elastic press-fit socket in total hip arthroplasty: A prospective 2-year follow-up study using quantitative CT BMD measurements in 25 patients. *Acta Orthop.* **2016**, *87* (6), 583–588 DOI: 10.1080/17453674.2016.1237439.

(12) Jaalouk, D. E.; Lammerding, J. Mechanotransduction gone awry. *Nat. Rev. Mol. Cell Biol.* **2009**, *10* (1), 63–73 DOI: 10.1038/nrm2597.

(13) Modulevsky, D. J.; Lefebvre, C.; Haase, K.; Al-Rekabi, Z.; Pelling, A. E. Apple derived cellulose scaffolds for 3D mammalian cell culture. *PLoS One* **2014**, *9* (5) DOI: 10.1371/journal.pone.0097835.

(14) Modulevsky, D. J.; Cuerrier, C. M.; Pelling, A. E. Biocompatibility of Subcutaneously Implanted Plant-Derived Cellulose Biomaterials. *PLoS One* **2016**, *11* (6), 1–19 DOI: 10.1371/journal.pone.0157894.

(15) Gershlak, J.; Hernandez, S.; Fontana, G.; Perreault, L.; Hansen, K.; Larson, S.; Binder, B.; Dolivo, D.; Yang, T.; Dominko, T.; et al. Crossing kingdoms: Using decellularized plants as perfusable tissue engineering scaffolds. *Biomaterials* **2017**, *125*, 13–22 DOI: 10.1016/j.biomaterials.2017.02.011.

(16) Fontana, G.; Gershlak, J.; Adamski, M.; Lee, J.-S.; Matsumoto, S.; Le, H. D.; Binder, B.; Wirth, J.; Gaudette, G.; Murphy, W. L. Biofunctionalized Plants as Diverse Biomaterials for Human Cell Culture. *Adv. Healthc. Mater.* **2017**, 1601225 DOI: 10.1002/adhm.201601225.

(17) Hickey, R. J.; Modulevsky, D. J.; Cuerrier, C. M.; Pelling, A. E. Customizing the Shape and Microenvironment Biochemistry of Biocompatible Macroscopic Plant-Derived Cellulose Scaffolds. *ACS Biomater. Sci. Eng.* **2018**, *4*, 3726–3736 DOI: 10.1021/acsbiomaterials.8b00178.

(18) Cheng, S.; Clarke, E. C.; Bilston, L. E. Rheological properties of the tissues of the central nervous system: A review. *Med. Eng. Phys.* **2008**, *30*, 1318–1337 DOI: 10.1016/j.medengphy.2008.06.003.

(19) Blehm, B. H.; Devine, A.; Staunton, J. R.; Tanner, K. In vivo tissue has non-linear rheological behavior distinct from 3D biomimetic hydrogels, as determined by AMOTIV microscopy. *Biomaterials* **2016**, *83*, 66–78 DOI: 10.1016/j.biomaterials.2015.12.019.

(20) Deffieux, T.; Montaldo, G.; Tanter, M.; Fink, M. Shear wave spectroscopy for in vivo quantification of human soft tissues visco-elasticity. *IEEE Trans. Med. Imaging* **2009**, *28* (3), 313–322 DOI: 10.1109/TMI.2008.925077.

(21) Hickey, R. J.; Pelling, A. E. Cellulose Biomaterials for Tissue Engineering. *Front Bioeng Biotechnol.* **2019**, *7* (45), 1–15 DOI: 10.3389/fbioe.2019.00045.

(22) Swartz, M. A.; Lund, A. W. Lymphatic and interstitial flow in the tumour microenvironment: Linking mechanobiology with immunity. *Nature Reviews Cancer*. March 2012, pp 210–219.

(23) Klimesch, W. The frequency architecture of brain and brain body oscillations: an analysis. *European Journal of Neuroscience*. Blackwell Publishing Ltd October 1, 2018, pp 2431–2453.

(24) Yoo, L.; Gupta, V.; Lee, C.; Kavehpore, P.; Demer, J. L. Viscoelastic properties of bovine orbital connective tissue and fat: Constitutive models. *Biomech. Model. Mechanobiol.* **2011**, *10* (6), 901–914 DOI: 10.1007/s10237-010-0281-z.

(25) Liu, Z.; Bilston, L. On the viscoelastic character of liver tissue: Experiments and modelling of the linear behaviour. *Biorheology* **2000**, *37* (3), 191–201.

(26) Krouskop, T. A.; Wheeler, T. M.; Kallel, F.; Garra, B. S.; Hall, T. Elastic Moduli of Breast and Prostate Tissues Under Compression . *Ultrason. Imaging* **1998**, *20*, 260–274.

(27) Kiss, M. Z.; Varghese, T.; Hall, T. J. Viscoelastic characterization of in vitro canine tissue. *Phys Med Biol* **2004**, *49* (18), 4207–4218.

(28) Huang, D.; Huang, Y.; Xiao, Y.; Yang, X.; Lin, H.; Feng, G.; Zhu, X.; Zhang, X. Viscoelasticity in natural tissues and engineered scaffolds for tissue reconstruction. *Acta Biomater.* **2019**, *97*, 74–92 DOI: 10.1016/j.actbio.2019.08.013.

(29) Pereira, D. R.; Silva-Correia, J.; Oliveira, J. M.; Reis, R. L.; Pandit, A.; Biggs, M. J. Nanocellulose reinforced gellan-gum hydrogels as potential biological substitutes for annulus fibrosus tissue regeneration. *Nanomedicine Nanotechnology, Biol. Med.* **2018**, *14*, 897–908 DOI: 10.1016/j.nano.2017.11.011.

(30) Pometto Iii, A. L.; Crawford, D. L. Effects of pH on Lignin and Cellulose Degradation by Streptomyces viridosporust. *Appl. Environ. Microbiol.* **1986**, *52* (2), 246–250.

(31) Österberg, M.; Claesson, P. M. Interactions between cellulose surfaces: effect of solution pH. *J. Adhes. Sci. Technol* **2000**, *14* (5), 603–618.

(32) Jones, E. M.; Cochrane, C. A.; Percival, S. L. The Effect of pH on the Extracellular Matrix and Biofilms. *Adv. Wound Care* **2015**, *4* (7), 431–439 DOI: 10.1089/wound.2014.0538.

(33) Lv, S.; Dudek, D. M.; Cao, Y.; Balamurali, M. M.; Gosline, J.; Li, H. Designed biomaterials to mimic the mechanical properties of muscles. *Nature* **2010**, *465*, 69–73 DOI: 10.1038/nature09024.

5.7 Supplementary Figures

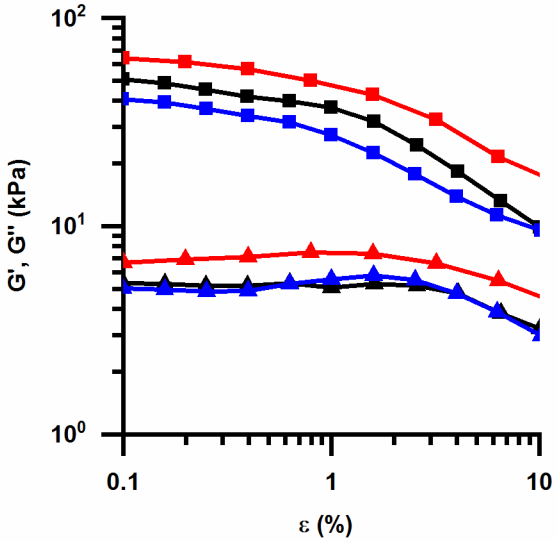

Figure S5.1. Amplitude sweep. An oscillatory strain sweep was used to determine if there was a LVR. The storage (squares) and loss (triangles) moduli of the bare scaffolds were measured as a function of strain. N = 3.

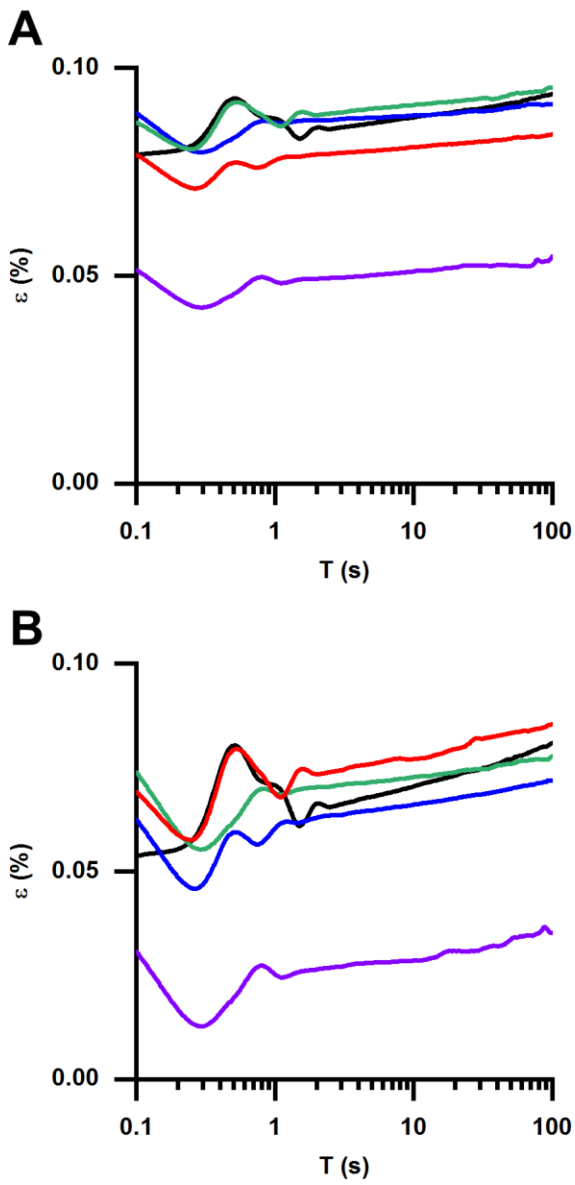

Figure S5.2. Creep. A step-stress experiment was conducted at (A) 5 Pa and (B) 10 Pa. Ringing was observed on short time scales, and creep occurred on longer time scales. N = 5.

Chapter 6

Cellular Nuclear Rotation on Soft 3D Scaffolds

This chapter is a short report manuscript in preparation:

Hickey, R. J. & Pelling, A. E. Cellular nuclear rotation on soft 3D scaffolds (2020).

§ 1 Motivation

The phenomenon of nuclear rotation has been observed for several decades; however, its functional role, if any, remains unknown. In our previous study published in Cytoskeleton[1], which is included as an Appendix, we revealed another layer of complexity to this process: nuclear rotation is dependent on the elasticity of 2D substrates. The substrate stiffness dependence in 2D was elucidated with a series of experiments conducted on traditional gelatin hydrogels with a physiologically relevant elastic modulus and compared to those performed on glass coverslips. We found that the rotation was drastically reduced on soft substrates that mimic soft tissue stiffnesses. Moreover, we confirmed that this process was dependent on microtubules rather than the actin network. We also reported a correlation between the rotation and the organization of the intermediate filaments. It was previously shown that vimentin slows rotation[2], and in a separate study the solubility of vimentin differed on different stiffnesses[3]. We integrated the two studies and presented the correlation as an avenue for future investigation in addition to differences in microtubule dynamics[4,5].

This earlier work (which was unrelated to cellulose biomaterials) highlighted the need to transition to soft 3D environments for investigating cellular processes and was a personal motivator for the development of the 3D scaffolds presented in this thesis. A direct consequence of our 2D substrate dependent nuclear rotation results is that stiff, noncompliant environments do not only fail to elicit a normal cellular response, but can also evoke other processes that would not normally occur. Therefore, as an extension of our original nuclear rotation experiment, I wanted to investigate effects of soft 3D environments on cellular rotation. This work highlights that plant-based, cellulose-derived biomaterials can be used as tools to investigate fundamental intracellular processes in addition to tissue engineering applications, which are highlighted in the previous chapters.

§ 2 Hypothesis and Objectives

I hypothesized that the nature of the rotation would change when the dimensionality of the system is altered. The objective was to gain an understanding of the dynamics of this process in a more biologically relevant environment.

6.1 Introduction

Nuclear rotation has been observed for decades; nevertheless, its biological significance remains unclear[6–10]. The rotation is primarily driven by microtubules and their associated motor proteins, and the current model for the mechanism is an imbalance of force applied to the nucleus as a result of dynamic instability of microtubules[2,11–15]. As this model suggests, the motion of the nucleus behaves as a persistent random walk[15]. Despite significant insights into the mechanism of this phenomenon, it is still unknown whether this process serves a particular biological function or is simply a by-product of the force imbalance stemming from parallel processes. Nuclear rotation has been observed in many different cell types and has been well characterized under standard cell culture techniques [6,7,10,12,14].

We have contributed another layer of complexity to this problem: nuclear rotation is dependent on substrate elasticity[1]. Despite the majority of experiments revealing that the phenomenon is microtubule-based and independent of actin, retrograde actin flow has been shown to be the driving factor in certain instances wherein the cells where confined to particular geometries[16]. Cell confinement can move the centrosome unnaturally close to the nuclear and suppress microtubule-based nuclear movement[15]. Therefore, not only does the location of the centrosome, as evidenced by confinement studies, affect nuclear rotation, but the mechanical environment does as well. Previous investigations have shown that intermediate filaments play an inhibitory role in governing nuclear movement, and we have shown a correlation between the location of the intermediate filament network and rotation on different substrate elasticities[1,2]. Moreover, the reduction of microtubule dynamics resulted in a basal level of rotation that was comparable to that of the diminished rotation on soft matrices, so it is hypothesized that alterations in microtubule dynamics may also be a significant factor in substrate elasticity dependent rotation. Clearly, the process of nuclear rotation is not fully understood, and the surrounding environment plays a significant role.

Recently, it was discovered that nuclear rotation occurs in mouse oocytes in vivo, and that this process is mediated by dynein and is mechanosensitive[17]. Consistent with our in vitro results, more compliant microenvironments lead to a decrease in the speed and velocity of rotation[1,17]. The study reports a correlation between the dormant state of the oocyte, nuclear localization of FOXO3, and nuclear rotation[17]. What is immediately clear is that further research is required to elucidate the

complete picture of this enigmatic process. As our research shows the physical environment dictates the nature of the rotation, and this process has been confirmed in vivo, we sought to further characterize nuclear rotation in soft, 3-dimensional (3D) environments. We have established a platform for tissue engineering that uses plant-derived, cellulose-based, decellularized scaffolds with rheological properties within the range of those of soft tissues and cells (See Chapter 5)[18]. It was hypothesized that alterations in the rotation dynamics of the nucleus would manifest in these milieus. In this preliminary characterization, we highlight how our novel biomaterials can be used as tools to study cellular phenomena in addition to providing scaffolding for tissue engineering purposes.

6.2 Results and Discussion

6.2.1 Creating the compliant 3D environment

In order to create a more biologically relevant environment to study the phenomenon of nuclear rotation, we exploited our novel cellulose-based, plant-derived biomaterials, as these constructs have been shown to be biocompatible in vitro and in vivo[18–20]. The scaffolds used here were prepared as in our previous biocompatibility and tissue engineering studies[18]. Cells grew extensively in the biomaterials and were organized in a 3D cellular matrix (Fig. 6.1 and Fig. S6.1). The apple-derived scaffolds were previously shown to have rheological properties that matched that of soft tissues and cells (See Chapter 5)[18]. As such, the effect of the dimensionality of the system could be investigated by transitioning to 3D environments endowed by our decellularized biomaterials in comparison to the 2D gelatin substrate we used previously.

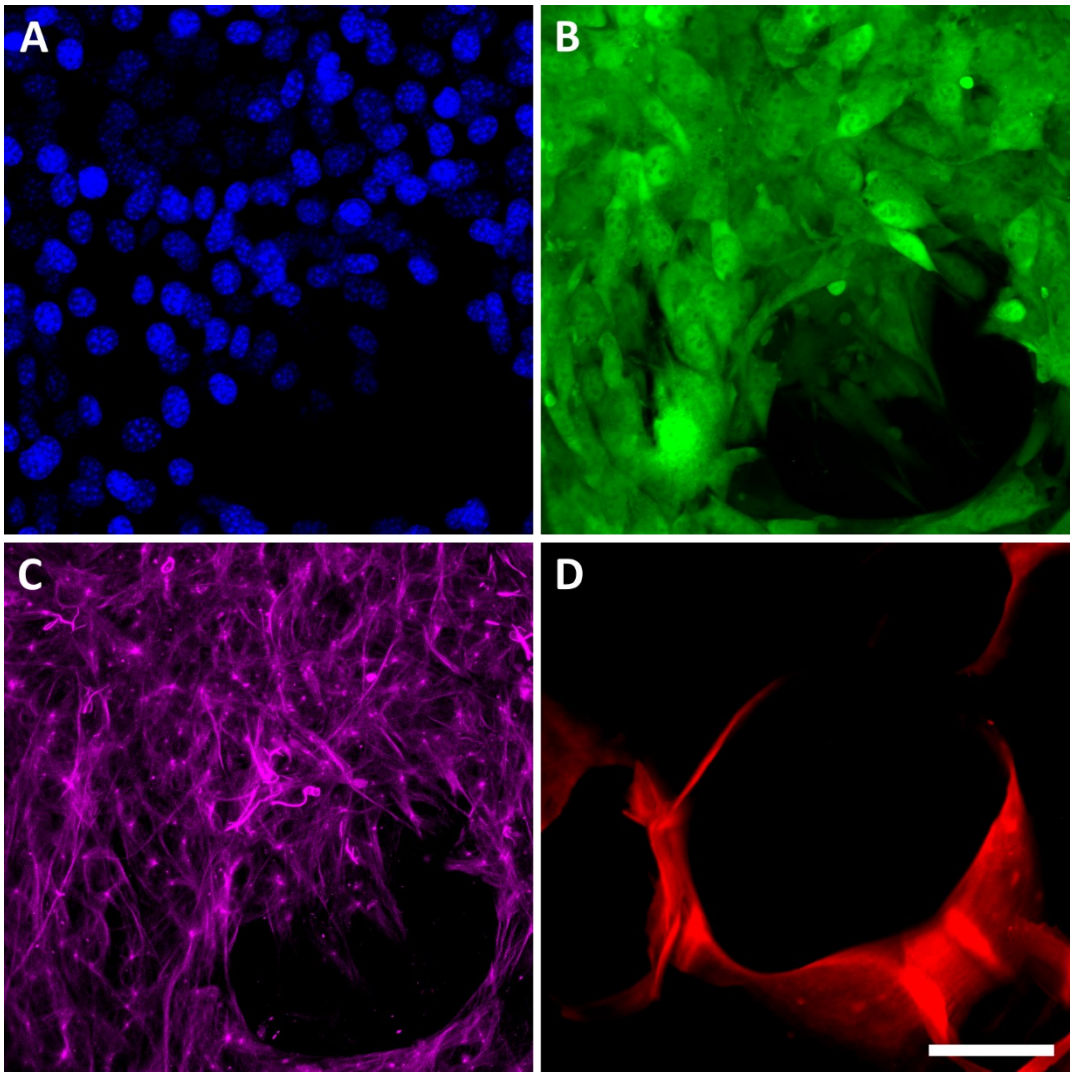

Figure 6.1. GFP 3T3 fibroblast cells on decellularized appl-derived scaffolds. Maximum projection confocal image of fibroblast cells grown on the cellulose-based scaffolds to create a 3D cell culture on a soft material. (A) Nuclei were stained with Hoechst 33342. (B) The cell body was identifiable as the cell line was stably transfected with Green Fluorescent Protein (GFP). (C) The microtubules which are responsible for driving the rotation were stained with live cell permeable SiR-Tubulin. (D) Scaffold visualization was accomplished with Congo Red staining. Scale = 50 µm.

6.2.2 Tracking nuclear rotation

As expected, the fraction of cells displaying nuclear rotation was low (~11%); which was congruent with our substrate stiffness dependent findings[1]. Previous research has shown that over 50% of nuclei exhibit nuclear rotation to some extent on stiff substrates[1,12]. Select nuclei exhibiting

substantial rotation were chosen to study the rotational dynamics. The tracking of the nuclear movement was accomplished by recording the (x,y,z) position of bright spots of Hoechst 33342 stained nuclei and the centroid position of the nuclei (for translational motion correction) with laser scanning confocal microscopy time-lapses. The ImageJ TrackMate plugin[21] was used to track the coordinates with the Difference of Gaussians (DoG) spot detector and the Linear Assignment Problem (LAP) particle linking algorithm. Tracks of a representative nucleus and the corresponding rotation are displayed in Figure 6.2.

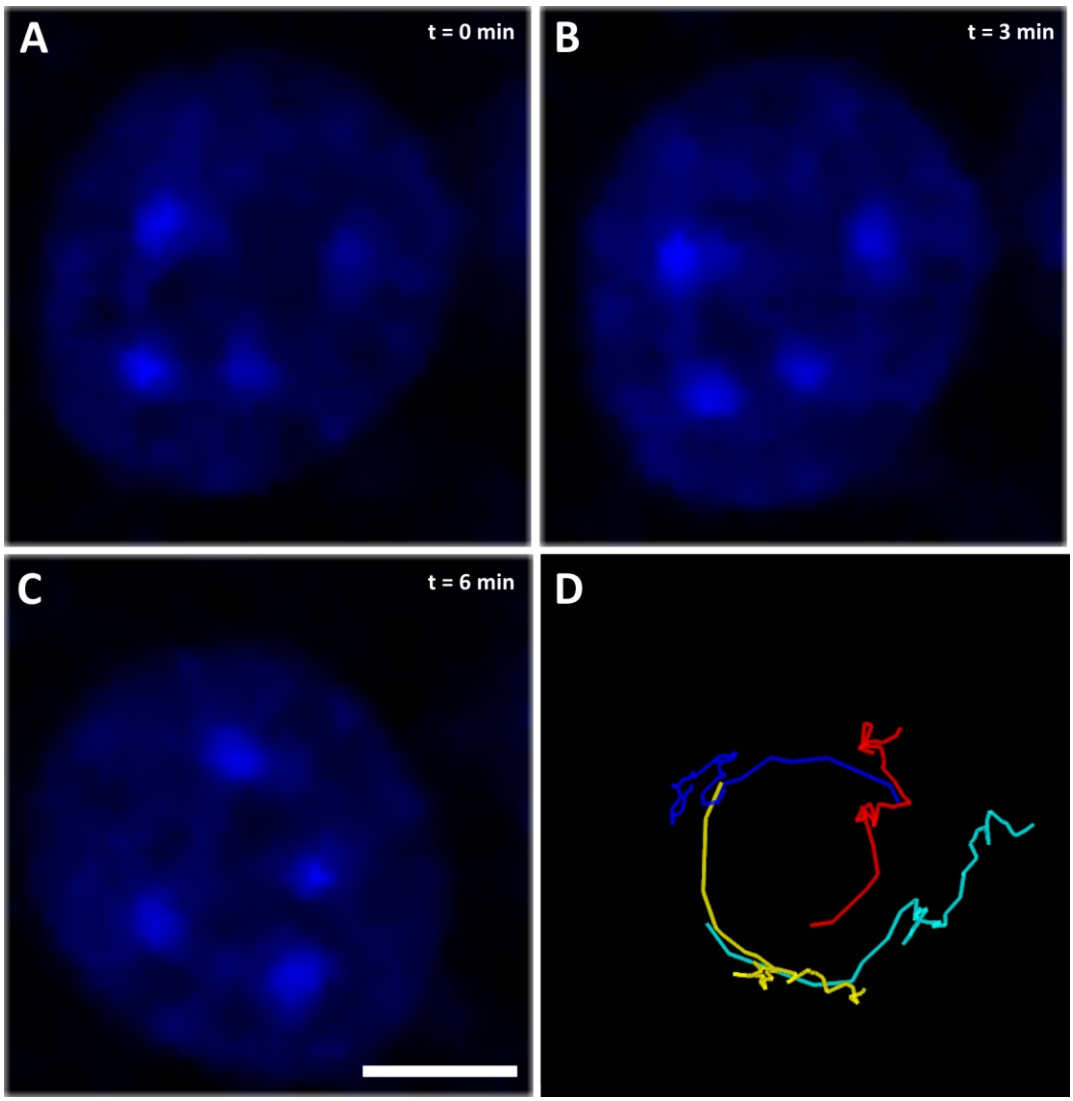

Figure 6.2 Tracking nuclear rotation. The positions of bright spots of Hoechst 33342 stained nuclei were recorded as time-lapse images of confocal volumes. The coordinates of the spots were tracked with TrackMate on Fiji ImageJ. (A-C) Three sequential 3-minute intervals show that the rotation can be monitored by recording the position of bright spots of the rotating fluorescently labelled nuclei. (D) The tracks of the bright spots tracked for the full duration of the experiment (180 min). Scale = 5 μm.

6.2.3 Angular fluctuations during rotation

To characterize the rotational movement, the change in the angular position of the nuclei with respect to its orientation at $t = 0$ was calculated. The transition from a soft 2D substrate to a soft 3D substrate enticed us to investigate whether there were changes to the nature of the rotational dynamics. Previous 2D characterization of nuclear rotation revealed that the axis of rotation is perpendicular to the long and short axes of the nuclei[7,11,12,14] . However, it is well established that cell morphology, specifically nuclear shape, is highly dependent on the physical environment[22]. As changes in nuclear shape are known to coincide with the transition from stiff 2D substrates to soft 3D substrates[23], we investigated whether the axis of rotation retained its perpendicular orientation.

Here we report two angles of rotation: ϕ and θ, corresponding to the azimuthal and polar angles respectively. The azimuthal angle is equal to the conventional angle investigated in nuclear rotation studies, whereas the polar angle is the perpendicular angle with the axis of rotation lying in plane parallel to that of the major component of the cell body. The extensively rotating nuclei investigated here underwent rotational motion primarily in the conventional azimuthal directions, although there was some degree of 3D rotation about the polar angle (Fig 6.3). It is plausible that friction and the nuclear shape are the main inhibitors of a randomly oriented rotational axis [2,15,16,24]. Moreover, elongated nuclei, as seen in C2C12 myocytes, did not exhibit nuclear rotation (Data not shown).

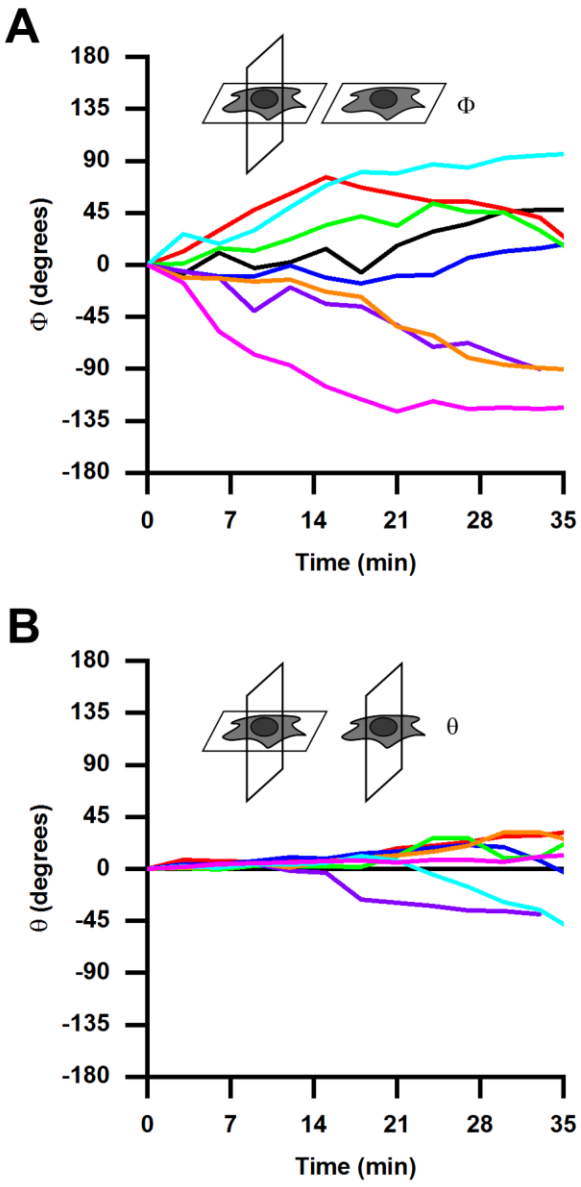

Figure 6.3 Nuclear rotation angles. The angular positions of rotating nuclei relative to their initial position after translational motion correction were calculated for both the azimuthal (A) and polar (B) angles identified as Φ and θ respectively. The insets illustrate the planes of rotation for each angle. The azimuthal direction showed a broad distribution of angles for nuclei undergoing extensive rotation, whereas the polar angle contained less angular fluctuations. The coloured lines represent individual nuclei tracks (N = 8).

6.2.4 Rotational model

A thorough previous study on nuclear rotation formulated a model wherein dynamic instability of microtubules and forces between the centrosome and the nucleus mediated by dynein leads to rotation[15]. This mathematical model predicts rotation from tensional forces on perinuclear microtubules. It dictates that rotations arise from an asymmetrical distribution of microtubules around the nucleus, and that the net torque in one direction persists until dynamic instability restores the balanced configuration. The parameters used in this model were the dynein force and speed, the dynein spring constant and dynein – nucleus off-rate, the number of microtubules and their polymerization/depolymerization speeds, the microtubule catastrophe and recovery rate constants, and the microtubule – nucleus distance[15]. The model successfully fits the experimental data and indicates that the rotational dynamics are a persistent random walk[15]. The mean squared angular displacement (MSAD) vs time plots follows parabolic shapes at short time scales and a linear relationship for extended time intervals. We show here, that the rotational dynamics follow the same model and exhibit parabolic MSAD time dependence on short time scales (Fig. 6.4). The significance of this result is that the previous research on nuclear rotation applies to 3D environments as well. Therefore, future studies can incorporate the model formulated by Wu et al. [15] and expand on it with extra cytoskeletal frictional components to investigate and predict nuclear dynamics in different scenarios.

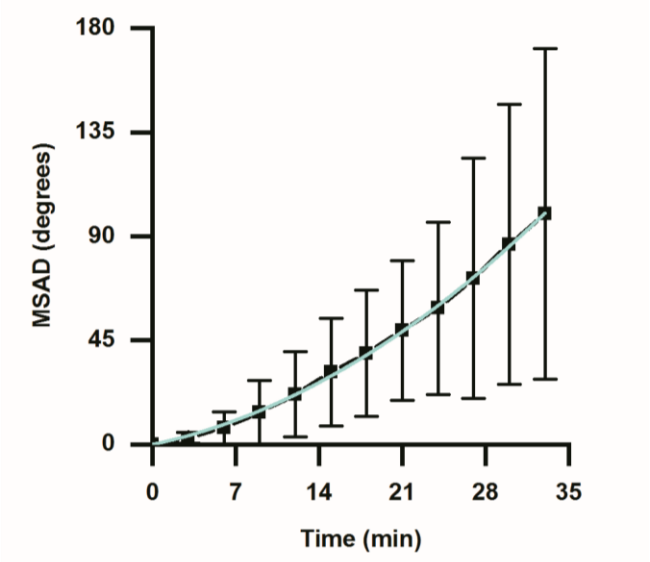

Figure 6.4. Mean squared angular displacement (MSAD). The MSAD was calculated for N = 8 cells exhibiting extensive rotation. Over the short time interval of 35 min, the data follows a parabolic shape. The cyan line shows the parabolic fit. $R^2 = 0.999$.

6.2.5 3D in vitro systems

The work presented here confirms that the previous knowledge gained from nuclear rotation studies is applicable to extension into 3D environments. This link is a critical characterization as this phenomenon has been implicated in vivo. Recently is was shown that dormant oocytes reside in a mechanically stiff environment, and their activation is stimulated by a loosening of the surrounding matrix[17]. Upon compression, restoration of the dormant state was achieved. Moreover, pausing the rotation triggered FOXO3 export from the nucleus. Although a direct link has yet to be made between the functional relationship between the physical rotational movement, nuclear transport, and cell activation, it is clear that these dynamic processes occur in specific cases in the body. Consequently, 3D biomimetic environments to study and manipulate rotational dynamics are required to advance our knowledge and to fill this gap in our understanding of this phenomenon. Studying biologically relevant tissue constructs will aid in deciphering whether or not there is a functional role for the persistent rotation. We and Nagamatsu et al. speculate that the rotational movement may be a mechanism by which cells sense the mechanical properties of the external environment by simultaneously pulling on many focal adhesion complexes around the cell via tensile forces exerted on microtubules, which are linked to the nuclear surface through dynein and SUN and KASH proteins [13,14,17,25–27]. In their paper, Nagamatsu et al. express the need for in vitro modelling systems[17] like the one we present here.

6.3 Conclusion

In conclusion we present a pragmatic approach to studying the phenomenon of nuclear rotation in 3D. We envision future studies combining tensile, compressive, and shear forces on the biomaterials to study the force response of the nuclear mechanics in terms of persistent angular motion. In particular, future work should investigate the centrosome nuclear distance as well as the intermediate filament organization in mechanically distinct environments. By extending our research into 3D biomaterials that more closely resemble native cell environments, the insights into the functional roles of cellular processes such as nuclear rotation can be tested. It may be found that this is simply an auxiliary statistical mechanical phenomenon that does not serve a biological function.

6.4 Materials and methods

6.4.1 Scaffold production

McIntosh apples (Canada Fancy) were carved into 3 x 3 x 3 mm cubes with a Shapeoko CNC machine with a 180° 0.8 mm drill bit. The samples were decellularized in sodium dodecyl sulfate (0.1%) for 3 days. The scaffolds were then washed in triplicate with dH_2O and incubated in 100 mM $CaCl_2$ for 24 h. After another 3 dH_2O washes, the samples were sterilized with 70% ethanol and then washed again 3 times with dH_2O. Following the washes, the samples were incubated in dH_2O for 24 h.

6.4.2 Cell culture and time-lapses

NIH 3T3 mouse fibroblast cells with a stable green fluorescent protein (GFP) were cultured at 37°C and 5% CO_2 in Delbecco's Modified Eagle Medium – High Glucose (DMEM), supplemented with 10% fetal bovine serum and 1% penicillin/streptomycin (100 U/mL and 100 µg/mL respectively) (Hyclone Laboratories Inc.). Cells were seeded onto the decellularized scaffolds in a dome of 25 µL of media and were permitted to attach for 1 h prior to submerging in media. During time-lapse imaging, the samples were not fully submerged. Fully submerging the samples would have caused them to float and the focus to drift to a large degree. The samples were placed in a low volume of media that ensured hydration while maintaining contact between the biomaterial and the glass plate. Time-lapse imaging was performed on a Nikon TiE A1 laser scanning confocal microscope with a 60X water immersion objective. Images were captured in 3-minute intervals, and the Z step size was set to 0.8 µm; the samples were held at 37°C and 5% CO_2. Other than adjusting brightness/contrast settings to maximize the fluorophore signal, no other image manipulations were performed.

6.4.3 Staining

The nuclei were stained with Hoechst 33342 (Invitrogen) (1:2000 dilution, 5µg/mL, 10 min incubation). Following the staining, the scaffold was washed twice with media before being transferred to a new glass bottom culture plate for imaging.

6.4.4 Quantification of nuclear rotation

Fiji ImageJ TrackMate was used to track the positions of the bright Hoechst 33342 stained heterchromatin and the centroid position using the LAP tracker. The DoG detector and LoG detector were used for the bright spots and the centroid respectively. Drift and translational movement corrections were accounted for by subtracting off the coordinates of the nucleus centroid. Microsoft Excel and OriginLab 2019 were used to calculate the angles of rotation and to plot and fit the data.

6.5 References

(1) Hickey, R.; Pelling, A. E. The rotation of mouse myoblast nuclei is dependent on substrate elasticity. *Cytoskeleton* **2017**, *74* (4), 184–194 DOI: 10.1002/cm.21357.

(2) Gerashchenko, M. V.; Chernoivanenko, I. S.; Moldaver, M. V.; Minin, A. A. Dynein is a motor for nuclear rotation while vimentin IFs is a "brake". *Cell Biol. Int.* **2009**, *33* (10), 1057–1064 DOI: 10.1016/j.cellbi.2009.06.020.

(3) Murray, M. E.; Mendez, M. G.; Janmey, P. A. Substrate stiffness regulates solubility of cellular vimentin. *Mol. Biol. Cell* **2014**, *25* (1), 87–94 DOI: 10.1091/mbc.E13-06-0326.

(4) Hookway, C.; Ding, L.; Davidson, M. W.; Rappoport, J. Z.; Danuser, G.; Gelfand, V. I. Microtubule-dependent transport and dynamics of vimentin intermediate filaments. *Mol. Biol. Cell* **2015**, *26* (9), 1675–1686 DOI: 10.1091/mbc.E14-09-1398.

(5) Tsuruta, D.; Jones, J. C. R. The vimentin cytoskeleton regulates focal contact size and adhesion of endothelial cells subjected to shear stress. *J. Cell Sci.* **2003**, *116* (Pt 24), 4977–4984 DOI: 10.1242/jcs.00823.

(6) Fung, L. C.; De Boni, U. Modulation of nuclear rotation in neuronal interphase nuclei by nerve growth factor, by gamma-aminobutyric acid, and by changes in intracellular calcium. *Cell Motil. Cytoskeleton* **1988**, *10* (3), 363–373 DOI: 10.1002/cm.970100303.

(7) Paddock, S. W.; Albrecht-Buehler, G. Rigidity of the nucleus during nuclear rotation in 3T3 cells. *Exp. Cell Res.* **1988**, *175* (2), 409–413 DOI: 10.1515/ling.1988.26.5.873.

(8) Park, P. C.; De Boni, U. Dynamics of nucleolar fusion in neuronal interphase nuclei in vitro: association with nuclear rotation. *Exp. Cell Res.* **1991**, *197* (2), 213–221.

(9) Paddock, S. W.; Albrecht-Buehler, G. The degree of coupling of nuclear rotation in binucleate 3T3 cells. *Exp. Cell Res.* **1986**, *166* (1), 113–126.

(10) Yao, K. T.; Ellingson, D. J. Observations on nuclear rotation and oscillation in Chinese hamster germinal cells in vitro. *Exp. Cell Res.* **1969**, *55* (1), 39–42.

(11) Levy, J. R.; Holzbaur, E. L. F. Dynein drives nuclear rotation during forward progression of motile fibroblasts. *J. Cell Sci.* **2008**, *121* (Pt 19), 3187–3195 DOI: 10.1242/jcs.033878.

(12) Wilson, M. H.; Holzbaur, E. L. F. Opposing microtubule motors drive robust nuclear dynamics in developing muscle cells. *J. Cell Sci.* **2012**, *125* (Pt 17), 4158–4169 DOI: 10.1242/jcs.108688.

(13) Brosig, M.; Ferralli, J.; Gelman, L.; Chiquet, M.; Chiquet-Ehrismann, R. Interfering with the connection between the nucleus and the cytoskeleton affects nuclear rotation, mechanotransduction and myogenesis. *Int. J. Biochem. Cell Biol.* **2010**, *42* (10), 1717–1728 DOI: 10.1016/j.biocel.2010.07.001.

(14) Ji, J. Y.; Lee, R. T.; Vergnes, L.; Fong, L. G.; Stewart, C. L.; Reue, K.; Young, S. G.;

Zhang, Q.; Shanahan, C. M.; Lammerding, J. Cell nuclei spin in the absence of lamin b1. *J. Biol. Chem.* **2007**, *282* (27), 20015–20026 DOI: 10.1074/jbc.M611094200.

(15) Wu, J.; Lee, K. C.; Dickinson, R. B.; Lele, T. P. How dynein and microtubules rotate the nucleus. *J. Cell. Physiol.* **2011**, *226* (10), 2666–2674 DOI: 10.1002/jcp.22616.

(16) Kumar, A.; Maitra, A.; Sumit, M.; Ramaswamy, S.; Shivashankar, G. V. Actomyosin contractility rotates the cell nucleus. *Sci. Rep.* **2014**, *4*, 3781 DOI: 10.1038/srep03781.

(17) Nagamatsu, G.; Shimamoto, S.; Hamazaki, N.; Nishimura, Y.; Hayashi, K. Mechanical stress accompanied with nuclear rotation is involved in the dormant state of mouse oocytes. *Sci. Adv.* **2019**, *5* (6) DOI: 10.1126/sciadv.aav9960.

(18) Hickey, R. J.; Modulevsky, D. J.; Cuerrier, C. M.; Pelling, A. E. Customizing the Shape and Microenvironment Biochemistry of Biocompatible Macroscopic Plant-Derived Cellulose Scaffolds. *ACS Biomater. Sci. Eng.* **2018**, *4*, 3726–3736 DOI: 10.1021/acsbiomaterials.8b00178.

(19) Modulevsky, D. J.; Cuerrier, C. M.; Pelling, A. E. Biocompatibility of Subcutaneously Implanted Plant-Derived Cellulose Biomaterials. *PLoS One* **2016**, *11* (6), 1–19 DOI: 10.1371/journal.pone.0157894.

(20) Modulevsky, D. J.; Lefebvre, C.; Haase, K.; Al-Rekabi, Z.; Pelling, A. E. Apple derived cellulose scaffolds for 3D mammalian cell culture. *PLoS One* **2014**, *9* (5) DOI: 10.1371/journal.pone.0097835.

(21) Tinevez, J. Y.; Perry, N.; Schindelin, J.; Hoopes, G. M.; Reynolds, G. D.; Laplantine, E.; Bednarek, S. Y.; Shorte, S. L.; Eliceiri, K. W. TrackMate: An open and extensible platform for single-particle tracking. *Methods* **2017**, *115*, 80–90 DOI: 10.1016/j.ymeth.2016.09.016.

(22) Lovett, D. B.; Shekhar, N.; Nickerson, J. A.; Roux, K. J.; Lele, T. P. Modulation of nuclear shape by substrate rigidity. *Cell. Mol. Bioeng.* **2013**, *6* (2), 230–238 DOI: 10.1007/s12195-013-0270-2.

(23) Skinner, B. M.; Johnson, E. E. P. Nuclear morphologies: their diversity and functional relevance. *Chromosoma*. Springer Science and Business Media Deutschland GmbH March 1, 2017, pp 195–212.

(24) Harada, T.; Swift, J.; Irianto, J.; Shin, J. W.; Spinler, K. R.; Athirasala, A.; Diegmiller, R.; Dingal, P. C. D. P.; Ivanovska, I. L.; Discher, D. E. Nuclear lamin stiffness is a barrier to 3D migration, but softness can limit survival. *J. Cell Biol.* **2014**, *204* (5), 669–682 DOI: 10.1083/jcb.201308029.

(25) Lammerding, J.; Hsiao, J.; Schulze, P. C.; Kozlov, S.; Stewart, C. L.; Lee, R. T. Abnormal nuclear shape and impaired mechanotransduction in emerin-deficient cells. *J. Cell Biol.* **2005**, *170* (5), 781–791 DOI: 10.1083/jcb.200502148.

(26) Mattioli, E.; Columbaro, M.; Capanni, C.; Maraldi, N. M.; Cenni, V.; Scotlandi, K.; Marino, M. T.; Merlini, L.; Squarzoni, S.; Lattanzi, G. Prelamin A-mediated recruitment

of SUN1 to the nuclear envelope directs nuclear positioning in human muscle. *Cell Death Differ.* **2011**, *18* (8), 1305–1315 DOI: 10.1038/cdd.2010.183.

(27) Jaalouk, D. E.; Lammerding, J. Mechanotransduction gone awry. *Nat. Rev. Mol. Cell Biol.* **2009**, *10* (1), 63–73 DOI: 10.1038/nrm2597.

6.6 Supplementary Figure

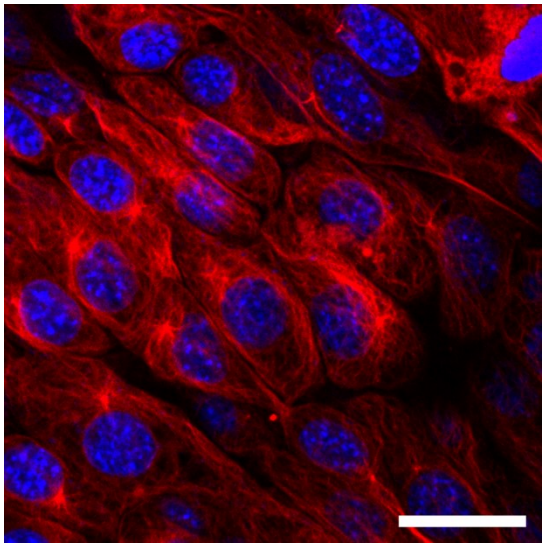

Figure S6.1. Extensive network of microtubules. In the three-dimensional environment, the microtubules (red) surround the nuclei (blue) in a complex fibrous network. Scale = 25 μm.

Chapter 7

Future Directions

The work presented in this thesis reveals that plant-derived, cellulose-based scaffolds constitute a promising approach for biomaterial design. Although these materials are highly biocompatible and share many key characteristics of in vivo tissues, they are still far from being fully biomimetic. This thesis serves as a launching point for various directions of studies aimed at the ultimate goal of recapturing the natural cellular environment. Here, four particularly important future directions are highlighted, and preliminary research on these next projects is already underway.

In this body of work, the repopulated biomaterials were studied in static conditions. This baseline characterization was required; static conditions are exceedingly rare in vivo, and in most circumstances, biophysical processes operate in dynamic or dynamic equilibrium states. As such, it is highly relevant to investigate how the biomaterials developed in this thesis and their successors respond to dynamic environments. In the body, cells and tissues experience a wide range of forces and deformations such as those produced during pulsatile flow, rhythmic breathing, and external stresses. The physics of the dynamic microenvironment are intertwined with biology and directly influence cell fate and function. The microscale response of the material to external stresses should be characterized in order to link the microstructure to the observed rheological properties and to formulate an all-encompassing model of the biomaterial's response to stresses and strains. This model should include the viscoelastic contributions of both the scaffold and the cells and extracellular matrices as well. In recent years, great strides have been taken in modeling cell mechanics.

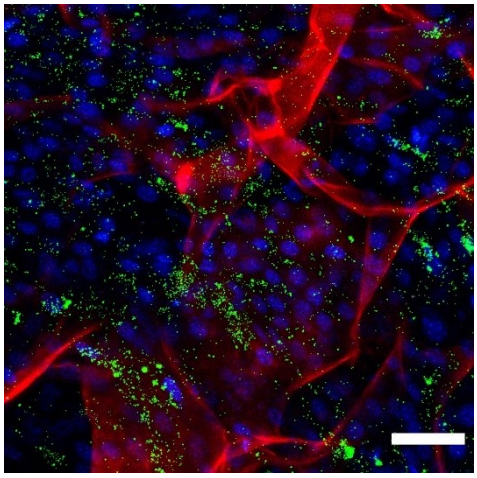

Figure 7.1. Biomaterial endowed with microbeads for local deformation tracking. Scaffolds can be coated with fluorescent microbeads to accurately track 3D deformations in response to physical forces. Blue = Hoechst 33342 stained C2C12 myoblast nuclei, green = fluorescent microbeads, red = Congo red stained cellulose scaffold. Scale = 50 μm.

Combining the knowledge of cell mechanics with the rheology of these novel biomaterials will likely be a major undertaking because the cellular response to strains and stresses will be different in the biomimetic 3D environment compared to conventional cell culture plates. Although this task is daunting and will require the collaborative effort of many scientists, it is highly important, as it will lead to a greater understanding of how tissues and cells function in vivo and guide tissue engineering endeavors.

In addition to material characterization and modelling, dynamic testing will produce valuable information about the long-term applicability of these biomaterials. In a medical context, this information is pertinent for estimating the lifetime of the implant. Dynamic testing below the ultimate and yield strengths over many cycles allows the fatigue properties to be quantified. Currently, limited data on stress/strain – cycle relationships has been collected, and it is currently unknown if a fatigue limit exists. For the implants to be functional in vivo, they must last the appropriate time scale, which could range from days to decades depending on the intended application. After the appropriate testing and characterizations are completed, the materials should be tested in animal models to validate the in vitro results.

Another direction of future research to increase the biomimicity of the materials is an investigation of the effects of growth factors and signaling molecules as well as extracellular matrix components and mineral content. In essence, combining a biochemical approach with biophysical studies will inherently increase the complexity of the construct, as tissue engineering lies at the intersection of biology, chemistry, and physics. Selectively tuning the cellular response on both temporal and spatial scales can lead to the generation of complex heterogenous materials. Preliminary research on combining the scaffolds with extracellular matrices with hydrogels and covalent bonding have commenced. This research may yield more complete tissue models and more effective biomaterials for in vivo applications.

The aforementioned future research directions should also be applied to the ETI platform presented in this thesis. Targeting specific interfaces will establish a unique set of parameters that must be met for adequate performance. In particular, repairing the entheses for both ligaments and tendons to bone is a significant challenge in orthopedic medicine. The novel ETI platform presented here used in combination with the future work outlined above may lead to prospective replacements for damaged entheses and insertion sites at the bone-connective tissue interface. Further development of these ETIs for a specific mechanical and biochemical profile are required to attain this goal. These developments will be concomitant with improvements and refinements of in vitro modeling systems for tissue interfaces.

The ability to “plug and play” with different subunits to make materials with customized components can also be explored to address some of the main obstacles in the fields of tissue engineering and biomaterial design. Specifically, the necrotic core of larger materials represents a major hurdle for recreating biological tissues. The insufficient oxygen and nutrient exchange lead to a non-viable core in the material. Introducing pores and vascular systems to combat

necrotic core formation has shown varying degrees of success, albeit none of which fully resemble the efficacy of the vasculature found in the body. In this thesis it is shown that by customizing the shape, small materials can exhibit extensive cell invasion, but when the size of the material is increased beyond a few hundred micrometers, the number of cells in the interior of the scaffold is reduced. By combining the "Lego-like" approach used in the tissue interface studies, larger materials can be built from subunits that have been fully infiltrated with cells. Although this method provides a simple mechanism for getting cells in the deep interior of the material, it will not ensure their viability; the diffusion of the media and oxygen will be insufficient as previously observed. In order to ensure the cells remain viable, a vascular system should be introduced. Two separate but not exclusive approaches are readily available for addressing the issue of vascular network construction: the first involves exploiting the natural vasculature of plant materials, and the second relies on combining the individual subunits with custom shapes that form vessels when assembled together.

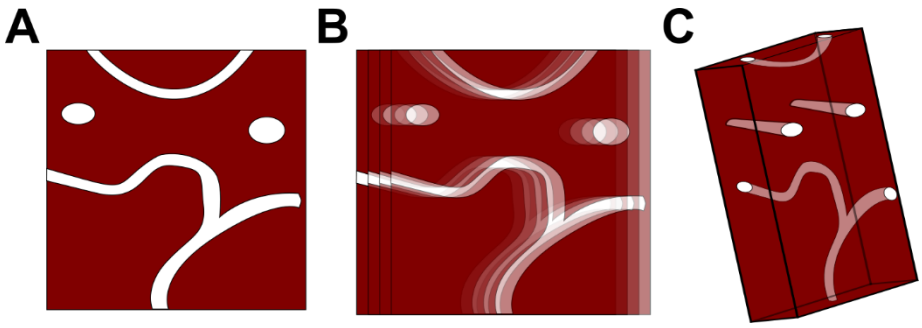

Figure 7.2 Vessel formation. Multilayered composites can conceivably be combined to produce a 3D network of vessels. (A) Individual components or sheets can be made with pre-defined etches and pores. (B) The components can be combined to produce a construct with complex 3D vessels (C) that cannot be produced by bulk carving and milling.

The four examples presented here are only a small subset of the future studies that can be inspired by the work presented in this thesis. Time will tell the full potential of plant-derived, cellulose-based biomaterials. It is anticipated that these materials will have significant impacts on the fields of cell biology, tissue engineering, and biomaterial design.

In conclusion, the work presented here attests to the applicability and prospective nature of this novel material, and with these results in hand, many more questions and exciting research avenues are open for investigation.

Appendix

The Rotation of Mouse Myoblast Nuclei is Dependent on Substrate Elasticity

This appendix is a reprint of a previously published research paper:

Hickey, R. & Pelling, A. E. The rotation of mouse myoblast nuclei is dependent on substrate elasticity. *Cytoskeleton* 74, 184–194 (2017).

§ 1 Motivation

The phenomenon of nuclear rotation, wherein the entire nucleus and its contents rotate in unison within the cell is ubiquitous and has been observed for several decades. Insights into the mechanism governing this process reveal that it is a microtubule-based persistent random walk motion. We originally sought to investigate the intracellular force distribution within the cell during rotation. However, upon placing the cells on compliant surfaces required for traction force microscopy, we found that there was a substrate stiffness effect to the rotation dynamics. Hence, we proceeded to investigate the effect of substrate rigidity on nuclear rotation.

§ 2 Hypothesis and Objectives

We hypothesized that nuclear rotation was a microtubule-based process that depends on the elasticity of the substrate. The objective was to gain insight into the dynamics of nuclear rotation when biologically relevant stiffnesses were used.

Abstract

The complex interplay of biochemical signaling and mechanical traction forces regulate the position of cellular nuclei. Although the phenomenon of nuclear rotation has been observed for many years, the influence of substrate elasticity was unknown. We discovered another layer of complexity of this phenomenon: nuclear rotation is dependent on substrate elasticity. Nuclear rotation is drastically reduced on physiologically relevant stiffnesses. Here, we studied nuclear rotation in mouse C2C12 myoblasts cultured on soft substrates designed to mimic resting tissue (~26 kPa) and on hard glass substrates. We examined the roles of the actin and microtubule cytoskeleton on the presence and dynamics of nuclear rotation in these two different

microenvironments. We demonstrated the clear dependence of nuclear rotation dynamics on matrix stiffness. These results will have important implications for the design of future studies of nuclear rotation and our understanding of the phenomenon as a whole. Unnaturally hard substrates do not only fail to mimic the *in vivo* microenvironment, but can also induce cellular processes that would not normally occur in the natural cellular environment.

Introduction

The ubiquitous phenomenon of cellular nuclear rotation has been observed for many years [1–11]; nevertheless, its significance remains poorly understood. Nuclear rotation involves the circular movement of the entire nucleus about its centre point [2,5,6,8]. This phenomenon has been observed in a variety of different cell types [1,2,4–9,12], and a broad range of velocities have been reported [5–8]. The nature of the rotation also depends on the physical environment of the cell. Nuclei in a three dimensional environment rotate in three dimensions [8,13], whereas in a two dimensional environment the nuclei rotate about the axis perpendicular to the plane of the substrate [2,5,6,9–11,14]. Furthermore, in the two dimensional case, clockwise and counterclockwise rotation occur, and the direction can change [2,5,6,9–11,14].
During this phenomenon, the nuclear interior, nuclear envelope, and nuclear pore complexes rotate collectively [2,5,6,8]. Since the nucleoli positions do not change relative to one another during this process, tracking the nucleoli positions serves as a convenient means of quantifying the rotation [2]. The majority of the intracellular structures, including the centrosome, do not rotate in conjunction with the nucleus [2,5,6,8,10,11,13–15]. Nuclear movement is largely dependent on microtubules. Depolymerizing the microtubule network induces a significant reduction in nuclear rotation, which can be restored by rescuing microtubule polymerization [2,5,8,10,11,15]. The microtubule associated protein dynein rotates the nucleus in single cells [5,10,11]. The role of kinesin has not been investigated in single cells. In myotubes, kinesin and dynein both localize at the nucleus and drive the rotation [8]. It is possible that the nature of the motor that drives the rotation is dependent on tissue type. Consistent with the model of microtubule associated motor protein driven nuclear rotation, adenosine triphosphate (ATP) depletion results in a reduction in rotation, which reveals that this process is ATP dependent [2]. Although the majority of evidence suggests that this phenomenon is driven by microtubules and their associated molecular motor dynein, it has also been proposed that it is driven by actomyosin contractility [3]. It is also known that the vimentin intermediate filament (IF) network impedes nuclear rotation [10]. This brake mechanism is plausibly mediated by binding vimentin to the nuclear surface through the multifunctional cytolinker protein plectin; however, direct evidence is required to confirm this hypothesis [10].

The cell nucleus is biochemically and physically connected to its surrounding microenvironment. The LINC (linker of nucleoskeleton and cytoskeleton) complex, which consists of SUN and KASH proteins, links the cytoskeleton to the nucleus [1,2,4,12,16]. The cytoskeleton is also connected to the

extracellular matrix (ECM) via focal adhesion complexes [17–20]. Probing of the local microenvironment involves the interaction between the cytoskeleton and focal adhesion complexes, and the generation of traction forces [21–23]. This is thought to be a mechanism through which cells gain an inherent ability to sense and adapt to changes in their physical environment. The elasticity of the microenvironment is now well known to impart significant influence over many cellular processes such as stem cell differentiation, myogenesis, and cancer transformation [24–27].

Importantly, in-vivo tissues can exhibit dynamic changes in their local mechanical properties due to contraction/relaxation, movement, pulsatile flow, etc. [28,29]. For example, the microenvironment of muscle tissue undergoes dynamic changes in elasticity during contraction. There is a large difference between the elasticity of resting and active muscle tissue (8-40 kPa and 40-97 kPa respectively, measured in mice) [30–34]. It has been shown that myogenesis occurs preferentially on soft substrates resembling resting muscle tissue stiffness [35]. Nuclei must be regularly spaced along myotubes for proper muscle function [36–38]. To achieve this uniform distribution, nuclei must translocate and rotate along the myofibre [8,39]. Improper nuclear positioning leads to a variety of pathologies such as Emery-Dreifuss muscle dystrophy [40]. Therefore, we speculated that there may be a relationship between substrate elasticity and the phenomenon of nuclear rotation.

To date, the majority of research in this field has focused on elucidating the physical mechanism of nuclear rotation by studying the rotation that occurs on unnaturally hard substrates. The influence of substrate elasticity on this process remained unknown. This is an important factor because it has been speculated that nuclear rotation may be an artifact associated with removing cells from their natural in-vivo environment and culturing them on two-dimensional hard substrates [9]. Importantly, previous studies of nuclear rotation have all been carried out on hard glass or plastic substrates (~1-90 GPa), which are approximately 6orders of magnitude stiffer than resting tissue. Therefore, the purpose of this study was to understand the effect of substrate stiffness (elasticity) on the phenomenon of nuclear rotation. Here, we studied nuclear rotation in mouse C2C12 myoblasts cultured on soft substrates mimicking resting tissue (~26 kPa) and on hard glass substrates. We examined the role of the actin and microtubule cytoskeleton on the presence and dynamics of nuclear rotation in these two different microenvironments. Importantly, we found that nuclear rotation is significantly abolished on substrates mimicking muscle tissue elasticity. These results will have important implications for the design of future studies of nuclear rotation and our understanding of the phenomenon as a whole.

Results

Soft gelatin gels mimic *in vivo* stiffness

The purpose of this study was to assess the dependence of nuclear rotation on substrate elasticity. Traditionally, mammalian cells have been cultured on hard glass or plastic substrates. Here, we created "soft" substrates by coating them with a thick gelatin cross-linked with glutaraldehyde gel (GXG gel), as described previously [22,41]. The GXG gel stiffness was tuned to be within the resting muscle tissue stiffness regime [30,31,33,42]. Atomic force microscopy was used to confirm the stiffness of the GXG substrate by fitting acquired force curves to the Sneddon-Hertz model for a conical indenter at shallow 200 nm indentations [43]. The stiffness of the GXG was determined to be 26.4 ± 0.5 kPa. As a comparison, we also applied a thin coat of gelatin to glass substrates to constitute a "hard" substrate. The stiffness of the glass substrate has been previously determined to be ~ 1 GPa [44].

Nuclear rotation can be monitored by tracking nucleolar positions

C2C12 myoblasts were cultured on both the hard and soft substrates in order to assess nuclear rotation on both environments. C2C12 myoblasts were used in this study because they are known to exhibit nuclear rotation upon fusion into myotubes [8], and they are well known to be mechanosensitive [22]. To monitor the nuclear rotation, time-lapse phase contrast experiments were conducted by capturing an image every 10 minutes for 12 hours. The axis of rotation was always clearly perpendicular to the surface of the substrate, consistent with other studies [2,5,6,9–11,14] (Fig. S1 in supplementary material). The rotation occurred in both clockwise and counterclockwise directions without any clear preference. It was observed that the positions of the nucleoli did not change relative to one another (Fig. S1 in supplementary material), consistent with previous studies [2]. The positions of the nucleoli served as a convenient means of tracking the rotation because the entire nucleus moved together as a unit [2]. The x,y coordinates of the nucleoli were tracked using the ImageJ plugin MTrackJ. Furthermore, the x,y coordinates of the centre of the nucleus were also recorded to monitor translational movement. Rotation and translation of the nucleus typically occurred simultaneously (Fig. S1 in supplementary material). It should be noted that translational movement was not a requirement for rotation to occur; nevertheless, translational movement often accompanied rotation. A correction for the translational movement of the cells was required in order to quantify and study the rotational movement of the nucleus. The correction for translational movement was accomplished by subtracting the x,y coordinates of the centre of the nucleus from the x,y coordinates of the nucleoli [3,5,10] (Fig. S1 in supplementary material). The corrected nuclear rotation is simply the rotational movement of the nucleus in the absence of any translation (Fig. S1 in supplementary material). The corrected data was then used to quantify the dynamics of the motion. Although the nature of the rotation described here is congruent with past results, this

appears to be the first study investigating nuclear rotation on soft, physiologically relevant substrate stiffnesses.

Rotating nuclei were defined as nuclear rotations greater than ± 90°

Over the course of the time-lapse experiments, all nuclei demonstrated angular movement to varying extents. At one extreme the nuclei completed multiple full rotations, while at the other extreme the nuclei only rotated by a few degrees. It was also observed that the direction of rotation could change during a single time-lapse measurement. Consistent with previous studies [2], we defined a critical angle (θ_{crit}) for rotation as ± 90°. As a result, nuclei that rotated more than ± 90° were identified as rotating nuclei, and nuclei that rotated less than ± 90° were classified as non-rotating nuclei (Fig. S2 in supplementary material). Angle-time plots were produced from the time-lapse data where the angular position at time t = 0 min was defined as 0°. Counterclockwise rotation was defined as positive rotation, and clockwise rotation was defined as negative rotation. Therefore, if a nucleus was to undergo multiple rotations in a single direction, the change in angle would approach 360° and then abruptly return to 0° as the nucleus undergoes a complete rotation (Fig. S2 in supplementary material).

Nuclear rotation is drastically reduced on a physiologically relevant substrate stiffness

After tracking the nuclear rotation on both the hard and soft substrates (N = 75 nuclei in both cases) the percentage of cells that exhibited this phenomenon was first determined. The mean percentage of nuclei rotating and the standard error of the mean were calculated from three replicate time-lapse experiments for each condition. A significantly higher percentage of nuclei rotated on the hard substrate (64.0 ± 4.0%) compared to the control on the soft substrate (33.3 ± 1.3%) ($P = 1.1\text{x}10^{-3}$) (Fig. 1A). Next, the microtubule drug nocodazole was added to interfere with microtubule polymerization, which resulted in microtubule destabilization (Fig. S3 in supplementary material). The addition of nocodazole abolished nuclear rotation on both the hard and soft substrates, and the percentage of nuclei that rotated was not significantly different than zero (N = 45 nuclei on both substrates, hard: $P = 5.7\text{x}10^{-2}$, soft: $P = 4.2\text{x}10^{-1}$) (data not shown). Since nocodazole completely eliminated nuclear rotation and displayed no dependence on substrate stiffness, we did not analyze the data for the other rotational dynamics that are reported below for the other conditions. Interestingly, when the cells were exposed to the microtubule stabilizing agent paclitaxel (Fig. S3 in supplementary material), a significant reduction in the percentage of rotating nuclei compared to the control (no drug) was observed for the hard substrate (31.1 ± 5.9%, N = 45, $P = 5.1\text{x}10^{-4}$), but not for the soft substrate (20.0 ± 3.8%, N = 45, $P = 3.2\text{x}10^{-}$

^{1}) (Fig. 1A). To investigate the role of actomyosin contractility in nuclear rotation the myosin II inhibitor blebbistatin was used (Fig. S3 in supplementary material). It was found that there was no significant change in the percentage of nuclei undergoing rotation compared to the control on the hard substrate (80.0 ± 3.8%, N = 45, P = $1.5x10^{-1}$); however, a significant increase compared to the control was observed on the soft substrate (77.8 ± 5.9%, N = 45, P = $1.4x10^{-5}$) (Fig. 1A).

To further characterize this process, the absolute value of the net rotation of only the rotating nuclei was investigated. This analysis was conducted independently of the direction of rotation. Although the average net rotation on the hard substrate (426.0 ± 55.2°, N = 48) was slightly larger than the soft substrate (275.2 ± 57.7°, N = 25), they were not significantly different (P = $2.7x10^{-1}$) (Fig. 1B). In the presence of paclitaxel there was a significant reduction in the net rotation compared to the control on the hard substrate (160.5 ± 19.5°, N = 14, P = $6.8x10^{-4}$); however, there was no significant change compared to the control for the soft substrate (105.4 ± 11.2°, N = 9, P = $4.1x10^{-1}$) (Fig. 1B). Moreover, no significant change in net rotation was observed after blebbistatin treatment for the hard (338.0 ± 30.1°, N = 36, P = $6.1x10^{-1}$) and soft (299.1 ± 28.9°, N = 35, P = 1.0) substrates compared to the control (Fig. 1B).

The analysis of the net rotation does not account for changes in direction that were occasionally observed. The total rotation was evaluated to account for the changes in direction. The total rotation was calculated as the sum of the absolute values of the changes in angular position of the rotating nuclei. For instance, suppose a nucleus first rotated +30° and then rotated -20°. The net rotation is +10°, whereas the total rotation is 50°. Unlike the net rotation analysis, the total rotation of the nuclei on the hard substrate (1300.2 ± 125.0°, N = 48) was significantly greater than that of the soft substrate (851.9 ± 74.1°, N = 25) (P = $3.1x10^{-2}$) (Fig. 1C). As was observed in the net rotation analysis, the treatment of paclitaxel resulted in a significant reduction of total rotation compared to the control on the hard substrate (559.5 ± 42.8°, N = 14, P = $6.8x10^{-4}$) but not the soft substrate (661.7 ± 53.3°, N = 9, P = $9.6x10^{-1}$) (Fig. 1C); however, treatment with blebbistatin did not significantly change the amount of total rotation compared to the control (hard: 1159.4 ± 72.7°, N = 36, P = $8.8x10^{-1}$ and soft: 1070.12 ± 56.9°, N = 35, P = $7.1x10^{-1}$) (Fig. 1C).

In addition to assessing the prevalence and amount of nuclear rotation, the angular velocity was also investigated in order to gain a more complete understanding of this phenomenon. The angular velocity of the rotating nuclei was evaluated independently of the direction of rotation. It was found that the angular velocity on the hard substrate (33.1 ± 2.5°/min, N = 48) was significantly greater than the angular velocity on the soft substrate (15.6 ± 1.1°/min, N = 25) (P = $5.6x10^{-8}$) (Fig. 1D). The addition of paclitaxel resulted in a significant decrease in angular velocity compared to the control on the hard substrate (11.0 ± 0.5°/min, N = 14, P = $1.7x10^{-8}$) but not the soft substrate (10.3 ± 0.7°/min, N = 9, P = $7.7x10^{-1}$) (Fig. 1D). Exposure to blebbistatin on the hard substrate led to a significant reduction in angular velocity compared to the control (26.7 ± 1.4°/min, N = 36, P

$= 4.2x10^{-2}$), whereas exposure to blebbistatin on the soft substrate resulted in a significant increase in angular velocity compared to the control (27.7 ± 1.2°/min, N = 35, $P = 1.2x10^{-4}$) (Fig. 1D).

Notably, throughout each of the nuclear rotation analyses there was no statistically significant difference between the paclitaxel treated samples on the hard substrate and the control samples on the soft substrate (percentage of nuclei rotating: P = 1.0 (Fig. 1A), net rotation: $P = 7.5x10^{-1}$ (Fig. 1B), total rotation: $P = 5.6x10^{-1}$ (Fig. 1C), and angular velocity: $P = 7.9x10^{-1}$ (Fig. 1D)).

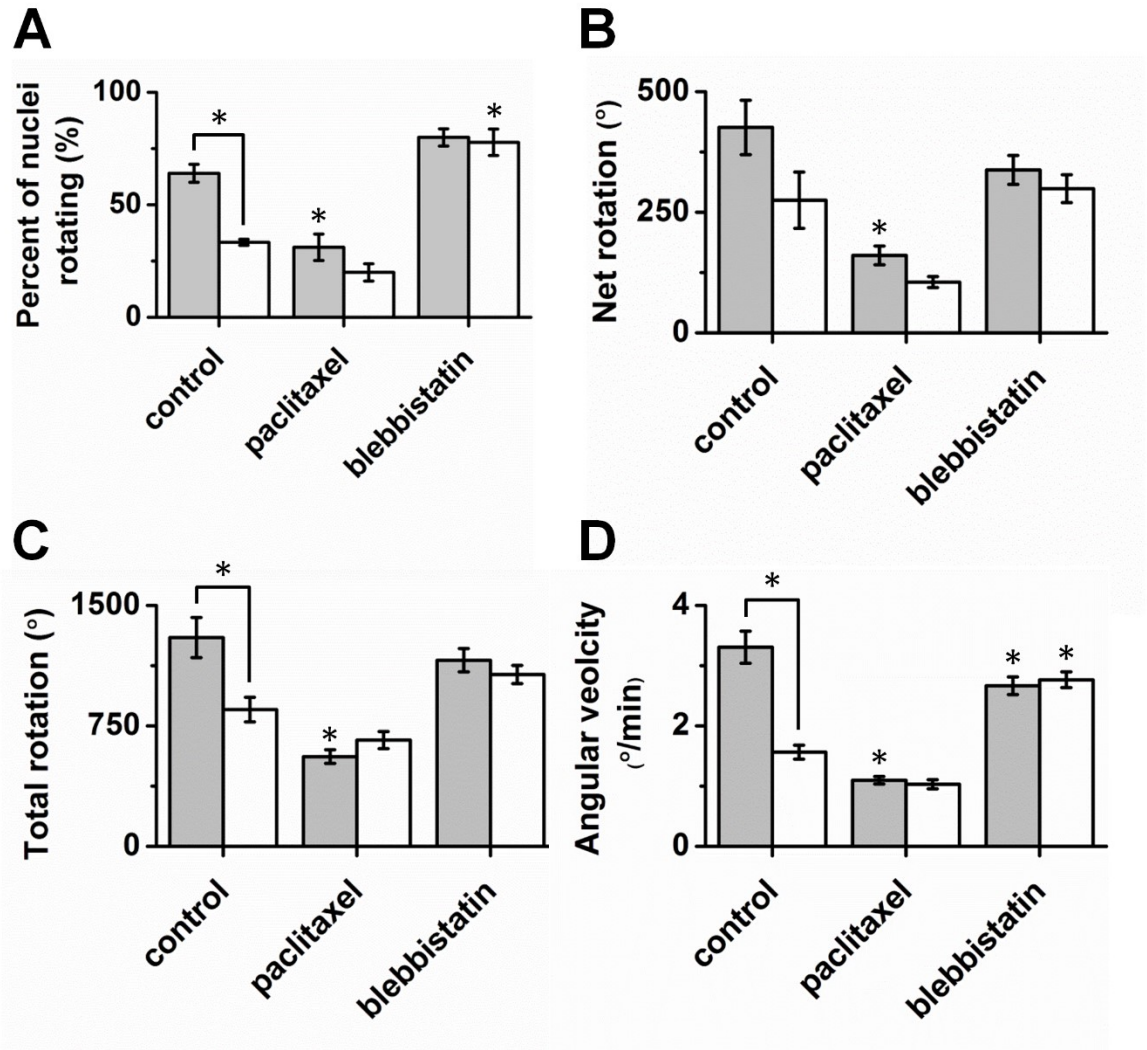

Figure 1: Nuclear rotation dynamics. The nuclear rotation dynamics were quantified for the rotating nuclei in the presence of the cytoskeletal drugs paclitaxel and blebbistatin on two different substrates. The hard substrate was glass with a thin layer of gelatin (grey), and the soft substrate was a GXG hydrogel (white). The (A) percent of nuclei rotating, (B) the net rotation, (C) total rotation, and (D) angular velocity were calculated. All values are mean ± s.e.m.

Substrate dependent nuclear rotation is not caused by differences in nuclear shape

Previous studies have shown that the nuclear shape changes with substrate stiffness [45]. Moreover, an early investigation of nuclear rotation claimed that a nearly circular nucleus is required for rotation to occur [15]. We speculated that it is possible that changes in rotation on varying stiffnesses are a result of differences in friction experienced by nuclei of different shapes. To assess whether the nuclear shape was different in our experimental conditions, the circularity of the nucleus was calculated for N = 35 cells on each substrate (Fig. 2). The circularity (C) was calculated in ImageJ as $C = 4\pi \frac{area}{perimeter^2}$. No significant difference between the cells on the hard and soft matrices was found for the circularity of the nuclei (hard: 0.73 ± 0.01 and soft: 0.70 ± 0.02, P > 0.05) (Fig. 2B). Furthermore, the apparent nuclear height was also compared because nuclei are 3D structures (Fig. 2). No significant difference in height was found between the nuclei on the hard and soft substrates (hard: 6.31 ± 0.34 and soft: 5.84 ± 0.34, N = 25, P > 0.05) (Fig. 2B).

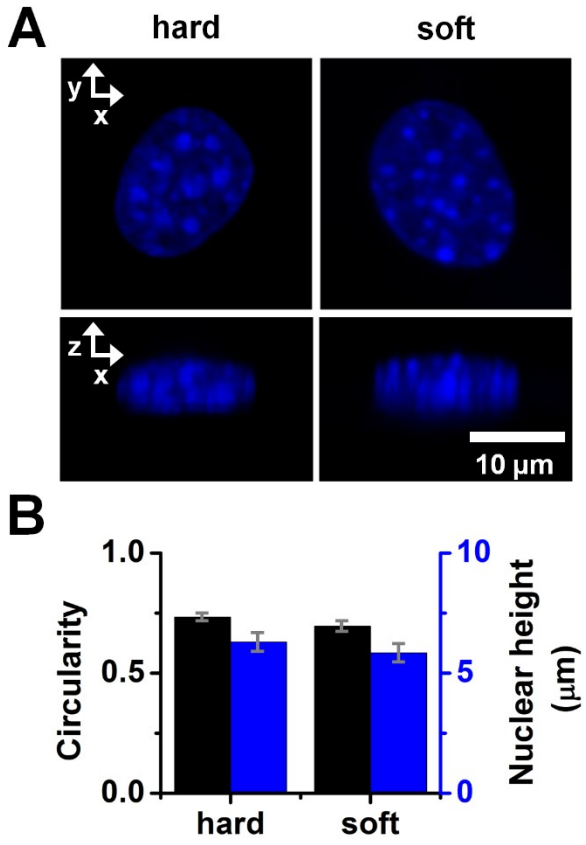

Figure 2: Nuclear shape. C2C12 myoblast cells were stained with dapi, and the circularity and apparent nuclear height were calculated. (A) XY and ZX maximum projections of dapi stained nuclei on the hard and soft substrates. (B) The circularity (left axis) and the apparent nuclear height

(right axis) of nuclei on the hard and soft substrates. The hard substrate was glass with a thin layer of gelatin, and the soft substrate was a GXG hydrogel. All values are mean ± s.e.m.

Vimentin localization is altered on soft substrate stiffnesses

Intermediate filaments (IFs), particularly Vimentin IFs, are known to play an important role in regulating nuclear rotation in fibroblasts [10]. Extensive nuclear rotation has been observed in vimentin null cells, and vimentin has been shown to inhibit the dynamics of the nucleus [10]. To assess a potential role of vimentin in the observed substrate stiffness dependent nuclear rotation, the C2C12 myoblasts were stained for vimentin and imaged using confocal microscopy. Different localization of the vimentin IF network was observed on the hard and soft substrates. Specifically, on the hard substrate the vimentin IF network extended to the cell periphery, while on the soft substrate the vimentin IF network condensed around the nucleus (Fig. 3A). The percentage of cell area coverage by the vimentin IF network was calculated for both substrates. A significantly higher percentage of the cell area was covered by the vimentin IF network on the hard substrate (39.5 ± 1.2%, N = 10) than on the soft substrate (31.7 ± 2.0%, N = 10) ($P = 3.0x10^{-2}$) (Fig. 3B). The addition of paclitaxel did not significantly change the vimentin IF area percentage on the hard (33.4 ± 1.6%, N = 10, $P = 1.6x10^{-1}$) and soft (28.3 ± 2.2%, N = 10, $P = 7.4x10^{-1}$) substrates compared to the control (Fig. 3B). Conversely, a significantly reduced vimentin IF area percentage compared to the control was observed after blebbistatin treatment on the hard (31.6 ± 0.9%, N = 10, $P = 2.6x10^{-2}$) and soft (24.1 ± 2.2%, N = 10, $P = 3.5x10^{-2}$) substrates (Fig. 3B).

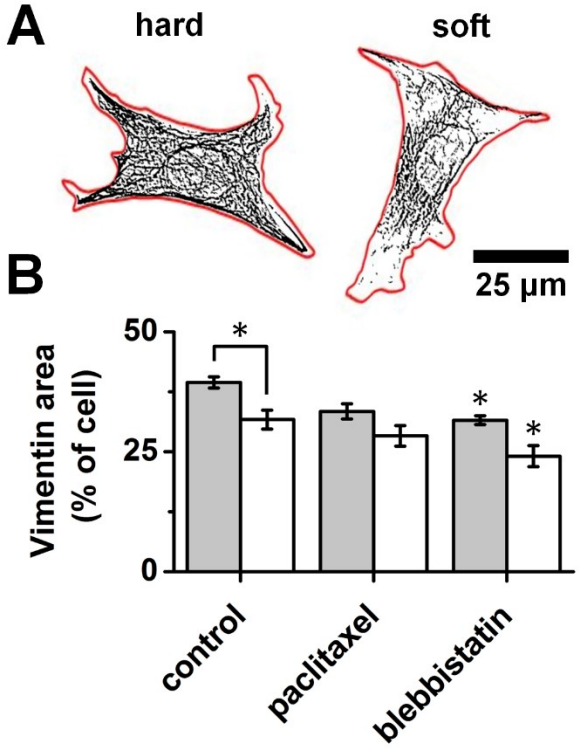

Figure 3: Vimentin IF localization. C2C12 myoblast cells were stained for vimentin, and the percentage of the total cell area coverage by the vimentin IFs was calculated. (A) Thresholded vimentin IF networks (black) and the cell border (red) on the hard and soft substrates. (B) Percentage of cell area coverage by vimentin IFs in the presence of the cytoskeletal drugs paclitaxel and blebbistatin on two different substrates. The hard substrate was glass with a thin layer of gelatin (grey), and the soft substrate was a GXG hydrogel (white). All values are mean ± s.e.m.

Myoblasts sense and respond to mechanical cues of the microenvironment

As our results demonstrate a clear sensitivity of the dynamics of nuclear rotation to the mechanical properties of the substrate, we also sought to characterize the morphology of the focal adhesion complexes [46]. Focal adhesions interact with the cytoskeleton and the ECM, and are crucial for mechanosensing and mechanotransduction [18,47–50]. Vinculin staining in combination with confocal microscopy was used to assess the size of focal adhesions on the hard and soft substrates. Large punctate focal adhesion complexes were observed on the hard substrate, whereas small and more diffuse focal adhesions were found on the soft substrate (Fig. 4) as expected [20,47,51,52]. In order to quantify the focal adhesion sizes on each substrate, the confocal images were segmented and thresholded, and only the z-planes containing the focal adhesion complexes were evaluated (Fig. 4A). These planes corresponded to the interface between the cell and the substrate because the focal adhesions allow the cell to adhere to the substrate. It was found that the average focal adhesion size was significantly larger for the cells on the hard substrate ($1.20 \pm 0.07\ \mu m^2$) in comparison to the soft substrate ($0.72 \pm 0.02\ \mu m^2$) ($N = 5$ cells, $P = 3.4 \times 10^{-3}$) (Fig. 4B). In the presence of paclitaxel, there was no significant difference in focal adhesion size for both the hard ($1.00 \pm 0.08\ \mu m^2$, $N = 5$ cells, $P = 6.1 \times 10^{-1}$) and soft ($0.71 \pm 0.07\ \mu m^2$, $N = 5$ cells, $P = 1.0$) substrates (Fig. 4B). Exposure to blebbistatin on the hard substrate led to a significant reduction in focal adhesion size ($0.82 \pm 0.06\ \mu m^2$, $N = 5$ cells, $P = 1.8 \times 10^{-4}$), whereas exposure to blebbistatin on the soft substrate resulted in a significant increase in focal adhesion size ($0.97 \pm 0.06\ \mu m^2$, $N = 5$ cells, $P = 5.2 \times 10^{-3}$) (Fig. 4B).

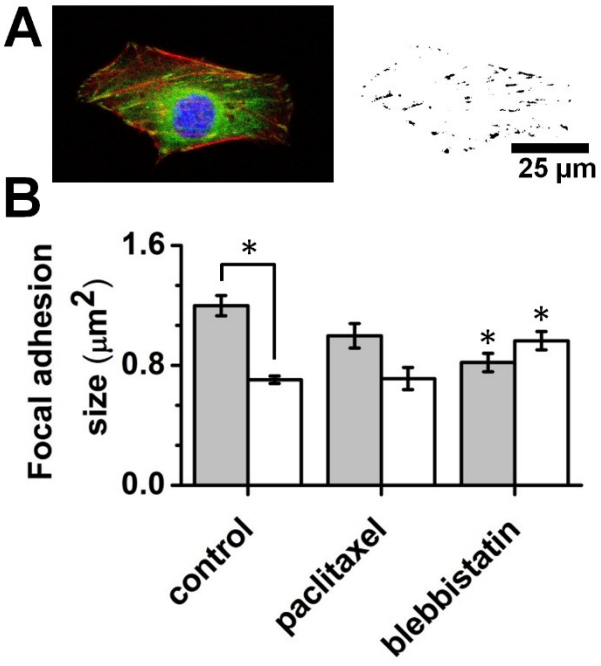

Figure 4: Focal adhesion size. The sizes of focal adhesion complexes of C2C12 myoblast cells were calculated. (A) Left: C2C12 myoblast stained for actin (red), vinculin (green), and the nucleus (blue). Right: thresholded and segmented image of the vinculin stain showing focal adhesions. (B) Average focal adhesion size in the presence of the cytoskeletal drugs paclitaxel and blebbistatin on two different substrates. The hard substrate was glass with a thin layer of gelatin (grey), and the soft substrate was a GXG hydrogel (white). All values are mean ± s.e.m.

Discussion

In this study we reveal another layer of complexity of the phenomenon of nuclear rotation. Our results indicate that nuclear rotation is dependent on substrate elasticity. Our results on hard substrates are coherent with previous studies; however, we showed for the first time that a significant reduction in the prevalence, magnitude, and speed of rotation occur on soft substrates designed to mimic the physical properties of resting muscle tissue [22,30,31,33,41,42]. Previous studies on nuclear rotation have been performed on hard substrates that can have a stiffness in the GPa range [1,2,5,6,8,9,15]. Such a high substrate stiffness is not generally relevant as tissues are typically in the 10-100 kPa range [25,53]. A moderate level of rotation was observed on an intermediate 100kPa stiffness. On the 100kPa GXG gels, the amount of rotation resembled the hard glass substrate, while the angular velocity was comparable to the soft gel substrate. In order to maintain the same surface biochemistry between the hard and soft substrates used in this study, the glass substrate was coated with a thin layer of gelatin [22]. As a result, the observed differences could be attributed to substrate elasticity and not surface chemistry.

The dynamics of the observed rotation on the hard substrate was consistent with previous studies [1,2,11,14,3–10]. We found that microtubule depolymerization induced by the addition of nocodazole completely abolished nuclear rotation. Conversely, the inhibition of actomyosin contractility mediated by the addition of blebbistatin had little effect. We conclude that nuclear rotation is a microtubule dependent phenomenon. This conclusion is in agreement with the vast majority of research on this process [2,5,8,10,11,15]. However, there is a small body of work proposing that the rotation may also be caused by actomyosin contractility, though the discrepancy in findings may be due to a number of factors including cell type, cell morphology and micropatterning, and drug concentrations [3]. For example, in the study that claimed actomyosin contractility causes the rotation [3], the concentration of microtubule inhibiting drugs was considerably lower than those used in other studies [5,8,10] as well as the present one. Moreover, the cells were confined to micropatterned geometries, which has been shown to cause the centrosome to move unnaturally close to the nucleus and suppress nuclear dynamics [11]. It is clear that the experimental conditions affect the nature of the nuclear movement and great care should be taken when making comparisons between previously published reports.

It is well known that there is cross-talk between the various cytoskeletal elements [54,55]. Transport of vimentin IF subunits is reliant on transport along microtubules [55,56]. The vimentin subunits are transported bidirectionally along dynamic microtubules, and are transported via motor proteins [55,56]. In a study involving vimentin null cells, it was found that nuclear rotation is regulated by two distinct mechanisms: the rotation is driven by microtubules and their associated motor proteins, and is inhibited by vimentin IFs [10]. Interestingly, the vimentin IF network changes localization on different substrate stiffnesses. The total amount of vimentin IF protein remains constant when the matrix stiffness is varied; however, the solubility and localization of the vimentin IFs change [57]. Our results and the results from previous investigations reveal that on soft substrates the vimentin IF network condenses around the nucleus, whereas on hard substrates the vimentin IF network extends to the cell periphery and interacts with focal adhesions [17,48,57]. The reduced vimentin IF area was concomitant with the reduction in nuclear rotation. Therefore, we suspect there are two levels of regulation that govern the observed matrix stiffness dependent nuclear rotation. The first is an alteration in microtubule dynamics, and the second is a change in vimentin IF localization.

Our results show that nuclear rotation is reduced on soft substrates. This novel phenomenon is a unique response to a soft microenvironment. The known mechanisms governing the rotation are modulated in response to the mechanical properties of the matrix. Since it was confirmed that the rotation is dependent on microtubules, a low concentration of paclitaxel was used to suppress microtubule dynamics. Although there was a decrease in rotation, a basal level persisted in the absence of dynamic microtubules. Interestingly, the prevalence, magnitude, and velocity of the rotation on the soft substrate in the absence of the microtubule stabilizing drug paclitaxel was not significantly different than that of the hard substrate in the presence of paclitaxel. This result suggests there may be a difference in the dynamics of the microtubules on the hard and soft

substrates. In light of the microtubule motor protein mechanism of rotation, wherein rotation is caused by an imbalance of force on the nucleus when more microtubules are in contact with one side of the nucleus, a reduction in microtubule dynamics can lead to a reduction in rotation [11]. It is also possible that the spatial distribution of microtubules around the nucleus changes on different substrate stiffnesses. Different spatial distributions can lead to differences in rotation. Our results did not show any spatial distribution differences (Fig. S3 in supplementary material); however, it is possible that minute but significant differences are present below our limit of detection.

Paclitaxel was used to assess the role of dynamic microtubules on the localization of vimentin IFs. No significant change in the vimentin IF organization was observed in response to microtubule stabilization. This data suggests the two proposed mechanisms governing the substrate stiffness dependent nuclear rotation are distinct. Surprisingly, the blebbistatin treatment resulted in a decreased vimentin area percentage. This result may be caused by the increased membrane ruffling induced by increased Rac activity in the presence of blebbistatin [54]. Initially it seemed curious that the high amount of nuclear rotation was observed in the presence of blebbistatin regardless of the collapse of the vimentin IF network around the nucleus; however, an increase in microtubule dynamics coincides with increased Rac activity, which is stimulated by blebbistatin treatment [58]. Thus, if the suggested mechanisms are correct, the increase in microtubule dynamics that drive the nuclear rotation may outweigh the effects of the vimentin IF dependent impairment of rotation. Future work will be required to more closely investigate these speculations.
The shape of nuclei can change on different substrate stiffnesses [45]. Consequently, it is plausible that nuclear rotation can be affected by the shape of the nucleus via differences in friction. However, our results show that under these experimental conditions, the shapes of the nuclei were not significantly different on the hard and soft substrates. Therefore, we conclude that the observed substrate stiffness dependent nuclear rotation was not governed by differences in friction due to altered nuclear shape.

Our results show that nuclear rotation is dependent on substrate stiffness. The nucleus is biochemically and physically connected to the surrounding microenvironment by the cytoskeleton. Probing the ECM involves the interaction between the cytoskeleton and focal adhesion complexes [17–23]. Focal adhesion complexes are heavily involved in mechanosensing and mechanotransduction pathways [19,22,26,49,59–61]. It was found that the focal adhesions were larger and more punctate on the hard substrate compared to the soft substrate, consistent with observations made in previous studies [20,47,51]. In the presence of paclitaxel, no change in focal adhesion size was observed; however, the addition of blebbistatin altered focal adhesion size. Tension, traction forces, cytoskeletal organization, cytoskeletal dynamics, and complex signaling involving FAK, Rac, Rho, and ROCK are known to regulate focal adhesion size [17–20,62]. It is important to note that focal adhesion size does not dictate nuclear rotation. Clearly the cells are sensing the mechanical properties of their microenvironment, and the mechanical cues from the microenvironment affect intracellular dynamics. Further investigations must be performed to discover the exact mechanism

in which the mechanical cues of the extracellular matrix are sensed at focal adhesions, lead to cytoskeletal reorganization, and ultimately dictate nuclear dynamics and positioning.

Nuclear rotation is an ATP dependent process [2,5,8]; thus, it is logical to postulate that nuclear rotation serves an important function inside the cell because of its large energy cost. However, our results demonstrate that nuclear rotation is significantly suppressed on physiologically relevant substrate stiffnesses. The results from this study have important implications for the design of future studies. Unnaturally hard substrates do not only fail to mimic the in vivo microenvironment, but can also induce cellular processes that would not normally occur in the natural cellular environment.

Methods

Preparation of glutaraldehyde cross-linked gelatin (GXG) substrates

A sterile stock solution of Porcine Type-A Gelatin (GE) (Sigma-Aldrich) was made by autoclaving 20% (mg/mL) GE in distilled water. For the 4% (26 kPa) and 10% (100 kPa) GE substrates, the 20% stock solution was diluted with sterilized distilled water. Next, 1 mL of the GE solution was crosslinked with 8 μL of 50% glutaraldehyde (GA) (Sigma-Aldrich). The solution was spread evenly over the surface of a 35 mm plastic culture dish (TPP), which was placed in a humidity chamber and stored in the refrigerator overnight. The gels were then rinsed with cold phosphate buffer saline (PBS) three times. Excess unreacted GA was reduced with $NaBH_4$ (2.5 mg/ml) dissolved in cold PBS on ice for 1 h. The dishes were rinsed with PBS three times and then UV sterilized for 1 min (Spectroline UV Crosslinker Select Series). The GXG gels were incubated with 2 mL of cell culture media for 4 h at 37°C, 5% CO_2. After 4 h, cells were seeded onto the GXG substrates. For the hard control substrates, the cells were cultured directly on 0.1% GE coated glass coverslips.

Cell culture and drug treatments

C2C12 mouse myoblast cells were maintained at 37°C and 5% CO_2. The cells were cultured in Delbecco's Modified Eagle Medium – High Glucose (DMEM), supplemented with 10% fetal bovine serum and 1% penicillin/streptomycin (100 U/mL and 100 μg/mL respectively) (Hyclone Laboratories Inc.). Experiments were performed 24-48 h after cells were plated on the 0.1% GE or 4% GXG substrates in 35 mm culture dishes (TPP) containing 2.5 mL of DMEM. All drugs were added 30 min prior to the start of the experiment. The cytoskeletal drugs used were nocodazole (10 μM), paclitaxel (250 nM), and blebbistatin (50 μM). The stock solutions of the drugs were maintained in DMSO.

Immunofluorescence staining

Actin, microtubules, and focal adhesions:

The cells were fixed with 3.5% paraformaldehyde and permeabilized with 0.5% Triton X-100. Cells were then quenched in 0.15 M glycine for 25 min. Vinculin was labelled with a monoclonal anti-vinculin primary antibody produced in mouse (Invitrogen) (1:100 dilution, 30 min incubation) and a rabbit anti-mouse IgG secondary (Invitrogen) antibody conjugated to AlexaFluor 488 fluorophore (1:200 dilution, 30 min incubation). Microtubule staining was accomplished with an alpha-tubulin primary antibody produced in mouse and a rabbit anti-mouse IgG secondary (Invitrogen) antibody conjugated to AlexaFluor 488 fluorophore (each at a 1:200 dilution, 30 min incubations). During the microtubule staining the samples were kept on ice. Actin filaments were stained with Phalloidin Alexa Fluor 546 (Invitrogen) (1:100 dilution, 30 min incubation), and the nuclei were stained with DAPI (Invitrogen) (1:200 dilution, 30 min incubation). Following each step in the procedure, the samples were washed and incubated with blocking buffer (5% horse serum (Sigma) in PBS). After the staining, phosphate buffer saline (PBS) was added to the samples to maintain hydration before imaging.

Vimentin:

Cells were fixed with methanol at -20°C for 3 min. The samples were washed three times at room temperature for 10 min. The vimentin was labeled with a monoclonal anti-vimentin primary antibody produced in rabbit (Abcam) (1:200 dilution, 1 h). After three PBS washes for 10 min, a goat anti-rabbit IgG secondary antibody (Invitrogen) conjugated to Alexa Fluor 488 (1:200 dilution, 30 min) and DAPI (Invitrogen) (1:200, 30 min) were added. After the staining, PBS was added to the samples to maintain hydration before imaging.

Atomic force microscopy

A Nanowizard II atomic force microscope (AFM) (JPK Instruments, Germany) was used to determine the substrate elasticity in all experiments. PNP-TR-50 cantilevers were used for each measurement and had an experimentally determined spring constant of 63.5 ± 7.2 mN/m. Force-indentation curves were acquired on substrates at 546 Hz with a set point of 1.0 nN. Substrate elasticity was calculated by fitting the force curves to the Sneddon-Hertz model for a conical indenter for shallow 200 nm indentations, assuming a Poisson ratio of 0.5 (PUNIAS 3D Software). For each substrate, N = 3 plates were prepared and 10 force curves were acquired at 25 random locations on the substrate for a total of 250 force curves.

Time-lapse microscopy and laser scanning confocal microscopy

Time-lapse phase contrast microscopy was performed on a Nikon Eclipse TiE epi-fluorescence and phase contrast microscope (Nikon, Canada). Nuclear rotation was monitored by acquiring a phase contrast image every 10 min for 12 h with a CCD camera (Photometric Cool Snap HQ^2) and a 10X objective lens. To ensure cell viability, cells were maintained at 37°C and 5% CO_2 on the microscope stage for the duration of the experiment. In some cases, the cells were imaged with laser scanning confocal microscopy. The confocal microscopy was used to image microtubules, intermediate filaments, actin, and DNA. A Nikon TiE A1-R high speed resonant scanner confocal microscope was used with a 60X water immersion objective. Confocal images presented here are maximum intensity z-projections of confocal volumes. Brightness/contrast settings were adjusted to maximize the fluorophore signal; otherwise, no other image manipulations were performed.

Quantification of nuclear rotation

Fiji ImageJ manual tracker and MTrackJ plugins were used to track the nucleoli over the course of the time-lapse experiment. The x,y positions of the nucleoli and the nucleus centroid were recorded. To account for the translational movement of the cells, the x,y coordinates of the nucleus centroid was subtracted from the x,y coordinates of the nucleoli. Origin 8.5 was used to calculate the angle of rotation and the angular velocity of rotation.

Quantification of nuclear shape

The nuclei were imaged using confocal microscopy. The maximum intensity z-projections were thresholded, and the circularity (C) of the nuclei was calculated using the Fiji ImageJ analyze particles plugin as $C = 4\pi \frac{area}{perimeter^2}$. The apparent nuclear height was measured from the orthogonal views of the confocal stacks in Fiji ImageJ.

Quantification of focal adhesion size

Focal adhesion complexes were imaged using confocal microscopy. The images were segmented and thresholded using the adaptive thresholding plugin available in Fiji ImageJ. The lower limit for the focal adhesion size was set to 0.25 μm^2. The focal adhesion sizes were measured using the Fiji ImageJ analyze particles plugin.

Quantification of vimentin intermediate filament cell area coverage

The vimentin intermediate filaments were imaged using confocal microscopy. The maximum z-projections were thresholded using the adaptive thresholding plugin available in Fiji ImageJ. The Fiji ImageJ analyze particles plugin was used to measure the area of the vimentin network. The lower limit for the particle size was set to 0.05 μm^2.

Statistical analysis

One-way ANOVA tests were used to identify statistical differences of the characteristics of nuclear rotation between the different substrates in the presence of the cytoskeletal drugs. The Tukey post hoc analysis was completed to decipher the statistical difference between the individual samples. For the comparison of more than two samples, the one-way ANOVA was used instead of multiple Student's t-tests to reduce the risk of type 1 statistical errors. When only two samples were compared, the Student's t-test was used. A one-tailed Student's t-test was used to compare the percentage of cells rotating for the nocodazole treated cells on the hard and soft samples to the null hypothesis value $H_0 = 0\%$. All values presented are the mean ± the standard error of the mean (s.e.m). The standard error of the mean was used instead of the standard deviation because when dealing with biological samples it is not possible to study the whole population; instead, a representative sample is used as an estimate for the population. Statistical significance refers to $P < 0.05$. The asterisks in the figures signify a statistically significant difference relative to the control for the corresponding substrate.

Acknowledgments

This work was supported by a Natural Sciences and Engineering Research Council (NSERC) Discovery Grant. R.H. was supported by an NSERC postgraduate scholarship and an Ontario Graduate Scholarship (OGS). A.E.P. gratefully acknowledges generous support from the Canada Research Chairs (CRC) program.

References

(1) Brosig, M.; Ferralli, J.; Gelman, L.; Chiquet, M.; Chiquet-Ehrismann, R. Interfering with the connection between the nucleus and the cytoskeleton affects nuclear rotation, mechanotransduction and myogenesis. *Int. J. Biochem. Cell Biol.* **2010**, *42* (10), 1717–1728 DOI: 10.1016/j.biocel.2010.07.001.

(2) Ji, J. Y.; Lee, R. T.; Vergnes, L.; Fong, L. G.; Stewart, C. L.; Reue, K.; Young, S. G.; Zhang, Q.; Shanahan, C. M.; Lammerding, J. Cell nuclei spin in the absence of lamin b1. *J. Biol. Chem.* **2007**, *282* (27), 20015–20026 DOI: 10.1074/jbc.M611094200.

(3) Kumar, A.; Maitra, A.; Sumit, M.; Ramaswamy, S.; Shivashankar, G. V. Actomyosin contractility rotates the cell nucleus. *Sci. Rep.* **2014**, *4*, 3781 DOI: 10.1038/srep03781.

(4) Lammerding, J.; Hsiao, J.; Schulze, P. C.; Kozlov, S.; Stewart, C. L.; Lee, R. T. Abnormal nuclear shape and impaired mechanotransduction in emerin-deficient cells. *J. Cell Biol.* **2005**, *170* (5), 781–791 DOI: 10.1083/jcb.200502148.

(5) Levy, J. R.; Holzbaur, E. L. F. Dynein drives nuclear rotation during forward progression of motile fibroblasts. *J. Cell Sci.* **2008**, *121* (Pt 19), 3187–3195 DOI: 10.1242/jcs.033878.

(6) Paddock, S. W.; Albrecht-Buehler, G. Rigidity of the nucleus during nuclear rotation in 3T3 cells. *Exp. Cell Res.* **1988**, *175* (2), 409–413 DOI: 10.1515/ling.1988.26.5.873.

(7) Park, P. C.; De Boni, U. Dynamics of nucleolar fusion in neuronal interphase nuclei in vitro: association with nuclear rotation. *Exp. Cell Res.* **1991**, *197* (2), 213–221.

(8) Wilson, M. H.; Holzbaur, E. L. F. Opposing microtubule motors drive robust nuclear dynamics in developing muscle cells. *J. Cell Sci.* **2012**, *125* (Pt 17), 4158–4169 DOI: 10.1242/jcs.108688.

(9) Yao, K. T.; Ellingson, D. J. Observations on nuclear rotation and oscillation in Chinese hamster germinal cells in vitro. *Exp. Cell Res.* **1969**, *55* (1), 39–42.

(10) Gerashchenko, M. V.; Chernoivanenko, I. S.; Moldaver, M. V.; Minin, A. A. Dynein is a motor for nuclear rotation while vimentin IFs is a “brake”. *Cell Biol. Int.* **2009**, *33* (10), 1057–1064 DOI: 10.1016/j.cellbi.2009.06.020.

(11) Wu, J.; Lee, K. C.; Dickinson, R. B.; Lele, T. P. How dynein and microtubules rotate the nucleus. *J. Cell. Physiol.* **2011**, *226* (10), 2666–2674 DOI: 10.1002/jcp.22616.

(12) Mattioli, E.; Columbaro, M.; Capanni, C.; Maraldi, N. M.; Cenni, V.; Scotlandi, K.; Marino, M. T.; Merlini, L.; Squarzoni, S.; Lattanzi, G. Prelamin A-mediated recruitment of SUN1 to the nuclear envelope directs nuclear positioning in human muscle. *Cell Death Differ.* **2011**, *18* (8), 1305–1315 DOI: 10.1038/cdd.2010.183.

(13) Boni, U. De; Mintz, A. H. Curvilinear, three-dimensional motion of chromatin domains and nucleoli in neuronal interphase nuclei. *Sci.* **1986**, *234* (4778), 863–866.

(14) Paddock, S. W.; Albrecht-Buehler, G. Distribution of microfilament bundles during rotation of the nucleus in 3T3 cells treated with monensin. *Exp. Cell Res.* **1986**, *163* (2),

525–538.

(15) Paddock, S. W.; Albrecht-Buehler, G. The degree of coupling of nuclear rotation in binucleate 3T3 cells. *Exp. Cell Res.* **1986**, *166* (1), 113–126.

(16) Jaalouk, D. E.; Lammerding, J. Mechanotransduction gone awry. *Nat. Rev. Mol. Cell Biol.* **2009**, *10* (1), 63–73 DOI: 10.1038/nrm2597.

(17) Tsuruta, D.; Jones, J. C. R. The vimentin cytoskeleton regulates focal contact size and adhesion of endothelial cells subjected to shear stress. *J. Cell Sci.* **2003**, *116* (Pt 24), 4977–4984 DOI: 10.1242/jcs.00823.

(18) Ezratty, E. J.; Partridge, M. A.; Gundersen, G. G. Microtubule-induced focal adhesion disassembly is mediated by dynamin and focal adhesion kinase. *Nat. Cell Biol.* **2005**, *7* (6), 581–590 DOI: 10.1038/ncb1262.

(19) Burridge, K.; Chrzanowska-Wodnicka, M. Focal adhesions, contractility, and signaling. *Annu. Rev. Cell Dev. Biol.* **1996**, *12*, 463–518 DOI: 10.1146/annurev.cellbio.12.1.463.

(20) Al-Rekabi, Z.; Haase, K.; Pelling, A. E. Microtubules mediate changes in membrane cortical elasticity during contractile activation. *Exp. Cell Res.* **2014**, *322* (1), 21–29 DOI: 10.1016/j.yexcr.2013.12.027.

(21) Del Álamo, J. C.; Meili, R.; Álvarez-González, B.; Alonso-Latorre, B.; Bastounis, E.; Firtel, R.; Lasheras, J. C. Three-dimensional quantification of cellular traction forces and mechanosensing of thin substrata by fourier traction force microscopy. *PLoS One* **2013**, *8* (9), e69850 DOI: 10.1371/journal.pone.0069850.

(22) Al-Rekabi, Z.; Pelling, A. E. Cross talk between matrix elasticity and mechanical force regulates myoblast traction dynamics. *Phys. Biol.* **2013**, *10* (6), 066003 DOI: 10.1088/1478-3975/10/6/066003.

(23) Legant, W. R.; Choi, C. K.; Miller, J. S.; Shao, L.; Gao, L.; Betzig, E.; Chen, C. S. Multidimensional traction force microscopy reveals out-of-plane rotational moments about focal adhesions. *Proc. Natl. Acad. Sci. U. S. A.* **2013**, *110* (3), 881–886 DOI: 10.1073/pnas.1207997110.

(24) Engler, A. J.; Sen, S.; Sweeney, H. L.; Discher, D. E. Matrix elasticity directs stem cell lineage specification. *Cell* **2006**, *126* (4), 677–689 DOI: 10.1016/j.cell.2006.06.044.

(25) Discher, D. E.; Janmey, P.; Wang, Y. Tissue cells feel and respond to the stiffness of their substrate. *Sci.* **2005**, *310* (5751), 1139–1143.

(26) Buxboim, A.; Ivanovska, I. L.; Discher, D. E. Matrix elasticity, cytoskeletal forces and physics of the nucleus: how deeply do cells “feel” outside and in? *J. Cell Sci.* **2010**, *123* (Pt 3), 297–308 DOI: 10.1242/jcs.041186.

(27) Wirtz, D.; Konstantopoulos, K.; Searson, P. C. The physics of cancer : the role of physical interactions and mechanical forces in metastasis. *Nat. Rev. cancer* **2011**, *11* (7), 512–522.

(28) Shinohara, M.; Sabra, K.; Gennisson, J.-L.; Fink, M.; Tanter, M. Real-time visualization of muscle stiffness distribution with ultrasound shear wave imaging during muscle contraction. *Muscle Nerve* **2010**, *42* (3), 438–441 DOI: 10.1002/mus.21723.

(29) Choudhury, N.; Bouchot, O.; Rouleau, L.; Tremblay, D.; Cartier, R.; Butany, J.; Mongrain, R.; Leask, R. L. Local mechanical and structural properties of healthy and diseased human ascending aorta tissue. *Cardiovasc. Pathol.* **2009**, *18* (2), 83–91 DOI: 10.1016/j.carpath.2008.01.001.

(30) Collinsworth, A. M.; Zhang, S.; Kraus, W. E.; Truskey, G. A. Apparent elastic modulus and hysteresis of skeletal muscle cells throughout differentiation. *Am. J. Physiol. Cell Physiol.* **2002**, *283* (4), C1219-27 DOI: 10.1152/ajpcell.00502.2001.

(31) Mathur, A. B.; Collinsworth, A. M.; Reichert, W. M.; Kraus, W. E.; Truskey, G. A. Endothelial, cardiac muscle and skeletal muscle exhibit different viscous and elastic properties as determined by atomic force microscopy. *J. Biomech.* **2001**, *34* (12), 1545–1553.

(32) Nyland, L. R.; Maughan, D. W. Morphology and transverse stiffness of Drosophila myofibrils measured by atomic force microscopy. *Biophys. J.* **2000**, *78* (3), 1490–1497 DOI: 10.1016/S0006-3495(00)76702-6.

(33) Ogneva, I. V. Transversal stiffness of fibers and desmin content in leg muscles of rats under gravitational unloading of various durations. *J. Appl. Physiol.* **2010**, *109* (6), 1702–1709 DOI: 10.1152/japplphysiol.00793.2010.

(34) Ogneva, I. V.; Lebedev, D. V.; Shenkman, B. S. Transversal stiffness and Young's modulus of single fibers from rat soleus muscle probed by atomic force microscopy. *Biophys. J.* **2010**, *98* (3), 418–424 DOI: 10.1016/j.bpj.2009.10.028.

(35) Engler, A. J.; Griffin, M. a; Sen, S.; Bönnemann, C. G.; Sweeney, H. L.; Discher, D. E. Myotubes differentiate optimally on substrates with tissue-like stiffness: pathological implications for soft or stiff microenvironments. *J. Cell Biol.* **2004**, *166* (6), 877–887 DOI: 10.1083/jcb.200405004.

(36) Metzger, T.; Gache, V.; Xu, M.; Cadot, B.; Folker, E. S.; Richardson, B. E.; Gomes, E. R.; Baylies, M. K. MAP and kinesin-dependent nuclear positioning is required for skeletal muscle function. *Nature* **2012**, *484* (7392), 120–124 DOI: 10.1038/nature10914.

(37) Schulman, V. K.; Folker, E. S.; Rosen, J. N.; Baylies, M. K. Syd/JIP3 and JNK signaling are required for myonuclear positioning and muscle function. *PLoS Genet.* **2014**, *10* (12), e1004880 DOI: 10.1371/journal.pgen.1004880.

(38) Folker, E. S.; Schulman, V. K.; Baylies, M. K. Muscle length and myonuclear position are independently regulated by distinct Dynein pathways. *Development* **2012**, *139* (20), 3827–3837 DOI: 10.1242/dev.079178.

(39) Folker, E. S.; Schulman, V. K.; Baylies, M. K. Translocating myonuclei have distinct leading and lagging edges that require Kinesin and Dynein. *Development* **2014**, *141* (2), 355–366 DOI: 10.1242/dev.095612.

(40) Folker, E. S.; Baylies, M. K. Nuclear positioning in muscle development and disease. *Front. Physiol.* **2013**, *4* (December), 363 DOI: 10.3389/fphys.2013.00363.

(41) Ali, S.; Wall, I. B.; Mason, C.; Pelling, A. E.; Veraitch, F. S. The effect of Young's modulus on the neuronal differentiation of mouse embryonic stem cells. *Acta Biomater.*

2015, *25*, 253–267 DOI: 10.1016/j.actbio.2015.07.008.

(42) Nyland, L. R.; Maughan, D. W. Morphology and transverse stiffness of Drosophila myofibrils measured by atomic force microscopy. *Biophys. J.* **2000**, *78* (3), 1490–1497 DOI: 10.1016/S0006-3495(00)76702-6.

(43) Carl, P.; Schillers, H. Elasticity measurement of living cells with an atomic force microscope: data acquisition and processing. *Pflugers Arch.* **2008**, *457* (2), 551–559 DOI: 10.1007/s00424-008-0524-3.

(44) Solon, J.; Levental, I.; Sengupta, K.; Georges, P. C.; Janmey, P. A. Fibroblast adaptation and stiffness matching to soft elastic substrates. *Biophys. J.* **2007**, *93* (12), 4453–4461 DOI: 10.1529/biophysj.106.101386.

(45) Lovett, D. B.; Shekhar, N.; Nickerson, J. A.; Roux, K. J.; Lele, T. P. Modulation of nuclear shape by substrate rigidity. *Cell. Mol. Bioeng.* **2013**, *6* (2), 230–238 DOI: 10.1007/s12195-013-0270-2.

(46) Dupont, S. Role of YAP/TAZ in cell-matrix adhesion-mediated signalling and mechanotransduction. *Exp. Cell Res.* **2015** DOI: 10.1016/j.yexcr.2015.10.034.

(47) Wormer, D. B.; Davis, K. A.; Henderson, J. H.; Turner, C. E. The focal adhesion-localized CdGAP regulates matrix rigidity sensing and durotaxis. *PLoS One* **2014**, *9* (3), e91815 DOI: 10.1371/journal.pone.0091815.

(48) Gregor, M.; Osmanagic-myers, S.; Burgstaller, G.; Wolfram, M.; Fischer, I.; Walko, G.; Resch, G. P.; Jörgl, A.; Herrmann, H.; Wiche, G. Mechanosensing through focal adhesion-anchored intermediate filaments. *FASEB J.* **2014**, *28* (2), 715–729 DOI: 10.1096/fj.13-231829.

(49) Grashoff, C.; Hoffman, B. D.; Brenner, M. D.; Zhou, R.; Parsons, M.; Yang, M. T.; McLean, M. a; Sligar, S. G.; Chen, C. S.; Ha, T.; et al. Measuring mechanical tension across vinculin reveals regulation of focal adhesion dynamics. *Nature* **2010**, *466* (7303), 263–266 DOI: 10.1038/nature09198.

(50) Graham, Z. A.; Gallagher, P. M.; Cardozo, C. P. Focal adhesion kinase and its role in skeletal muscle. *J. Muscle Res. Cell Motil.* **2015** DOI: 10.1007/s10974-015-9415-3.

(51) Yip, A. K.; Iwasaki, K.; Ursekar, C.; Machiyama, H.; Saxena, M.; Chen, H.; Harada, I.; Chiam, K.-H.; Sawada, Y. Cellular response to substrate rigidity is governed by either stress or strain. *Biophys. J.* **2013**, *104* (1), 19–29 DOI: 10.1016/j.bpj.2012.11.3805.

(52) Pelham Jr., R. J.; Wang, Y.-L. Cell locomotion and focal adhesions are regulated by substrate flexibility. *Proc. Natl. Acad. Sci. U. S. A.* **1997**, *94* (25), 13661–13665.

(53) Wells, R. G. The role of matrix stiffness in regulating cell behavior. *Hepatology* **2008**, *47* (4), 1394–1400 DOI: 10.1002/hep.22193.

(54) Even-Ram, S.; Doyle, A. D.; Conti, M. A.; Matsumoto, K.; Adelstein, R. S.; Yamada, K. M. Myosin IIA regulates cell motility and actomyosin–microtubule crosstalk. *Nat. Cell Biol.* **2007**, *9* (3), 299–309 DOI: 10.1038/ncb1540.

(55) Robert, A.; Herrmann, H.; Davidson, M. W.; Gelfand, V. I. Microtubule-dependent

transport of vimentin filament precursors is regulated by actin and by the concerted action of Rho- and p21-activated kinases. *FASEB J.* **2014**, *28* (7), 2879–2890 DOI: 10.1096/fj.14-250019.

(56) Hookway, C.; Ding, L.; Davidson, M. W.; Rappoport, J. Z.; Danuser, G.; Gelfand, V. I. Microtubule-dependent transport and dynamics of vimentin intermediate filaments. *Mol. Biol. Cell* **2015**, *26* (9), 1675–1686 DOI: 10.1091/mbc.E14-09-1398.

(57) Murray, M. E.; Mendez, M. G.; Janmey, P. A. Substrate stiffness regulates solubility of cellular vimentin. *Mol. Biol. Cell* **2014**, *25* (1), 87–94 DOI: 10.1091/mbc.E13-06-0326.

(58) Ory, S.; Destaing, O.; Jurdic, P. Microtubule dynamics differentially regulates Rho and Rac activity and triggers Rho-independent stress fiber formation in macrophage polykaryons. *Eur. J. Cell Biol.* **2002**, *81* (6), 351–362 DOI: 10.1078/0171-9335-00255.

(59) Balaban, N. Q.; Schwarz, U. S.; Riveline, D.; Goichberg, P.; Tzur, G.; Sabanay, I.; Mahalu, D.; Safran, S.; Bershadsky, a; Addadi, L.; et al. Force and focal adhesion assembly: a close relationship studied using elastic micropatterned substrates. *Nat. Cell Biol.* **2001**, *3* (5), 466–472 DOI: 10.1038/35074532.

(60) McCain, M. L.; Parker, K. K. Mechanotransduction: the role of mechanical stress, myocyte shape, and cytoskeletal architecture on cardiac function. *Pflugers Arch.* **2011**, *462* (1), 89–104 DOI: 10.1007/s00424-011-0951-4.

(61) Plotnikov, S. V; Waterman, C. M. Guiding cell migration by tugging. *Curr. Opin. Cell Biol.* **2013**, *25* (5), 619–626 DOI: 10.1016/j.ceb.2013.06.003.

(62) Mitra, S. K.; Hanson, D. a; Schlaepfer, D. D. Focal adhesion kinase: in command and control of cell motility. *Nat. Rev. Mol. Cell Biol.* **2005**, *6* (1), 56–68 DOI: 10.1038/nrm1549.

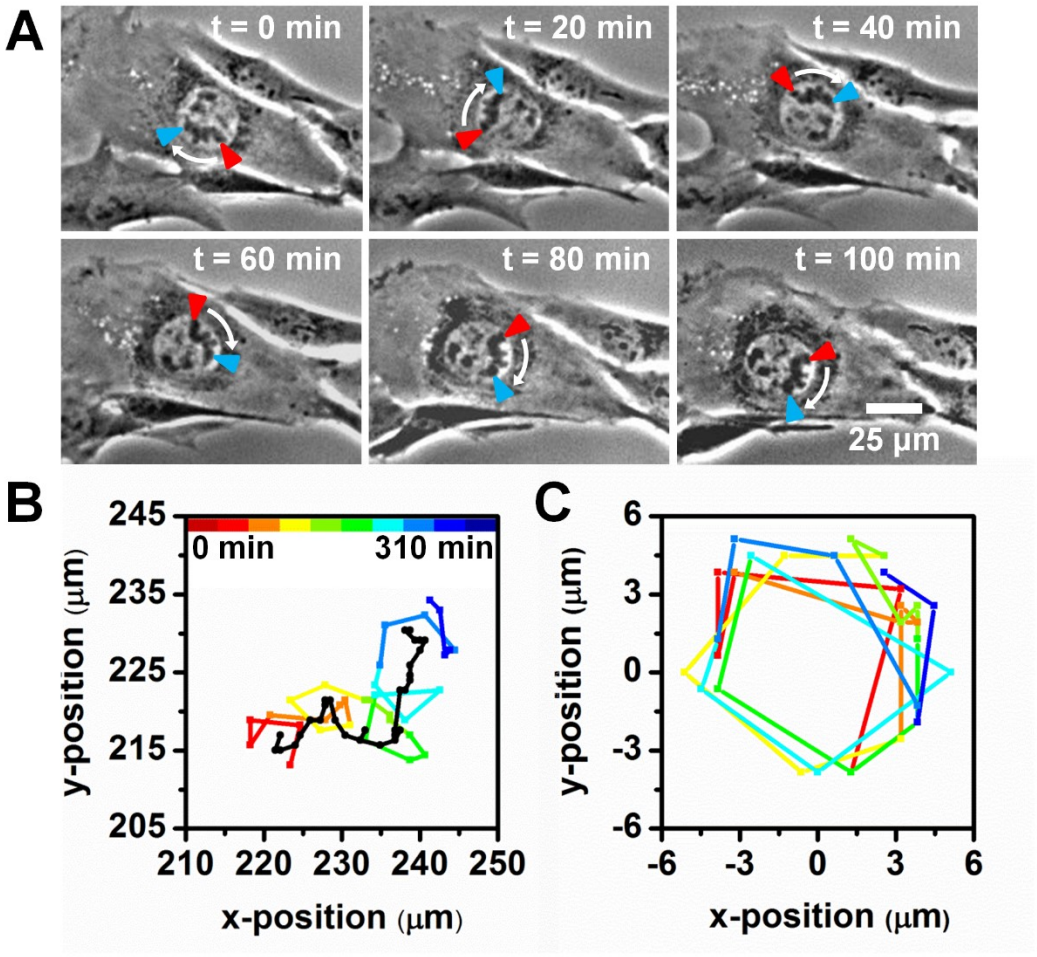

Supplementary Figure S1: Tracking cellular nuclear rotation. The ImageJ plugin MTrackJ was used to track the x,y positions of the nucleoli and the centre of the nucleus. (A) A phase contrast time-lapse experiment of a C2C12 myoblast undergoing nuclear rotation. Two nucleoli are highlighted by the red and blue arrow heads. The white arrow depicts the clockwise direction of the nuclear rotation. (B) Nuclear rotation and translation of a C2C12 myoblast nucleus. Tracks of a single nucleolus (colour) and the centre of the nucleus (black). The time is represented in the colour map (red=start, blue=end). (C) Corrected nuclear rotation. The translational movement was corrected for by subtracting the coordinates of the centre of the nucleus from the coordinates of each nucleolus.

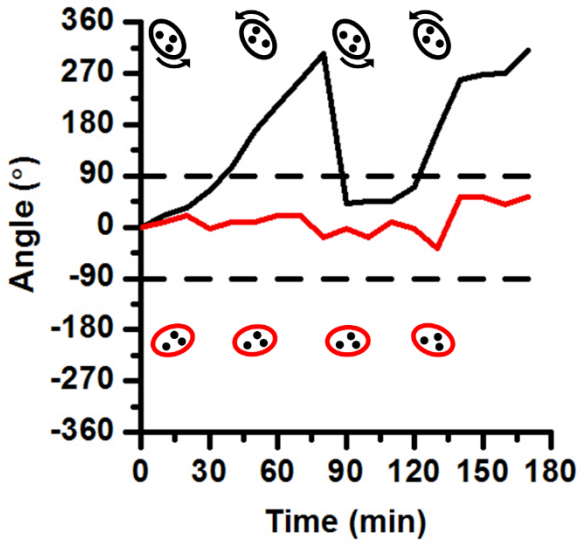

Supplementary Figure S2: Defining nuclear rotation. The nucleolar positions normalized to 360° were plotted as a function of time. Nuclei that rotated more than ± 90° were identified as rotating nuclei (black line) while nuclei that rotated less than ± 90° were identified as non-rotating nuclei (red line). The ± 90° critical angle for nuclear rotation is indicated by the dashed lines.

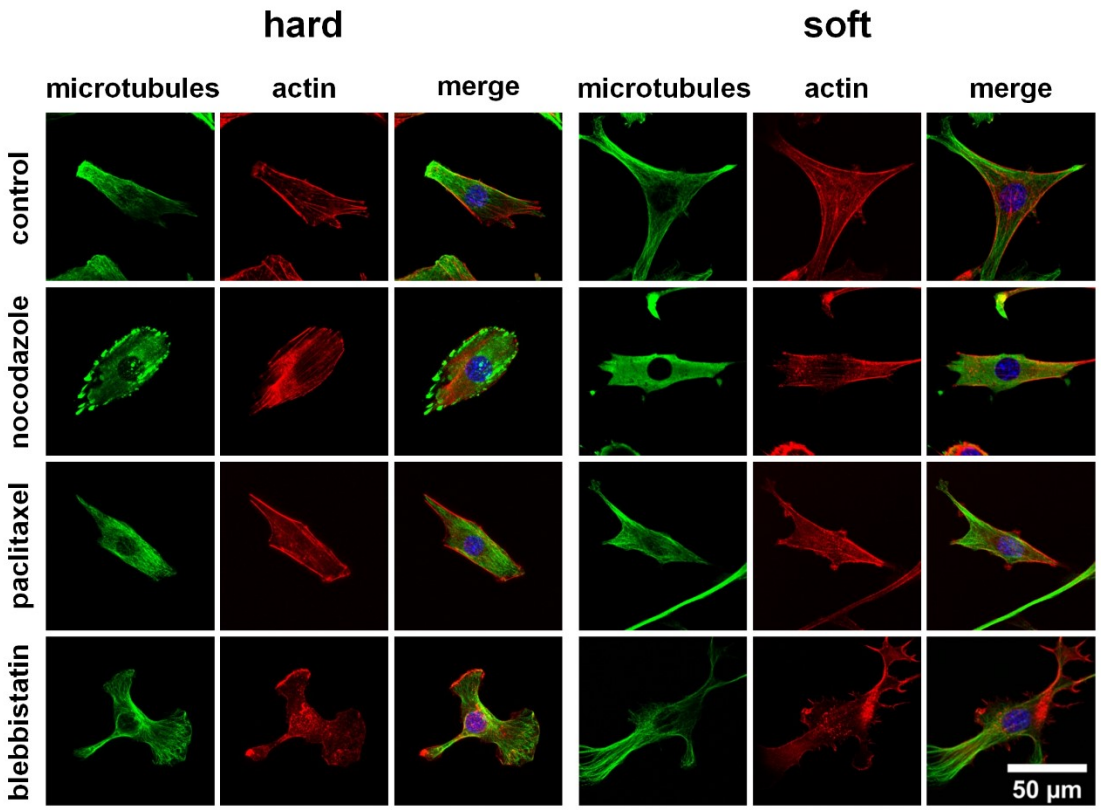

Supplementary Figure S3: Effects of microtubule and actin drugs. The microtubules (green), actin filaments (red), and DNA (blue) were stained in the presence of the cytoskeletal drugs nocodazole, paclitaxel, and blebbistatin on the hard and soft substrates. The hard substrate was glass with a thin layer of gelatin, and the soft substrate was a GXG hydrogel.